Massive Ice and Topographic Controls on Retrogressive Thaw Slump Dynamics: Peninsula Point, Western Canadian Arctic

Samuel J. Hayes

Northumbria University
NEWCASTLE

PhD

2020

Massive Ice and Topographic Controls on Retrogressive Thaw Slump Dynamics: Peninsula Point, Western Canadian Arctic

Samuel Hayes

A thesis submitted in partial fulfilment of the requirements of the University of Northumbria at Newcastle for the degree of Doctor of Philosophy

This research was undertaken in the Faculty of Engineering and Environment

June 2020

Abstract

Retrogressive Thaw Slumps (RTSs) — a highly dynamic form of mass wasting, are now exerting a dominant influence on geomorphic changes in the ice-cored terrain of the western Canadian Arctic. However, the main controls on their activity are poorly understood. This research aims to assess the response of RTS dominated coasts to variations in massive ice and terrain morphology. This is achieved through a multi-scale analysis of Peninsula Point — the site type for intra-sedimental massive ice. Long-term coastal change, up to 2018, is assessed using a range of metrics, including shoreline retreat (SLR) from 1935, headwall retreat (HWR) from 1994, and topographic and volumetric analysis from 2004. Inter-annual variations and fine-scale characteristics of coastal change are explored through quantitative analysis of the high-resolution structure from motion multi-view stereo data, sedimentological analysis and the novel application of passive seismic monitoring for detecting and mapping subsurface massive ice and overburden variations. Modern observations, published descriptions and historic aerial photos are used to assess changes in massive ice since 1935. Between 2016 and 2018, headwalls containing an overburden of less than 4 m in all years and an exposure of massive ice (regardless of thickness) in 2018 retreated over three times faster than other active headwalls. Furthermore, passive seismic surveys in 2017 allowed for the creation of a 3D site model, highlighting both the cross-shore and along-shore variability in the massive ice surface elevation and overburden thickness. The modelled ice closely matched subsequent observations in 2018, allowing for an accurate prediction of the relative HWR rates between 2017 and 2018. Nearshore elevation and slope display statistically significant, but weak, correlations with SLR, HWR and volume loss between 2004 and 2018, while variability in massive ice thickness and surface elevation strongly modulates both the strength and direction of these correlations. The long-term SLR rate on Peninsula Point was reduced from 5.8 m a^{-1} between 1935 and 1985, to 3.4 m a^{-1} from 1985 to 2018, in contrast with other ice-rich coasts. This disparity is explained by a thinning of the massive ice body, from widespread exposures of 5 m to 10 m during the 20th century, to patchy, thin exposures with maximum thicknesses under 5 m in recent years. The overall results have been condensed into a series of conceptual models, illustrating the coastal geomorphic response to massive ice. This research highlights how massive ice variability shapes coastal dynamics across a range of time scales, how the ice surface can be mapped by non-invasive means and the data used to improve predictions of coastal change. By allowing for more refined estimates of variability in SLR and volume loss, these findings have implications for the planning and protection of coastal infrastructure, quantifying the nutrient and sediment input to the nearshore zone and in assessing the past and future contribution of permafrost coastal change to global carbon budgets.

Table of Contents

List of Figures

List of Tables

List of Acronyms and Abbreviations

ACDD	Arctic Coastal Dynamics Database
ALD	Active Layer Depth
ALI	Advanced Land Imager
AO	Arctic Oscillation
BP	Before Present
CC	Cloud Compare
CMOS	Complementary Metal-Oxide-Semiconductor
CSLM	Continuous Surface Layer Model
CSV	Comma Separated Value
CTS	Conductivity, Total dissolved solids and Salinity
DEM	Digital Elevation Model
DI	Depth to Ice
DJI	Dà-Jiāng Innovations
ESRI	Environmental Systems Research Institute
ETM+	Enhanced Thematic Mapper Plus
GCP	Ground Control Point
GPS	Global Positioning System
GRASS	Geographic Resources Analysis Support System
HWR	Headwall Retreat
IDW	Inverse Distance Weighting
IT	Ice Thickness
LiDAR	Light Detection and Ranging
MAE	Mean Absolute Error
MP	Megapixel
NAD	North American Datum
NIR	Near Infra-Red
NRCan	Natural Resources Canada
OB	Overburden
PI	Proportion of Ice
PRTS	Polycyclic Retrogressive Thaw Slump
P4	Phantom 4
QTM	Quick Terrain Modeller
RMSE	Root Mean Square Error
RTK	Realtime Kinematic Differential Global Navigation System
RTS	Retrogressive Thaw Slump

SD	Standard Deviation
SfM-MVS	Structure from Motion Multi-View Stereo
SL2HW	Shoreline to Headwall
SLR	Shoreline Retreat
SWIR	Short Wave Infra-Red
TDS	Total Dissolved Solids
UTM	Universal Transverse Mercator
WGS	World Geodetic System
2CR	Twentieth Century Reanalysis

List of Definitions

Shoreline Retreat	Inland movement of the land/water boundary
Polycyclic Retrogressive Thaw Slump	A retrogressive thaw slump that has undergone two or more phases of activity
Ice Rich	Where ice volume of a soil exceeds that of total unfrozen pore volume
Massive Ice	Where soil ice content is more than 250% of the dry soil by weight
Quasi-cyclic	Resembling a cyclic pattern
2.5 Dimensional	A surface layer where each individual X-Y location can only have a single Z value
3 Dimensional	A 2.5D surface that includes internal layering, allowing individual X-Y locations to have more than one Z value

Acknowledgements

This thesis has proven to be a major challenge, and one I am incredibly glad to have overcome. I would not have lasted long enough to even write this acknowledgments section if it was not for the contribution of many people.

To my supervisors, Dr Mike Lim, Dr Paul Mann, Dr Roger Penlington and Dr James Martin. Mike, for providing me with this opportunity, for the guidance, patience and great whisky recommendations, thank you! Paul, your input and perspective has been invaluable throughout this process. Roger, although the research focus shifted from the initial plans, our chats early provided clarification on topics and put my mind at ease. James, the passive seismic noise would have remained largely as just noise without your help and calm explanations.

The feedback provided by Dr Robert Devoy and Dr Matt Westoby improved the structure, flow and robustness of the work, for which I am very grateful.

I am grateful to many of the geography and engineering staff, too numerous to name, for the assistance in the labs, training, advice and the odd fun night out in Toon!

The fieldwork around Tuktoyaktuk was one of the greatest experiences of my life. To those involved, from Natural Resources Canada, Aurora Research Institute, and the people of Tuktoyaktuk: Dustin Whalen, Vladimir Kostylev, Paul Fraser, Roger Macleod, Scott Dallimore, Emily Wai-Nee, Erika Hille, Andrew Gordon, Frank Pokiak and many others, you have my sincere appreciation. I am also indebted to the staff at INTERACT. The fieldwork would not have been possible without their transnational access grant, for which I am truly grateful.

To my partner, Zainab. Your love, laughter and wit helped pull my mind out from the PhD abyss.

My family – Mum (Susan), Dad (John), Alex, Amy, Courtney and Faye, none of this would have been possible without the love and support you have provided, and on which I can always rely. I can never express my gratitude and appreciation adequately.

To anyone whom I have shamefully left out, *go raibh maith agaibh*!

Declaration

I, Samuel Hayes, declare that the work contained in this thesis has not been submitted for any other award and that it is all my own work. I also confirm that this work fully acknowledges opinions, ideas and contributions from the work of others.

Any ethical clearance for the research presented in this thesis has been approved. Approval has been sought and granted by the University Ethics Committee on 14/07/2017

I declare that the word count of this thesis is: 51,913

Name: Samuel Hayes

Signature:

Date: 10/06/2020

1 Introduction

1.1 Permafrost

Permafrost, ground which has remained below 0°C for at least two consecutive years, underlies about 25% of the world's land surface and up to 34% of the global coastline (Lantuit *et al.,* 2012a; Marchenko & Etzelmuller, 2014). The majority of this exists in the northern hemisphere, primarily in the Arctic (Figure 1.1), but is also a feature of exposed parts of Antarctica and many high elevation environments. Permafrost can also be found in the shallow Arctic coastal shelves, especially along the Eurasian coastlines. This is a relic from the last ice age when eustatic sea level variability exposed the continental shelf to the cold sub-aerial Arctic environment resulting in permafrost formation, before being inundated during the Holocene sea level rise (Lantuit, 2016).

Permafrost varies from continuous spatial coverage over the most northern terrestrial regions, with depths of up to 1,600 m measured in northern Siberia (Brown, 1967), to patchy, shallow permafrost in more southern and maritime locations. It can contain a range of geotechnically diverse materials on vertical and horizontal scales, with large variations occurring from one region to another. These include, but are not limited to:

- a seasonally thawed active layer
- massive ice bodies
- unfrozen talik layers
- ice wedges
- peat
- variable soil and sediment types

Additionally, a large range of volumetric ice contents can also occur. Furthermore, the characteristics of these soils will vary based on their absolute and relative temperatures, often switching from brittle to ductile as they thaw. Taken together, these features make permafrost soils a particularly challenging material to understand and model.

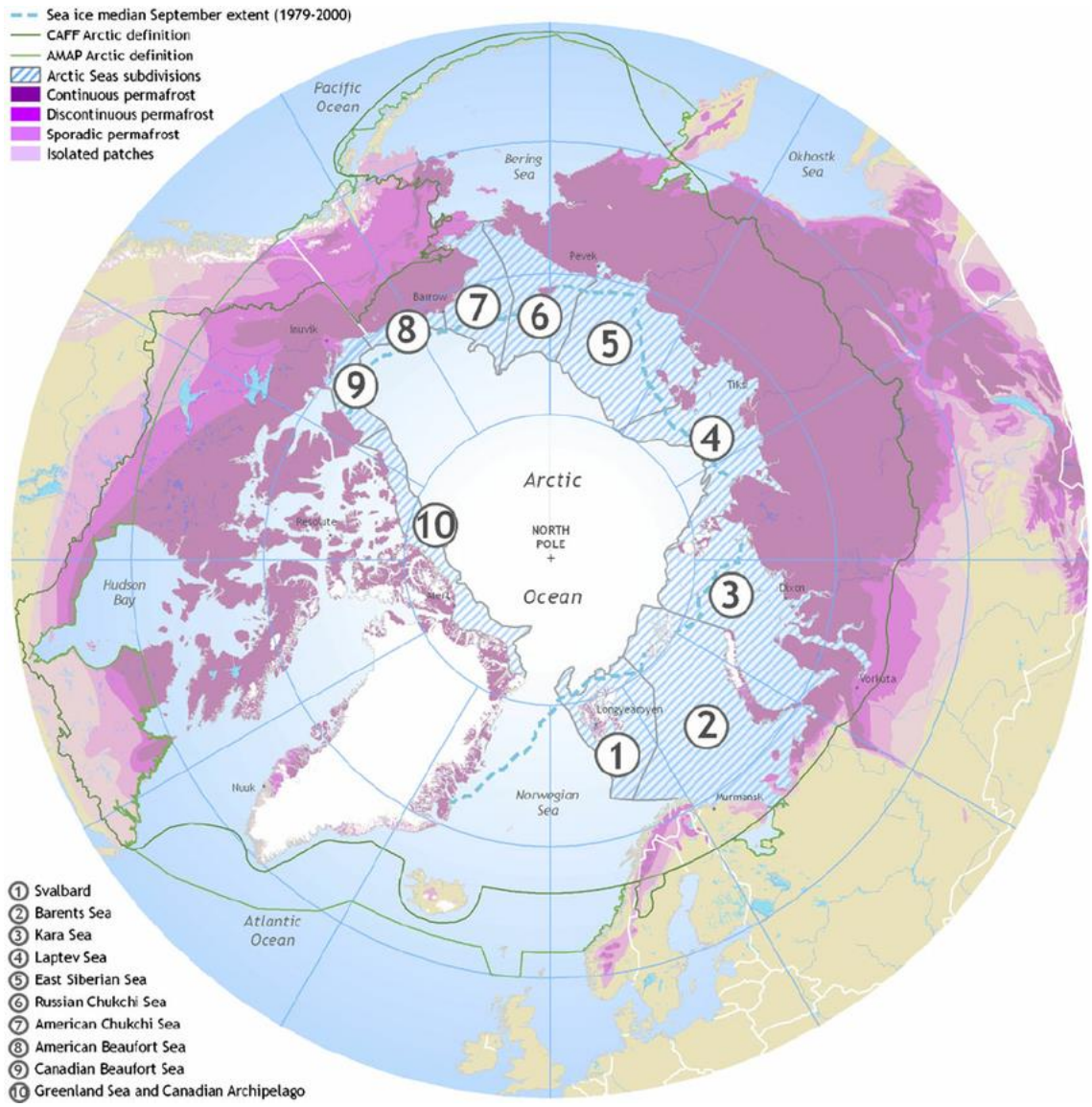

Figure 1.1: Distribution of permafrost and permafrost coasts. Adapted from Lantuit et al., 2012a

1.2 Arctic Permafrost Coasts

Arctic coastal morphology exhibits both the complexity and variability found in other regions of the world. The largest and most comprehensive attempt to characterise these coasts can be found through the Arctic Coastal Dynamics Database (ACDD) (Lantuit *et al.,* 2012a). This involved the segmentation and classification of over 100,000 km of Arctic Ocean coasts, including many factors involved in cryology, lithology and geomorphology, to better explain and predict coastal sediment and carbon fluxes and their relationship to shoreline heterogeneity. The database mainly focused on coasts around the Arctic Ocean, excluding much of the Canadian Archipelago, Greenland, Scandinavia and parts of Siberia and Alaska outside the Arctic Ocean (Figure 1.1). It was found that 34% of the coasts were lithified, while the remaining 66% were unlithified and typically contained excess ground ice. Weighted

mean backshore elevations found in the ACD database ranged from 1.54 m in the American Beaufort Sea to 14.54 m along the Russian Chukchi Sea, with an overall mean of 8.38 m. The mean backshore elevation of the unlithified coasts, where erosion rates are highest, is 4.4 m.

Long-term pan-Arctic coastal retreat rates are 0.5 m a^{-1}, but exhibit substantial variability on a regional basis, from retreat of over 20 m a^{-1} to slow progradation (Lantuit *et al.,* 2012a). Rocky coasts tend to produce much slower retreat rates, especially areas undergoing isostatic uplift, while unlithified coasts produce faster retreat rates, with more local scale variability (Lantuit *et al.,* 2012a). As well as the more traditional mechanical erosion from wave action, the unique presence of ground ice within permafrost coasts also results in other forms of erosion. These are thermal abrasion, i.e., the thawing of permafrost from relatively warm sea water combined with the mechanical effects of wave energy (Aré, 1988), and thermal denudation, i.e., the thawing of ice and degradation of permafrost above sea level due to relatively warm air. As such, Arctic permafrost coasts are sensitive to rapid changes across three domains: terrestrial, marine and atmospheric. Indeed, since the turn of the 20th century, a broad scale coastal destabilisation has been observed (Arp *et al.,* 2010; Günther *et al.,* 2013, Günther *et al.,* 2015; Jones *et al.,* 2008; Jones *et al.,* 2009a; Jones *et al.,* 2018; Lewkowicz and Way, 2019; Mars and Houseknecht, 2007; Novikova *et al.,* 2018; Ping *et al.,* 2011; Pizhankova *et al.,* 2016; Ramage *et al.,* 2018). Together, the transformation within these three domains are helping to drive, what some authors describe as, a *coastline collapse* (Fritz *et al.,* 2017).

1.3 Arctic Environmental Change

Over recent decades, surface air temperatures in the Arctic have warmed at close to twice the rate of the global average in a feedback cycle know as Arctic Amplification (Serreze and Francis, 2006). Arctic warming is expected to outpace every other region of the planet during the coming century (Collins *et al.,* 2013; Comiso, 2006). Consequently, the Arctic is undergoing, and will continue to undergo, numerous significant changes that influence coastal processes, among them:

- Reductions in sea ice cover and increases in the open water season length (Markus *et al.,* 2009; Stroeve *et al.,* 2014)
- Increases in sea surface temperatures (SSTs) (Steele *et al.,* 2008)
- Changes to storm numbers and tracks (Zhang *et al.,* 2004, Hakkinen *et al.,* 2008)
- Accelerated sea level rises relative to the global average (Yin *et al.,* 2010)

- Degradation of permafrost and enhanced thermokarst processes (Jorgenson *et al.,* 2006; Liljedahl *et al.,* 2016)
- Increased incidences of extreme rainfall (Kojelj *et al.,* 2013; Kojelj *et al.,* 2015)

One of the main controls on erosion along Arctic permafrost coastlines is sea ice. The presence of sea ice is one of the main factors that differentiates Arctic coastal processes from elsewhere in the world by providing a protective barrier that minimises erosion for most of the year, leaving only a few months during summer and early Autumn during which erosion can occur. Despite this, coastal erosion rates along Arctic permafrost coasts are typically greater than annual rates in more temperate climates (Lantuit *et al.,* 2013) — a clear demonstration of the importance of sea ice for Arctic coastal stability. Arctic sea ice is already in a state of rapid decline, with September sea ice volume only 30% of its 1979 value (Schweiger *et al.,* 2011). The latest IPCC report (AR5) now suggests the possibility of ice-free late summer conditions in the Arctic Ocean by mid-century (Collins *et al.,* 2013).

Sea ice and snow cover act to modulate Arctic air, soil and ocean temperatures too. Near surface air masses near regions with sea ice and thick snow have their temperatures limited to approximately 0˚C during the melt period due to the latent heat of fusion of ice. Energy input from the atmosphere or solar radiation is utilised in the melting of sea ice (snow cover) before contributing to temperature increases in other media. This means that the majority of the ice (or snow) has to melt before heat can be used to raise local air, soil and SSTs. An example of this process can be seen in the surface air temperature north of 80˚N in 2017 (Figure 1.2), where, despite a rapidly warming climate and strong positive trends in all other seasons, summer air temperatures have remained remarkably stable due to the persistence of sea ice at these latitudes.

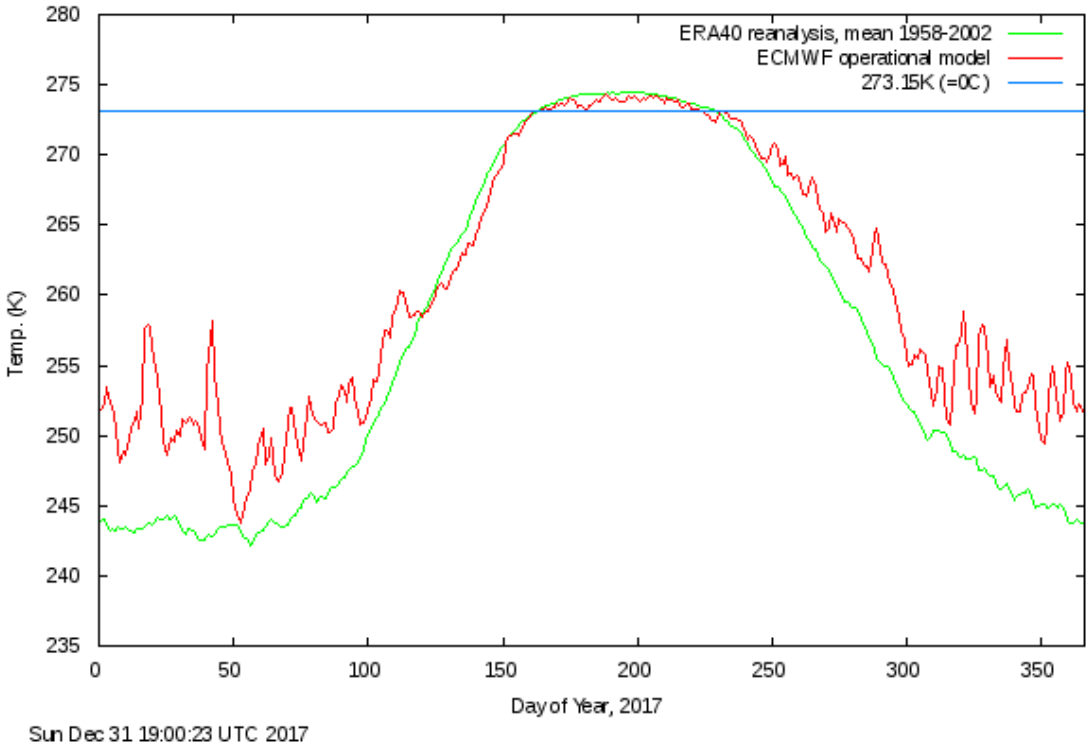

Figure 1.2: An example of the latent heat of fusion influencing the Arctic climate. The graph displays temperatures north of 80ºN, as monitored by the Danish Meteorological Institute using the European Centre for Medium-Range Weather Forecasting operational model (http://ocean.dmi.dk/arctic/meant80n_anomaly.uk.php)

Once the sea ice and snow have melted, heat input can raise air, soil and SSTs. Warmer air (thermal denudation) can increase the melt rates of exposed permafrost ice and increase the seasonally thawed active layer depth (ALD), both of which can decrease slope stability and increase erosion rates. Near 24-hour daylight can also cause a substantial increase in coastal SSTs, increasing their potential for thawing the ice rich coastlines (thermal abrasion). In addition to raising SSTs, melting sea ice increases the open water fetch, allowing for greater waves and swells and increasing the erosion potential from strong onshore winds and late summer/early autumn storms. Indeed, across the Arctic, ALDs appear to be growing (Letterly, 2018), permafrost temperatures are increasing (Biskaborn *et al.,* 2019), near-surface permafrost is degrading (Kokelj *et al.,* 2017; Liljedahl *et al.,* 2016), early summer snow cover is in decline (Mudryk *et al.,* 2019) and SSTs are increasing (Steele *et al.,* 2008).

The enhanced warming of the Arctic is also implicated in changes to rainfall events and weather patterns. Warmer air is capable of holding more water vapour, and thus producing more intense bursts of rain. This rain can contribute to additional thawing of the permafrost surface, increasing the chances of triggering erosion and helping to facilitate the transport of thawed material away from the erosion site (Kojelj *et al.,* 2015). Additionally, reductions in the poleward temperature gradient due to Arctic

Amplification is believed to increase the meridional variance on the northern polar jet stream, contributing to enhanced extreme weather patterns both in the mid-latitudes and peripheral Arctic regions. This can increase the risk of warmer pulses of air and extreme rainfall events along Arctic permafrost coasts (Francis and Varvus, 2012; Francis and Vavrus, 2015; Mann *et al.,* 2017).

1.3.1 Implications of Arctic Coastal Change: Global

Recent studies have estimated the quantity of soil organic carbon within the top 3 m of northern circumpolar soil, as well as Deltas and Yedoma regions, to be 1307 Pg, of which 999 Pg is stored in permafrost terrain (Hugelius *et al.,* 2014). The contribution of permafrost carbon to the global carbon cycle is expected to grow during the 21st century (Crowther *et al.,* 2016; Hugelius *et al.,* 2014; Schuur *et al.,* 2015). The contribution of costal erosion to the global carbon budget is very likely to grow as coastal retreat rates increase. For example, Rachold *et al.,* (2000) suggests that even by the year 2000, sediment supply to the Arctic ocean was greater from coastal erosion than river discharge in the Laptev sea. Along the Yukon coast, thermokarst processes are already contributing significant amounts of carbon to the nearshore (Ramage *et al.,* 2018). Global carbon models have only recently begun to include the contribution of permafrost carbon, yet these models still do not incorporate Arctic coastal erosion and related rapid thawing process to the global carbon budget (Hugelius *et al.,* 2014; Vonk *et al.,* 2012). Permafrost degradation has been identified as one of the largest areas of uncertainty within the permafrost carbon feedback cycle (Abbott *et al.,* 2016; McGuire *et al.,* 2010), which highlights the global importance of Arctic coastal dynamics and the need to improve our understanding and predictive capability of the Arctic coastal erosion processes.

1.3.2 Implications of Arctic Coastal Change: Regional

Past instances of rapid Holocene sea level rise in the Arctic have been associated with increased sedimentation rates across the shelves and slopes of the Arctic Ocean. However, there is little evidence of increased river discharge during this time, which suggests that enhanced levels of coastal erosion were the main contributor (Wegner *et al.,* 2015). Sea level rise, relative to the rest of the planet, is expected to occur at an accelerated rate across the Arctic. This is due primarily to a combination of mass redistribution and the inverse barometric effect, with sea levels increasing as the Arctic high-pressure weakens (Yin *et al.,* 2010). Modern and projected sea level rise may be analogous to previous sea level rises. As such, the current estimate for organic carbon input to the Arctic nearshore from coastal erosion, 14 Tg, is likely to increase over the coming century (Wegner *et al.,* 2015). The increasing amount of carbon, nutrients and

pollutants are already having a notable impact on some regions. In the East Siberian Seas, terrestrial carbon input has caused a marked increase in ocean acidification with aragonite under saturation reaching levels not projected to occur until 2100 (Semiletov *et al.,* 2016). This may ultimately lead to conditions which negatively affect the survival of carbonate species resulting in a chain reaction that impacts the coastal food web (Fritz *et al.,* 2017). The warming Arctic seas and extra carbon input is also decreasing the relative partial pressure gradient of CO_2 between the air and the water. Should this trend continue, as is anticipated, many parts of the Arctic, especially eastern Arctic seas, may flip from being net atmospheric carbon absorbers to emitters (Razumov and Grigoriev, 2011). In addition to carbon, increased levels of other elements, such as nitrogen and phosphorus, are expected to enter the Arctic nearshore. This is likely to contribute to additional algal blooms in summer that decrease oxygen availability with related knock on effects for shallow water species (Fritz *et al.,* 2017). A report by Clement *et al.,* (2013) suggests that changes occurring on the Alaskan north coast could contribute to an estimated 20% increase in the cost of building and maintaining infrastructure state-wide. These types of cost increases are likely to be borne out in other Arctic coastal regions also.

1.3.3 Implications of Arctic Coastal Change: Local

From global, to regional and down to local scales, Arctic coastal erosion is having widespread and growing impacts. Local heritage and cultural sites have been lost, while some infrastructure built in recent decades has already disappeared, with more under threat. Jones *et al.,* (2008), through analysis of historical maps displaying historical place names, infrastructure and cultural sites, identified many features that had been lost along the Alaskan Beaufort Sea coastline, and more that were now under threat given the measured erosion rates in the region. The authors of that study conclude:

"*Of the seven coastal features identified in the 1830s, only two remain. Also, of the four known cultural/historical sites along this coastline, only one remains. This last remaining site is being threatened by shoreline erosion, and steps should be taken to preserve the site if it is deemed important"* (Jones, 2008, p.369).

Coastal protection works in the Arctic are already expensive due to the remote locations and hostile climate. It is estimated that protecting the runway at the Cape Lisburne Long Range Radar site could cost in excess of $47,000,000US (Frederick *et al.,* 2016). In Tuktoyaktuk in the western Canadian Arctic, schools and other building have already been abandoned while significant funds are going into coastal defence

works. A similar sized town, Shishmaref, off the NW Alaskan coast, is suffering the effects of rapid coastal erosion and degrading permafrost. Plans to move the town to a new inland location (at a cost of $180,000,000) were abandoned when it was found that permafrost at the proposed site was also rapidly degrading, making it unsuitable for building work (Couture and Spiridonov, 2006). Numerous other examples exist across the Arctic, from Hershel island (Radosavljevic *et al.,* 2016), to Varandey in NW Russia (Sinitsyn *et al.,* 2019), and as the Arctic climate continues to change, these problems can reasonably be expected to grow.

1.4 Research Gap and Summary

The dramatic transformation now being observed across Arctic coastlines is having, and will continue to have, implications from local to global scales. A detailed understanding of the processes governing the rates and variability of permafrost coastal degradation, and the tools required to more adequately model these changes, is vital for future planning and adaptation approaches. Improving observational methods and modelling will play a key role in enhancing our understanding of the coastal response to climate change. While focus on this topic has increased over the last two decades and progress is being made, the processes and drivers of some of the most dynamic and rapidly changing coastlines are still poorly understood (Frederick *et al.,* 2016).

2 Literature Review

The following literature review will examine the regional and local variations in Arctic coastal change. This will allow for identification of the most dynamic and quickly changing regions. Secondly, the unique types of coastal erosion mechanisms associated with these regions will be explored. The mechanism least understood will be examined in greater details, highlighting the major knowledge gaps and the means with which they can be addressed.

2.1 Introduction

The unlithified Arctic coastlines are situated on the boundary of three rapidly changing and intertwined systems – terrestrial, oceanic, and atmospheric. Near surface permafrost temperatures are increasing (Biskaborn *et al.,* 2019), and ALDs are growing (Letterly, 2018). Sea ice cover is in a state of rapid decline, and ocean temperatures are increasing (Markus *et al.,* 2009; Steele *et al.,* 2008; Stroeve *et al.,* 2014). Surface air temperatures are warming at an accelerated rate relative to the rest of the planet (Johannessen *et al.,* 2016; Serreze and Francis, 2006). All these changes are expected to continue through the 21st century in response to anthropogenic climate change (AMAP, 2017; Collins *et al.,* 2013; Comiso, 2006). This transformation of the Arctic environment is already resulting in significant widespread degradation of coastal permafrost, a process expected to continue over the coming century (Arp *et al.,* 2010; Fritz *et al.,* 2017; Günther *et al.,* 2013, Günther *et al.,* 2015; Jones *et al.,* 2008; Jones *et al.,* 2009a; Jones *et al.,* 2018; Lewkowicz and Way, 2019; Mars and Houseknecht, 2007; Novikova *et al.,* 2018; Ping *et al.,* 2011; Pizhankova *et al.,* 2016; Ramage *et al.,* 2018). Significant knowledge gaps exist regarding many Arctic coastal processes, from the controls on coastal retreat rates through to the eventual fate of mobilised carbon and nutrients, placing a major limitation on predicting and planning for future changes (Fritz *et al.,* 2017, Figure 2.1). A prerequisite to constraining future rates of change and their knock-on effects, will be identifying and quantifying the key controls on the most dynamic and rapidly changing Arctic coastlines. As such, this literature review will first assess the Arctic-wide coastal retreat, identifying the regions displaying the fastest and most dynamics rates of change. Secondly, the relationship between the dominant failure mechanisms and coastal dynamics in these regions will be investigated. Thirdly, the key areas of uncertainty within the failure mechanisms will be identified and assessed. This will be followed by a summary, a description of the research gap and the thesis aims and objectives.

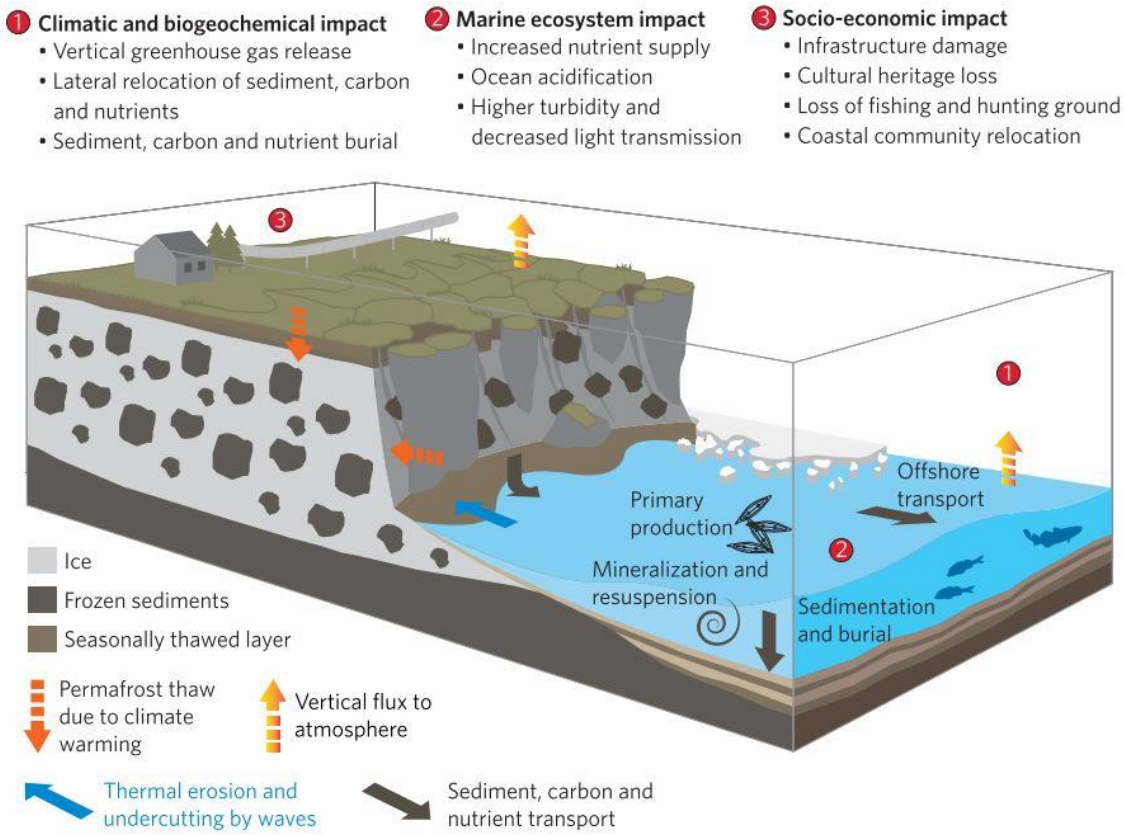

Figure 2.1: Impact of Arctic coastal erosion, from Fritz et al., (2017).

2.2 Arctic Coastal Change

Few long-term records exist of Arctic coastal retreat rates owing to the paucity of aerial imagery and the difficulty in conducting repeat field surveys in such a harsh and sparsely populated region. Studies utilising satellite imagery have aided in reconstructing recent retreat rates but imagery with a suitably high spatial resolution has only been available during the last four decades. Furthermore, the lack of ground truth data and stable surface features makes the co-registration of both satellite and aerial imagery difficult and reduces their overall accuracy. This problem is particularly prevalent along the Siberian coastline, where records are spatially sporadic and only 4% is estimated to have been studied (Grigoriev *et al*., 2006). However, coastal retreat rates and trends have been established for numerous sites across the Arctic, particularly along the Beaufort Sea coast.

2.2.1 Russian Arctic Coast

Along the Russian Arctic coastline, reports appear mixed in terms of retreat rates and trends. Vasiliev *et al.,* (2005) noted no significant trends across four sites monitored in the Kara and Barents Seas, despite a broad range of elevation, ice contents and

nearshore profile types, and measurement periods ranging from three to 54 years. In the Bykovsky Peninsula in the Laptev Sea, Lantuit *et al.,* (2011) similarly found no strong significant trend in retreat rates going back to 1951.

In contrast, numerous reports have observed an increase in coastal retreat rates. Grigoriev *et al.,* (2009) noted retreat rates for the 2004 to 2007 period have increased by a factor of 1.5 to 2 relative to preceding decades at several sites in Eastern Siberia. Günther *et al*., (2013) observed recent retreat rates 1.6 times greater for the 2007 to 2011 period than historical norms in three sites across the Laptev sea (Figure 2.2), up to a maximum of 16 m a^{-1}. Several more recent studies have also noted an acceleration in retreat rates across multiple sites along the Russian coastline (Günther *et al*., 2015; Novikova *et al.,* 2018), including an almost three-fold increase of up to 11.6 m a^{-1} on the Bolshoy Lyakhovsky Island and Oygos Yar in the eastern Laptev Sea (Pizhankova, 2016).

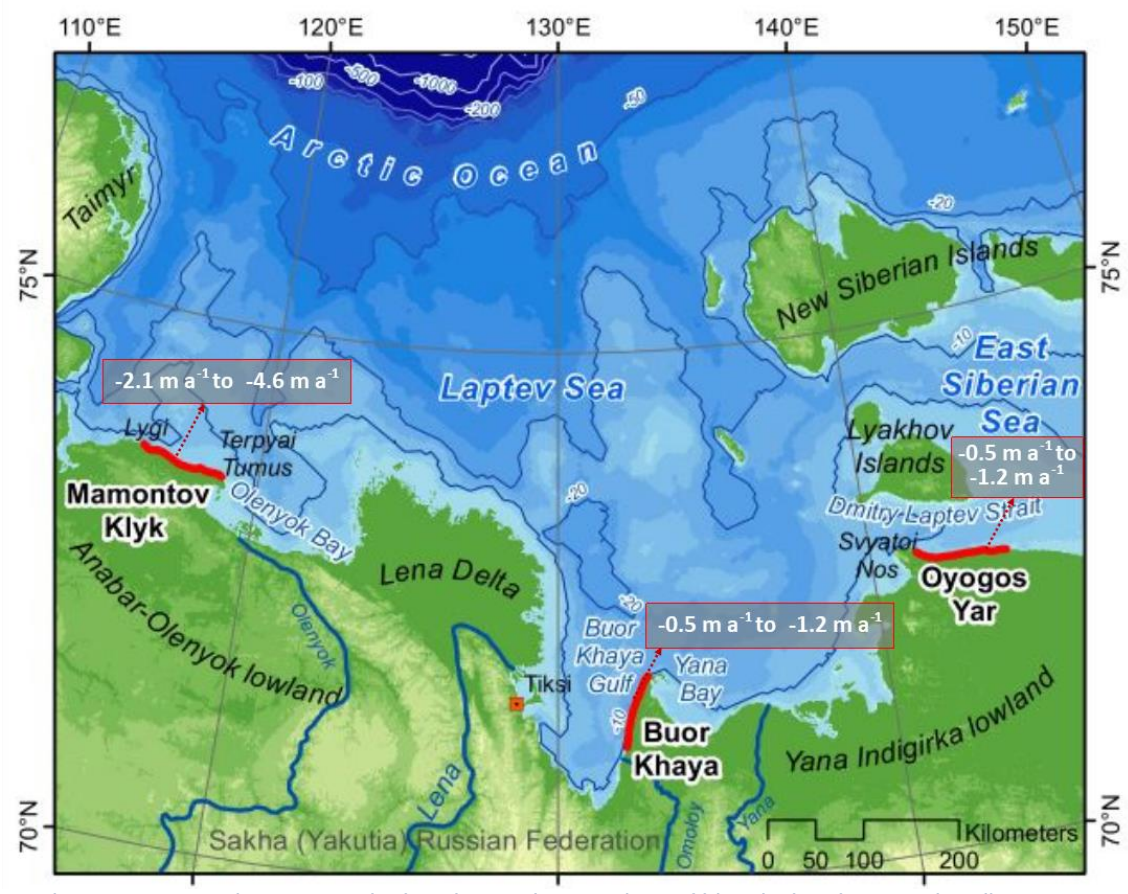

Figure 2.2: Coastal retreat monitoring sites and comparison of historical and recent shoreline retreat. Adapted from Günther et al., (2013)

2.2.2 American Beaufort Sea Coast

The American Beaufort Sea coast is one of the most intensely monitored in the Arctic. Gibbs and Richmond (2015) analysed the long-term retreat rates from the mid-20th

century to the early 21st century at 50 m intervals (Figure 2.3). 84% of the measurement transects were found to be erosional. The overall mean retreat rate was 1.4 m a^{-1}, with a range from 18.6 m a^{-1} retreat to 10.9 m a^{-1} accretion. An updated version (Gibbs and Richmond, 2017) also included recent rates, since 1980. Instances of maximum retreat rates >20 m a^{-1} were widespread in recent decades compared to the long-term (since 1940) rates. Many other regional studies have documented a general increase in coastal retreat rates over the last two decades compared to the mid and late 20th century, from slow increase (Jones *et al*., 2008; Jones *et al.,* 2009b) to a moderate increase (Ping *et al*., 2011) and even a rapid acceleration (Arp *et al*., 2010; Jones *et al.,* 2009a; Mars and Houseknecht, 2007). Furthermore, some studies note large degrees of spatial and temporal variability (Gibbs and Richmond, 2015; Gibbs *et al*., 2011) in coastal retreat rates, while some regions are becoming less variable (Jones *et al*., 2009a). However, one of the notable elements reported is the increased occurrence of retreat rates >10 m a^{-1}, with reports in excess of 20 m a^{-1} also occurring more frequently over the last 15 years (Gibbs and Richmond, 2017; Jones *et al.,* 2008; Jones *et al.,* 2018).

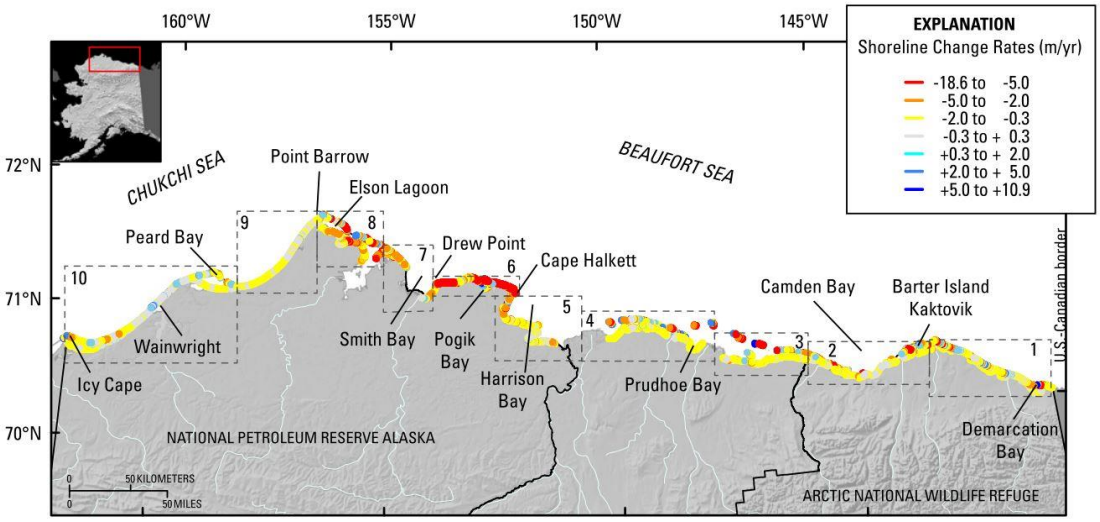

Figure 2.3: Coastal retreat rates along the American Beaufort Sea coast. Adapted from Gibbs and Richmond (2015).

2.2.3 Canadian Beaufort Sea

Around the Mackenzie Delta and Tuktoyaktuk Peninsula region, massive spatial variations in retreat rates were noted, ranging from 0.6 m a^{-1} to 22.5 m a^{-1}, between 1972 and 2000. While there was a slight reduction in retreat rates overall in the 1985 to 2000 period relative to 1972 to 1985, most of that reduction was in regions with slower rates of retreat. Areas with faster rates were more variable, with the majority

experiencing an increase in retreat rates (Solomon, 2005). Other studies produce a similar mixed picture. On Herschel island alone, large variations in trends and rates, both spatially and temporally, are present. Lantuit *et al.,* (2008) found an overall reduction in coastal retreat rates from 1952 to 1970 compared with 1970 to 2000, from 0.61 m a^{-1} to 0.45 m a^{-1}. A later study observed a significant change in the rates from 2000 to 2011, increasing to 1.3 m a^{-1} (Radosavljevic *et al.,* 2016). Long-term observations along a 210 km stretch of the Yukon coast noted that erosion rates have changed from 1.3 m a^{-1} from the 1950 to 70s, to 0.5 m a^{-1} from the 70s to 90s, before increasing again to 1.3 m a^{-1} from the 90s to 2011. With this increase came a large degree of local and regional variability (Irrgang *et al*., 2018). The situation gains additional complexity with many recent studies revealing an acceleration in mass loss not entirely reflected in coastal retreat rates. Lantz and Kokelj (2008) first noticed a significant increase in the number of retrogressive thaw slumps (RTSs – a form of dynamic thermokarst associated with mass wasting in coastal and upland permafrost) in the Mackenzie delta region from 1973 to 2004. Obu *et al.,* (2016) suggests that coastal volume measurements on Herschel Island may correspond better to environmental forcing than planimetric rates of change. Furthermore, RTSs were associated with the greatest levels of mass loss and the greatest ranges of shoreline variability along the Yukon coast (Obu *et al.,* 2017). An increase in the number, spatial coverage and mass loss from RTSs was also noted along the Yukon coast from 1952 to 2011 (Ramage *et al.,* 2018). The most extreme example of change comes from Banks Island, where a 60-fold increase in the number of RTSs occurred between 1984 and 2015 (Lewkowicz and Way, 2019), with the authors predicting further growth in their number through the 21st century under the representative concentration pathway (RCP) 4.5 emissions scenario.

2.2.4 Summary: Arctic Coastal Change

Significant spatial and temporal variability is evident across all Arctic shorelines. Reports from individual sites appear to suggest that the fastest rates of retreat occur along the Beaufort Sea coast, especially the American Beaufort Sea. While based on pre-2012 data, the ACDD largely confirms this, with the largest range and fastest average retreat rates associated with the American and Canadian Beaufort Sea regions (Figure 2.4). The ACDD also reveals that ground ice content correlated best with retreat rates, explaining 23% of the variance observed.

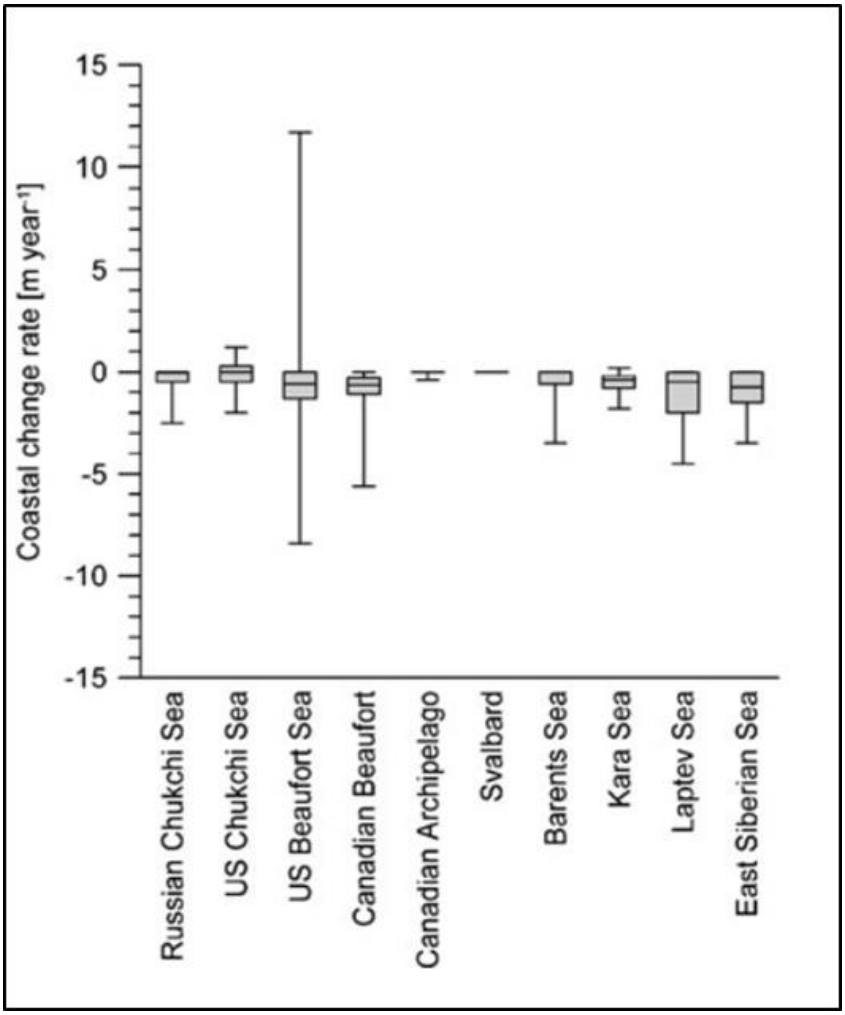

Figure 2.4: Coastal change rates and ranges from across the Arctic from the Arctic Coastal Dynamics Data Base. Adapted from Lantuit et al., (2012)

Along the American Beaufort Sea coast, the fastest rates of retreat, and those increasing the most, are found around the northern Teshekpuk Lake Special Area, particularly in the vicinity of Drew Point (Arp *et al*., 2010; Jones *et al.,* 2008; Jones *et al.,* 2009a; Jones *et al.,* 2009b; Jones *et al.,* 2018; Mars and Houseknecht, 2007). This is also confirmed by the long-term rates measured by Gibbs and Richmond (2015) shown in Figure 2.3. This region is dominated by low cliffs, between 2 m and 6 m tall, that primarily undergo a form of coastal retreat called block failure (Mars and Houseknecht, 2007).

Across the Canadian Beaufort Sea coast, the greatest rates of change are occurring through mass loss rather than planimetric coastal retreat. From Banks Island (Lewkowicz and Way, 2019), to the Mackenzie Delta (Lantz and Kokelj, 2008) and the Yukon Coast (Ramage *et al.,* 2018), a significant and even dramatic increase in RTSs has occurred. With the observed increase in the number and size, RTSs have been

described as "*emerging as the dominant driver of geomorphic change in areas of ice-rich moraine in the western Canadian Arctic*" (Segal *et al.,* 2016, p.8).

As block failure and RTSs appear to be the most significant forms of change affecting the Beaufort Sea coasts, the next section will explore them in more detail.

2.3 Arctic Coastal Erosion Mechanisms

The fastest coastal changes in the Arctic are typically associated with two distinct erosional mechanisms unique to permafrost environments, these are block failure and retrogressive thaw slumping.

2.3.1 Block Failure

Where block failure dominates, winds drive sea water against the base of an ice-rich permafrost cliff, whereby the combination of the mechanical impact of the waves and the thermal erosion of the ice bonded sediment initiates thermo-erosional niche development (Kobayashi, 1985). After a long phase of increased relative sea level or repeated short increases, the niche will extend sufficiently into the base of the cliff to allow the overhanging block to slump or collapse – the failure plane often altered by the presence of ice wedges (Figure 2.5). The collapsed block will then quickly erode, allowing the next round of niche development and subsequent block collapse. For these types of coasts, the action, both thermal and mechanical, of the ocean is the biggest driver of erosion, outweighing the contribution of thermal denudation from atmospheric warming (Aré, 1988). While block collapse is widespread and associated some of the fastest eroding shorelines in the world, the key factors governing their rates and variability are relatively well understood. This has allowed for the development of numerous models describing block failure erosion (Barnhart *et al*., 2014a; Hoque and Pollard, 2009; Hoque and Pollard, 2016; Kobayashi,1985; Kobayashi and Atkins, 1986; Ravens *et al*., 2012; Wobus *et al*., 2011). Furthermore, retreat of block failure shorelines can be tracked and measured using traditional planimetric methods, such as from satellite and aerial imagery. This allows their retreat rates and variability, and volume input to the nearshore environment, to be quantified and monitored accurately.

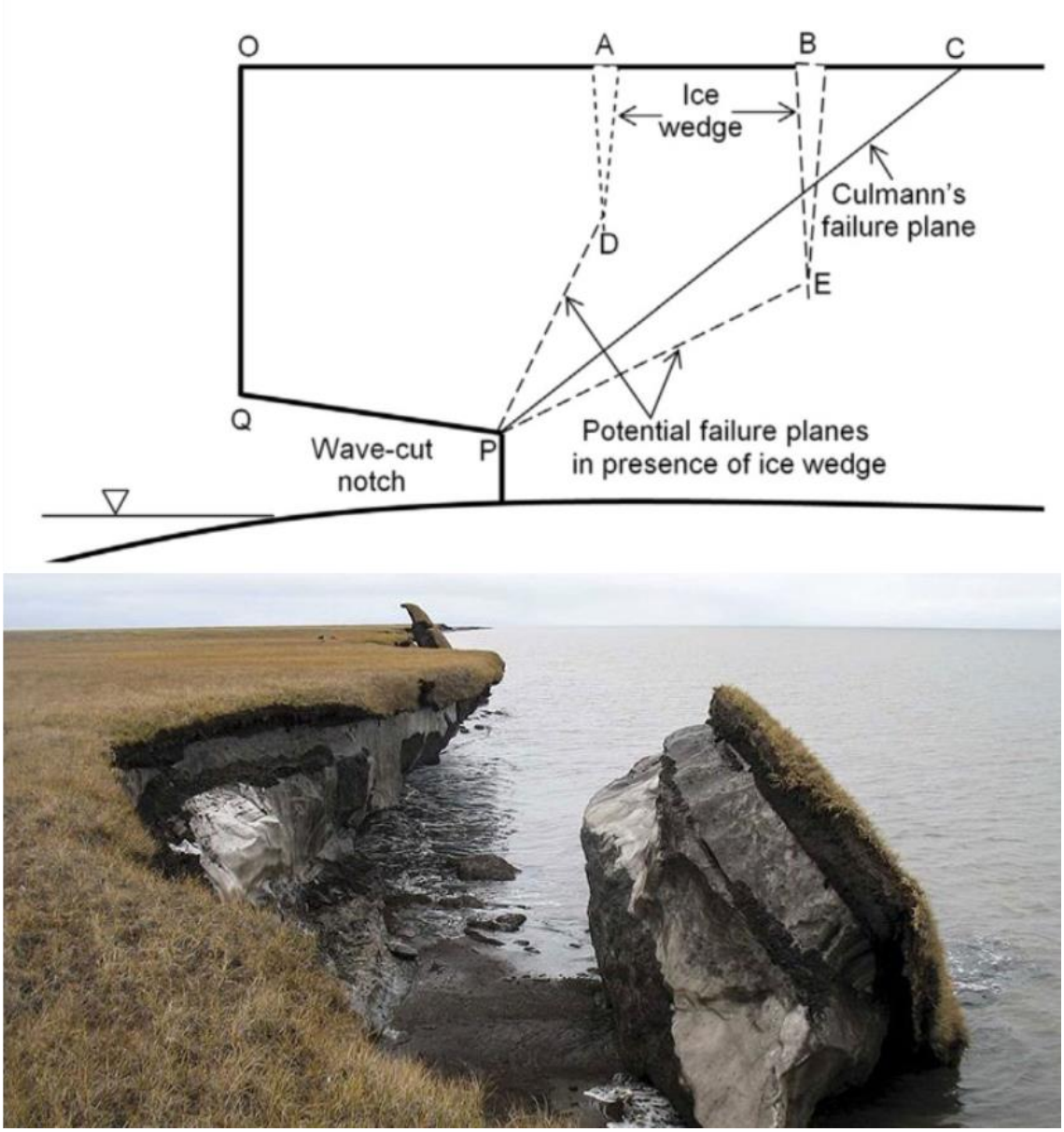

Figure 2.5: Top: Schematic block failure diagram (Hoque and Pollard, 2016). Bottom: Block failure along the Alaskan Arctic coastline (Overland et al., 2019).

2.3.2 Retrogressive Thaw Slumping

One of the most active forms of thermokarst are RTSs, a form of slope failure in which thawed soils flow along a massive ice body or layer of ice rich permafrost. Active thaw slumps are traditionally characterised by a distinctive “C” shaped scar zone up to 1,000 m wide, containing three main elements (Figure 2.6 and Figure 2.7);

(i) A near vertical headwall consisting of ice poor permafrost and the active layer

(ii) A steep angled headscarp with exposed ice – the ablation of which drives the back wasting of the RTS

(iii) A low angled slump floor, where thawed permafrost material from the headwall combines with meltwater to form a muddy mixture which flows downslope

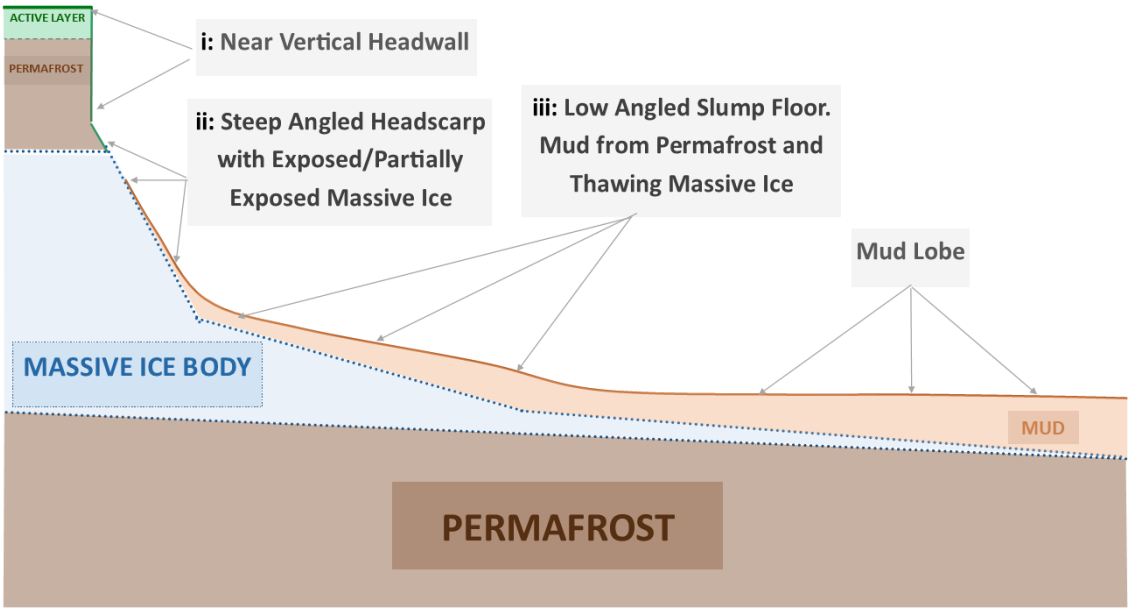

Figure 2.6: Schematic diagram highlighting the main features of a retrogressive thaw slump

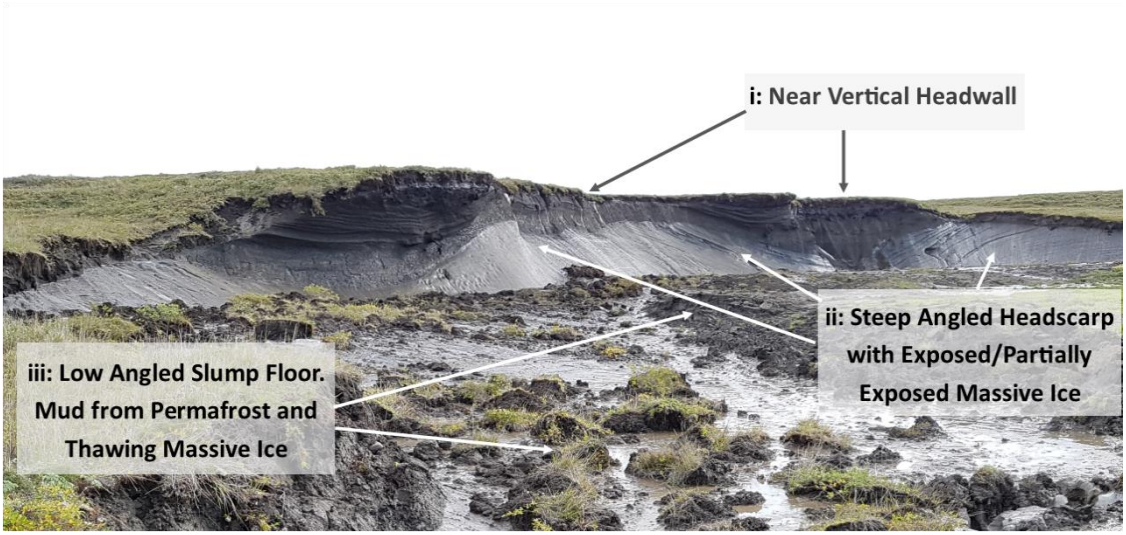

Figure 2.7: An example of a RTS displaying the features highlighted in Figure 2.6. Photo taken on Pelly Island, August 2017

RTSs are triggered when the massive ice body becomes uncovered and exposed to surface energy fluxes. Ablation of the massive ice drives the upslope progression of the headwall. The thawed headwall material falls down the headscarp and combines with the melt water, forming a muddy mixture that flows downslope over the basal ice of the slump floor, keeping the headscarp clear and allowing ablation to continue. When the massive ice is no longer exposed, whether due to covering by thawed debris or retreat into an area with low elevation or absent massive ice, they can quickly stabilise. As RTS can be up to a kilometre wide and extend 100s of metres upslope, these

processes result in significant vertical changes in the landscape and large volumes of material being transported into the nearshore. This mass loss can be difficult to estimate from traditional planimetric analysis, making long-term and accurate measures of their activity difficult.

Many RTSs are polycyclic, going through phases of dormancy that can last from years to centuries (Lantuit *et al.,* 2012b). Even after stabilisation, RTSs can alter the vegetation and ground thermal regime for over a century (Burn, 2000; Burn and Friel, 1989). Furthermore, there has been a dramatic increase in the size, activity and density of RTSs over recent decades (Lantz and Kokelj, 2008; Lewkowicz and Way, 2019; Ramage *et al.,* 2018; Segal *et al.,* 2016). These changes are expected to grow over the coming century due to climate change, allowing the affected regions to experience some of the most dynamics landscape changes in the world (Lewkowicz and Way, 2019).

2.3.3 Summary: Erosion Mechanisms

Both block failure and RTSs are altering the coastal landscapes of the Arctic in often dramatic ways. While there are still considerable uncertainties (Jones *et al.,* 2018) significant progress has been made in constraining the controls and drivers of block failure erosion – as evidenced by the numerical and analytical models developed (Barnhart *et al.,* 2014a; Hoque and Pollard, 2009; Hoque and Pollard, 2016; Ravens *et al.,* 2012). In contrast, the controls on and drivers of RTS activity have only recently begun to be analysed in a quantitative manner (Ramage *et al.,* 2017). Modelling attempts have largely been confined to simple predictors of headwall retreat (HWR) rates (Heginbottom, 1984; Lewkowicz, 1987A; Robinson, 2000; Zwieback *et al.,* 2018). As such, there is a greater need to identify, observe and quantify the controls and drivers of RTS activity.

The following sections will describe RTSs in more detail, from their spatial distribution to the modelling attempts and descriptive/subjective assessments of the key controls and drivers.

2.4 RTS Analysis

2.4.1 Spatial Distribution

RTSs form in a variety of ice rich permafrost landscapes, from coasts and riverbanks, to mountains and lake edges, from Siberia to Alaska and Canada (Alexanderson *et al.,* 2002; Burn, 1989; Burn, 2000; Lacelle *et al.,* 2015; Lantuit *et al.,* 2011; Ramage *et al.,* 2017). RTS-like (and other thermokarst) features have even been identified on the

surface of Mars, and the terrestrial controls and drivers of these features used to assist in understanding the periglacial processes on Mars and the presence ice-rich banded Martion soils (Ulrich *et al.,* 2010; Séjourné *et al.,* 2012). Indeed, the Tuktoyaktuk coastlands have been described as a wet, periglacial analogue to the Utopia Planitia region of Mars (Soare *et al.,* 2011).

Typically, RTSs tend to form where excess ground ice, especially massive ice bodies, are present within the subsurface (massive ice is defined as a section of permafrost with an ice content at least 250% that of the dried soil [Harris *et al.,* 1988]). In the western Canadian Arctic, this most commonly occurs near the northern and western limits of the Laurentide ice sheet, where permafrost aggradation and abundant glacial meltwater contributed to the formation of widespread intra-sedimental massive ice layers (Kokelj *et al.,* 2017; Mackay, 1971; Murton *et al.,* 2005). The highest densities of RTSs are found in the Mackenzie Delta regions, the Tuktoyaktuk Coastlands, along the Yukon coast and, in particular, on Banks Island (Figure 2.8). However, in terms of number, size and rates of RTS activity, there are marked regional differences across the western Canadian Arctic.

The Yukon coastline, between 1952 and 2011, has experienced a 73% increase in the number of RTSs and a 14% increase in the total area they cover. The relatively small increase in total area is due to a significant reduction in their average size, of 67% (Ramage *et al.,* 2018). Lantz and Kokelj (2008) recorded a doubling of the HWR rates and 1.4 times increase in the rate of slump growth between 1973 and 2004 relative to 1950 to 1973 through the Mackenzie Delta regions. Similar has been observed in the Tuktoyaktuk coastlands in 2004 relative to 1950, where a reduction in the number of observed RTSs (-38%) has been outweighed by a significant increase in their size (+67%) resulting in a slight increase in the RTS affected areas (+2%). The growth in the number of RTSs on Banks Island has also been the most dramatic. Lewkowicz and Way (2019) observed a total of 63 active RTSs on Banks Island in 1984. Between then and 2015, more than 4,500 developed, increasing their spatial coverage from 1.0 km^2 to 64.1 km^2. These were typically clustered within a band 25 to 50 km wide along the south and east coast.

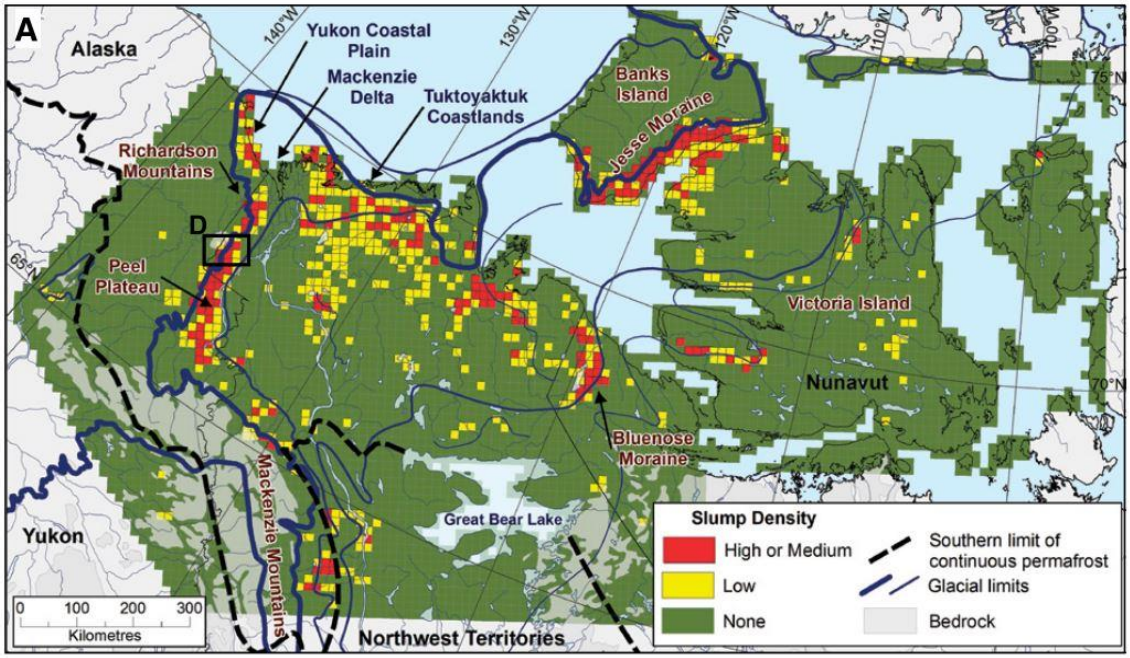

Figure 2.8: Location and density of RTSs in the western Canadian Arctic. Adapted from Kokelj et al., (2017)

The regional differences further highlight the complexity of change being experienced across the western Canadian Arctic. The next section will explore attempts to model different aspects of RTS activity within the literature, including the findings and opinions on their primary controls and drivers.

2.4.2 RTS Modelling and Controls

2.4.2.1 Temperature and Surface Energy Balance

While no models have been published that attempt to simulate all processes within a RTS, numerous studies have attempted to explain HWR rates using simple energy balance models or comparisons with surface air temperature metrics, such as thawing degree days. Three studies have applied simple surface energy metrics and/or headwall geometry models to predict HWR rates in three separate locations across the Canadian Arctic (Heginbottom, 1984; Lewkowicz, 1987A; Robinson, 1990). These models tend only to perform well in predicting maximum HWR rates and under a narrow set of conditions – consistent exposure of thick headwall ice relative to overburden (OB) and no rapid changes in topography. A similar pattern was found by Jones *et al.,* (2019), where weak, but variable, correlations existed between thawing degree days and HWR rates at 12 slumps in the Canadian high Arctic. Furthermore, Zwieback *et al.,* (2018) found sub seasonal thaw slump activity in the Tuktoyaktuk coastland is not energy limited, with local characteristics required for accurate estimates of RTS activity. These studies illustrate that simple energy balance models are highly limited by local ground ice and topographic conditions.

In terms of trends and distribution, rising temperatures and increased rainfall are also believed to play a role in the increased occurrence of RTSs. Lantz and Kokelj (2008) suggest that warming air temperatures have overridden local and site-specific characteristics in triggering more RTSs in the Mackenzie Delta. This is supported by Lewkowicz and Way (2019), that observed increases in RTS formation on Banks Island to be almost entirely driven by increased summer temperatures, with particularly warm seasons resulting in step changes in new RTS numbers (Figure 2.9). Indeed Balsar *et al.,* (2014) found that RTS activity and formation is particularly sensitive to early summer warmth, and possibly intense precipitation events. Segal *et al.,* (2016), in finding that thaw slumps are becoming increasingly influential in driving landscape changes in many parts of the western Canadian Arctic, placed the blame on precipitation, as well as rising air and permafrost temperatures. In contrast, Kokelj *et al.,* (2015) found a significant increase in the size and number of mega-RTS (5-40 ha) across the Peel Plateau region of Canada. They found no corresponding trends in summer temperatures indices and instead implicate an increase in the intensity and magnitude of summer rainfall.

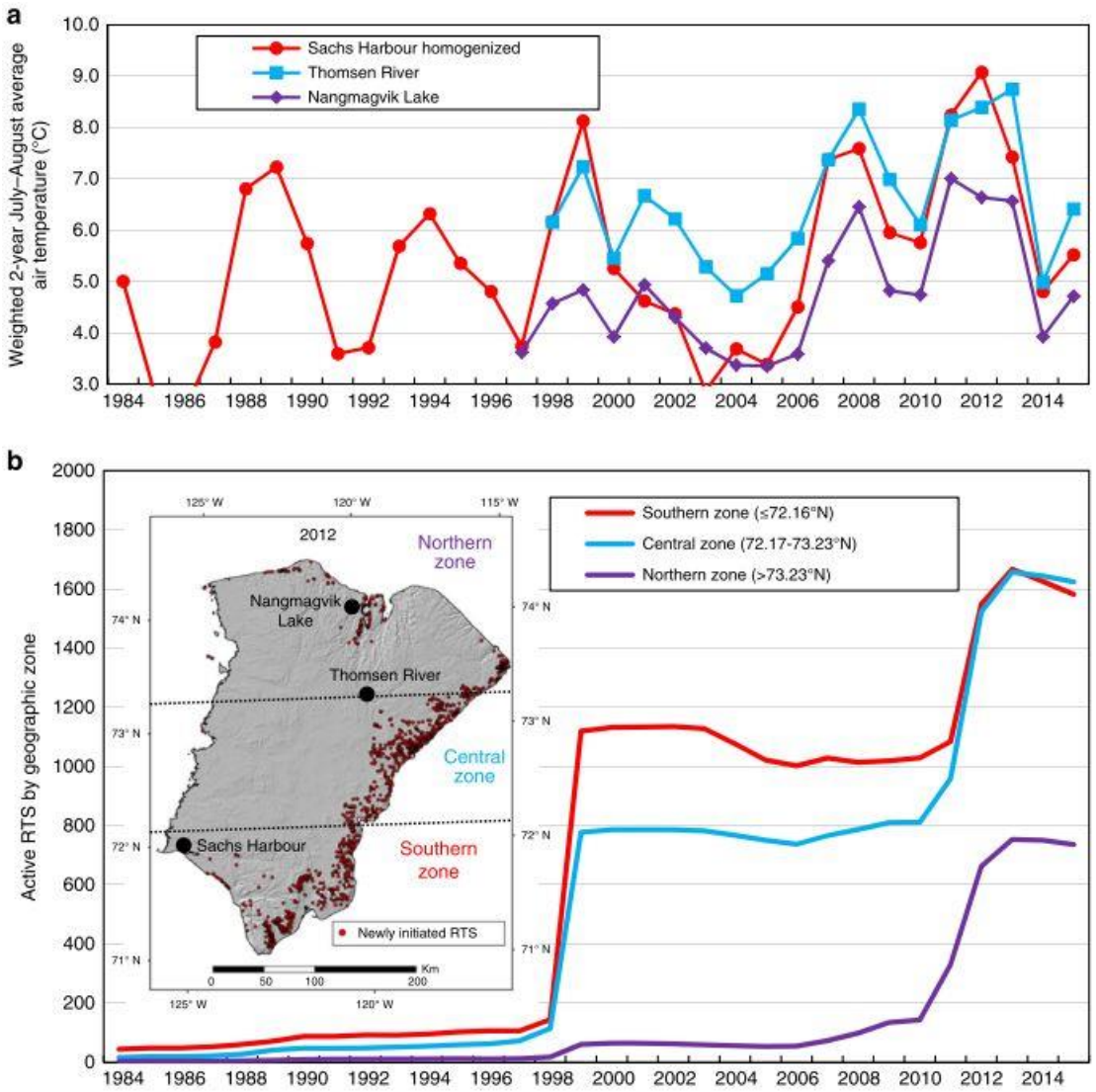

Figure 2.9: The combined influence of July and August temperatures on RTS initiation and geographic zones on Banks Island. Adapted from Lewkowicz and Way (2019).

2.4.2.2 Storms and Sea ice Cover

Numerous studies have placed much importance on the role of reduced sea ice cover and the subsequent increased level of coastal retreat through storm activity for the exposure of ground ice and initiation of coastal RTSs. Frequent removal of material from the base of headwalls and the floor of coastal RTSs have long been considered a vital element to sustaining ice ablation and mass wasting.

Lantuit and Pollard (2008) provide mixed evidence for the role of storms by noting that RTSs on Herschel Island occur more frequently on the south east facing coast, which experiences high rates of coastal retreat. Despite an increase in RTS formation, however, storm activity has been stable or decreasing in the area. A later study found that storms are likely to play integral role in the polycyclic nature of RTSs on Herschel Island (Lantuit *et al.,* 2012b). The authors state that during periods of enhanced mass

wasting, the massive ice can become buried in a thick layer of sediment. Storm driven coastal retreat is the primary means of re-exposing the massive ice and re-initiation thaw slump activity (Figure 2.10). Kokelj *et al.,* (2009) found that waves from strong winds could initiated thaw slump activity along lakes in the Mackenzie Delta region. Winds on smaller lakes were unlikely to provide enough energy to remove thawed debris fast enough to account the observed frequency of RTS re-initiation, thus some other factors must be at play. Along the Yukon coast, Ramage *et al.,* (2017) found that coastal retreat rates, which are linked with wave and storm activity, were not good predictors for RTS activity and that local terrain morphology and internal ice body characteristics were more influential.

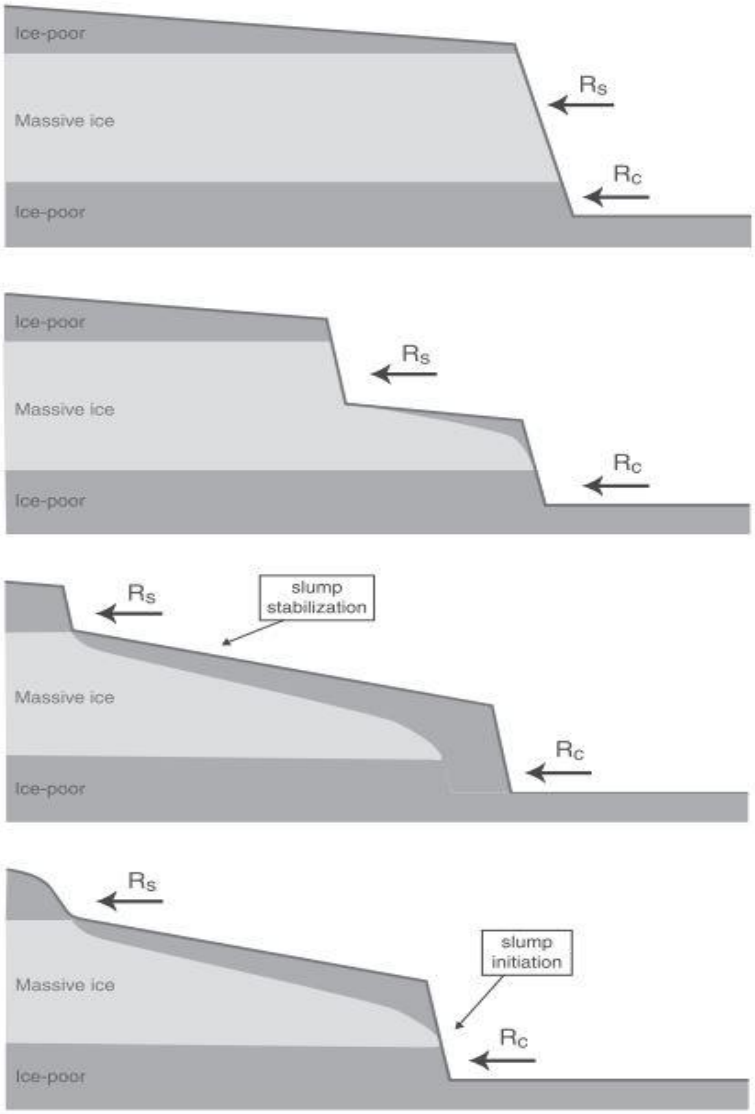

Figure 2.10: Conceptual model of RTS polycyclicity. R_S represents HWR and R_C coastal retreat. Adapted from Lantuit et al., (2012B)

2.4.2.3 Coastal Morphology

Coastal morphology has long been believed to play an important role in the evolution of RTSs, but only recently has topographic data become available at the spatial and temporal resolution required to effectively analyse the link between coastal morphology and RTS evolution. Previously, researchers could make educated guesses about the influence or factors such as cliff height, slope, aspect, etc, from infrequent visits to a small number of RTSs. For example, French (1974) mentions the importance of geomorphic features based on a qualitative description of RTSs on Banks Island, while Lewkowicz (1987a) attributes the stabilisation of one of three monitored RTS to the HWR reaching a section of flat terrain. Similarly, Robinson (2000) highlights the importance of slope angle for removing thawed debris and maintaining HWR.

Ramage *et al.,* (2017) was the first to use LiDAR to systematically assess the relationship between coastal morphology and the occurrence and activity of RTSs along a section of the Yukon coast. A total of 287 RTSs were mapped and classified along 238 km stretch. The slope of the coastline (>3.9°) and cliff height (>11 m) were the best predictors and RTS activity, but not their spatial coverage or density.

2.4.2.4 Internal Permafrost Layering

Heginbottom (1984) made repeat visits to a RTS between 1977 and 1982, noting that initial observations found a 2 m thick massive ice exposure within the exposed headwall and fast HWR rates. The ice exposure gradually reduced in thickness and became completely covered by 1982, during which time the HWR slowed and came to a stop. Similarly, Lewkowicz (1987a) described the stabilisation of one slump occurring due to the headwall reaching an area of flatter terrain where the ice exposure was reduced relative to the OB. The author also noted periods where north facing headwalls retreated at greater rates than those facing south, due to the former having a thicker massive ice exposure relative to OB. Similar qualitative observations, highlighting the importance of massive ice and OB thickness, are common throughout the literature (Burn and Lewkowicz, 1990; Lantuit *et al.,* 2012b; Robinson, 2000; Segal *et al.,* 2016; Zwieback *et al.,* 2018).

The most quantitative analysis of internal layering and RTSs comes from Ramage *et al.,* (2017). They found that ice body thickness was the primary predictor of RTS density along the Yukon coasts, while the percentage of massive ice by volume was key to explaining the spatial coverage of RTSs. Ice body thickness of at least 1.5 m appeared to be important for creating coastal landscapes with a high density of RTSs. However, data on massive ice variability were derived from cliff face observations or

from a model used to estimate ground ice volume and type (Couture and Pollard, 2017). This model uses the presence of RTSs, cliff face exposures and extrapolation of data from surrounding areas to produce a model of massive ice thickness and elevation variability, the characteristics of which are assumed to remain consistent 100 m inland. However, massive ice can display considerable variability over distances of 10s of metres (Pollard, 1990; Rampton and Mackay, 1971; Robinson, 2000). As such, the along-shore interpolation and cross-shore extrapolation may not provide locally accurate representations of massive ice.

2.4.3 RTS Knowledge Gaps

Analysis of RTSs can be split into two broad categories:

1. Controls and drivers of sub-seasonal to inter-annual RTS activity
2. Controls and drivers of inter-decadal to multi-decadal RTS activity, initiation and distribution

Both categories appear to suffer from the same problems i.e., a lack of effective monitoring and measuring tools for massive ice body variability, and quantitative, temporal topographic analysis.

For category 1, the energy balance models display highly variable results, not only between slumps separated by thousands of kms, but also between slumps that form part of the same site. Much of these differences are ascribed to variations in massive ice thickness and topography, but without a way of effectively quantifying their influence (Heginbottom, 1984; Lewkowicz, 1987A; Robinson, 1990; Zwieback *et al.,* 2018). With the increasing availability of high-resolution topographic data (Kokelj and Jorgenson, 2013) it should be possible to determine the finer scale influence of elevation and slope on RTS activity. However, even with a model or formula that accurately describes HWR rates under idealised conditions, the main limitation will be massive ice variability – it's exposure and thickness being the ultimate determinant of RTS activity and stabilisation. This is also true of the coastal activation of new and polycyclic RTSs. Local scale variability in massive ice, both along-shore and inland, may explain why coastal retreat along the Yukon coast fails as a useful predictor of RTS activity (Ramage *et al.,* 2017).

For category 2, there has been a long-term, often dramatic, increase in the number and (generally) size of RTS across the western Canadian Arctic, with a warming climate and increased summer precipitation largely blamed for the changes. However, the landscape responses vary significantly, both in terms local geomorphic responses and

especially regional landscape responses. Examples include the reduction in slump sizes and increase in number along the Yukon coast (Ramage *et al.,* 2018), the increase in size and reduction in number in the Tuktoyaktuk coastlands (Segal *et al.,* 2016) and the dramatic increase in the number of RTSs on Banks Island (Lewkowicz and Way, 2019). Segal *et al.,* (2016) suggest that ground ice conditions and topography can explain much of the variability:

"Landscape factors including topographic relief, ground ice conditions, and Quaternary history strongly influence slump development, including the magnitudes and rates of geomorphic change" (p.10).

They also provide the example of the typically shallow (~1 m) depth to massive ice on Banks Island vs the 2 m to 3 m depth to ice more common around the Tuktoyaktuk coastlands for the difference. The combined effect of terrain morphology and massive ice variability as a control on regional RTSs was further supported by Ramage *et al.,* (2017), noting the strong connection between elevation, slope and massive ice thickness in explaining the occurrence and activity of RTSs. Pollard (2000) emphasises the importance of ground ice variability in understanding Arctic landscape evolution. While the comments were focussed on western Ellesmere Island, they are equally applicable to other regions with subsurface massive ice:

"Ground ice remains one of the most problematic aspects of permafrost and a major obstacle to development in Arctic regions. Knowledge of ground ice, particularly massive ice and ice-rich sediments, is necessary not only to understand the evolution of the Late Quaternary landscape in this region, but also to assess the potential geomorphic response of the landscape to natural and anthropogenic disturbances of permafrost regimes" (p. 208).

2.5 Thesis Aim and Objectives

From the literature review presented, it is evident that suitable topographic data and information on subsurface massive ice variability are considered two of the primary limiting factors for predicting the short-term activity of RTSs and variations in their geographical distribution and regional characteristics. As such, the primary aim of this thesis will be to:

Quantify the role of massive ice and topographic variability on the dynamics of RTS dominated coasts

This will be achieved through the following objectives:

1. Investigate the influence of fine scale, topographic characteristics and internal layering on seasonal and inter-annual RTS dynamics.
2. Explore the interaction between massive ice, decadal changes in terrain morphology and RTS activity.
3. Investigate the role of massive ice variability on the historical (1935 to 2018) evolution of RTS dominated coasts

These objectives will be met through a multi-scale analysis of the intra-sedimental massive ice type locality, Peninsula Point, in the western Canadian Arctic.

Objective 1 will involve sedimentological analysis and the novel application of passive seismic monitoring to detect and map subsurface massive ice body variability. This will be combined with a quantitative topographic analysis using high-resolution structure from motion multi-view stereo (SfM-MVS) data. The combination of these data sets will allow for the analysis of inter-annual RTS dynamics.

Objective 2 will incorporate Light Detection and Ranging (LiDAR) data from 2004, and high-resolution aerial imagery from 1993 and 1994. This will allow changes in terrain morphology and RTS activity to be tracked over decadal timescales, highlighting the time varying interaction between these features.

Objective 3 will re-analyse and extend (up to 2018) previously published shoreline retreat (SLR) rates and variability from 1935 to 1985, using freely available satellite imagery. A combination of modern measurements, published descriptions and historic aerial photos will be used to assess changes in massive ice since 1935. Applying the insights gained from the first two objectives to the historical data will allow influence of massive ice on the long-term coastal evolution to be explored.

2.6 Thesis Structure

Chapter 1 has introduced Arctic permafrost coasts, Arctic environmental change and its implications. Preceding the aims and objectives, **chapter 2** provided a look and Arctic coastal erosions, the primary erosional mechanisms, and the trends, distribution and current understanding of RTS dynamics, allowing the major knowledge gaps to be identified.

Chapter 3 will provide details on the field site, Peninsula Point, and an overview of the regional landscape characteristics.

Chapter 4 presents the fine scale characteristics and internal layering at Peninsula Point, based on the field data capture and analysis of disturbed and undisturbed terrain in 2017. This includes ALD, soil characteristics and fine scale surface topography derived from the SfM-MVS analysis. In addition, the novel application of passive seismic monitoring for the detection of subsurface massive ice will be presented. Much of the data are combined into two 3D models, highlighting the relationship between massive ice thickness, OB thickness, ground surface elevation and RTS dynamics.

Chapter 5 provides a record of the coastal dynamics and RTS activity across a range of timescales. Spatial variability, trends and analysis of volume, elevation and slope are presented for 2004 to 2018, and long-term HWR rates for 1994 to 2018, using a combination of aerial imagery, LiDAR and SfM-MVS point clouds. Previously published SLR rates from 1935 to 1985 are re-examined to include spatial variability and extended to 2018 using satellite imagery.

Chapter 6 explores the drivers and controls of the records provided in Chapter 5, across multiple timescale. These include the influence of massive ice and OB thickness on inter-annual HWR rates, the decadal controls of terrain morphology on coastal and RTS dynamics, and the role of massive ice variability on the long-term trends and spatial patterns of SLR.

Chapter 7 provides an overview of the results, discussing and comparing them with similar results from the academic literature, assessing their application to the knowledge gaps and their influence on existing theories. The role of massive ice variability on RTS dynamics will be presented through a series conceptual models, followed by a discussion of the implications and limitations of the key findings.

Chapter 8 presents the overall conclusions of the thesis, the results in terms of achieving the aim and objectives, the key contributions to knowledge and potential areas for future work.

Three appendices are provided.

Appendix 1 provides information of the soil grain size distribution and horizontal accuracy analysis points.

Appendix 2 provides data for the SLR, HWR, volume and topographic metrics.

Appendix 3 provides monthly temperature and meridional wind graphs. It also contains the active HWR rates and exposed headwall constituent values.

3 Field Site

3.1 Site Selection

Peninsula Point was selected as the main area of study for a number of reasons:

1. It's a "type locality" for massive intra-sedimental ice, containing clear coastal exposures during its observational history dating back to 1935. This includes field surveys since 1954, allowing a more detailed analysis of long-term change than most Arctic sites.
2. It contains many RTSs and Polycyclic Retrogressive Thaw Slumps (PRTS), with sizes ranging from 10s to 1,000s of m^2. The landscape is a mixture of different levels of thermokarst, with some relatively undisturbed terrain, stabilised areas and many actively retreating headwalls. There is also a large range of massive ice and OB thicknesses, allowing for the study of their relative effects.
3. It's close proximity to Tuktoyaktuk provides relatively easy access by boat, allowing for multiple visits during a single field season.

3.2 Regional Landscape

Peninsula Point is located within the Pingo National Park about 6 km southwest of Tuktoyaktuk, Northwest Territories, Canada (Figure 3.1). The Tuktoyaktuk coastland region is within the zone of continuous permafrost, dominated by rolling hills with a maximum elevation of about 50 m, and thermokarst lake coverage of between 30 and 50% (Mackay, 1963). Surficial soils consist of various glaciolacustrine and glaciofluvial deposits, a result of its position at the northern edge of the Laurentide ice sheet at the end of the last glacial period (Murton *et al.,* 2005; Mackay, 1971).

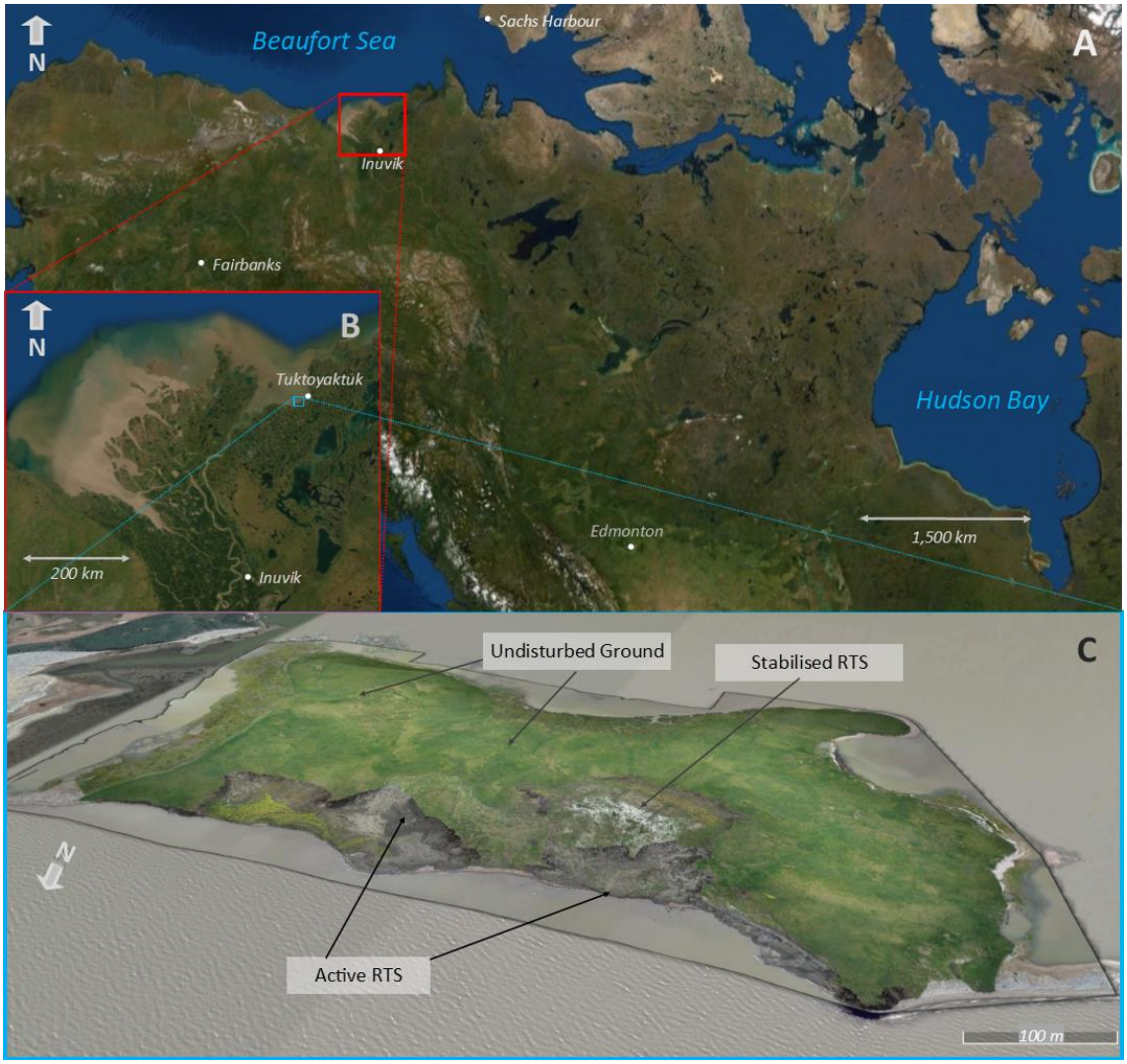

Figure 3.1: Field site location within (A) northwest North American continent, (B) Mackenzie Delta regions and (C) the Peninsula Point field site itself

3.3 Permafrost, Climate and Sea Level Rise

Permafrost temperatures are between -6 and -7°C (measured between 2003 and 2007), an increase of 2°C since the late 1960s and early 1970s (Burn & Kokelj, 2009). The climate in the region is considered subarctic, with temperatures below freezing from October to late May, reaching a low of about -25°C from December to March. Temperatures typically warm above 0°C from late May to September, coinciding with the period when snow and sea ice cover are typically absent (Burn & Kokelj, 2009). With sea ice absent, thermal erosion can occur along the shoreline, while warm temperatures and a snow free surface allows for warming of the active layer and thawing of exposed ice, creating a distinct thaw season. Like much of the Arctic, the local climate has warmed significantly in recent decades, with thaw season temperatures increasing by +0.43°C per decade since 1935, from 4.4°C to 7.3°C. The tidal range is only 0.3 m locally and so is unlikely to contribute to significant coastal

change (Mackay, 1986). However, storm surges can raise sea levels by up to 2 m and can result in significant coastal inundation, though their frequency and magnitude remain uncertain (Pisaric *et al.,* 2011). Furthermore, the local region is projected to undergo one of the fastest rates of sea level rise in the Arctic, with current rates around Tuktoyaktuk estimated to be 3.5 mm a^{-1} (Manson and Solomon, 2007), with projections of a 60 cm increase in 2100 relative to 1986-2005 (James et al., 2014; Figure 3.2A). This is a result of large region of glacio-isostatic subsidence in the eastern Beaufort Sea area, which includes annual subsidence rates of close to >2 mm a^{-1} in the Tuktoyaktuk Coastlands (Manson *et al.,* 2005; Peltier, 1994). The combination of regional warming, enhanced sea level rise, ice-rich soils, sea ice loss and low relief terrain makes the region highly vulnerable coastal erosion (Manson *et al.,* 2005).

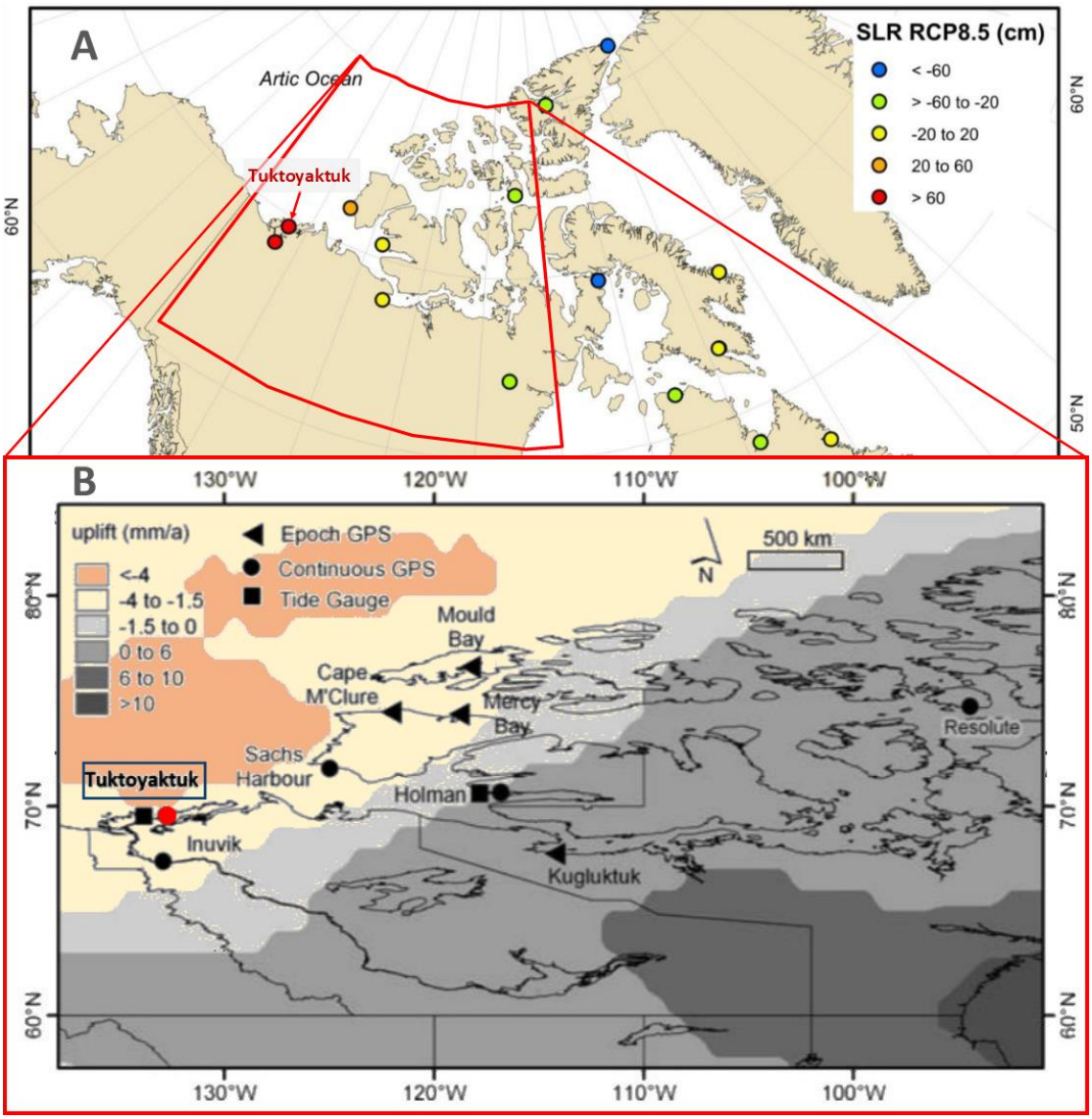

Figure 3.2: A: Projected median relative sea-level change by 2100, relative to 1986-2005, for RCP8.5 (Adapted from James et al., 2014). B: Rates of crustal uplift, with negative values indicating subsidence (Adapted from Manson et al., 2005).

3.4 Peninsula Point: Ice, Soil and Morphology

The Peninsula Point site itself is characterised by a 2 m to 10 m thick layer of clay rich diamicton, atop a massive ice body of between 5 m and 20 m thickness, some of which lies below sea level. Below the ice lies a layer of thick deltaic sands. The massive ice layer that is common to the region is understood to have formed as ground water, sourced from nearby receding glaciers, was forced toward an aggrading permafrost table less than 14,000 years BP (Mackay & Dallimore, 1992; Moorman *et al.,*1998). Evidence, such as the variations in ice bedding folds and inclined ice veins, suggest that the massive ice has undergone differential uplift during the Holocene. The infilling of topographic depressions and the presence of wood above the current massive ice elevation (dated at close to 10,000BP) indicate that mass wasting was occurring during the early Holocene warm period and that Peninsula Point originally had a much greater topographic relief than observed during the 20th century (Mackay and Dallimore, 1992). This is supported by the subsequent work of Lacelle *et al.,* (2004), where three distinct phases of thaw slump activity were noted during the Holocene, the greatest of which occurred around 8,000-9,000BP, and Murton (2009), who found deepening of the active layer and enhanced thermokarst activity 10,000BP associated with temperatures about 3°C warmer than today on the Tuktoyaktuk Peninsula. The early Holocene warmth may even have been more pronounced, as van der Bilt *et al.,* (2019) found that temperatures in Svalbard approximately 10,000BP were 7°C warmer than today, due to an increase in incident solar radiation from orbital forcing and enhanced inflow of Atlantic waters. All these point towards a period of enhanced Arctic-wide warming, and a likely period of enhanced thermokarst and mass wasting at Peninsula Point during the early Holocene warm period.

SLR and massive ice exposures at Peninsula Point have been monitored since 1935 (Mackay 1986), allowing it to become a “type locality” for massive intra-sedimental ice in the western Canadian Arctic (Figure 3.3). The site has typically experienced phases of large polycyclic retrogressive thaw slumping and frequent massive ice exposures of up to 10 m. Currently, ice exposures range from thin stretches under 2 m to short sections close to 4 m thick. The zone within 200 m of the north coast consists of variations from gentle slopes extending over 100 m inland to cliffs >15 m, with a mix of stable, active and undisturbed terrains. This makes Peninsula Point an ideal location for assessing the role of massive ice on permafrost coastal dynamics.

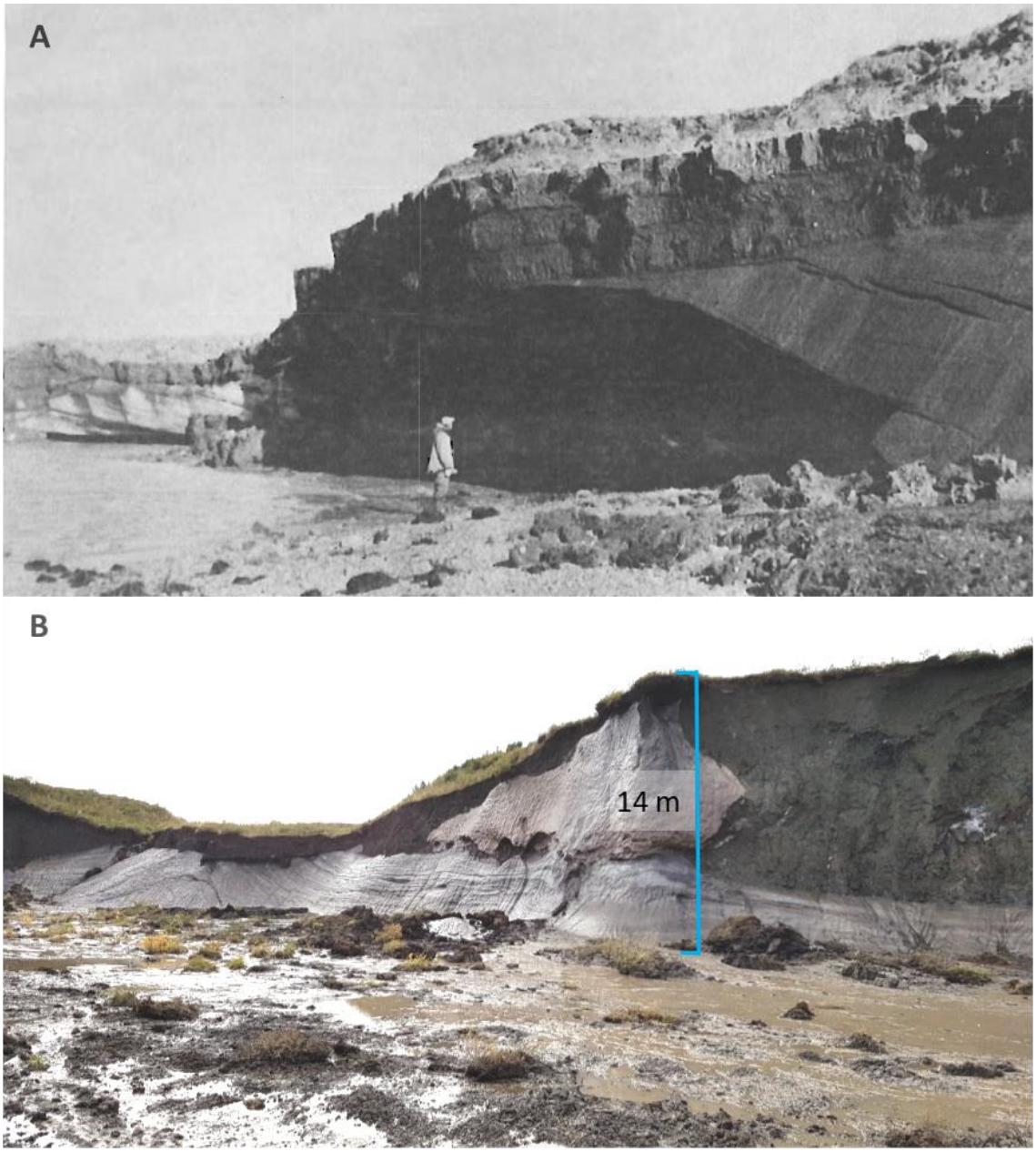

Figure 3.3: An example of the massive ice exposure in 1954 (Mackay and Rampton, 1971) and 2017

4 Surface Characterisation and Internal Structure

4.1 Introduction

There has been a dramatic increase in the number and size of RTSs across ice marginal glaciated landscapes of the western Canadian Arctic in the last two decades (Segal *et al.,* 2016). A combination of both climatic warming and increased extreme rainfall events appear to explain much of the enhanced RTS activity (Kokelj *et al.,* 2015; Lewkowicz and Way, 2019; Segal *et al.,* 2016). Despite research identifying connections between climatic trends and RTS activity, the ability to understand, model and predict short-term variations in factors such as HWR rates and sediment loss remain highly limited. This also applies to our ability to understand why the occurrence of individual thaw slumps, or thaw slump complexes, display such spatial and temporal heterogeneity, even within settings that appear to have favourable characteristics for their formation.

4.1.1 An approach to Site Characterisation and Internal Structure Mapping

Only a few studies have examined the local (<10 km) or site specific (<1 km) variations in soil and morphology with the aim of identifying characteristics involved in the formation of RTSs, and with limited success (Lantuit *et al.,* 2012b). However, several features have been noted in previous research as contributing, or potentially contributing, to the occurrence of RTSs, and their subsequent progression once initiated. These include the:

- ALD (Burn, 2000; Chipman *et al.,* 2016; Lantuit and Pollard, 2008)
- Soil Characteristics (Farquharson *et al.,* 2019; Lantuit *et al.,* 2012b; Wang, 2009)
- Soil OB Thickness (Ramage *et al*, 2017; Segal *et al.,* 2016)
- Massive Ice Body Variability (Lantuit and Pollard, 2008; Ramage *et al.,* 2017; Rampton and Mackay, 1971; Rudy *et al.,* 2017; Segal *et al.,* 2016)

Using these four features, this chapter will characterise the fine scale and internal structure of an active (A) and undisturbed (U) portion of Peninsula Point. This information can be used as a basis for better understanding the local spatial and temporal variability in RTS activity.

4.2 Point Clouds and Topographic Data

To effectively characterise variations in the thickness and elevation of the internal structures, and to analyse changes in surface features and RTS activity, high resolution topographic data were required. These data were generated through the application of the SfM-MVS technique in Agisoft Photoscan 1.2.4 (Agisoft, 2016). SfM-MVS is a photogrammetric range imaging approach that allows for high resolution 3D object or landscape reconstruction through the analysis of overlapping 2D images. Images can be captured using consumer grade hand-held digital cameras (Carrivick *et al.,* 2016; Westoby *et al.,* 2012), and can produce results with similar levels of accuracy to terrestrial laser scanners, but with a fraction of the cost (James and Robson, 2012; Westoby *et al.,* 2018). Image datasets are being increasingly captured using relatively cheap (~£1,000) off-the-shelf drones. This has expanded the application of SfM-MVS techniques within the field of geoscience, from coastal sand dunes (Lim *et al.,* 2015), to rock cliffs (Obanawa, 2015), landslides (Lucieer *et al.,* 2013), glaciers (Immerzeel *et al.,* 2014) and more recently, along permafrost coasts too (Cuncliffe *et al.,* 2018, Whalen *et al.,* 2017).

A description SfM-MVS methodology is provided in the next section. However, as the Photoscan algorithms are proprietary the exact algorithms used are not widely known. As such, the following methodology will consist of the steps taken within Photoscan and the common algorithms used for typical SfM-MVS workflows at each stage. An overview of the SfM-MVS methodology is provided in the Figure 4.1 flow diagram.

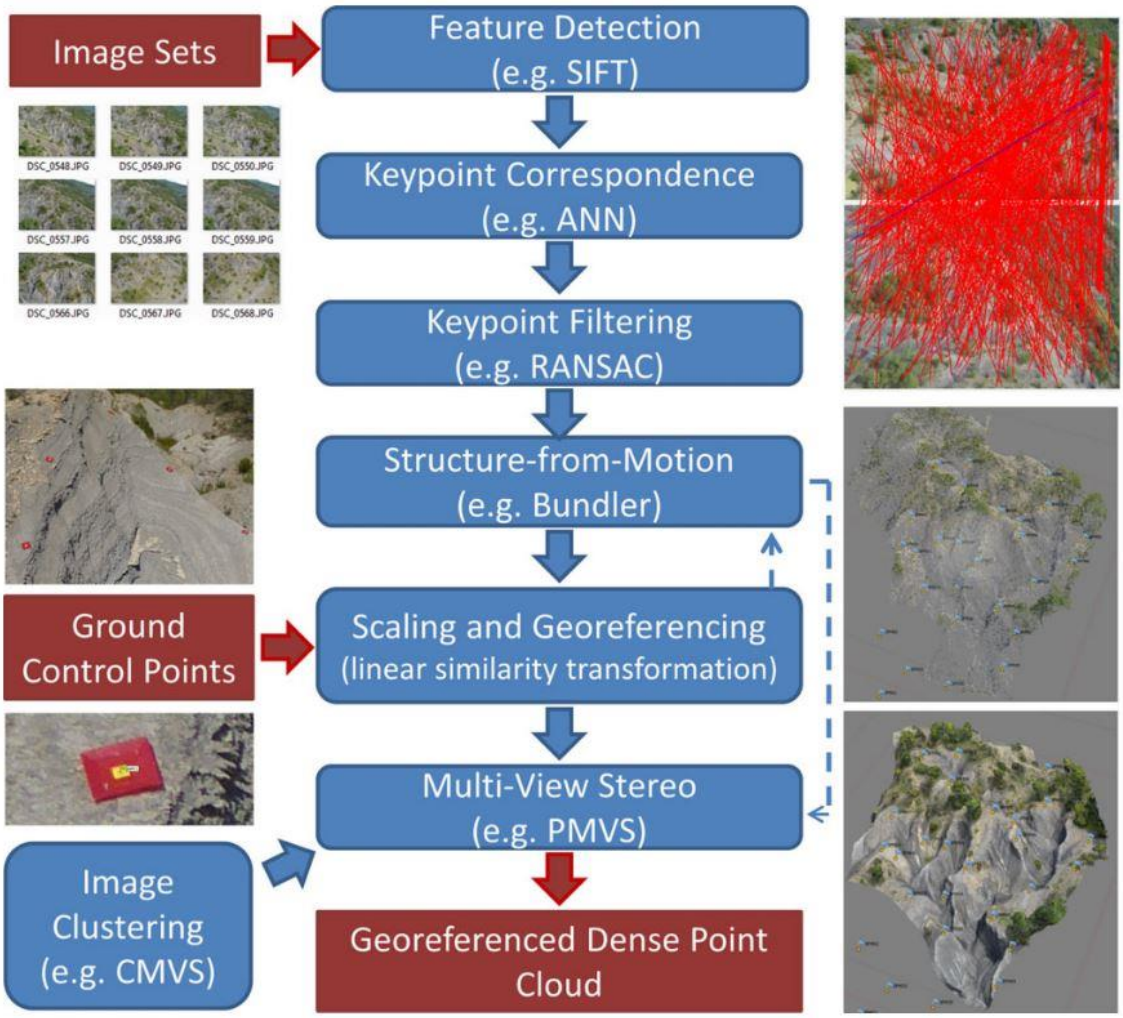

Figure 4.1: SfM-MVS generalised workflow from Smith et al., (2015).

4.2.1 Image Capture

During the summers of 2016, 2017 and 2018 members of Natural Resources Canada (NRCan) captured high resolution aerial imagery at Peninsula Point using the DJI Phantom 4 drone (P4). This drone is consumer grade containing a 12MP camera with a 1/2.3" CMOS sensor stabilised using a 3-axis Gimbal. The flight path was typically 70 m above the surface creating an effective spatial resolution of about 1.8 cm^2 at nadir, with distortions occurring towards the image edges. A total of between 600 and 1000 usable aerial images were collected in each survey, an example of which can be seen in Figure 4.2. Ten black and white markers were distributed throughout the site to use as ground control points (GCPs). These were georeferenced using Real-Time Kinematic differential global navigation satellite system (RTK) to produce cm scale locational accuracy.

4.2.2 Image Processing

The 2016 SfM point cloud was created at NRCan, processing the images through the software Pix4D and georeferenced using RTK. This resulted in a horizontal and vertical accuracy of ±0.10 m and ±0.25 m respectively (P. Fraser, personal communication, June 2018). SfM model generation from the 2017 survey was carried out in Agisoft Photoscan 1.2.4 (Agisoft, 2016). The steps involved in the processes are briefly described here. All the images are loaded into Photoscan and all irrelevant data, such as sky, water and background land, are manually masked out (Figure 4.3). Additionally, Photoscan provides an estimate of the quality of each image and any below 0.5 are removed from the selection. This leaves only the useful data from each image that will then be used in the subsequent processing steps, increasing the accuracy and reducing the processing time. With the high quality and relevant images remaining, the photos are then “aligned” within Photoscan. Alignment involves several steps, the first being the identification of features, or keypoints, that are invariant to scale, orientation and partially to illumination. The Scale Invariant Feature Transform (SIFT) method (Lowe, 2004) is commonly applied for this task. Next, the correspondence of keypoints across multiple images is assessed. A modified k-dimensional trees approach (Muja and Lowe, 2009) is commonly employed to reduce the computational workload for this task. Filters are also applied to the keypoints during this process, such as RAN-dom SAmple Consensus (RANSAC; Fischler and Bolles, 1981), to reduce the number of erroneous matches (Smith *et al.,* 2016). The next step is creation of the SfM model. This is performed using bundle adjustment algorithms (such as Bundler [Snavely *et al.,* 2008]) to reconstruct the 3D geometry while simultaneously estimating the camera positions, orientations and settings. The resulting output is a sparse, unscaled 3D point cloud (Figure 4.4).

Figure 4.2: Example of a single P4 image, with a researcher within the red box for scale

Figure 4.3: P4 image, with the water masked out

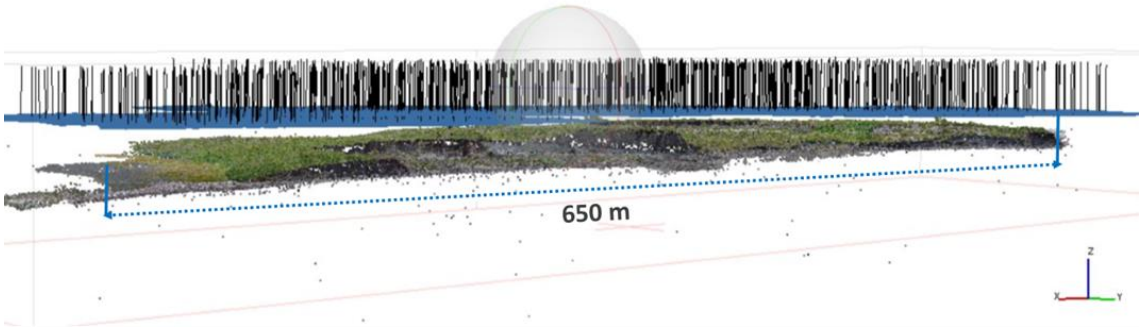

Figure 4.4: Sparse point cloud and the camera positions shown in blue

With the initial alignment complete, points are removed if they contain a reprojection error >0.5, are common in less than three photos or are clearly erroneous. At this stage, a dozen points visible in both the 2016 point cloud and 2017 sparse point cloud are used to scale and georeferenced the model. This is done by manually selecting points from the 2016 point cloud with known and accurate X, Y and Z coordinates. These points are then identified in the 2017 images within Photoscan and markers with their coordinates are added. After these steps, the alignment is optimised to improve the point cloud and camera accuracy. This process is iterative, reducing the reprojection errors and removing erroneous points (Figure 4.5).

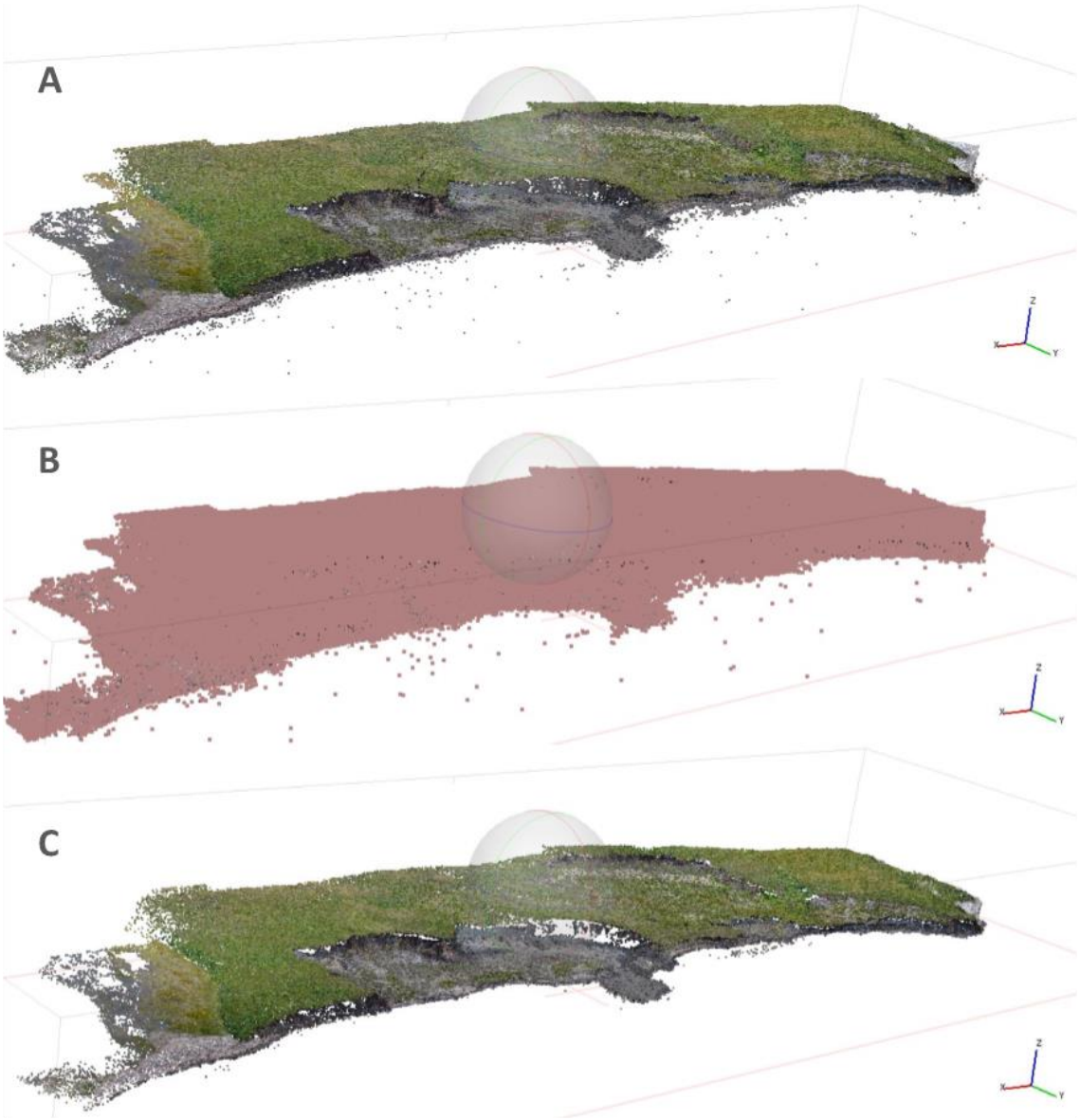

Figure 4.5: All tie points (A), selected tie points in three or less images (B), remaining tie points after removal (C)

The MVS method is then used to generate the dense point cloud. Detailed descriptions of the MVS algorithms used within geosciences and elsewhere can be found in Smith *et al.,* (2015) and Seitz *et al.,* (2006). For generating the dense point cloud within Photoscan, a high accuracy setting is chosen, and depth filtering is set to mild. Once generated, erroneous points are once more deleted, and the file is exported for further analysis.

4.2.3 SfM-MVS Model and LiDAR Accuracy Assessment.

This section will outline both the methods and results of the vertical and horizontal accuracy assessments. This includes four SfM-MVS models using aerial imagery from

1993 and 1994 for one, and drone-based imagery from 2016, 2017 and 2018 for the other three. A separate LiDAR dataset from 2004 is also included.

As accurate co-registration is important for assessing the relative change between each time period, it was necessary to choose a dataset from which the others could be closely aligned. Traditionally, the LiDAR data would be considered the most tested and reliable, and thus would be selected for this purpose. However, in this instance the 2016 SfM-MVS model was chosen. The main reason for this is that the visual imagery and high spatial resolution as part of the SfM-MVS model makes it easier to find points for accurate co-registrations and accuracy assessments. It also had the largest area of undisturbed terrain of the drone-based, highest resolution SfM-MVS models, which is also required for accurately registering the 1993/94 imagery. In addition, the co-ordinates of 10 markers spread throughout the site were accurately defined using RTK, giving the model a high degree of locational accuracy. For these reasons, 2016 will be used as the reference model going forward.

4.2.3.1 Data Sets and Alignment

SfM-MVS models generated from drone-based imagery (for 2017 and 2018) were created in Agisoft Photoscan and registered to the 2016 model using the point cloud alignment tool in CloudCompare (CC) software (CloudCompare v2.7.0, 2020). Approximately 50 points, evenly distributed throughout the overlapping point clouds, were selected from the 2016 data and matched with identical points in the 2017 and 2018 data. These points are distributed to include a large range of elevation variations and with broad spatial coverage. Once aligned, the point cloud can be analysed or compared with others within CC. The point clouds were also exported into Quick Terrain Modeller V8.0.5.2 (QTM [Quick Terrain Modeller, 2019) where they were converted into a digital elevation model (DEM) for additional analysis. An additional SfM-MVS model was created in the same fashion using aerial imagery from the summers of 1993 and 1994 (National Air Photo Library, Canada). As there were no RTK measurements, nor enough common points between 1993/94 and 2016 on which to accurately align the models, the vertical accuracy was innadequate for many of the 2.5D and volumetirc analysis. As such, the use of the 1993/94 data are limted to detailed planimetric analysis, identification of headwalls and general overviews of the large scale topographic features at the time.

The LiDAR data were collected in summer 2004 using the Airborne Laser Terrain Mapper 2050 LiDAR system and processed in house at Geological Survey of Canada. The raw data were gridded in Geographic Resources Analysis Support System

(GRASS). Elevation was determined using a nearest neighbour technique, and a 3*3 gridded interpolation method was used to fill in gaps. The resulting ASCII data set was imported into ArcInfo, and the ArcInfo ASCII grid was important into ArcGIS 9.0 where it was converted into a raster data and assigned to the UTM Zone 8 WGS84 projection. The data are estimated to have a vertical and horizontal accuracy of 0.3 m, based on the analysis of the GIS specialists contained in the metadata. The 2004 model contained no visual imagery, was at a much lower spatial resolution and, given the rate of change at Peninsula Point, was substantially different, topographically, to 2016. As such, it could not be finely co-registered. However, the data have strong spatial accuracy due to the GPS on board during data capture and the subsequent processing. Additionally, a simple observation of the overalapping areas with the 2016 SfM-MVS model shows them to be in close alignment. These factors suggest that the LiDAR data are well aligned with the SfM-MVS models and suitable for further analysis.

4.2.3.2 Horizontal Accuracy Assessment

2017 & 2018

As the ground surface appeared to remain stable away from actively retreating edges, 10 distinct features across the three models were used to assess 2D positional accuracy. The locations of the features used, as well as examples using details on features 3 and 9, are provided in Figure 4.6. Identifiable features ranged from distinct vegetation and wooden boards, to linear ice-wedge patterns and vegetation free patches (Appendix 1: Table 0.2). The X and Y coordinates are based on UTM zone 8 and so the differences can be treated as errors in metres. Compared to the 2016 baseline data, the Root Mean Square Error (RMSE) for 2017 was 0.12 m for X, and 0.14 m for Y. Mean Absolute Error (MAE) for 2017 was 0.11 m for both X and Y, with a range from 0.01 m to 0.19 m and 0.01 m to 0.27 m, for X and Y respectively. The RMSE for 2018 was 0.15 m in X and 0.11 m in Y. MAE for 2018 was 0.11 m for X and 0.08 m for Y. The ranges were 0.0 m to 0.37 m and 0.0 m to 0.23 m respectively.

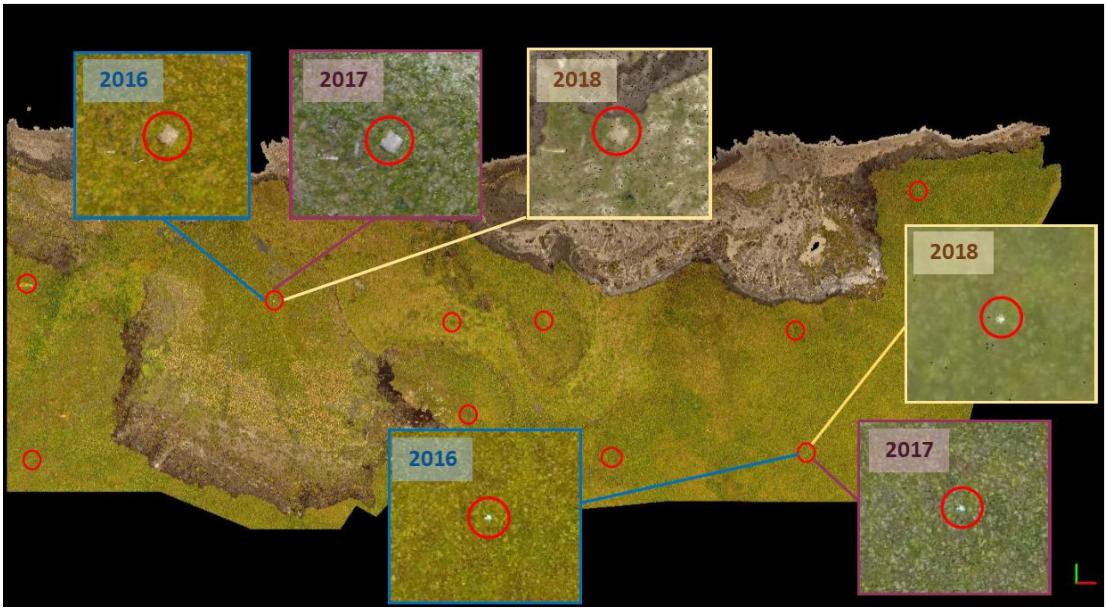

Figure 4.6: Location of features used for the horizontal accuracy assessment with 2016, 2017 and 2018. Details are provided for features 3 and 9.

1993/1994

Due to the time between the historic and contemporary SfM-MVS models (22 years from the 1993 and 1994 data to the 2016 data), the number of identifiable surfaces features present in both data sets was much reduced. However, five clear points were used for the error analysis. These are described in Appendix 1, Table 0.3, and the locations and details of three features can be seen in Figure 4.7. Longer lasting features, such as ice wedge polygons or ponds/lakes visible in the earlier imagery that had drained leaving clear corresponding surface changes in the newer imagery, were used. Identifying exact matching points from these larger features proved difficult, so the centre of any feature was used as the closest matching point. The RMSE was 0.23 m for X and 0.54 m for Y. The MAE was 0.22 m for X and 0.49 m for Y, with ranges from 0.15 m to 0.34 m and 0.14 m to 0.73 m for X and Y respectively.

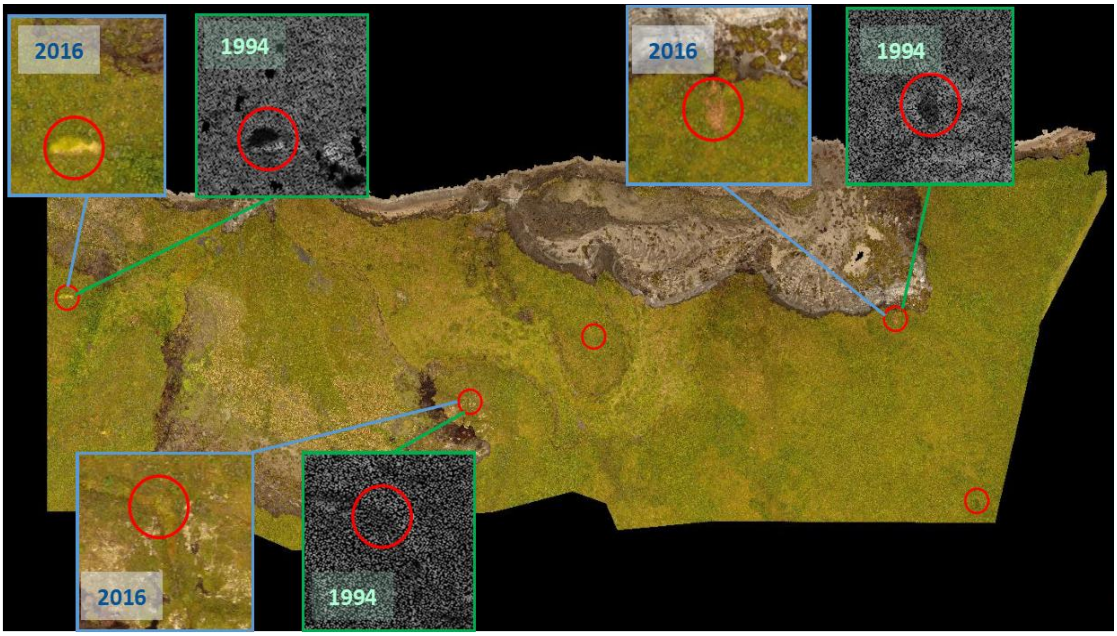

Figure 4.7: Location of features used in accuracy assessment between 1994 and 2016. Details of three features used are also displayed.

2004

Given the lack of visible imagery and lower resolution of the LiDAR data, it was not possible to carry out a similar style of horizontal accuracy assessment. On visual inspection the LiDAR data appeared closely aligned with the 2016 SfM-MVS model where they overlapped. In combination with the estimated horizontal accuracy of 0.3 m, it was deemed suitable for further analysis.

4.2.3.3 Vertical Accuracy Assessment

In this section, the vertical accuracy of the data relative to the 2016 SfM-MVS model will be assessed to ensure an accurate and useful representation of the relative change between the different years is possible. The 1993/94 data will not be included in this, as a visual inspection revealed the elevation to be exaggerated along the shoreline, likely due to a lack of accurate points here with which to finely co-register the models. Another consideration in this chapter is a general lowering of the landscape due thawing induced thermokarst. Farquharson *et al.,* (2019) found localised subsidence of between 0.4 m and 0.9 m between 2003 and 2016 across multiple sites in the Canadian High Arctic. It is necessary to consider the potential for similar subsidence at Peninsula Point in seemingly undisturbed terrain when assessing the relative elevation changes over time.

2017

The overall differences between the 2016 and 2017 elevation can be seen in Figure 4.8 (created using the cloud to cloud distance tool in CC). All large differences, >0.5 m, appear related to actively eroding and prograding shoreline, and retreating headwalls. Away from these locations, most of the cloud to cloud difference is under 0.5 m.

To carry out a more detailed assessment of the elevation difference, eight 25 m long strips along undisturbed terrain were compared between 2016 and 2017. The locations of these strips can be seen in Figure 4.8. Each strip contained 628 individual points for comparison. The average MAE difference across all eight strips was 0.07 m (RMSE of 0.10 m). The strip with the largest MAE averaged 0.32 m, while the smallest was 0.03 m. The statistics for each strip can be seen in Table 4.1.

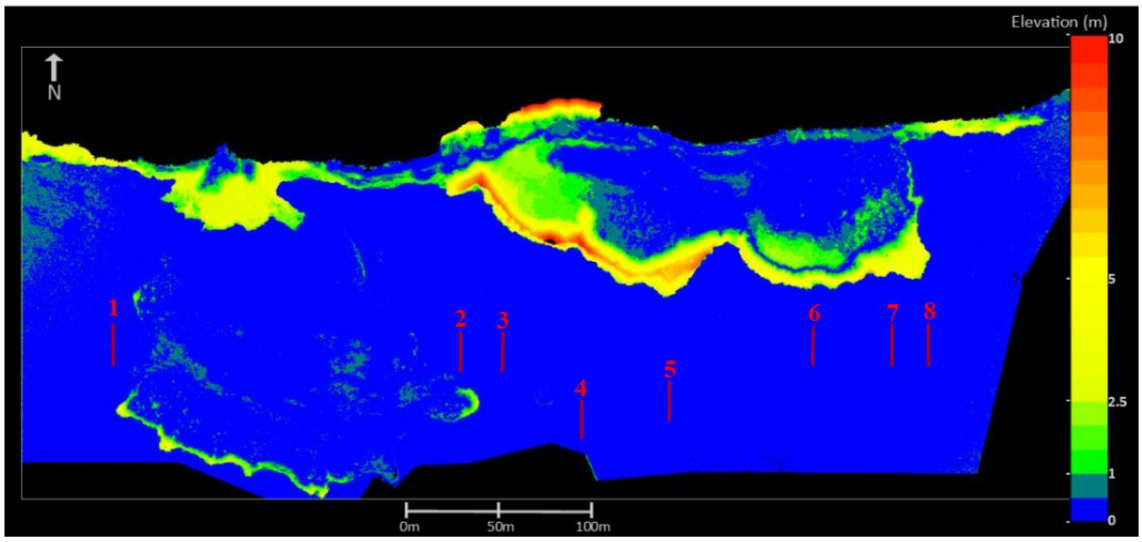

Figure 4.8: Point to point distance between the 2016 and 2017 point clouds, with red lines representing the locations for further detailed analysis

Table 4.1: Statistics generated for each 25m elevation strip on undisturbed terrain. MAE = Mean Absolute Error. Max = Maximum Error. Min = Minimum Error. SD = Standard Deviation. 95% = The value below which 95% of the differences lie for each strip.

	Strip1	Strip2	Strip3	Strip4	Strip5	Strip6	Strip7	Strip8
MAE	0.32	0.03	0.07	0.04	0.07	0.05	0.04	0.03
RMSE	0.33	0.04	0.09	0.05	0.10	0.07	0.06	0.04
Max	0.51	0.12	0.42	0.15	0.33	0.19	0.35	0.14
Min	0.18	0.00	0.00	0.00	0.00	0.00	0.00	0.00
SD	0.06	0.02	0.06	0.03	0.07	0.04	0.04	0.03
95%	<0.44	<0.03	<0.19	<0.08	<0.26	<0.14	<0.11	<0.08

Strips 5 and 6 were used for further analysis as they lie towards the middle of the site and are less likely to be influenced by strong thermokarst and so the elevation changes here between 2016 and 2017 are expected to be less than those near cliff edges or

along the coast. Each strip had 628 points of comparison, totalling 1256 points between both sections. An elevation profile for both strips in both years and the error distribution from each strip and both strips combined can be seen in Figure 4.9.
In strip A, the average difference between 2016 and 2017 was -0.02 m, with a range from -0.33 m to +0.26 m. The MAE was +0.07 m. Out of 628 points 560, or 89.2%, of the differences lay between -0.15 m and +0.15 m. In strip B, the average difference was +0.04 m, with a range from -0.07 m to +0.19 m. The MAE was +0.06 m. Out of 628 points 563, or 89.6% of the differences lay between -0.1 m and +0.1 m. Combining the data from both strips produces an average difference of +0.01 m, with a range of -0.33 m to +0.26 m. The MAE was +0.06 m. Out of 1256 points 1064, or 84.7%, lie between -0.1 m and +0.1 m. The 2016 and 2017 point clouds appear to be co-registered very well, with 0.1% of the elevation difference on the measured undisturbed terrain being greater than 0.5 m. The point cloud is thus suitable for further analysis and combination with other spatial data.

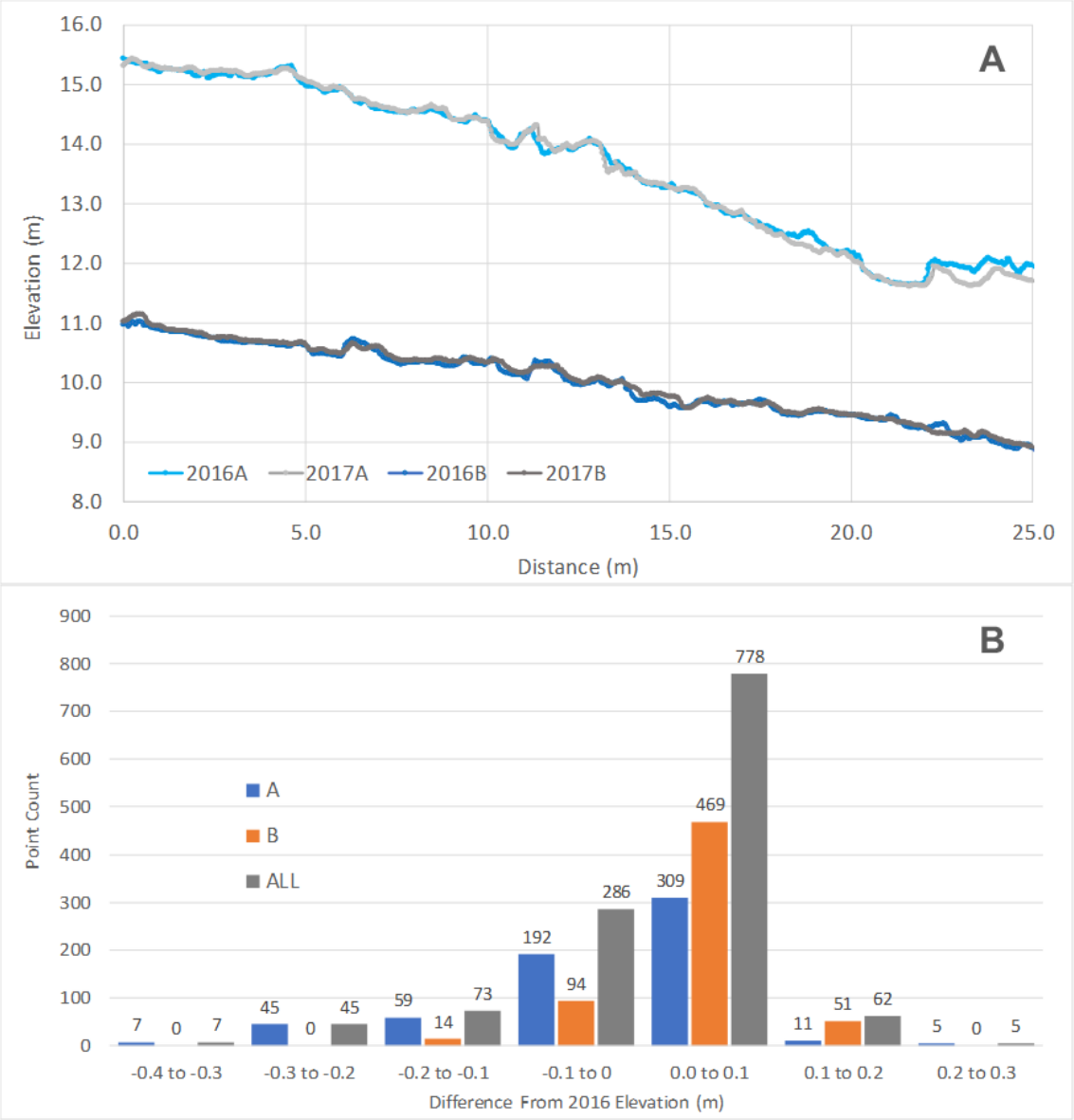

Figure 4.9: Elevation profiles for both 2016 and 2017 strips (A) and their subsequent point error distributions (B)

2018

The overall difference between 2016 and 2018 can be seen in Figure 4.10. The differences are much larger than between 2016 and 2017. The largest changes are associated with the progradation, shoreline and HWR. However, an overall banded pattern is also apparent, with anomalies of up to 2.5 m on the outer segments, gradually reducing back to 0 m towards the middle, before increasing again up to -1.0 m in the centre. This is an issue associated with a “bowling” effect, that can occur during the creation of the SfM-MVS models within Agisoft Photoscan. This is a parabolic distortion due to a lack of overlapping images along the model edge, resulting in an overestimation of the elevation (Brunier *et al.,* 2016; Ouédraogo *et al.,* 2014).

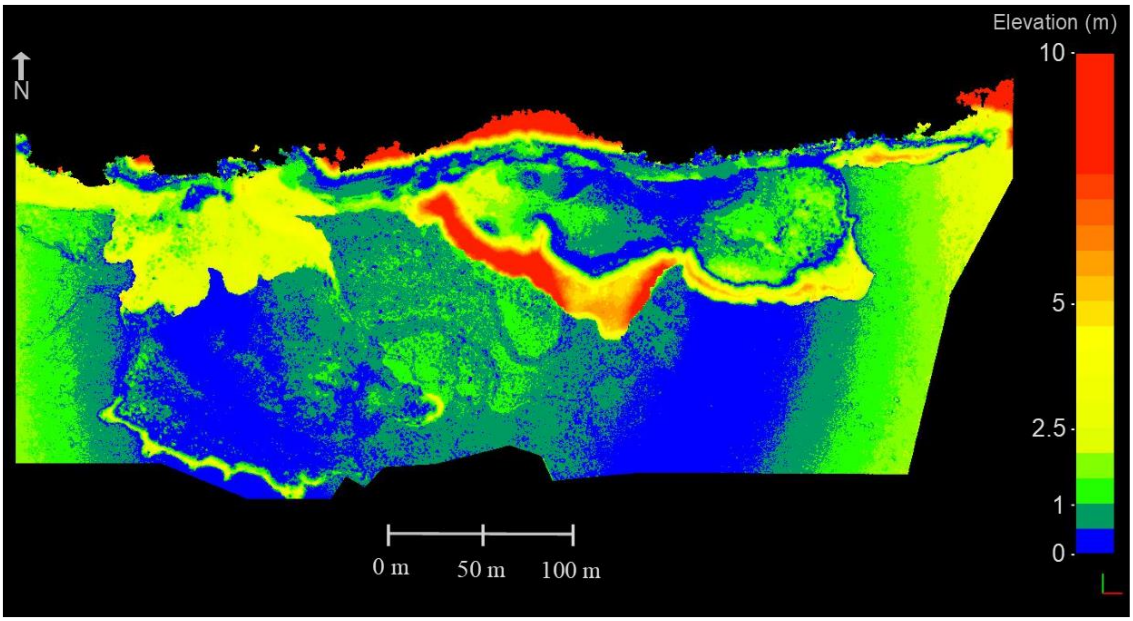

Figure 4.10: Point to point distance between the 2016 and 2018 SfM-MVS point clouds

Typically, this error would cast considerable doubt onto the utility of the 2018 data. However, as the analysis across the years will be performed using transect lines and the distortion in the 2018 elevation occurs in bands, it is possible to add a specific offset to each transect line to bring the elevation values in the undisturbed regions closer together, significantly improving the alignment and allowing for useful change analysis. An example of this is provided in Figure 4.11, which displays the elevation along the transect lines for 2016 and 2018 that follow the northing 573150W. A is the unadjusted value for 2018. It clearly follows the elevation variability of 2016 closely in the undisturbed area, but with a positive bias. By applying a downward adjustment of 1.3 m, the alignment is much improved, as can be seen in Figure 4.11B.

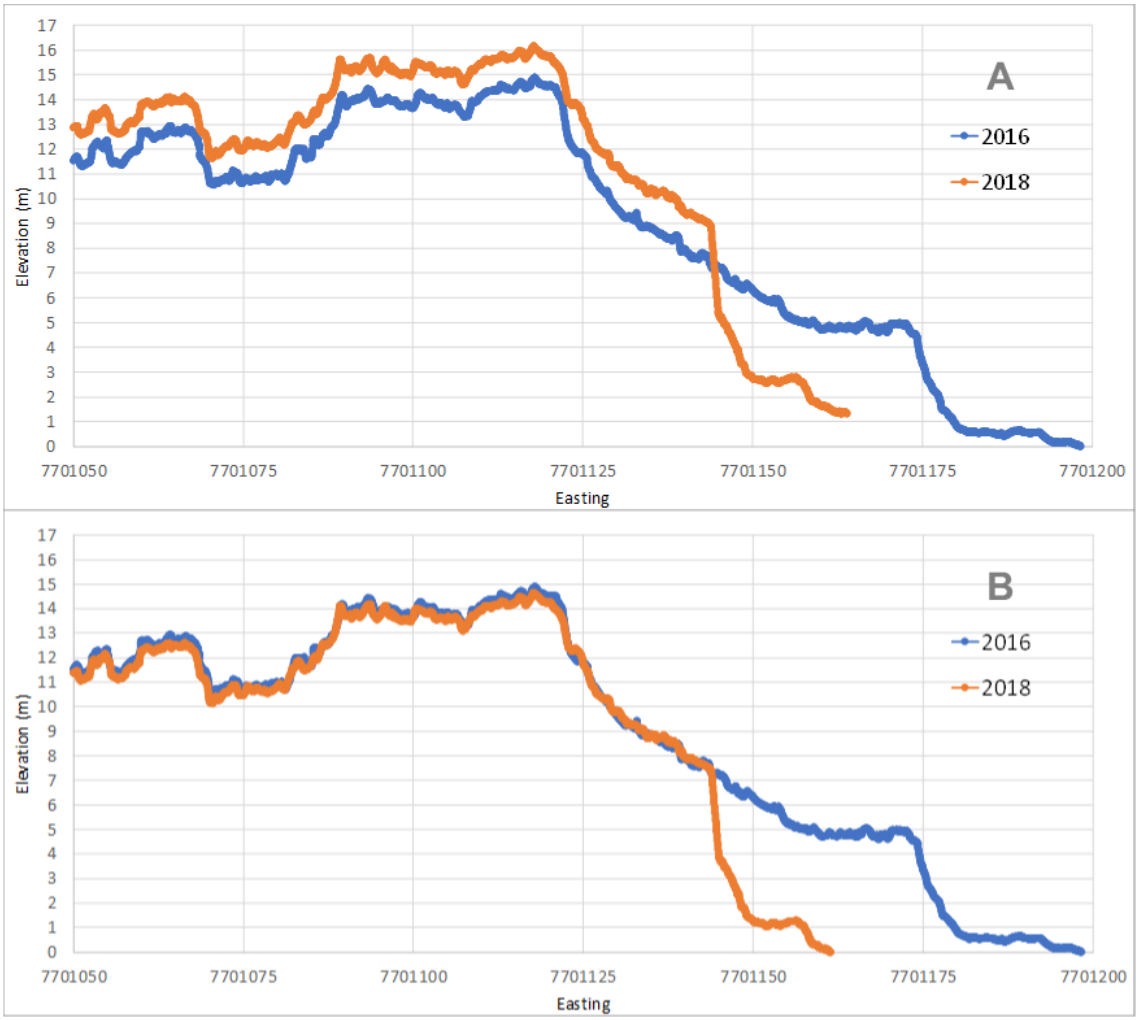

Figure 4.11: Original elevation profiles along northing 573150W (A) Adjusted 2018 elevation profile (B)

Corrections were also applied to the other elevation transects to improve the alignment, varying from -1.8 m on the eastern edge to +0.9 m near the centre, with an average absolute correction of 0.65 m (Figure 4.12). With the corrections applied, the accuracy assessment was carried out in the same way as the 2017 comparison, using eight strips of 25 m length along the undisturbed terrain.

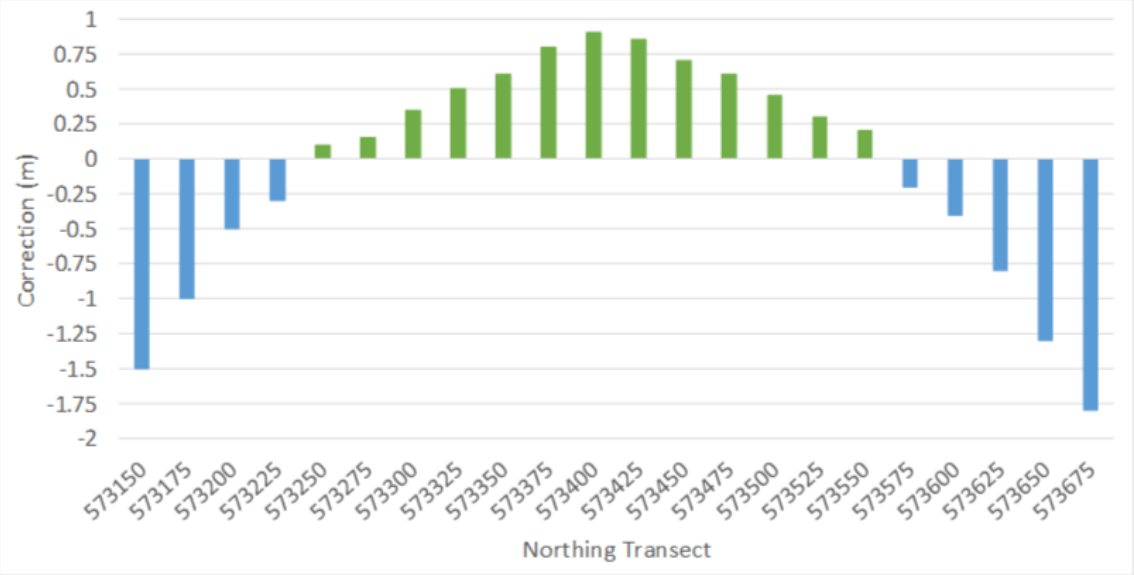

Figure 4.12: Correction applied to each elevation transect in 2018 to account for the "bowling" effect

Before corrections were applied, the average MAE across all eight strips was 0.84 m (average RMSE 0.85 m), with a range from 0.06 m to 1.19 m. After corrections were applied, the average MAE dropped to 0.21 m (RMSE of 0.20 m), with a range from 0.09 m to 0.39 m (Table 4.2), resulting in a much more consistent match overall.

Table 4.2: Statistics, in meters, generated for each 25m elevation strip on undisturbed terrain. MAE = Mean Absolute Error. Max = Maximum Error. Min = Minimum Error. SD = Standard Deviation. 95% = The value below which 95% of the differences lie for each strip.

	Strip 1	Strip 2	Strip 3	Strip 4	Strip 5	Strip 6	Strip 7	Strip 8
MAE	0.22	0.39	0.24	0.24	0.22	0.09	0.12	0.15
RMSE	0.22	0.40	0.26	0.24	0.24	0.11	0.13	0.18
Max	0.37	0.54	0.47	0.39	0.42	0.28	0.34	0.33
Min	0.07	0.26	0.00	0.11	0.00	0.00	0.00	0.00
SD	0.06	0.05	0.10	0.05	0.09	0.07	0.06	0.06
95%	<0.30	<0.48	<0.40	<0.34	<0.36	<0.33	<0.22	<0.25

Strips 5 and 6 were used for further analysis once more, as they lie towards the middle of the site and are the least likely to have undergone substantial change (Figure 4.13). In strip A, the average difference between 2016 and 2018 was -0.22 m, with a range from -0.42 m to +0.14 m. The MAE was 0.22 m. Out of 628 points 619, or 98.6%, of the differences lay between -0.42 m and 0 m. In strip B, the average difference was -0.07 m, with a range from -0.28 m to +0.21 m. The MAE was 0.09 m. Out of 628 points 582, or 92.7% of the differences lay between -0.20 m and +0.20 m. Combining the data from both strips produces an average difference of -0.15 m, with a range of -0.42 m to +0.21 m. The MAE was +0.16 m. Out of 1256 points 1131, or 90.0%, lie between -0.30 m and

+0.20 m. With the corrections applied, 2016 and 2018 point clouds appear to align closely over the undisturbed terrain, with 0.5% of the elevation difference on the measured undisturbed terrain being greater than 0.40 m. Given these results, the 2018 data are suitable for further analysis.

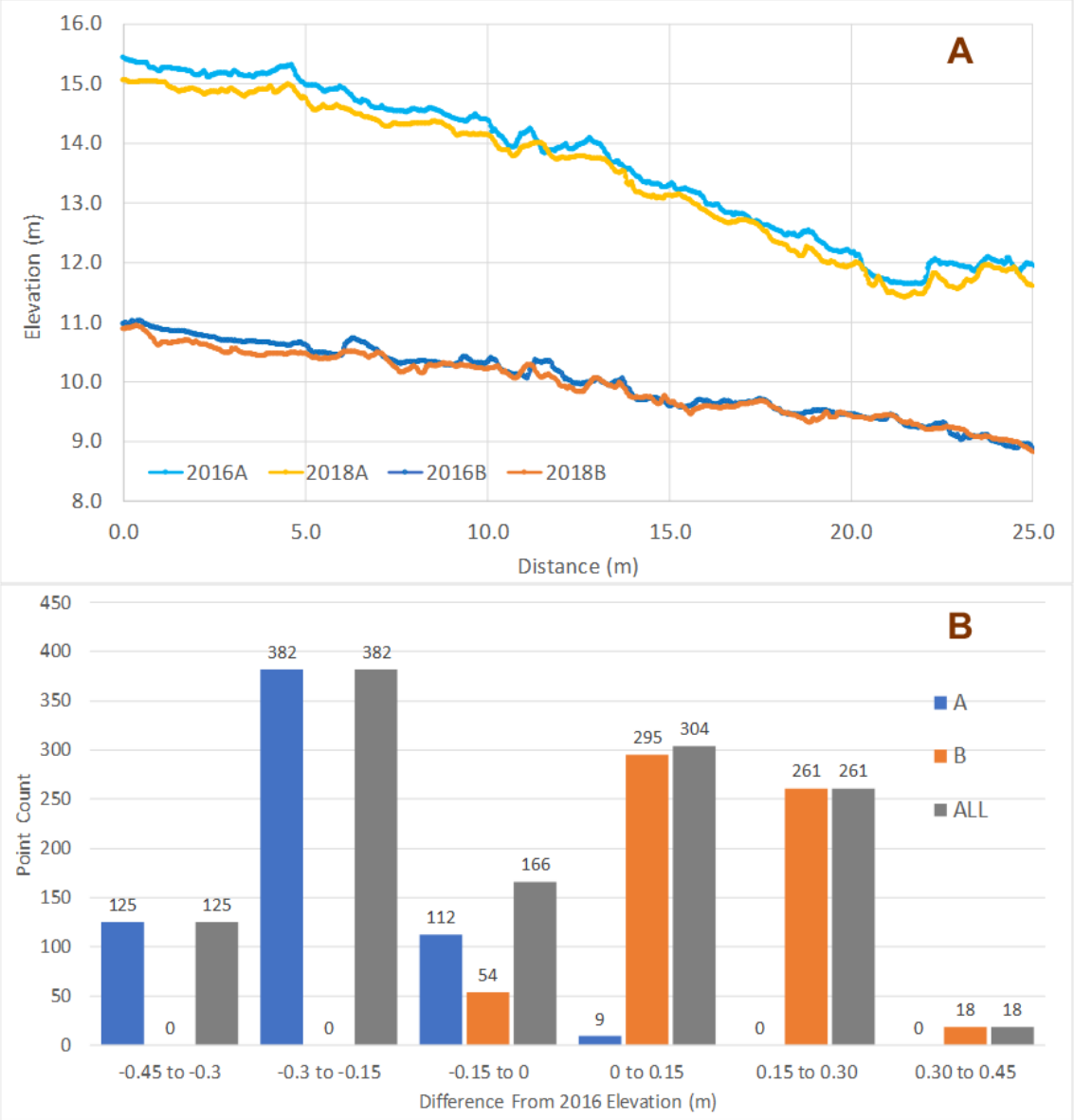

Figure 4.13: Elevation profiles for both 2016 and 2018 strips (A) and their subsequent point error distributions (B)

2004

The overall elevation distance between 2004 and 2016, overlain on 2016, can be seen in Figure 4.14. The only areas with little or no elevation change are across the eastern sections away from retreating headwalls and the high ground in the centre, where the differences are typically less than 1.0 m. The distinctive high ground section in the centre appears not to have been affected by PRTS, while the reduction in elevation suggests that headwalls have retreated around and behind it.

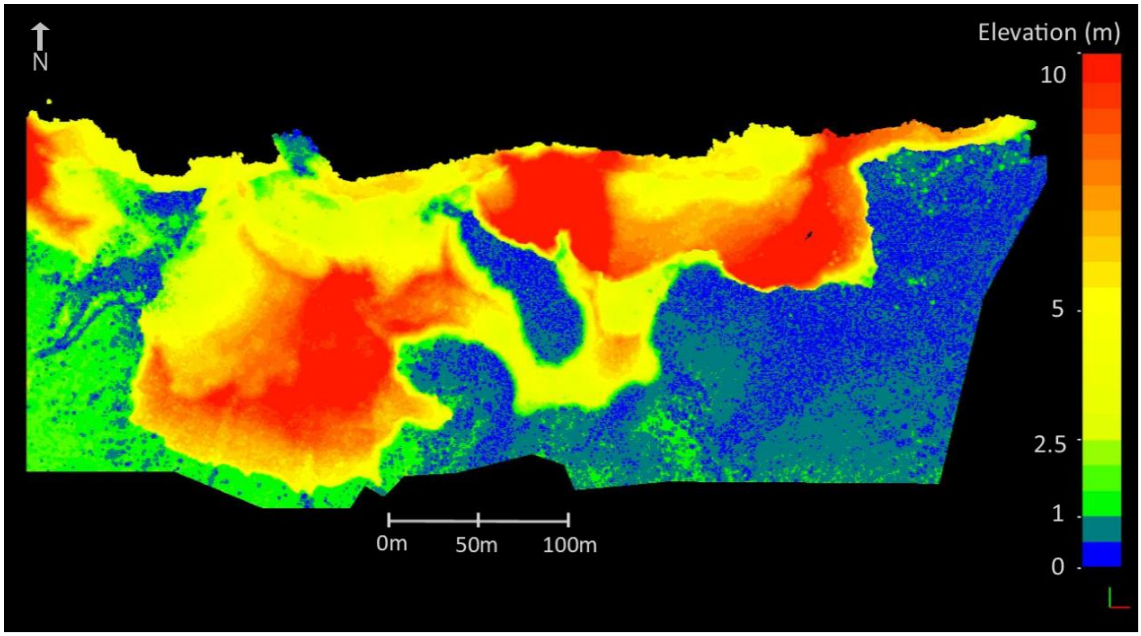

Figure 4.14: Point to point distance between the 2016 SfM data and the 2004 LiDAR data.

As with previous comparisons, the elevation assessment was carried out using the same eight strips as before, with the overall stats presented in Table 4.3. The MAE across all eight strips was 0.43 m.

Table 4.3: Statistics generated for each 25m elevation strip on undisturbed terrain. MAE = Mean Absolute Error. Max = Maximum Error. Min = Minimum Error. SD = Standard Deviation. 95% = The value below which 95% of the differences lie for each strip.

	Strip 1	Strip 2	Strip 3	Strip 4	Strip 5	Strip 6	Strip 7	Strip 8
MAE	0.91	0.23	0.52	0.61	0.66	0.21	0.14	0.20
RMSE	0.92	0.26	0.50	0.62	0.70	0.23	0.16	0.23
Max	1.36	0.52	0.72	0.76	1.29	0.45	0.37	0.45
Min	0.64	0.00	0.00	0.30	0.20	0.00	0.00	0.00
SD	0.16	0.13	0.17	0.08	0.26	0.09	0.09	0.12
95%	<1.21	<0.48	<0.67	<0.72	<1.17	<0.36	<0.30	<0.41

The overall average error is +0.41 m, indicating a positive offset between 2004 and 2016. Finer analysis using strips 5 and 6 highlight this fact (Figure 4.15). In strip A, the average difference between 2004 and 2016 was +0.66 m, with a range from +0.20 m to +1.29 m. The MAE was also 0.66 m. Out of 628 points 558, or 88.9%, of the differences lay between +0.25 m and +1.0 m. In strip B, the average difference was +0.21 m, with a range from -0.05 m to +0.45 m. The MAE was also 0.21 m. Out of 628 points 614, or 97.8% of the differences lay between 0 m and +0.5 m. Combining the data from both strips produces an average difference of +0.43 m, with a range of -0.05

m to +1.29 m. The MAE was +0.13 m. Out of 1256 points 1184, or 94.3%, lie between 0.0 m and +1.0 m.

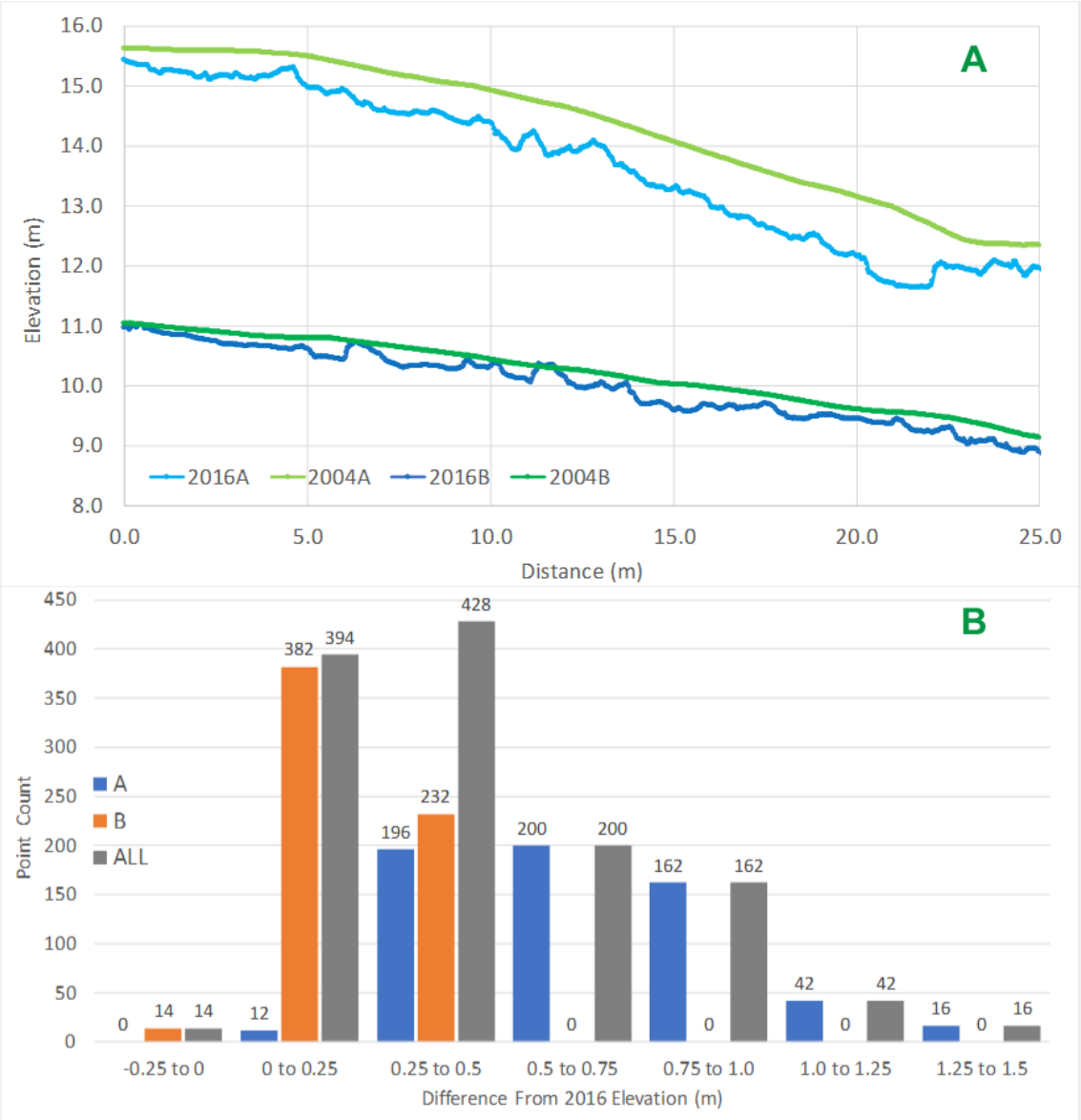

Figure 4.15: Elevation profiles for both 2016 and 2004 strips (A) and their subsequent point error distributions (B)

The amount of variability is likely due to different levels of thermokarst and resulting topographic change across Peninsula Point, even in areas that should be the most stable. The general lowering of the mainly stable areas may be due to a seaward creep of the soil or subsidence due to thawing internal ice and deepening active layer. There may also be a contribution of errors by the data collection, processing and horizontal alignment differences. While a detailed analysis of the reasons behind this change is beyond the scope of this thesis, the overall offset of +0.41 m lies in the lower range noted by Farquharson *et al.,* (2019), of 0.4 m to 0.9 m in sites across the Canadian

High Arctic between 2003 and 2016. This lends weight to the idea that similar processes operating elsewhere in the Canadian Arctic may also be contributing to subsidence in Peninsula Point, rather than the observed difference in elevation being a consequence of errors. As such, the elevation reduction between 2004 and 2016 is most likely a result of local thaw and subsidence, and thus the LiDAR data are suitable for further analysis.

4.3 Grain Size, Conductivity, Total Dissolved Solids and Salinity

Fine grained soils tend to form muddy flows when mixed with thawed ice. These flows help to transport sediment away from the ablating ice face, contributing to RTS development (McRoberts and Morgenstern, 1974; Wang *et al.,* 2009). As such, variability in grain size at local and site-specific scales may play an important role in RTS development. However, few studies have assessed the contribution of grain size variability to RTS variations at these scales. On Herschel Island and Kings Point, variation in the grain size distribution was noted between active slumps, previously affected areas and undisturbed terrain, although none of the differences were statistically significant (Lantuit *et al.,* 2012b).

4.3.1 Soil Sampling and Processing Methodology

To assess the influence of soil variability on the likelihood of thaw slump development at Peninsula Point, a total of five 500 g soil samples were collected. Two from the high, undisturbed ground (labelled with Us) and three from the low, slump affected ground (labelled with As), in Figure 4.16. Samples were placed in plastic sample bags, labelled and sealed in preparation for transportation.

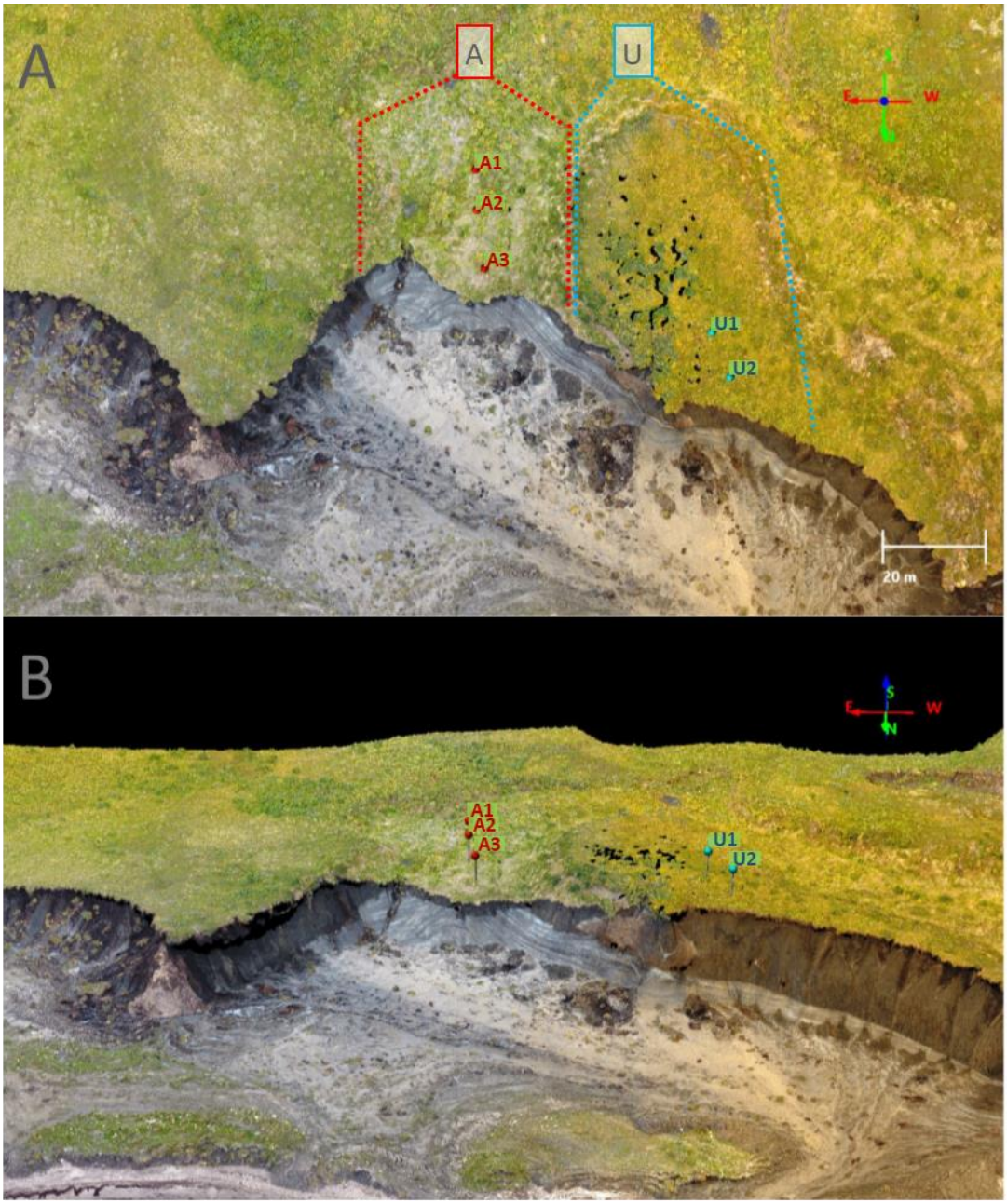

Figure 4.16: Soil sampling locations on Peninsula Point, both plan (A) and oblique (B) views.

Grain size variation measurements were conducted using the Mastersizer 300E laser particle size analyser. From each 500g sample, nine separate subsamples were taken and analysed using the following method:

- Run the standard operating procedure based on the hydro EV accessory
- Samples ground up and mixed with deionised water
- A beaker with 500ml of deionised water and 0.5g of anti-flocculant (Sodium Hexametaphosphate) is placed in the wet dispersion unit

- The sample is gradually added to the beaker until the density of suspended soil causes obscuration to measure between 10 and 20%, the required density for analysis
- The machine analyses the samples six times
- Once completed, the beaker from the Hydro EV unit is removed, cleaned, refilled with deionised water and anti-flocculant in preparation for the next sample or sub sample measurement.
- Results are saved as CSV files for later analysis

The results were organised, analysed and graphed in Microsoft Excel (grain size data are included in Appendix 1).

4.3.2 Soil Conductivity, TDS and Salinity Methodology

Conductivity, total dissolved solids and salinity (CTS) measurements were carried out *in situ* using an ExStik EC500 probe. Measurements were made in nine locations on Peninsula Point, three on the slump affected ground labelled with red As, and three on both the left and right undisturbed high ground terrain labelled with blue Us (Figure 4.17). The method for conducting the measurements was as follows:

- Soil from a sample site was placed in a small container and mixed with water.
- Electrodes from the ExStik EC500 were placed in the mixture and measurements of conductivity, total dissolved solids and salinity were taken.
- This process was repeated for the low ground segment and the upper ground on both sides
- Values were written in the field and added to excel files later for further analysis.

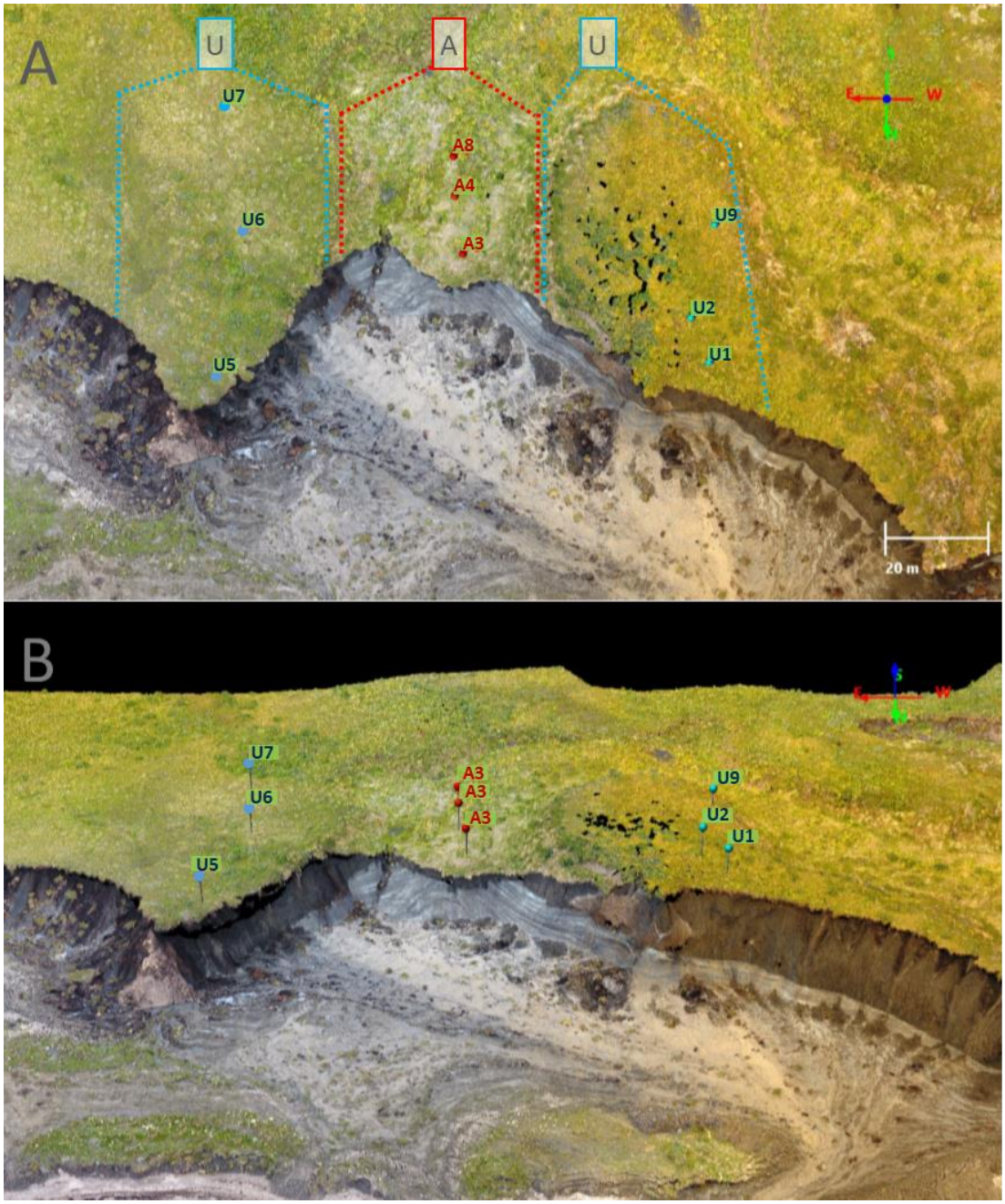

Figure 4.17: Conductivity, TDS and salinity measurement locations on Peninsula Point, both plan view (A) and oblique view (B).

4.3.3 Grain Size Distribution Results

Grain size analysis from the undisturbed terrain display particles ranging from 0.46 to 400 µm with 90% occurring within a range of 0.77 and 45.6 µm. The proportions of clay, silt and sand were 17.48%, 78.94% and 3.59% respectively. The active slumping area displayed a slightly altered grain size distribution (Figure 4.18), with particles ranging from 0.40 to 3080 µm with 90% occurring within a range of 0.52 and 127 µm. The proportions of clay, silt and sand were 17.67%, 66.67% and 15.65% respectively (Figure 4.19). While there are notable differences in grain size distribution, none of the

differences measured were found to be statistically significant. What small differences exist may be explained by hydrological processes and topography. The active area is situated in a depression, allowing meltwater to flow into and through it. This flow may cause finer grains to be washed out and transported towards the sea. At the same time, thawing permafrost from the headwalls may slump into the active area, depositing coarser grains. Additionally, coarse grains embedded within the massive ice might also be deposited upon thawing, altering the grain size distribution.

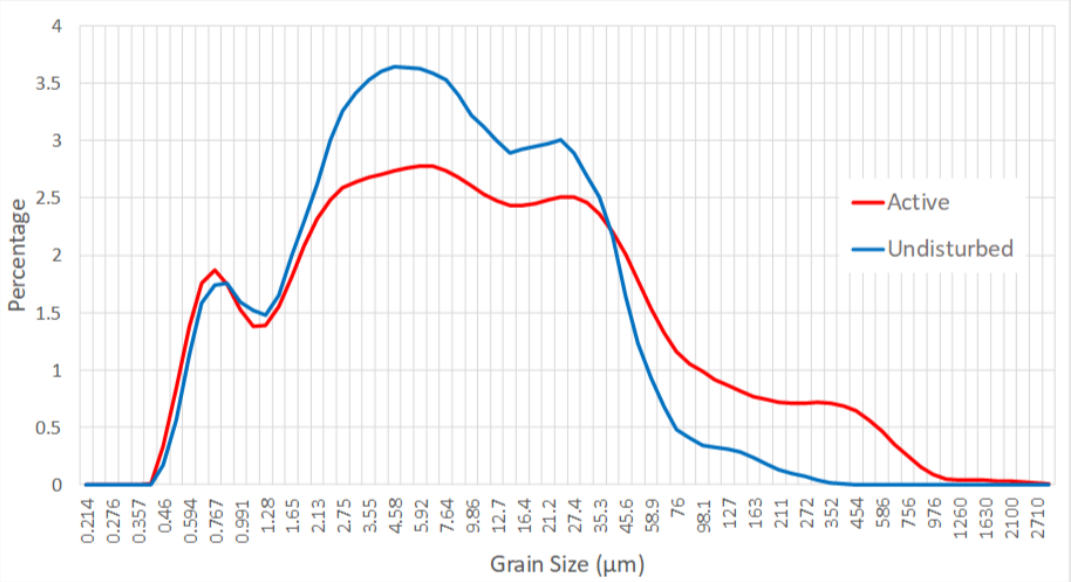

Figure 4.18: Grain size distribution between the active (blue) and undisturbed (orange) soil samples

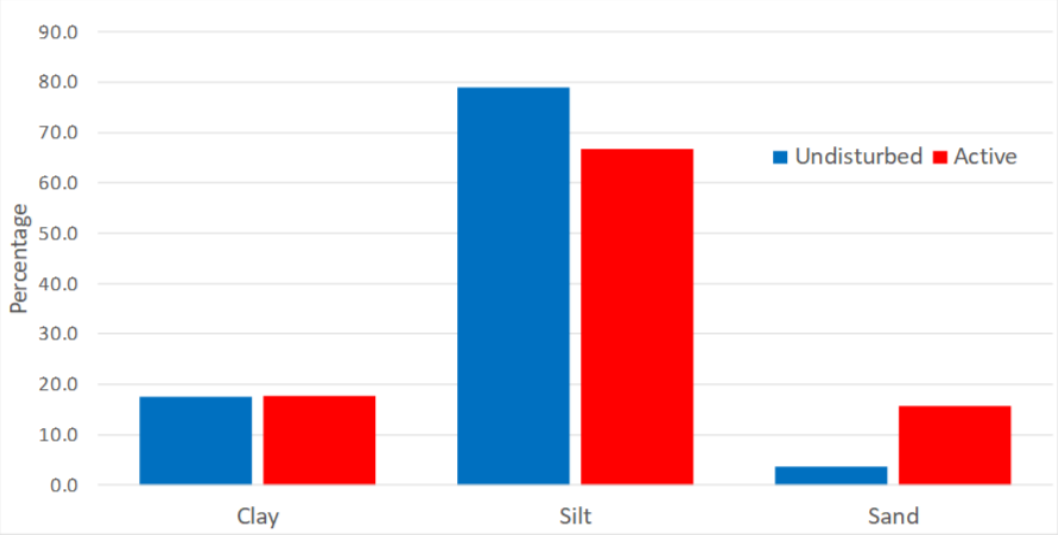

Figure 4.19: Grain type proportions

4.3.4 Conductivity, TDS and Salinity Results

CTS values on the undisturbed soil to the east (Table 4.4) were typically lower than those observed to the west (Table 4.5), although the differences were not statistically significant. There were no clear trends observable based on distance to the shoreline.

The active slumping segment exhibited significantly higher values and more variability in each CTS category based on the students t-test (Table 4.6). The reason for these differences is not immediately obvious.

Table 4.4: Measured values for the undisturbed soils to the East

Measurement	Mean	Max	Min
Conductivity (µ^s)	187	247	151
TDS (ppm)	131	173	105
Salinity (ppm^s)	82	118	51

Table 4.5: Measured values for the undisturbed soils to the West

Measurement	Mean	Max	Min
Conductivity (µ^s)	259	293	242
TDS (ppm)	189	205	180
Salinity (ppm^s)	128	140	121

Table 4.6: Measured values for the active slump soils

Measurement	Mean	Max	Min
Conductivity (µ^s)	875	1088	710
TDS (ppm)	621	761	498
Salinity (ppm^s)	433	530	346

It has been noted in previous studies that terrain disturbances can lead to localised intense changes in soil salinity. Processes such as RTSs can expose salt frozen within the permafrost to surface energy fluxes and thawing, causing them to leach out of the soil. This was the case in Banks Island also, where efflorescence was discovered on the floor of RTSs (Kokelj and Lewcowicz, 1999). As such, while it appears that high CTS values may be useful for identifying RTSs that are active or recently stabilised, it does not appear to offer any clues as to why the thaw slumps occurred.

4.4 Active Layer Depth

4.4.1 Active Layer Depth Methodology

ALD was recorded using a thin metal probing rod and a measuring tape (Figure 4.20). The rod was pressed into the soil through the active layer until the resistance of the solid permafrost prevented it from going any deeper. The length of the deepest point reached on the rod was then measured using the tape and recorded. This depth was

considered the depth to the top of the permafrost, or the ALD. Measurements, at the nine locations seen in Figure 4.21, were taken in August, when the active layer is near its maximum depth. The main source of measurement error comes from determining where the soil begins. Much of Peninsula Point contains a spongy, vegetation rich layer on top of the soil, which varies between 0.05 m and 0.3 m in thickness when uncompressed and gradually blends into the loose organic rich topsoil. The thickness of the vegetation mat was subtracted from the total depth. However, the precise point at which the soil starts and the vegetation layer ended was not a clearly defined boundary, and so a measurement error of ± 0.05 m is possible.

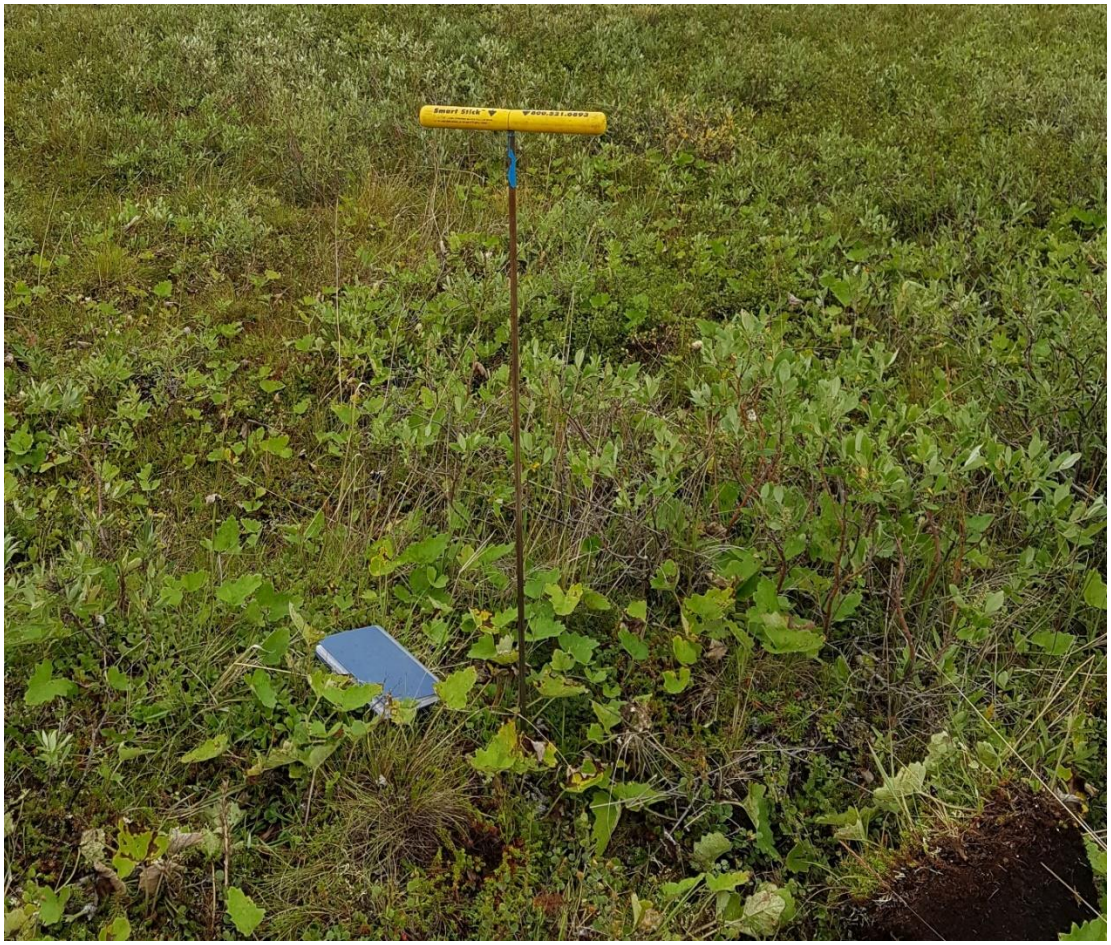

Figure 4.20: Probing rod used for measuring the active layer depth

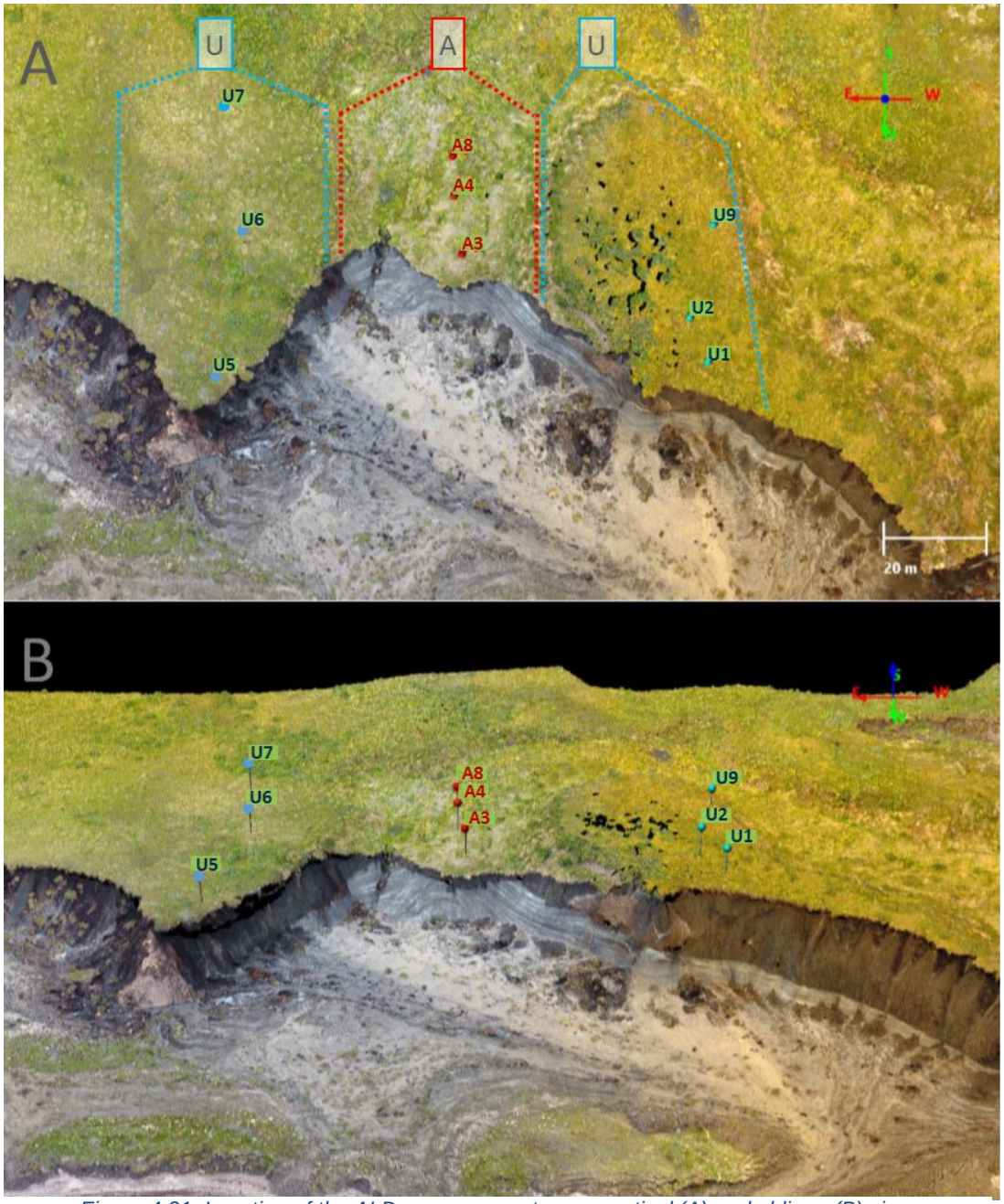

Figure 4.21: Location of the ALD measurements on a vertical (A) and oblique (B) view

4.4.2 Active Layer Depth Results

The measured ALD depth for both the undisturbed terrain and the active terrain are provided in Table 4.7 and Table 4.8 respectively. ALD in the undisturbed terrain averaged 0.39 m, with a range from 0.30 m to 0.50 m, and a surface vegetation layer of 0.26 m (one measurement of vegetation layer was 0.05 m while all others were 0.30 m). In the active terrain, each of the three ALD measurements exceeded the maximum depth (1.3 m) capable of being detected by the probing rod. The surface vegetation layer was observed to be 0.05 m at each measurement site. There are two main possibilities regarding the depth of the active layer in the active terrain. The first is that

a thin permafrost layer exists, present between 1.3 m depth and the surface of the massive ice. The other scenario involves the ALD extending all the way to the buried massive ice. The latter theory is support by observations of water flowing from the headwall closest to the sea, where the massive ice was exposed. The volume of melt water is suggestive of thaw along much more than the visually exposed massive ice, supporting the conclusions that the active layer extends to the buried ice surface. This ties in well with previous studies that noted large, long-term disturbances to the ground thermal regimes and ALDs on areas affected by thaw slumping (Burn, 2000; Burn and Friel, 1989).

Table 4.7: Active layer depth measurements for the undisturbed terrain

Location	**Undisturbed East**			**Undisturbed West**			
Site Label	U1	U2	U9	U5	U6	U7	**Mean**
ALD (m)	0.5	0.45	0.30	0.35	0.35	0.40	**0.39**

Table 4.8: Active Layer depth measurements for the active slumping terrain

Location	**Active Slumping Terrain**			
Site Label	A3	A4	A8	**Mean**
ALD (m)	>1.3	>1.3	>1.3	**>1.3**

4.5 Massive Ice Surface Variations

Passive seismic noise is present throughout the planet and can be used to gather data on subsurface geology. Monitoring of this noise has thus been used in various geological settings to determine features such as the depth of subsurface strata or the different seismic wave velocities of the buried rock and soil (Cultrera *et al.,* 2012; Scheib, 2014; Tellett-Williams *et al.,* 2016). This section will apply the monitoring and analysis of passive seismic noise to Peninsula Point to determine the variations in depth to the buried massive ice body.

4.5.1 Passive Seismic Monitoring Methodology

Passive seismic data have been collected in three separate North to South transects, one along the slump affected floor and two transects extending inland from the headwall edge along high ground to both the east and west of the slump (Figure 4.21), all using the Tromino® device. Positioning the device correctly involved cutting away the loose, spongy vegetation layer and grounding the device into the soil using the spikes attached to the base (Figure 4.22). The device was orientated towards the

shoreline (facing north) and recorded passive seismic noise with components in the vertical, E-W and N-S directions for 20 minutes at each recording position. The data collected by the Tromino was analysed using the H/V (horizonal to vertical) ratio method (Nakamura, 1989) within the Grilla software package. This involves analysis of the ratio between the vertical and horizontal components of the seismic signals to identify the natural resonance frequencies of the subsurface strata. With this information the thickness and depth of the strata can be calculated. An example of the processing window can be seen in Figure 4.23. Window “C” shows the noise in the signal, which needs to be reduced through filtering and averaging to reveal the signal that contains useful data. “A” displays the amplitude spectra of the three seismic components. Where the vertical component separates from the horizontal, due to impedance contrasts in the different layers, peaks and troughs are produced in the H/V window “B”. These peaks can represent the resonance frequencies of the main strata. For a simple two-layer system, the frequency can be used in the following formula to calculate depth:

$$f_r = \frac{V_s}{4h}$$

Where f_r is the resonance frequency, V_s the shear velocity and h is the depth.

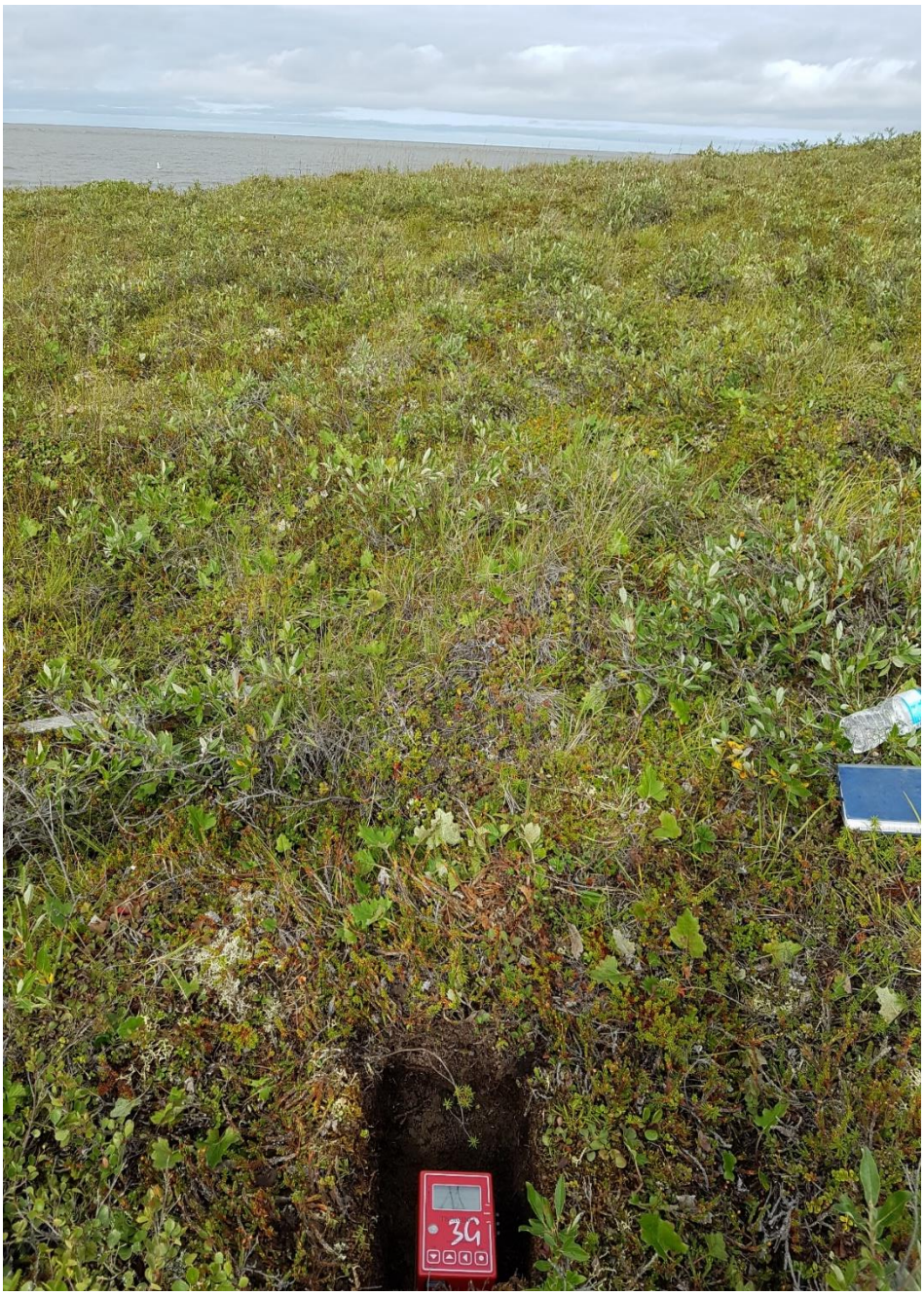

Figure 4.22: Positioning of the Tromino™ passive seismic noise recorder

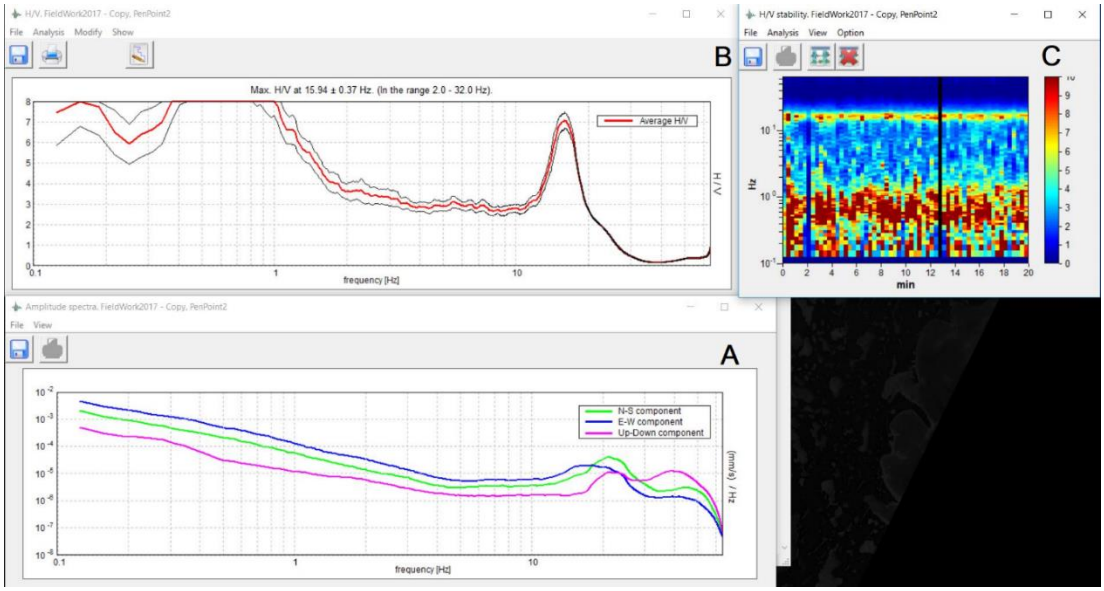

Figure 4.23: Passive seismic processing windows from the Grilla software. With the amplitude spectra (A), H/V plot (B) and the H/V stability field (C)

4.5.2 Passive Seismic Interpolation

In addition to the nine passive seismic measurements, five additional observation points of ground surface and massive ice height, taken along the exposed headwall, were also included (Figure 4.24). The total of 14 ice surface depths were added to ESRI ArcMap 10.3 using CSV files and converted into shapefiles. Using a boundary layer to define the edge of the massive ice and the interpolation region, the Inverse Distance Weighted (IDW) interpolation method was employed to create a continuous surface of the massive ice body, as well as two additional surfaces to represent the upper and lower error bounds. Once created, the surface was converted to a GeoTiff format for further analysis and visualisation.

4.5.3 Massive Ice Surface Results

4.5.3.1 Calibration

Passive seismic measurement points closest to the headwall of the undisturbed sections, where the internal layering was exposed, were used as calibration points using the depth formula described in section 4.5.1. Using known depths (h) to the massive ice based on field measurements, and the resonance frequencies (f_r) from the processing of the seismic signal, the shear wave velocities (V_s) could then be calculated. Over the relatively short distances with which the passive seismic recordings were taken (<50 m) it can be assumed that the V_s of the soil permafrost layer remains consistent. Therefore, by processing the seismic data to calculate f_r for the locations away from the exposed ice and adding in the V_s from the calibration sites, the depth to ice can then be calculated. An additional calibration point was used for the

exposed retreating headwall in the active segment. Here, the active layer extends to a much greater depth and the CTS measurements were significantly different from the undisturbed ground either side. A separate V_s was thus calculated along the exposure of the slumped section to use in calculations of ice depth on the active low ground transect.

Using the T5 location from Figure 4.24, a depth to ice of approximately 11.5 m is visible at the base of the cliff, h. Processing of the seismic signal for the same location produces a f_r of 23.03 Hz. Rearranging the formula from section 4.5.1 produces the following:

$$h * (f_r * 4) = V_s$$

or

$$11.5 * (23.03 * 4) = V_s$$

This results in a shear wave velocity of 1059.38 m s^{-1}, which is then used for the remaining five measurements from the two high elevation, undisturbed segments. These produced depth to ice surface values of between 16.6 m and 10.9 m.
The same process was used for the active low ground area. Here, the ice surface elevation depth along the cliff edge near the T3 location produces a h value of 2.5 m, while processing of the seismic signal yields a f_r of 21.38 Hz. Filling in the formula the results in a V_s of 213.8 m s^{-1}. This second shear wave velocity is then used for the two other low ground passive seismic recordings, producing depth to ice values of between 2.5 m and 3.2 m.

4.5.3.2 Error Ranges

While observations of ice body height along the headwall edge were assumed to be accurate, the calibration points, where the seismic signals were collected, were typically a 2-3 meters from the headwall edge. It is thus reasonable to assume that the massive ice surface may have varied by ± 1 m from the observed height at the exposure, based on variations in massive ice height laterally along the north facing exposures. To account for these potential errors, two additional shear wave velocities were calculated for both the active and undisturbed soils. These values have then been used to calculate two more estimates of the massive ice surface, representing the upper and lower error bounds. Using the different V_s values produces a maximum difference of 1.45 m either side of the best estimated massive ice surface, with an average difference of 0.69 m. There is no noticeable difference made to the general pattern or directional trends in the ice surface.

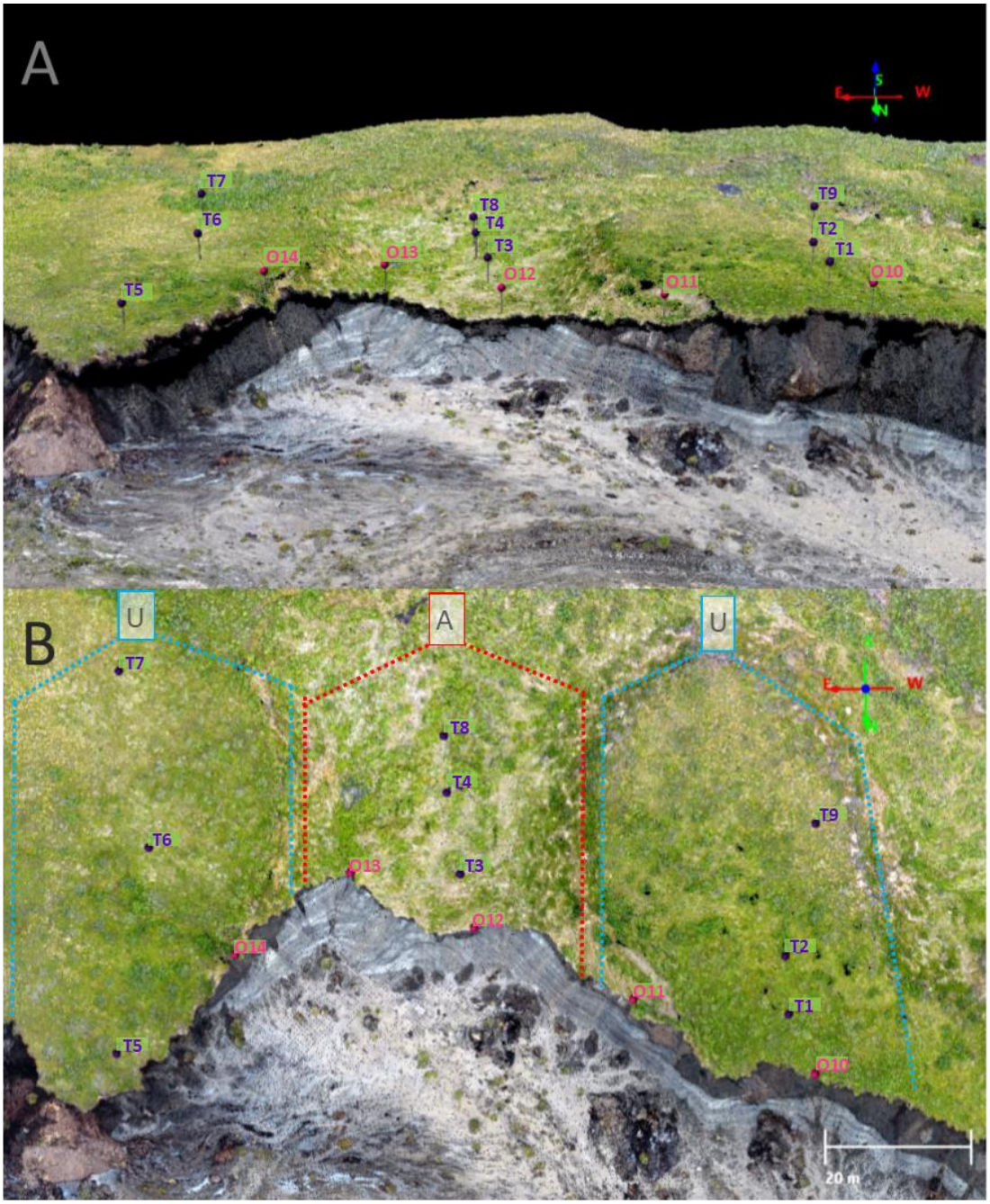

Figure 4.24: Location of all passive seismic measurement sites (purple) and all surface and ice height observation (pink) in both oblique (A) and plan (B) view

4.5.3.3 Ice Surface Model

The average ice surface model, as well as the maximum errors based on the upper and lower models, can be seen in Figure 4.25. The ice surface has an average height of 5.5 m above sea level, with a range from 0.5 to 8.9 m and a standard deviation (SD) of 1.8 m. The surface model was split into three separate sections for further analysis, central dome, lower massive ice body east and lower massive ice body west (Figure 4.25).

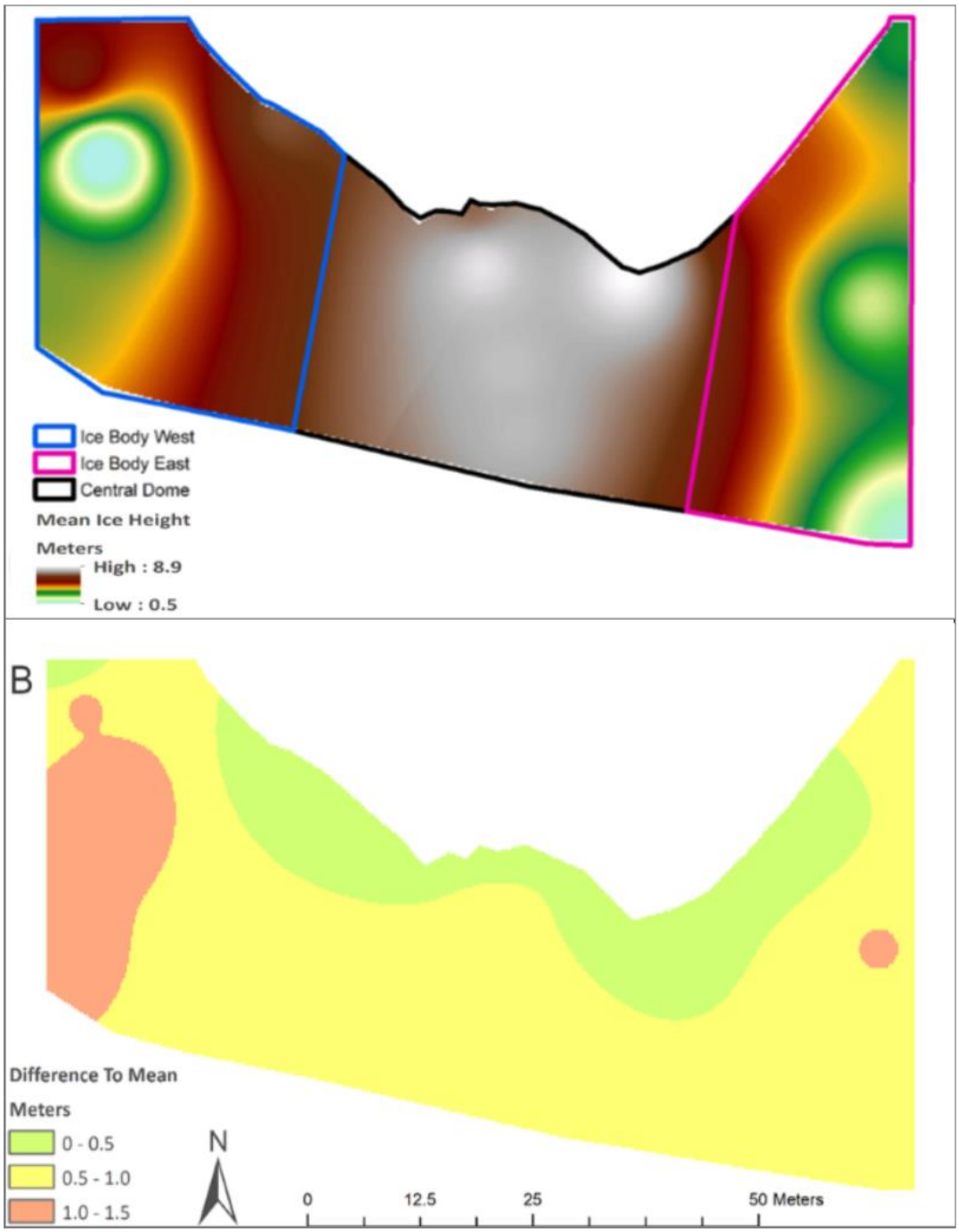

Figure 4.25: Best estimate ice surface model derived from passive seismic measurements and IDW interpolation (A) and the difference to the upper and lower ice body estimates (B)

4.5.3.3.1 Central Dome

As is hinted at from the ice exposure in the visual imagery, the buried ice is domed in the centre of the model and lower to the east and west. The average height of this central dome is 7.5 m, with a range from 5.4 m to 8.9 m and a SD of 0.5 m. The central dome extends back the entire length of the model area and contains all the ice above 7.0 m, including the highest point of 8.9 m, located near the exposed ice edge. There is also a slight trend from higher elevation to lower away from the coast, with a fall of about 1 m from the northern to the southern modelled edge.

4.5.3.3.2 Ice Body East

The eastern section of the massive ice has an average height of 4.1 m, with a range of 1.1 m to 6.5 m and a SD of 1.1 m. It exhibits a trend of decreasing elevation from both west to east and north to south, with the massive ice elevation decreasing away from the central dome and headwall exposure. The lowest point is located on the third passive seismic measurement on the southeast corner. The exposed visible ice in this section is the lowest in elevation of all three, and the average elevation is also the lowest of the three segments.

4.5.3.3.3 Ice Body West

The western section of the massive ice has an average height of 4.8 m, with a range of 0.5 m to 7.0 m and a SD of 1.4 m. Although there is a thick ice exposure on the northern edge, internally the ice dips steeply towards a bowl-like structure west of centre, which contains the lowest elevation ice surface measured, at 0.5 m, before rising again toward the southern end of the model. The cause of this low point is not obvious from any surface features or otherwise.

4.6 Peninsula Point Layer Models

The Peninsula Point layer models consist of three separate elements, the ground surface, the permafrost surface and the massive ice surface. For the continuous surface layer model (CSLM), these are treated simply as the surface layer of each of these elements from the main active headwall inland, while the fence diagrams also provide a sense of thickness within each of these layers. As the fence diagram is derived from the CSLM, the CSLM will be the first model described.

4.6.1 Continuous Surface Layer Model Methodology

The CSLM consists of three 2.5D surface layers representing the ground surface, the permafrost surface (or active layer depth) and the massive ice surface, all under the 2011 Universal Transverse Mercator Zone 8 projection, with the 1983 North American Datum.

4.6.1.1 Ground Surface

The ground surface layer was derived from the SfM-MVS model of Peninsula Point from August 2017, clipped to the area where the ALD and seismic surveys were carried out (Figure 4.26). For the CSLM, the slump floor and the headwall were also removed to later reveal the internal layering, i.e., permafrost and massive ice surfaces. (Figure 4.27).

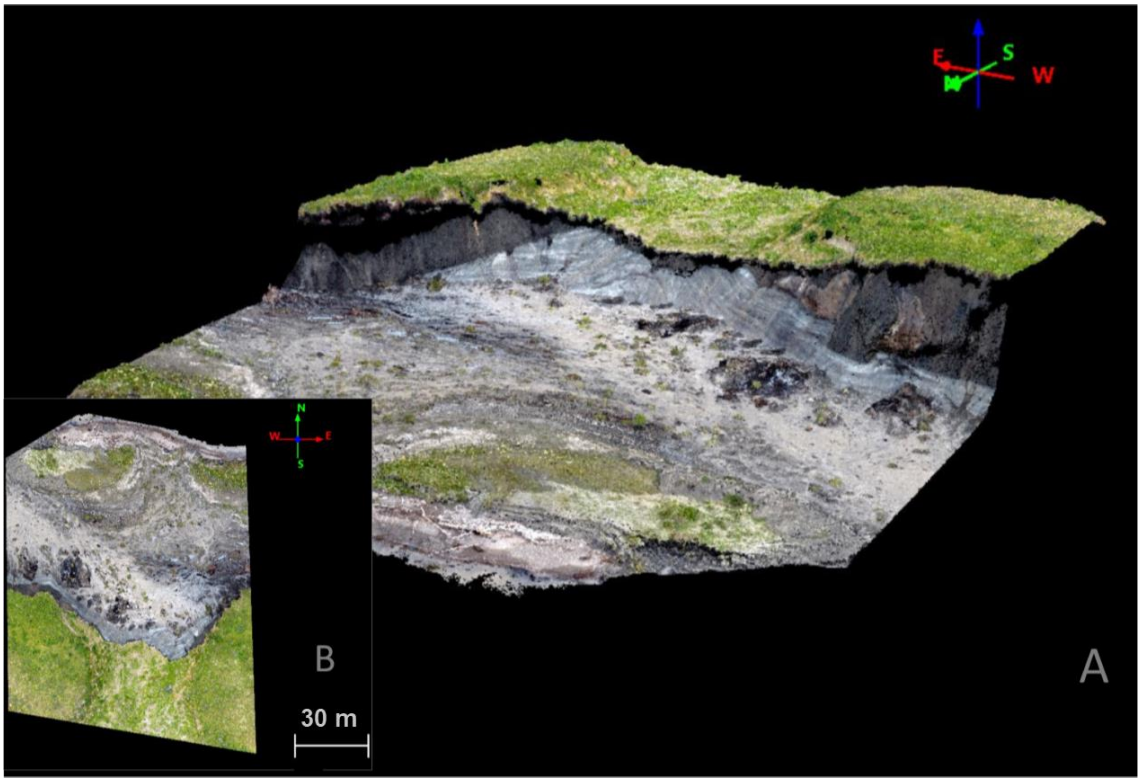

Figure 4.26: Oblique view (A) and plan view (B) of the Peninsula Point ground surface model layer

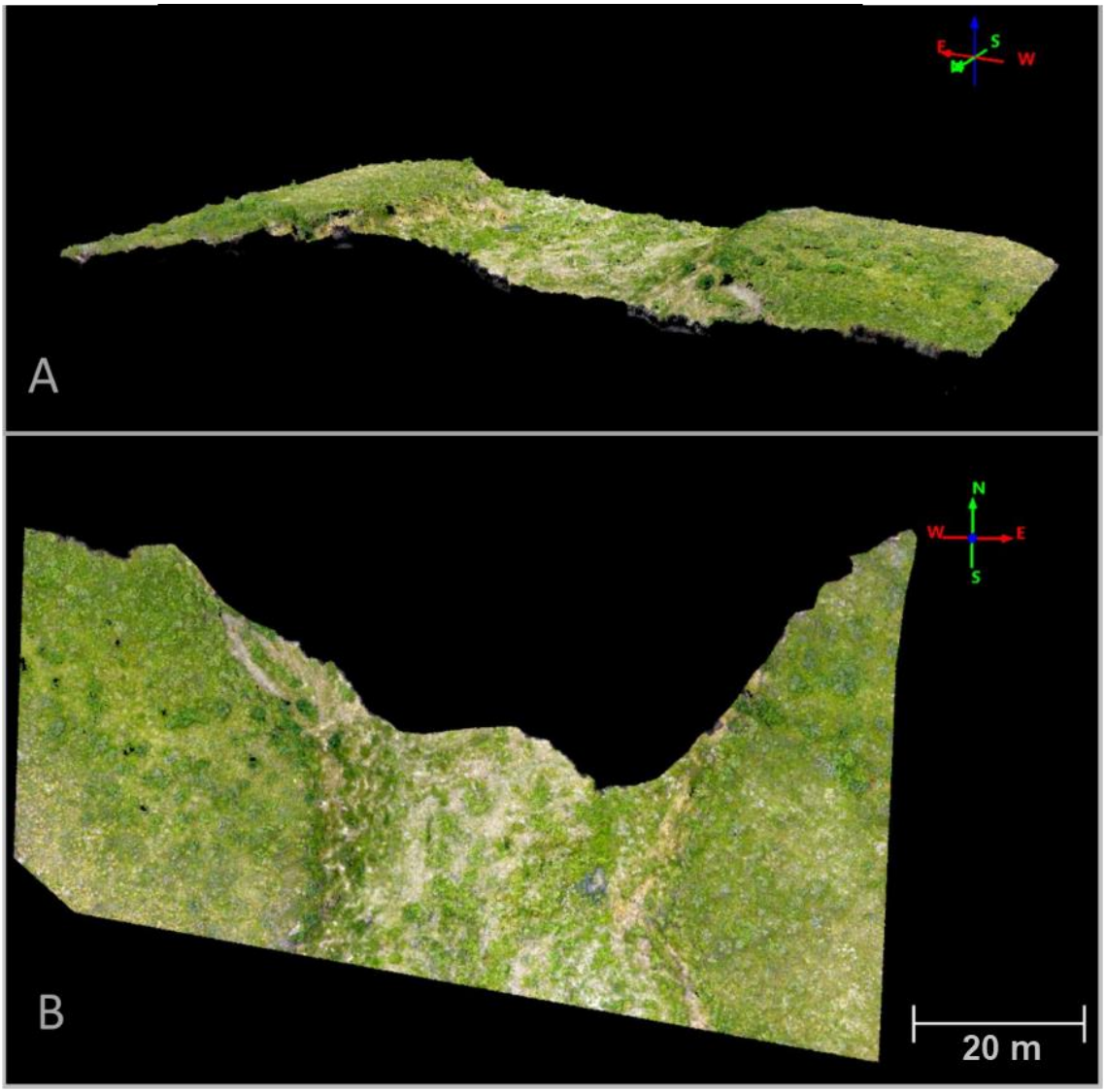

Figure 4.27: Oblique view (A) and plan view (B) of the Peninsula Point ground surface model layer, without the headwall and slump floor

4.6.1.2 Internal Layering

From the active layer depth section 4.4.2, it was found that the average depth to the permafrost on the undisturbed terrain was 0.39 m, while it was determined that permafrost had been removed between the ground surface and the massive ice in the active terrain. To represent the average 0.39 m depth to permafrost from the two undisturbed sections, the low ground was clipped out of the ground surface model and the two remaining sections had their elevations reduced by 0.39 m and their base colours altered, effectively creating two new layers that could represent the top of the permafrost. The ice surface model described in section 4.5.3.3 was used to represent the internal surface of the massive ice body (Figure 4.28).

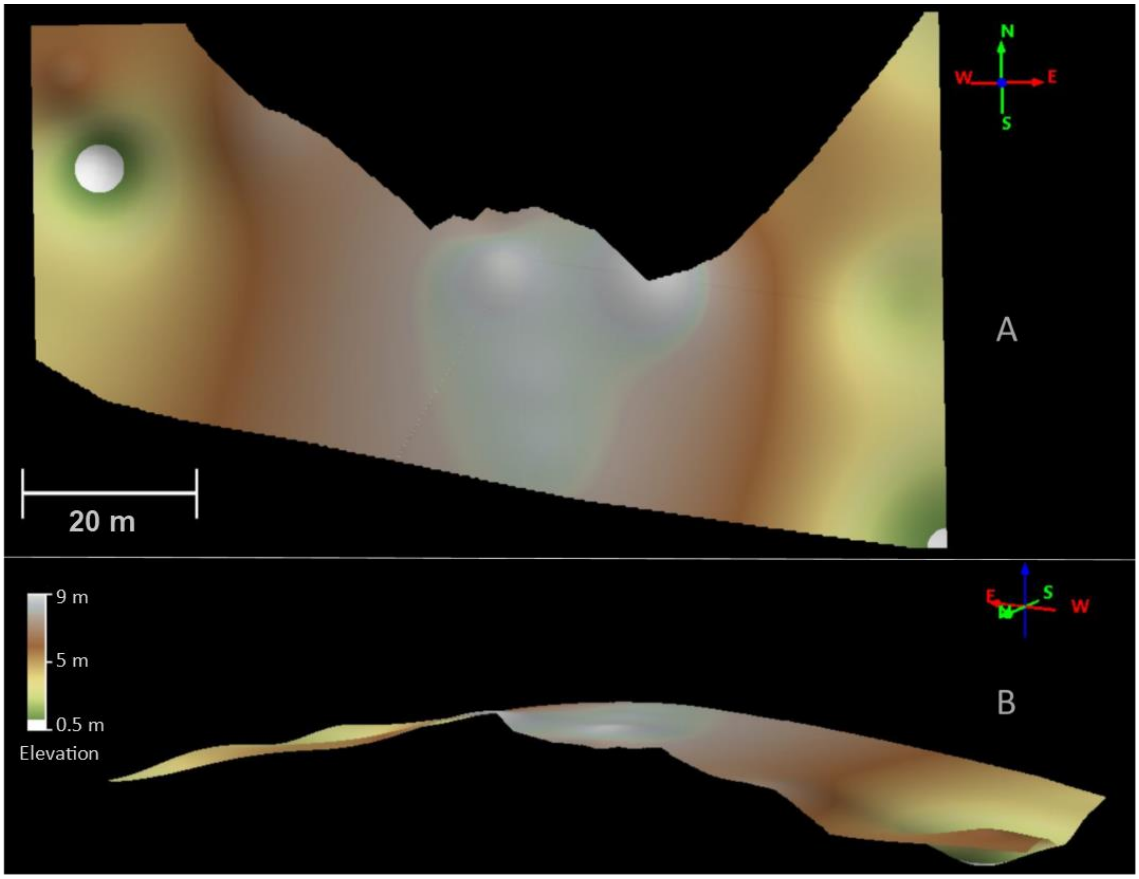

Figure 4.28: Plan view (A) and oblique view (B) of the Peninsula Point ice surface model

4.6.2 Fence Diagram Methodology

4.6.2.1 Elevation Profiles

The fence diagram was created using the ground surface, permafrost and ice models from the previous sections. A grid was created along which elevation profiles could be taken of each layer within the QTM software (Figure 4.29). The first set, with fine dashed lines, passed through the passive seismic measurement points. The second set, with broad dashed lines, aimed to capture the main sources of variation within the model, primarily within the massive ice surface. Lines oriented from broadly north to south are red, and east to west are blue. Each of the twelve profiles captures data on five layers:

- Ground Surface
- ALD/Permafrost Top
- Massive ice Surface – Upper Estimate
- Massive ice Surface – Best Estimate
- Massive ice Surface – Lower Estimate

The profiles were exported as CSV files and subsequently imported in Excel where they were displayed as XY scatter graphs and formatted in a consistent matter for further use (Figure 4.30).

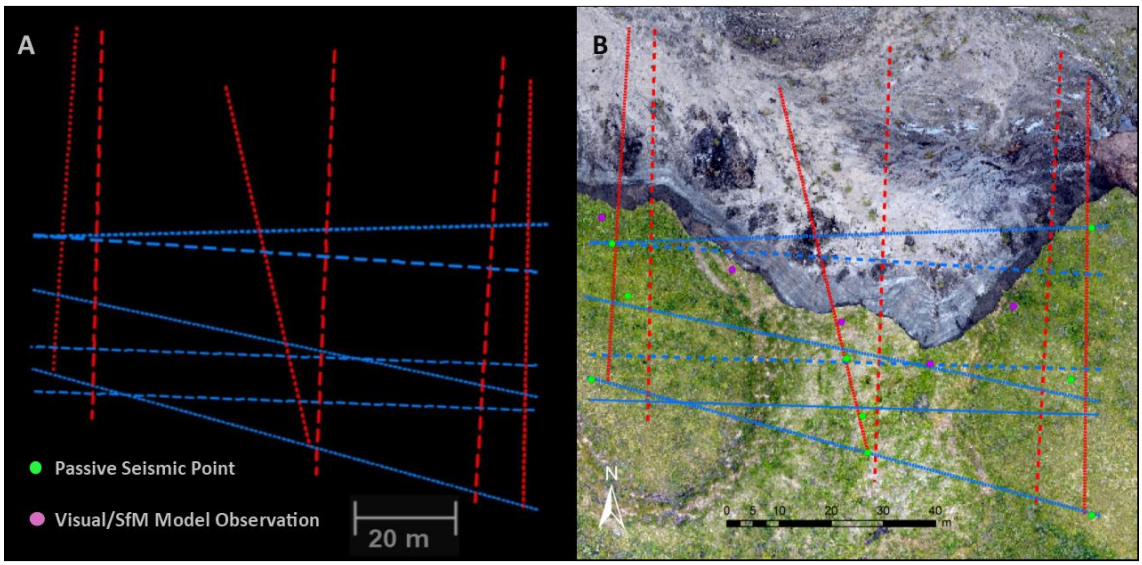

Figure 4.29: Layer elevation profile grids used for the fence diagram (A) and overlaid on the SfM-MVS model (B)

4.6.2.2 Formatting

The scatter plots were exported as images and their different layers were filled in using consistent colours to highlight their variations (Figure 4.31). The grid from Figure 4.29 and the twelve filled in scatter plots were then added to the Microsoft paint 3D application. Each filled in scatter plot was aligned along its appropriate grid line, the combination of which then forms the final fence diagram.

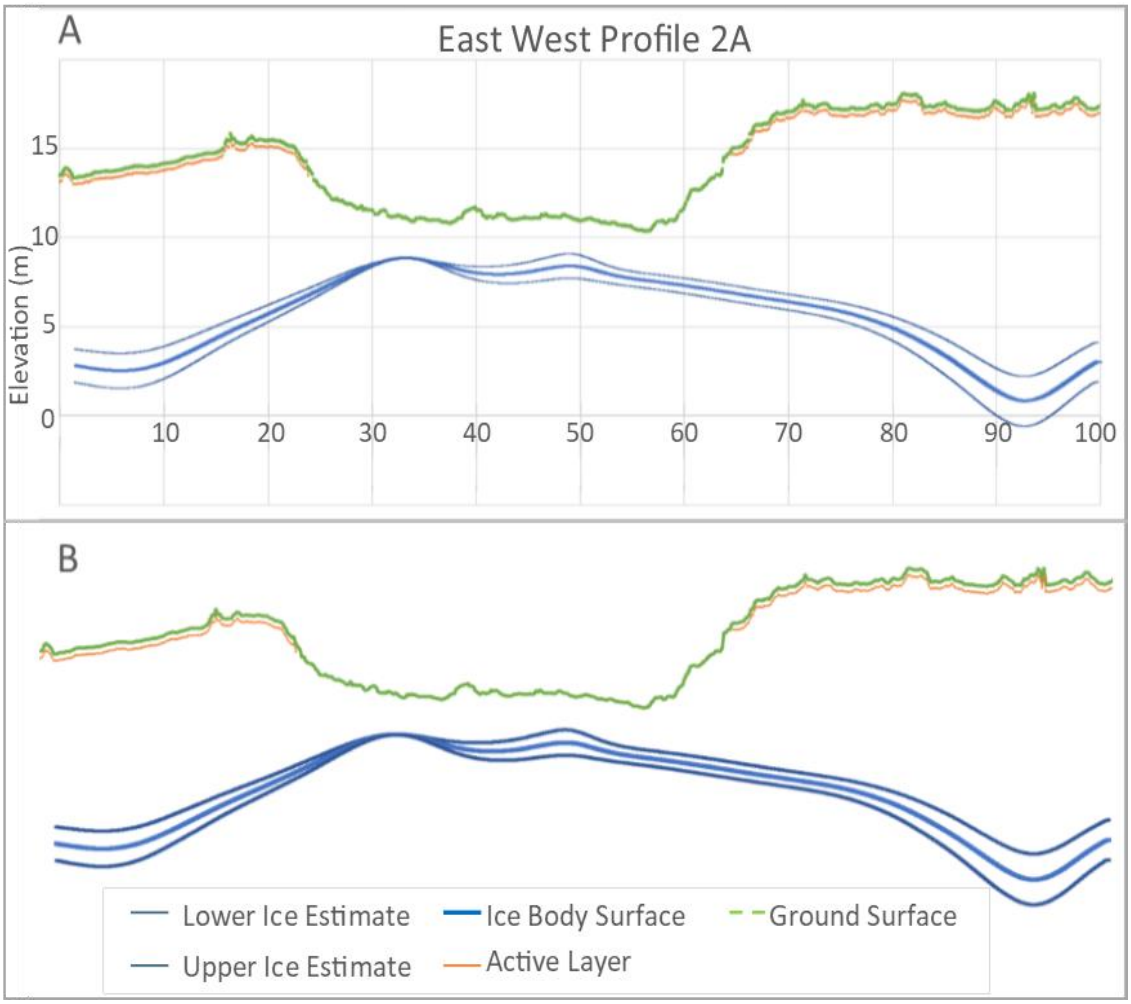

Figure 4.30: Original scatter plot (A) and the same plot edited for infilling and use in the fence diagram (B)

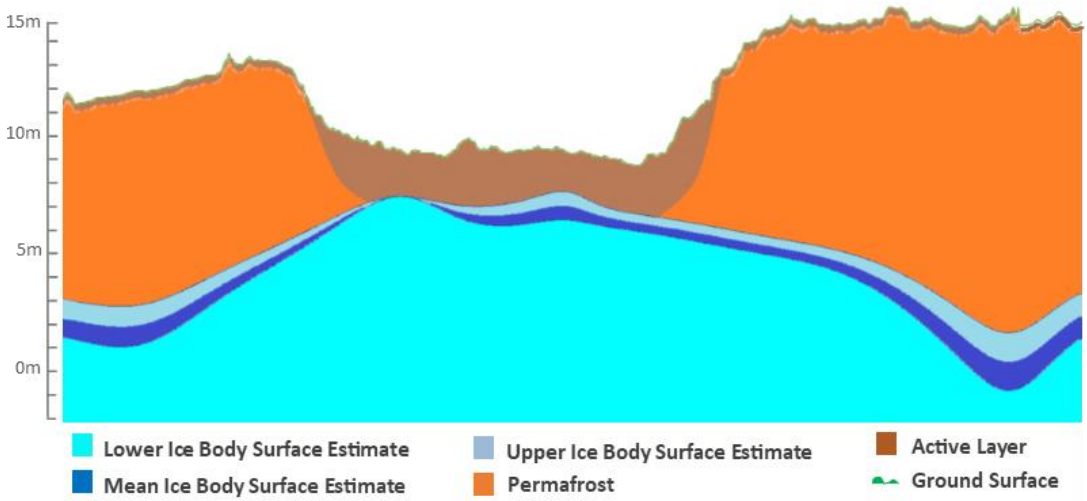

Figure 4.31: Filled in profiles, with green for the top, brown for the active layer, orange for the permafrost, grey for the upper ice estimate, dark blue for the medium and light blue for the lower ice body estimate

4.6.3 Continuous Surface Layer Model Results

Figure 4.32 displays the CSLM from multiple angles. In the model, the surface of the permafrost (or the active layer depth) is included as two separate white layers under the eastern and western segments, but as it lies only 0.39 m below the ground surface, it is very difficult to distinguish from the ground surface itself. The permafrost that lies above the massive ice on the open exposure was removed to improve the visualisation of the modelled ice surface layer generated from the passive seismic data. The ice surface layer, using the medium or best estimate height, was coloured based on elevation to improve the sense of elevation variability (ranging from 0.5 m to 8.9 m above sea level). Variations in the layer elevations were analysed both qualitatively and quantitatively through a sequence of profiles running from north to south at 10 m intervals. These resulted in three transects for both for the east and centre, and four for the western segment.

4.6.3.1 Undisturbed Terrain

The undisturbed terrain to the east has an average permafrost thickness, or depth to ice (DI), of 9.0 m, a SD of 1.8 m and a range from 4.8 m to 10.9 m. However, there are notable longitudinal differences between the middle and outer segments and the inner segment, where the ice begins to dome. The outer, eastern most, edge and centre of the eastern segment have an average DI of 9.8 m with a SD of 0.6 m and a range of 8.9 m to 10.9 m. The inner, western most part, of the segment has an average DI of 6.1 m and a SD of 1.1 m. Moving from the coast inland (north to south), the average elevation of both the ice and ground surface typically decreased at a similar rate, resulting in no horizontal, cross-shore trend in the DI.

The undisturbed terrain to the west has an average DI of 10.7 m, with a SD of 2.5 m and a range from 5.3 m to 14.7 m. The region demonstrates a large change from the inner to outer (east to west) segment once more, with the average DI increasing by 5.3 m from the inner edge to the middle of the segment. The outer edge has the thickest permafrost of the modelled area, at 14.7 m, which is related to the bowl like depression that marks the lowest ice surface elevation. As is the case in the eastern section, there is a trend for a decrease in the elevation of both the ice and ground surface from north to south, but despite much variation, there are no significant cross-shore trends in the DI.

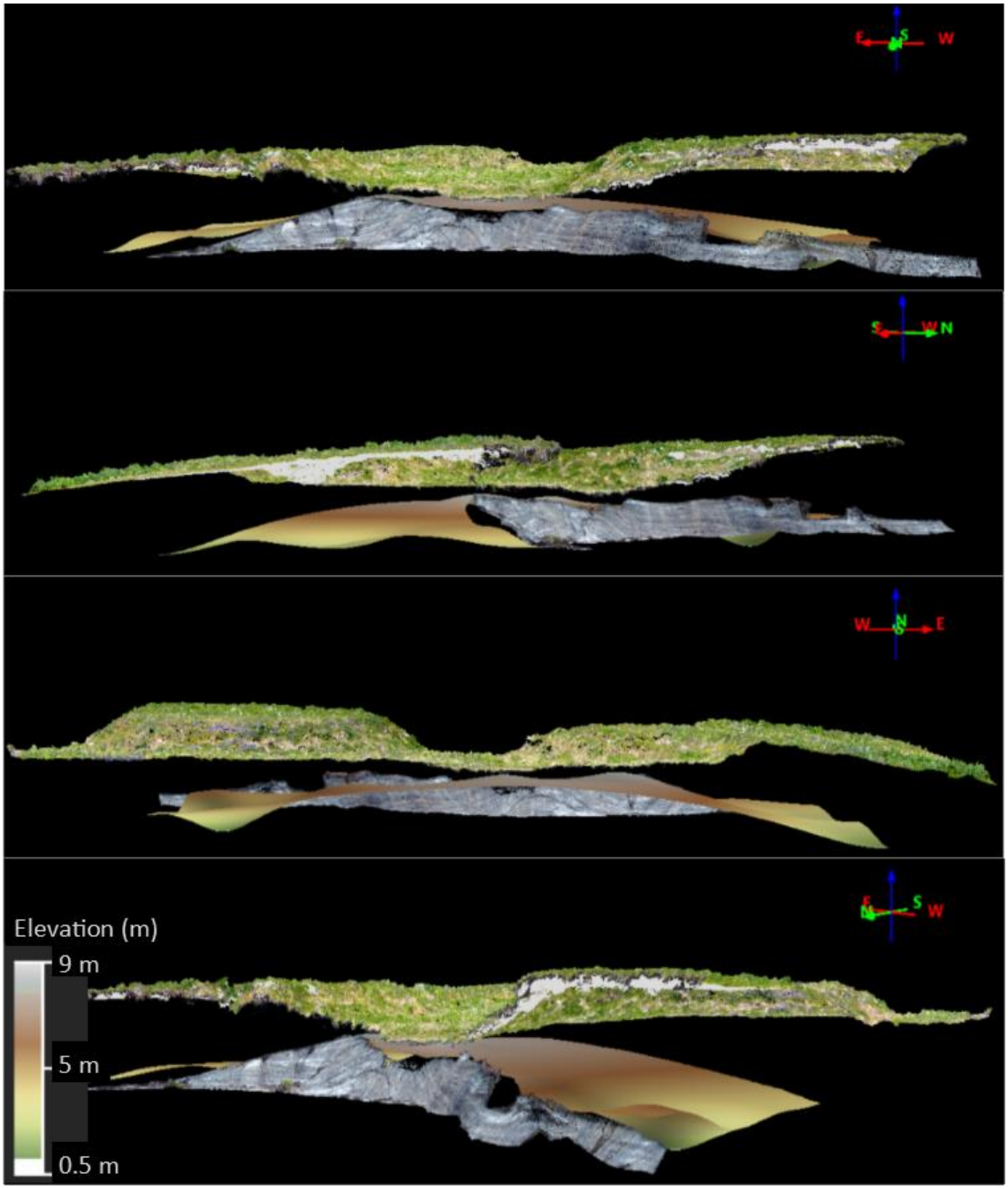

Figure 4.32: CSLM from multiple angles highlighting the ice surface variability

4.6.3.2 Active Terrain

The active terrain in the middle has an average DI of 2.5 m, with a SD of 0.6 m and a range from 1.4 m to 3.9 m. There is much less longitudinal variation compared to the undisturbed segments, with SDs or DI. The eastern undisturbed segment has an east to west drop in DI of 3.7 m, the western undisturbed segment has a west to east drop in DI of 5.3 m, while the active segment displays a longitudinal variation of 0.3 m. However, unlike the undisturbed segments, there is a trend for increasing DI from north to south, due to a slight decrease in ice surface elevation (0.4 m) in combination with a

slight increase in ground surface elevation (0.8 m) resulting in an average DI increase of 1.2 m.

4.6.3.3 Overall CSLM

Table 4.9 summarises the variations in DI across the CSLM. The undisturbed terrain to the east and west have similar stats, with high ground surface elevation and low massive ice elevation producing a thick DI. Conversely, the middle, active terrain has a higher massive ice elevation and lower ground surface elevation, creating a much thinner DI, with the massive ice generally less than 3 m from the surface.

Table 4.9: Depth to Ice variations (m) across the CSLM

Depth to Ice Variations in the CSLM at Peninsula Point				
	Average	Maximum	Minimum	SD
East (U)	9.0	10.9	4.8	1.8
Middle (A)	2.5	3.9	1.5	0.6
West (U)	10.7	14.7	5.3	2.5

4.6.4 Results: Fence Diagram

The fence diagram reaches to the north of the CSLM, into the active slump floor where the massive ice, reduced in elevation, was observed to extend (Figure 4.33). This near surface ice allows for the rapid transport of thawed permafrost and meltwater towards the sea resulting in a fan like deposit observed in the field in 2017. The length and width of the area covered by the fence diagram is approximately 95 m. Like in the CSLM, the active layer, in brown, is difficult to distinguish from the orange permafrost on the high ground segments, as it forms such a thin strip at the top. However, it is clearly visible in the low ground segment in the middle, where it extends to the surface of the ice. Views A and C (Figure 4.33) clearly show where the massive ice gently increases in elevation from either side towards the centre, forming a distinctive dome, and where the active layer extends down towards the surface of the ice. View B exhibits some marked variation in the ice surface, such as the bowl like depression where the lowest estimate of the ice surface elevation is slightly below sea level, and also has the thickest permafrost layers measured. This contrasts with view D, where the ice surface displays a shallow wave-like pattern and a clear drop in the average massive ice elevation inland.

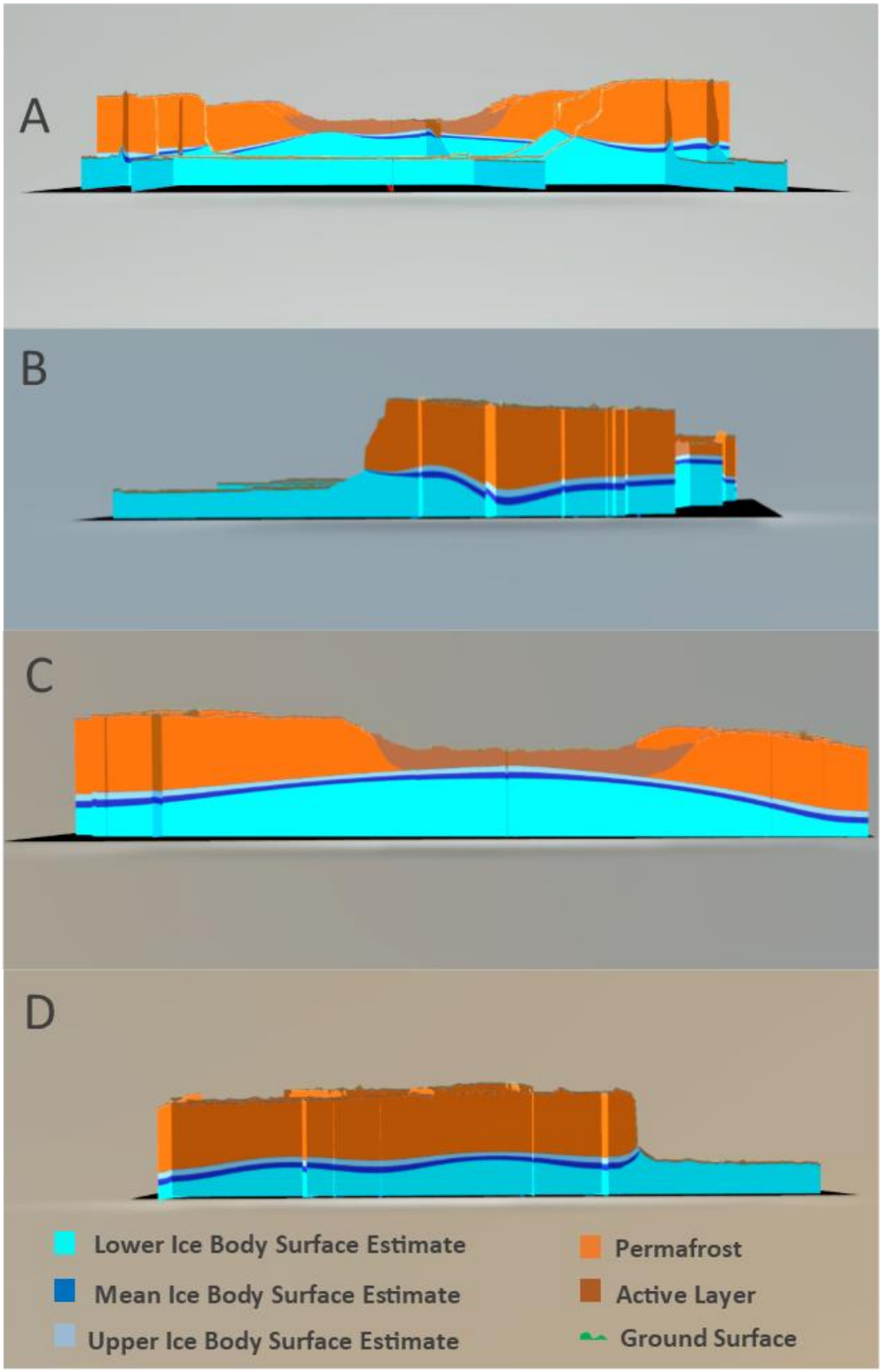

Figure 4.33: Fence diagram with views facing south (A), east (B), north (C) and west (D)

Figure 4.34 displays the same diagram, but from four separate oblique views. This figure makes the individual profiles, or slices, used to create the image more visible, but also highlights some features that are difficult to distinguish in Figure 4.33. Views A and B show the exposed ice along the inner sides of the active headwall, which is thinner than towards the centre. Figure 4.34 also highlights the relatively thin nature of the soil cover above the domed massive ice. It highlights the complexity and counterintuitive nature of this landscape. It would be reasonable to assume that land overlying the thickest ice may naturally be higher in elevation, such as in pingos, than those over thin ice or absent of ice bodies. The model reveals the opposite to be true, that thick massive ice can be linked to a lower surface elevation and vice versa.

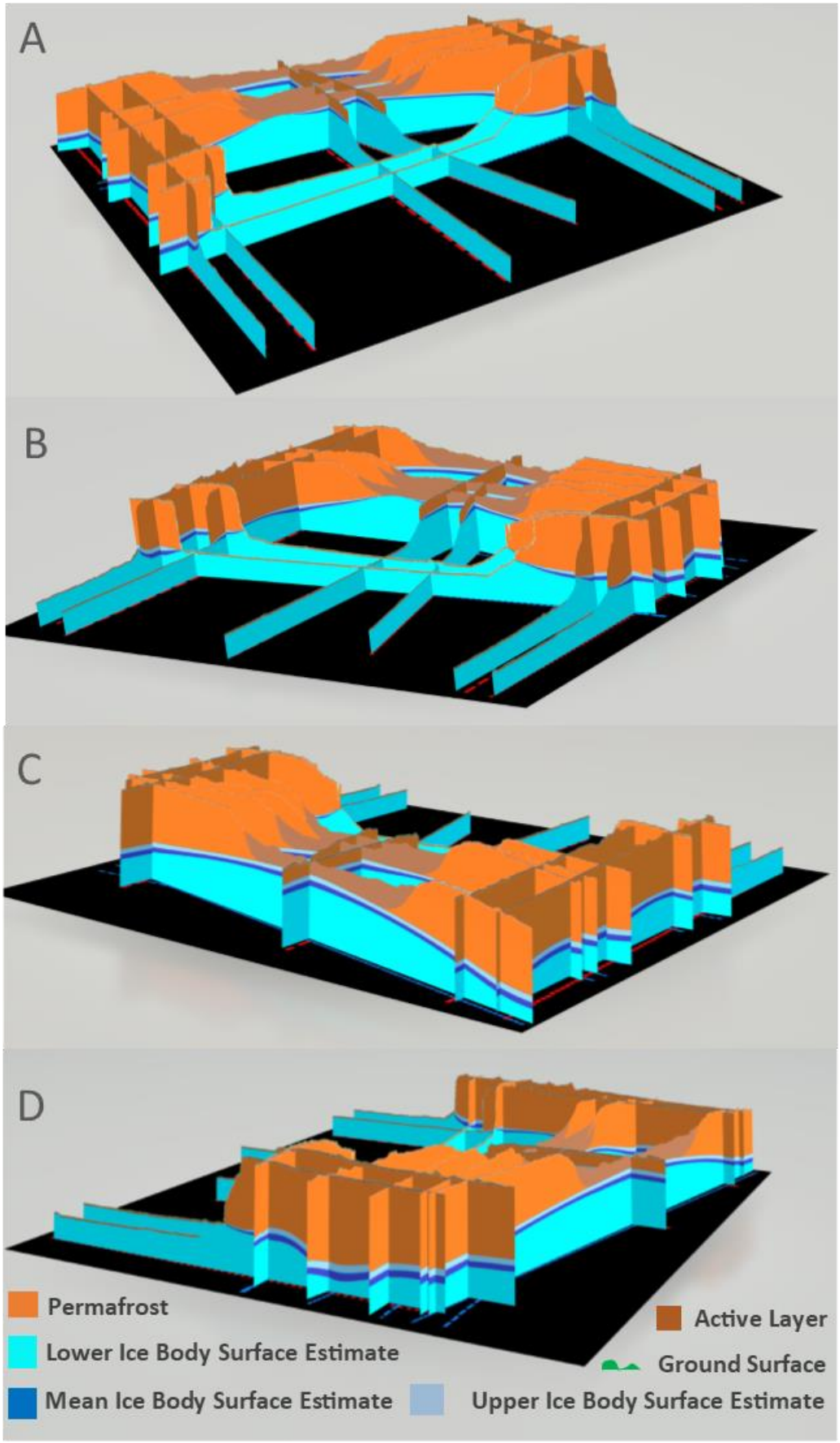

Figure 4.34: Fence diagram from multiple oblique angles, facing south west (A), south east (B), north west (C) and north east (D).

4.7 Summary: Surface Characterisation and Internal Structure

Grain size exhibited no statistically significant differences between the undisturbed high ground samples and the active low ground previously affected by RTS activity, consistent with similar work by Lantuit *et al.,* (2012b). On the other hand, each of the CTS measurements displayed significant differences between the active and undisturbed soils. Rather than being pre-existing features, the CTS differences may be a result of RTS activity. Thawing of salt rich permafrost, ground ice, sediment reworking and salt leaching may all have contributed to the differences measured. As such, these CTS differences may be a useful feature to help in identifying areas previously affected by slumping in the field, where visual cues and other aspects do not make their presence clear.

While each of the factors, ALD, massive ice variability and soil OB thickness, have an individual influence on the local occurrences of RTSs and the differences between the active and undisturbed terrain, the three factors are also inter-connected. Numerous studies have proposed that a key factor in the different densities of RTSs across a range of locations can be the thickness of the soil overlying buried massive ice bodies. A clear example of this is the much more dramatic increase in RTS density across Banks Island compared to other western Arctic locations (Lewkowicz and Way, 2019; Rudy *et al.,* 2017). This acceleration, according to Segal *et al.,* (2016), has occurred even though Banks Island is colder, drier and warming more slowly than other regions. The authors suggest the thinner soil OB is to blame, by allowing even the slow warming to more easily reach the massive ice bodies, triggering RTS activity. In a similar fashion, Lantuit and Pollard (2008) theorise that the lack of RTS features greater than 500 m inland on Herschel Island is related to the increased soil OB, preventing surface energy fluxes from reaching the buried massive ice. Soil OB thickness is thought to play an important role in determining the likelihood of RTS triggering across different geographical locations. It stands to reason that it must also be important laterally across site specific coastal locations, explaining partially why one spot may experience RTSs while the site only meters away does not. Evidence from Peninsula Point suggests that this is an accurate proposition. There was a clear and notable difference in the OB thickness between the low, active ground that had previously been affected by RTSs (2.5 m) and the high, undisturbed ground (9.0 m). Other studies have suggested that the massive ice thickness is also an important factor in the density of RTSs, allowing for the eroded headwall material to be easily washed away and allowing multiple phases of slumping to occur before the ice thickness is exhausted (Ramage *et al.,* 2017). While the base of the massive ice was not easily

detectable, the surface elevation of the massive ice may act as a proxy for thickness. As such, the surface elevation of the ice in the active low ground segment averaged 7.5 m, compared to 4.1 m in the eastern high ground and 4.8 m in the western segment. It is not unreasonable to assume the ice elevation was once even higher than recent measurements suggest but has been reduced in recent decades due to thawing from active phases within the RTS, further supporting the idea of ice thickness being an important consideration for RTS development. The last element to consider is the ALD, the altered ground thermal regime on slump affected areas and their contribution to the triggering of more phases of slumping. It has been noted previously that slump affected areas can see the removal of permafrost down to the massive ice (Burn and Freile, 1989). Significant deepening of the active layer also occurs, with the ground thermal regime requiring over a century to return to equilibrium (Burn, 2000; Burn and Freile, 1989). The average active layer depth in the undisturbed upper ground segments of Peninsula Point was 0.39 m, compared to the active terrain, where the average depth exceeded the maximum depth of the probing rod, at 1.30 m, and likely reached the surface of the buried massive ice. This suggests that the near surface permafrost has been completely degraded, exposing the massive ice to surface energy fluxes. This ice surface melting has the potential to trigger further phases of HWR as part of the RTS.

When considering the three different features together (ALD, massive ice and OB thickness), it is thus apparent that the low ground segment in Peninsula Point displays evidence of polycyclic slumping while the adjacent upper ground regions have not. The upper ground has the combination of low elevation massive ice, thick soil OB and a shallow active layer (Figure 4.35). This protects the massive ice from surface energy, reducing the chances of it thawing and forming a PRTS. Should slumping occur, the large OB to ice thickness ratio increases the chances of the headwall ice becoming covered in eroded material, thus slowing or stopping HWR. In contrast, the low ground has a combination of higher elevation ice (thicker massive ice), a thin soil OB and a deep active layer. It is likely that the deep active layer was not present before the first phase of HWR occurred. Once the near surface permafrost was largely eliminated it increased the likelihood of future active slumping phases being triggered. The higher elevation (and thus thicker) massive ice in combination with a thinner OB may have contributed to the initial phase of HWR. Thawing of the thick ice would have facilitated the transport of material away from the headwall, allowing ablation to be maintained and the HWR to continue.

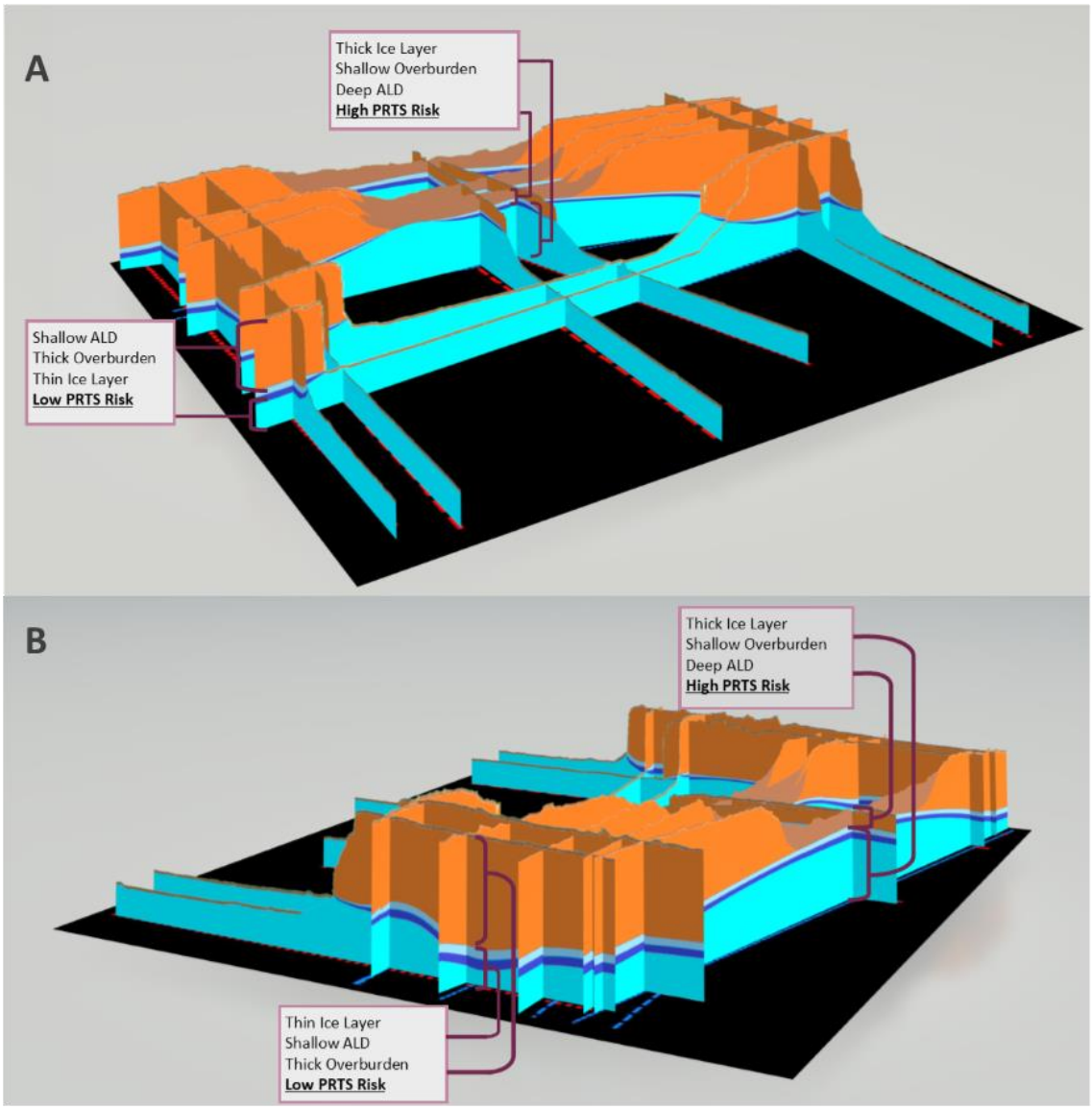

Figure 4.35: Fence Diagrams with the variations in ALD, soil overburden and ice body thickness on Peninsula Point

The layer models also allow us to assess the variability in these three important aspects inland from the coastal exposure. The general patterns evident from the outcrops appear to broadly extend cross-shore, but with substantial variability superimposed over the broadscale structure not visible from headwall exposures. The thin OB, thick ALD and thick massive ice reaching far back from the ice exposure in the active low ground section. Similarly, albeit with significantly more variability, the pattern of shallow ALD, thick soil OB and thin ice continues inland from the high ground areas. Considering these features, the pattern of polycyclic RTSs on the low ground segment, and regular erosion or simple thaw slumping on the high ground segments either side, will likely continue for the next decade. The evidence from this chapter supports the importance of *in situ* controls on slump initiation and activity.

5 Coastal Change

5.1 Introduction

Across the coastlines of the Arctic, the majority of studies indicate that SLR rates have increased since the turn of the 21st century and have even accelerated in the last decade (Arp *et al.,* 2010; Günther *et al.,* 2013, Günther *et al.,* 2015; Jones *et al.,* 2008; Jones *et al.,* 2009a; Mars and Houseknecht, 2007; Novikova *et al.,* 2018; Ping *et al.,* 2011; Pizhankova *et al.,* 2016). However, this increase is neither uniform nor ubiquitous (Gibbs and Richmond, 2015; Gibbs *et al.,* 2011; Lantuit *et al.,* 2008). Attempts have been made to link SLR variability to weather conditions and environmental factors, such as open water season length, storms, air and sea surface temperatures, but with limited success (Barnhart *et al.,* 2014b; Irrgang *et al.,* 2018; Jones *et al.,* 2018; Lantuit *et al.,* 2008; Lantuit *et al.,* 2011). Other studies have suggested that variations in coastal morphology and ground ice type/content can play a role too (Gibbs *et al.,* 2011; Irrgang *et al.,* 2018; Novikova *et al.,* 2018; Obu *et al.,* 2017; Solomon, 2005), but a strong consistent relationship between these factors and SLR trends remains elusive.

There has been some success in recent years linking morphology with retreat rates, as DEMs with high spatial and temporal resolutions have become more accessible. Areas with large volume losses have been revealed to produce more short-term variability in SLR rates (Obu *et al.,* 2016). This appears to be, at least, partially related to RTS activity, where large sediment fluxes associated with HWR and mass wasting can result in temporary progradation events — slowing or even reversing SLR (Obu *et al.,* 2017). Yet in other areas, the presence of RTS can be clearly associated with increased rates of SLR (Lantuit *et al.,* 2008). Meanwhile, Ramage *et al.,* (2017) has identified the morphological characteristics that contribute to the formation of RTS and their density along the Yukon coastline, namely the slope angle, elevation and massive ice thickness.

Analysis of the changes in coastal morphology over time appear to be lacking, which is reasonable given the lack of DEMs at sufficient spatial and temporal resolutions. Planimetric analysis from satellite imagery has allowed long-term SLR trends to be measured. However, it is difficult to acquire DEMs from satellite imagery with a sufficiently high spatial and temporal resolution to analyse fine scale coastal morphology. LiDAR provides high resolution elevation data ideal for DEMs, but the high cost and logistical difficulties make it impractical for frequent data capture. On the other hand, drone-based photogrammetry has proven to be useful for generating 2D and

2.5D products, at a low cost and at both high spatial and temporal resolutions (Clapuyt *et al.,* 2015; Cunliffe *et al.,* 2018; Lim *et al.,* 2015; Westoby *et al.,* 2018). But the technology and its applications are new, meaning only recent years can be assessed with these tools.

For a morphologically complex site like Peninsula Point, an integrated approach is most ideally suited to accurately assessing the long-term coastal changes.

5.2 Peninsula Point: Long-term Coastal Change Approach

This chapter will attempt to analyse the long-term evolution of Peninsula Point by combining by both 2D and 2.5D monitoring methods to:

- Establish the SLR rates and trends since 1935.
- Track HWR rates and variability since 1994.
- Assess the trends and variations in morphology, such as elevation and slope angle since, 2004.
- Monitor volumetric changes since 2004.

Long term SLR rates and their spatial variations will be examined by reanalysing previous published rates between 1935 and 1985 (Mackay, 1986). SLR since 1985 will use a mix of satellite, aerial and drone-based imagery, tracking changes with the use of 22 line transects at 25 m intervals across the north coast of Peninsula Point. These transect lines will also be used to track changes to the other metrics, HWR, slope angle, elevation and volume. By establishing the trends and variability in the metrics described, it may be possible to discover new relationships and drivers of the coastal evolution of Peninsula Point.

5.3 Two-Dimensional (2D) Monitoring

This section will utilise planimetric views to calculate rates of change and spatial variability in shoreline retreat since 1935. This involves the use of freely available satellite imagery, geo-registered orthomosaics and rates calculated from previously published research (Mackay, 1986).

5.3.1 Methods

5.3.1.1 2D Imagery

Satellite images were downloaded from the United States Geological Survey Earth Explorer website (https://earthexplorer.usgs.gov/) using only images that cover the entire Peninsula Point site. The stitching together of separate images introduces errors and uncertainty that are unnecessary given the large amount of imagery available and

the purpose of establishing long-term trends. Images were only searched for between the 1st of June and the 30th of September. This ensured minimal amounts of sea ice and snow cover, which may alter the accuracy of coastal delineation. These dates also ensured adequate levels of solar illumination, allowing for easier demarcation of the land/water boundary. To minimise the obscuration of the land/water boundary, only images with under 30% cloud cover were selected. To extend the 1935 to 1985 SLR rates established by Mackay (1986), image acquisition dates were restricted to between 1985 and 2017.

Imagery from Landsat 5, 7 and 8, processed to level L-1TP with terrain and precision corrections (the highest accuracy pre-processing level available) accounted for the majority of the images used. This eliminated the need for pre-processing of the raw imagery and ensured a consistent and accurate set of images was collected. Data from the Advanced Land Imager (ALI) aboard the Earth Observer 1, and Sentinel 2A were also used for more recent periods when suitable Landsat imagery was more sparse (partially due to the scan line corrector failure on Landsat 7 ETM+). The above criteria resulted in 232 separate scenes, with an average of seven per year and a range from zero in 1987 (the only year with none) to 14 in 2009.

5.3.1.2 Processing

Table 5.1 presents the bands used for the different Landsat images.

Table 5.1: Landsat band numbers used for further processing. NIR = Near Infra Red. SWIR = Short Wave Infra Red. Pan = Panchromatic

Platform	Blue	Green	Red	NIR	SWIR1	Pan
Landsat 5	1	2	3	4	5	N/A
Landsat 7	1	2	3	4	5	8
Landsat 8	2	3	4	5	6	8

Within ArcGIS 10.3, model builder was used to carry out the following steps, iterating through multiple folders and images:

1. Bands were clipped to an area encompassing only Peninsula Point (Figure 5.1) to reduce the workload and processing time.
2. True colour composites were made using bands blue, green and red, for visual inspection.
3. False colour composites using the NIR, SWIR1 and red bands were used to highlight the boundaries between land and sea (Figure 5.2)

With the bands clipped and the composites created, the images were manually inspected for cloud, sea ice, snow cover, scan line errors and other errors. Of the remaining images, the closest usable images to July were selected for further analysis. This resulted in 13 remaining scenes, one each for the following years: 1985, 1988, 1990, 1993, 1997, 2000, 2002, 2004, 2006, 2010, 2013, 2016 and 2017.

Finally, drone-based orthomosaics, derived from georegistered SfM-MVS models, for 2016, 2017, and 2018, and another orthomosaic from aerial imagery collected in 1993/94, were also used.

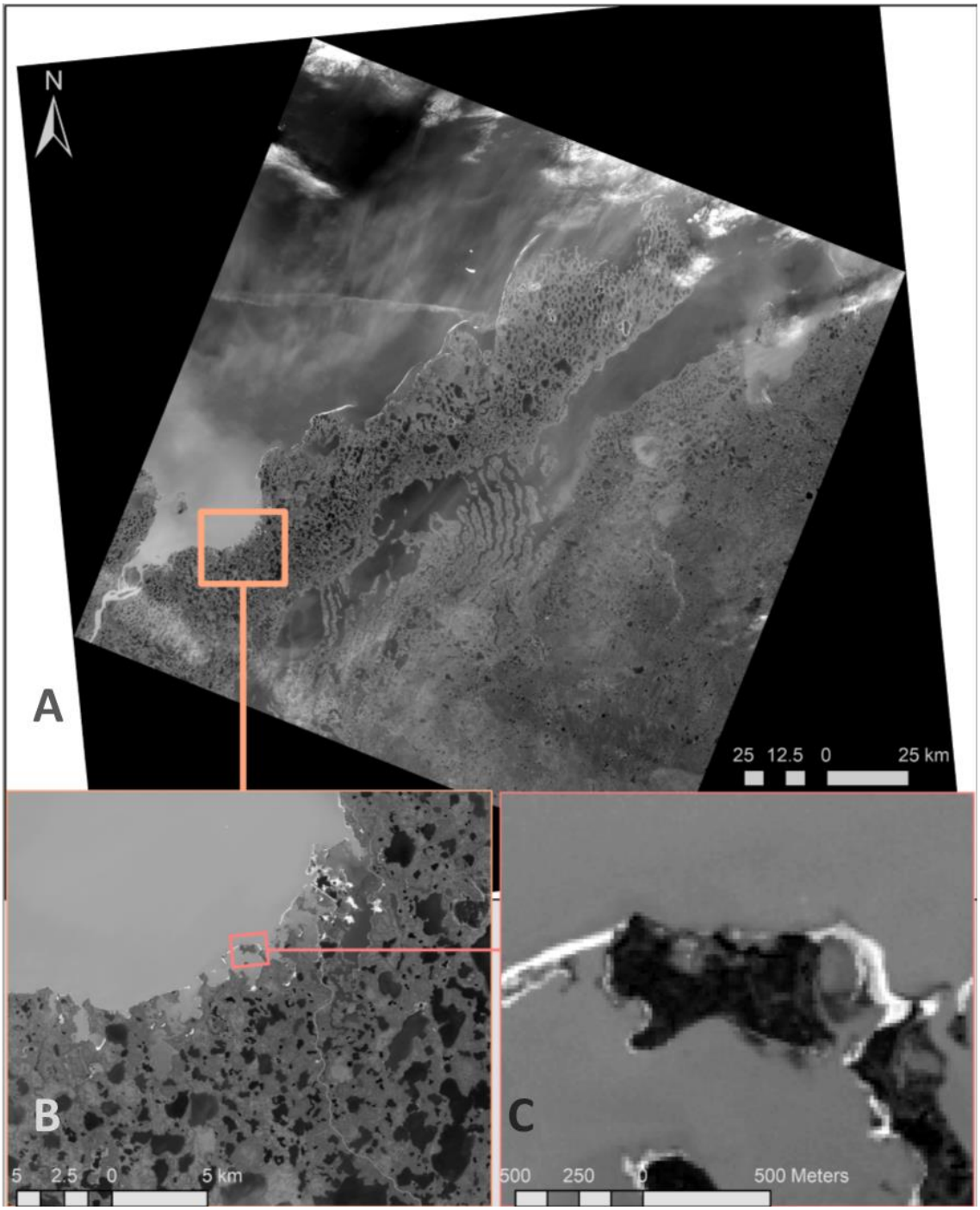

Figure 5.1: Original scene size (A) through to the clipped analysis images (C)

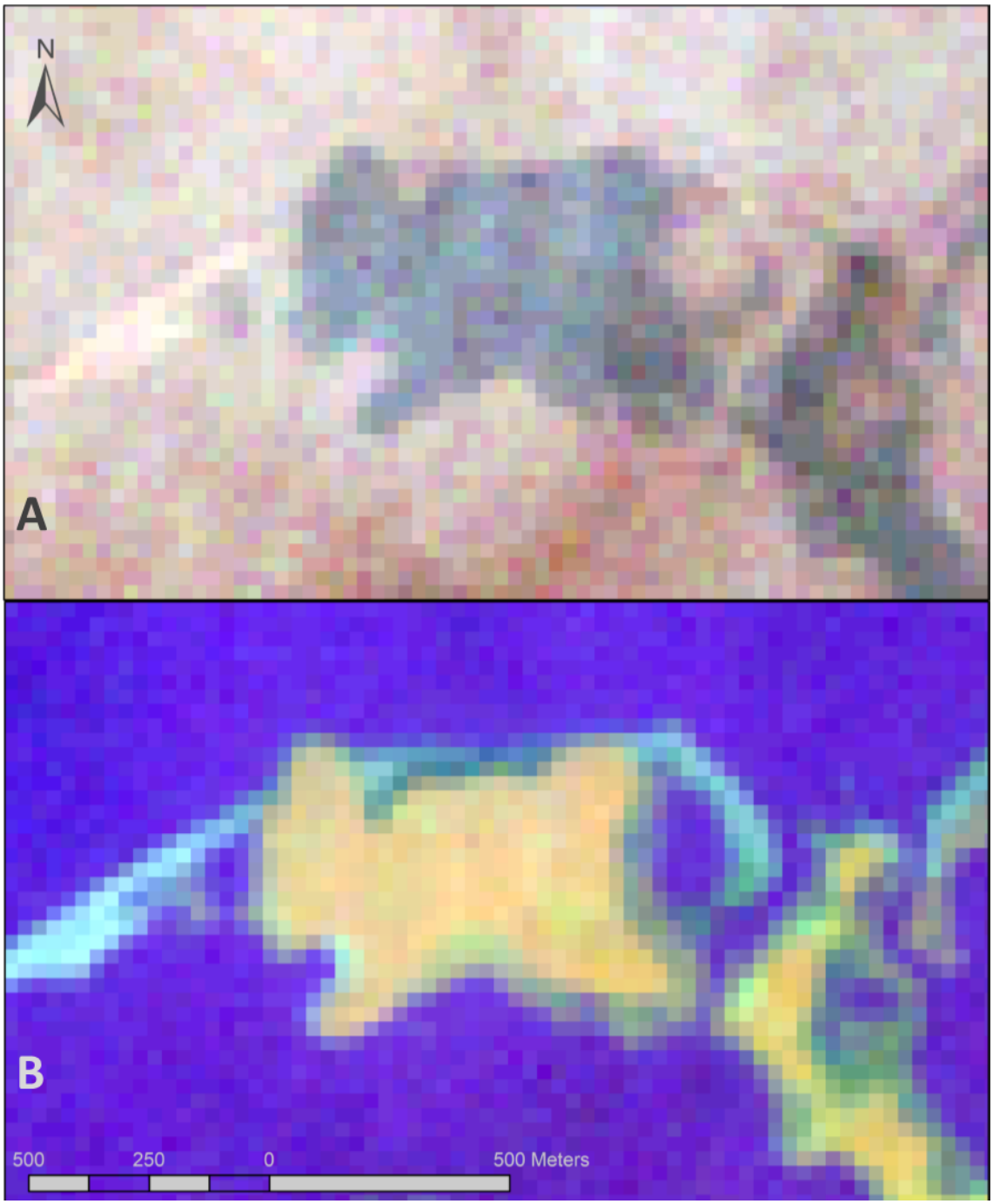

Figure 5.2: Difference in coastal boundary clarity between true colour composite and false colour bands 453 composite

5.3.1.3 Shoreline Mapping

As Peninsula Point lies within a micro-tidal region, the land/water boundary was treated as a shoreline delineator (Lantuit and Pollard, 2008; Solomon, 2005). The false colour composites, with Landsat 7 and 8 imagery pan-sharpened using band 8, were used and the brightness and contrast adjusted to highlight the shoreline. Shorelines were manually digitised within ArcGIS 10.3 to create a line shapefile for each scene, an example of which can be seen in Figure 5.3. For the ALI imagery, pan sharpened true

colour composites were used for digitising the north coast. With the orthomosaics, the north shoreline was also digitised in ArcGIS, based on visual delineation of the land/water boundary.

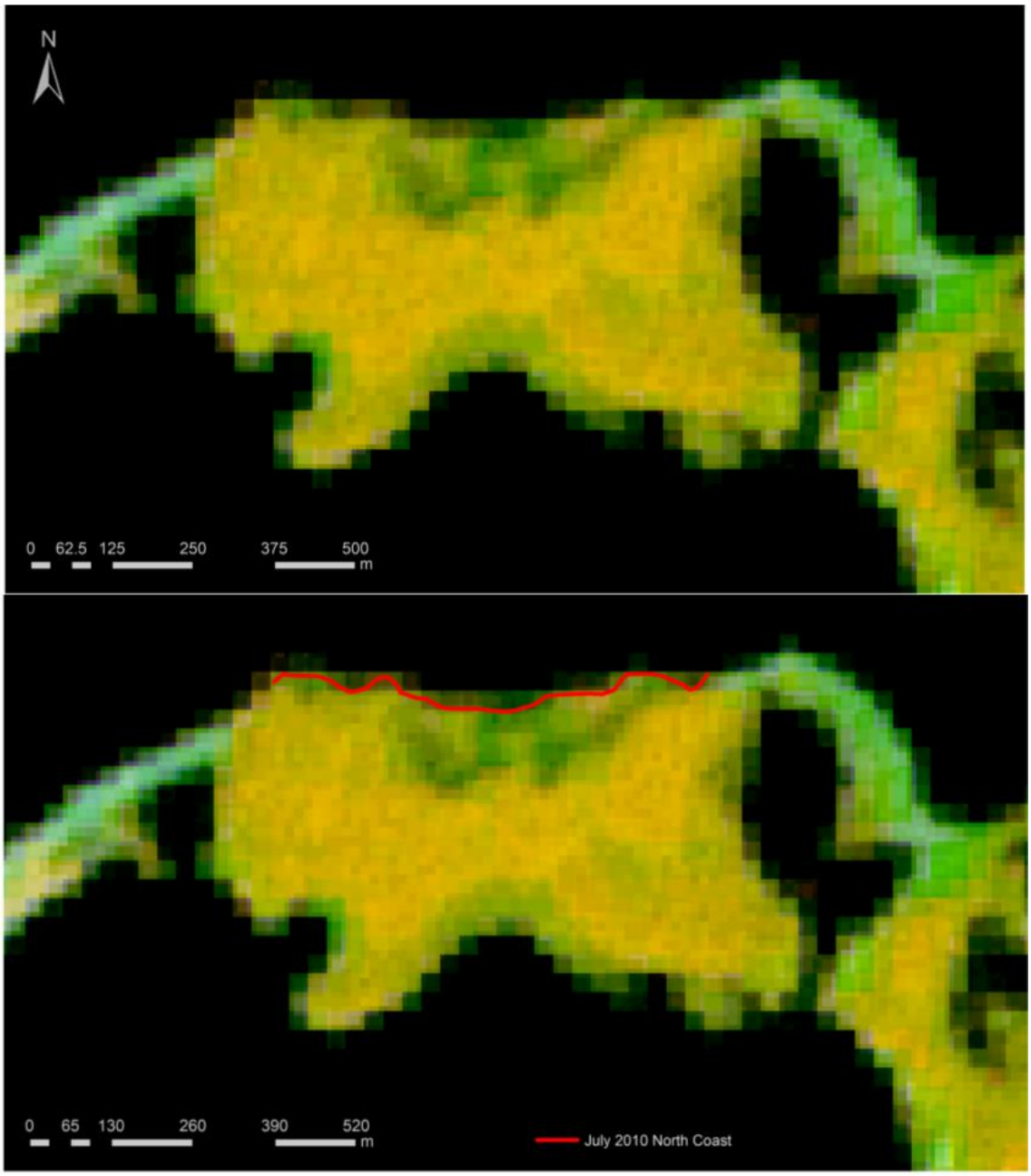

Figure 5.3: Before and after digitising of the 2010 north shoreline using a false colour composite image

To track variability and rates of change for both the shoreline and the headwall positions, a grid was set up with transect lines running perpendicular to the coast every 25 metres. This amounted to 22 detection points for each available year along which changes over time could be tracked (Figure 5.4).

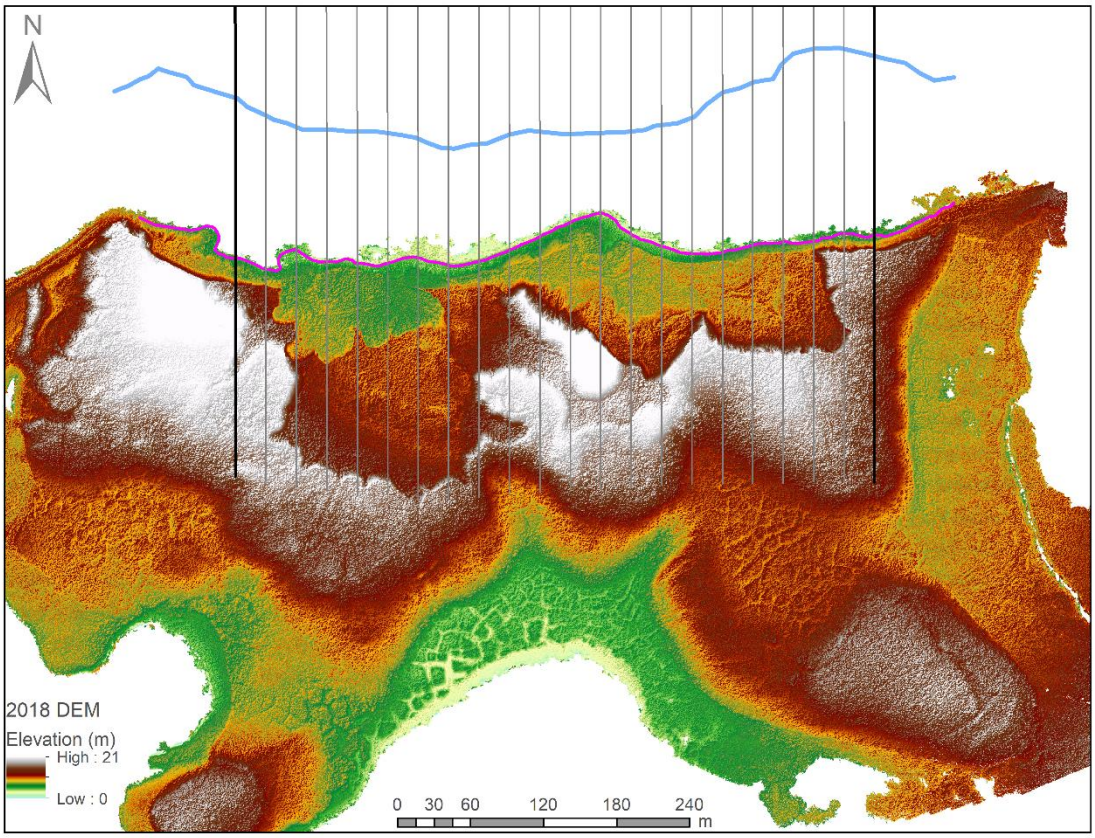

Figure 5.4: 2018 DEM with 2018 shoreline (pink), 1985 shoreline (blue) and transect lines (black and grey) along which coastal changes are tracked

5.3.2 Results

5.3.2.1 SLR Rates and Variability

5.3.2.1.1 Historical SLR: 1935 to 1985

Mackay (1986) published an analysis of SLR rates at Peninsula Point between 1935 and 1985 using a mix of vertical and oblique aerial imagery from 1935, 1950, 1971 and 1985. The study reported a rate of 7 m a^{-1} but made no mention of spatial variability or the variability between individual observation periods. However, an aerial image with the shorelines of the different years used was provided. On this, gridlines were added at regular intervals and retreat rates and variability were calculated (Figure 5.5). The 1935 to 1985 average SLR rate calculated from Figure 5.5 was 5.8 m a^{-1} ±0.6 m, ranging from 3.5 m a^{-1} to a maximum 7.4 m a^{-1} along the individual transects (Appendix 2). The highest rates occurring towards the middle of the site, with much lower rates on the eastern and western segments. Average retreat rates exhibited considerable variability in the timespans measured, from 7.7 m a^{-1} between 1935 and 1950, down to 3.5 m a^{-1} between 1950 and 1971, before climbing to 7.1 m a^{-1} between 1971 and 1985 (Figure 5.6).

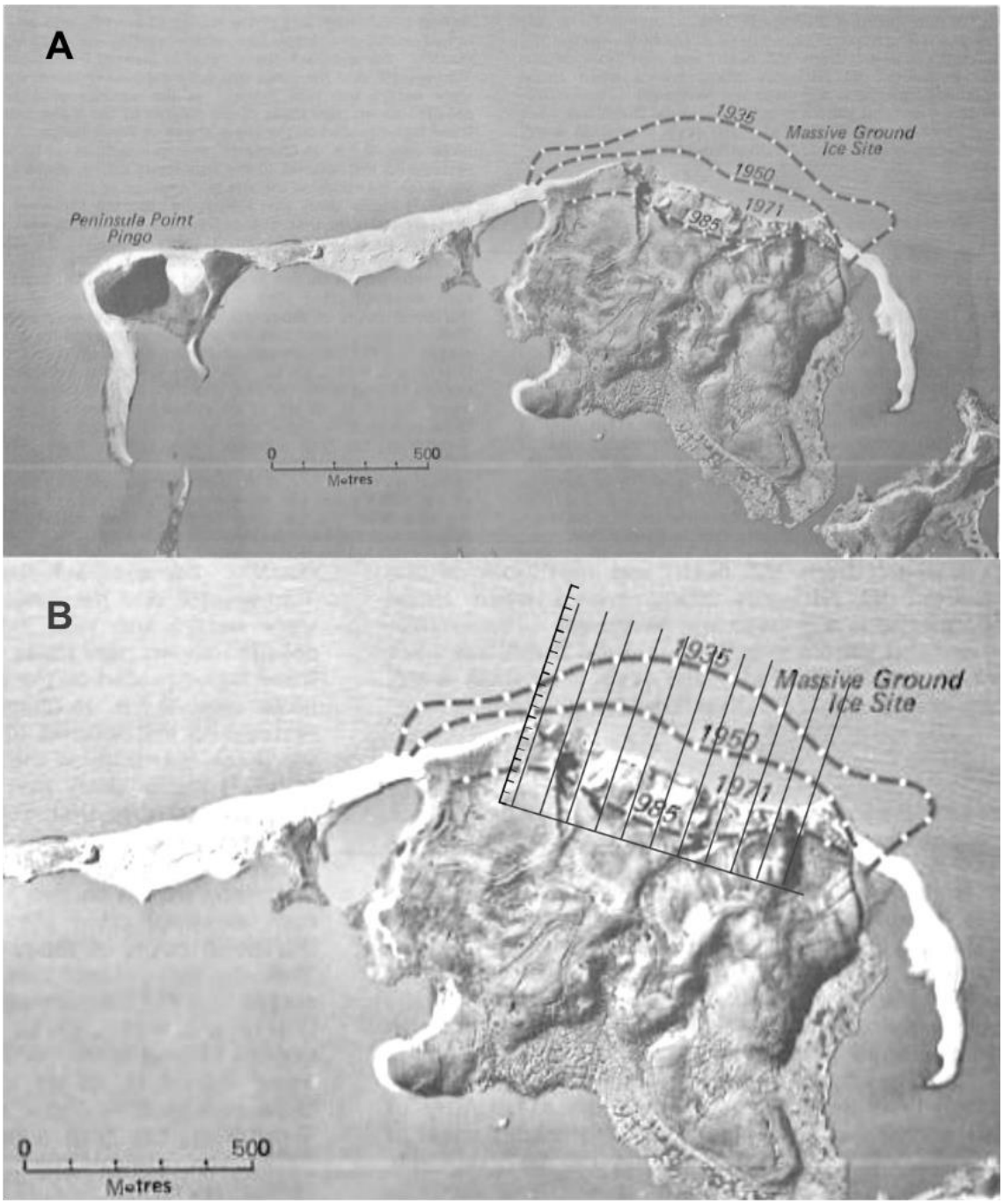

Figure 5.5: Original figure from Mackay, 1986 (A). Modified image used from retreat rate analysis (B)

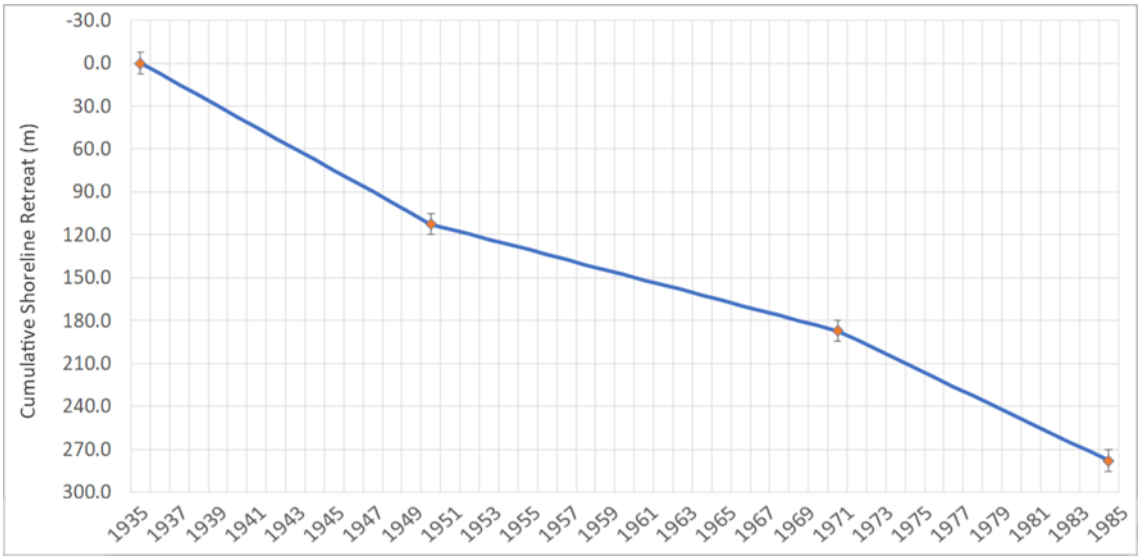

Figure 5.6: 1935 to 1985 cumulative SLR at Peninsula Point with 15m error bands. Adapted from Mackay (1986)

5.3.2.1.2 Modern SLR: 1985 to 2018

The average retreat rate for the period of 1985 to 2018 along all 22 transect lines was 3.4 m a^{-1} ±0.5 m (Appendix 2). The maximum measured rate was 4.8 m a^{-1} while the minimum was 2.0 m a^{-1}. The spatial distribution of the maximum and minimum retreat rates from 1985 to 2018 stand in contrast with those from 1935 to 1985, with the outer segments of Peninsula Point retreating at the fastest rates while the inner section retreats most slowly (Figure 5.7).

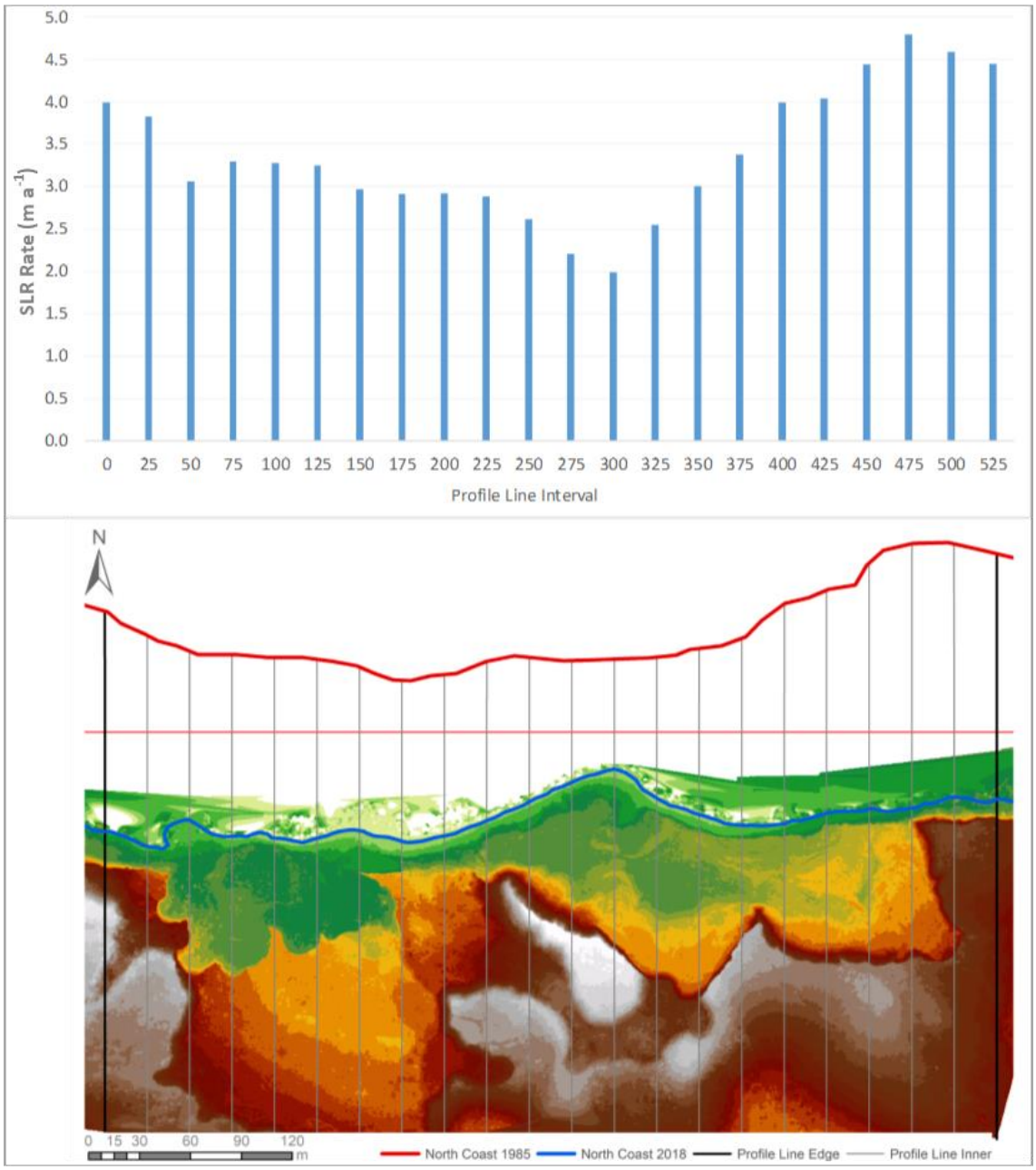

Figure 5.7: Average annual retreat rates between 1985 and 2018 (A) and 2018 DEM with transect lines, 1985 and 2018 north coastlines (B)

Average SLR rates have also varied considerably overtime, ranging from 1.1 m a^{-1} progradation between 2010 and 2013 to retreat of 6.0 m a^{-1} between 1988 and 1990 (Figure 5.8). Along individual transect lines this variation is more pronounced, ranging from progradation of 51.4 m a^{-1} to retreat of 32 m a^{-1}. However, large progradation events appear rare, with only 2.6%, or eight, of the 308 individual rate values reaching 10 m progradation or more. Conversely, 13.3%, or 41, rate values reached 10 m of retreat or more. Figure 5.9 shows the frequency distribution of these rates. SLR rates of between 0 and 7.5 m a^{-1} account 45.1% of the total measurements.

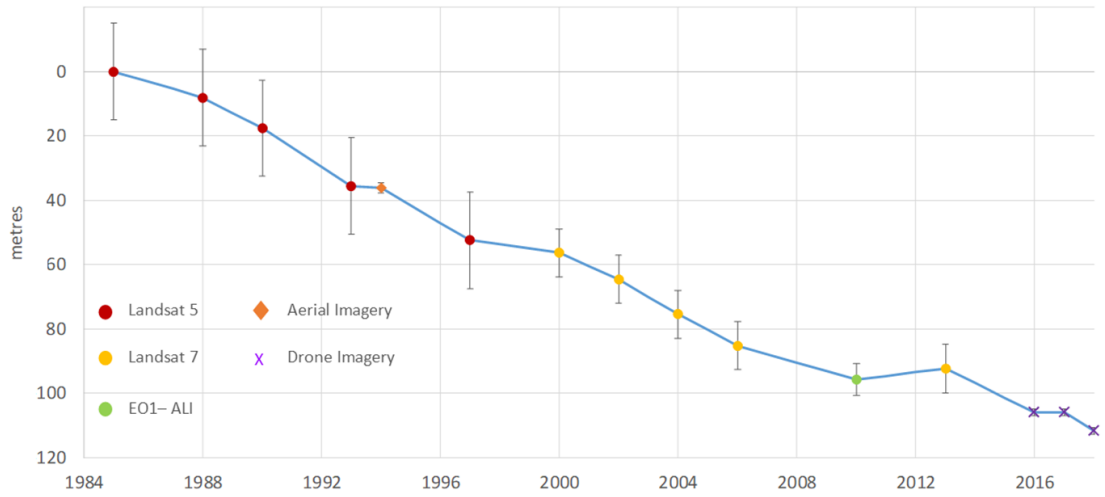

Figure 5.8: 1985 to 2018 coastal retreat rate, error ranges and data sources for Peninsula Point

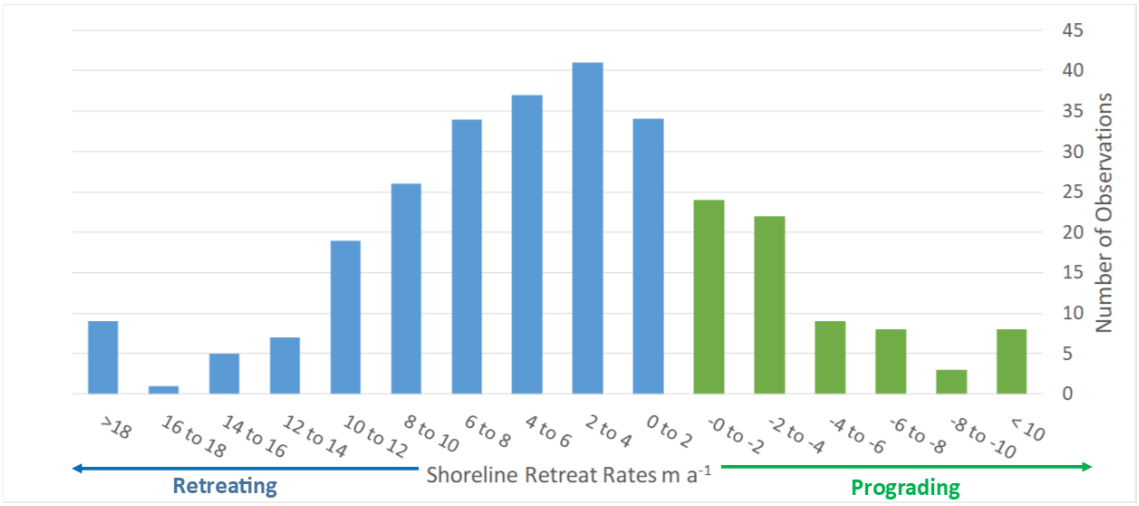

Figure 5.9: Frequency distribution of retreat rates across all 308 individual measurements from 1985 to 2018

5.3.2.1.3 Extended Historical SLR: 1935 to 2018

By combining the 1935 to 1985 SLR rates from Mackay (1986), with the rates between 1985 and 2018, the average 1935 to 2018 retreat rate is 4.6 m a^{-1}. While there is considerable variability, a notable reduction in SLR rates is apparent in recent decades (Figure 5.10). However, the trend falls slightly short of statistical significance (p = 0.07).

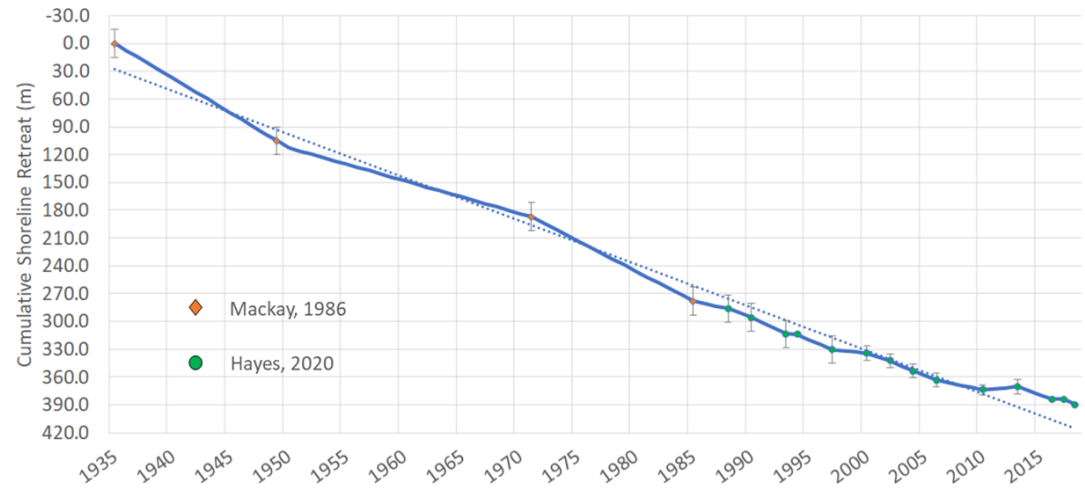

Figure 5.10: 1935 to 2018 SLR at Peninsula Point

In addition to the overall trends, of note is the contrast in along-shore variations in SLR rates. The main focus of retreat was the inner segment of the north coast from 1935 to 1985 (Figure 5.5), after which the outer regions experienced the fastest retreat rates (Figure 5.7). The reason for this switch in along-shore retreat rates is not immediately apparent. However, the following sections will examine trends and variability in other topographic features along Peninsula Point, which may offer some insight into the along-shore variations and long-term trends.

5.4 2.5-Dimensional Monitoring

In this section, 2.5D monitoring will allow for an analysis of morphological changes along the Peninsula Point coastline. Data utilised in this section includes the SfM-MVS models from 1993/1994, 2016, 2017 and 2018, and LiDAR data from 2004.

5.4.1 2.5D Change Detection

A range of topographic changes were assessed from 1994 to 2018. These include *in situ* controls on coastal change and RTS dynamics, such as elevation and slope, and coastal responses such as volume and HWR. These were measured using transect lines, as shown in Figure 5.4, running inland at 25 m intervals starting at UTM easting 573,150 m and finishing at 573,675 m, a total of 22 transects covering 525 m. Elevation profiles were extracted along these lines with the QTM software and exported as CSV files for use in Excel. An example of a profile series can be seen in Figure 5.11. As the data were assigned to the North American Datum of 1983 (NAD83), 57 m represented sea level at Peninsula Point. For each profile in each year, the first point where an elevation of 57 m or more was maintained was considered the land water boundary, i.e., sea level. While most statistics generated relied upon the 22 profiles, the HWR

data also involved the use of digitised headwalls and tracking of their movements along the transect lines, the details of which will be described in section 5.4.1.3.

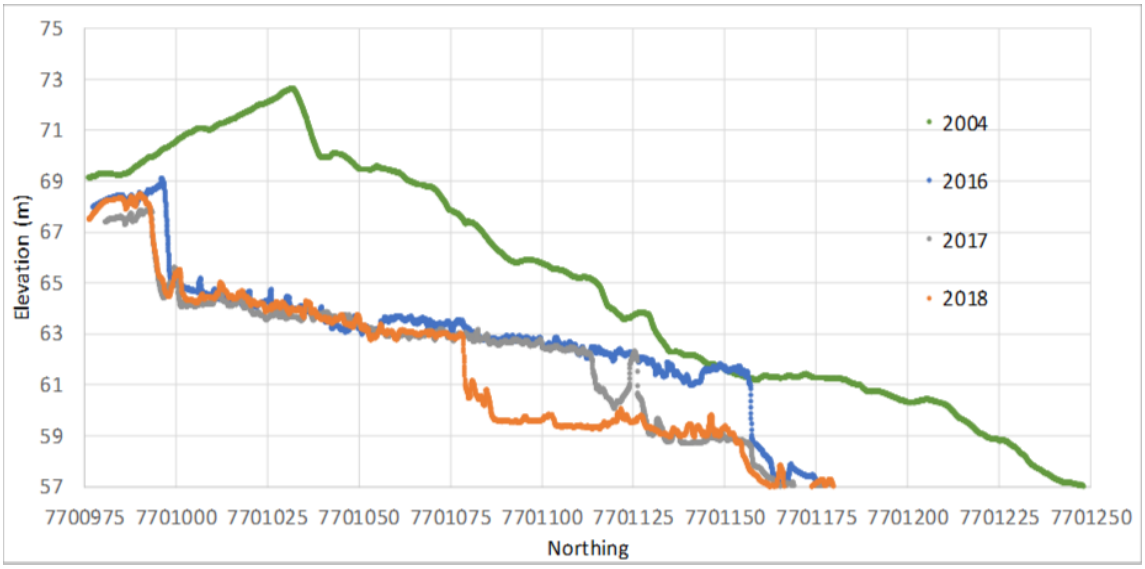

Figure 5.11: Example elevation profile series for each of the four years along the 573225 Easting

5.4.1.1 Elevation and Slope Monitoring Methodology

Average and maximum elevation were measured along intervals of 0 to 30 m, 0 to 50 m, 0 to 70 m, 0 to 100 m and 0 to 150 m inland from the shoreline. This was performed by taking the average elevation from the point where 57 m or above is maintained, inland along each of the distances measured, or for the maximum, taking the maximum reading along the same distance intervals. For example, along an individual transect of any one year, the 150 m interval would consist of the **average** elevation as measured from the shoreline to 150 m inland, the **maximum** elevation at any point from the shoreline to 150 m inland, and the average **slope** angle from the shoreline to 150 m inland. This resulted in a total of 110 average and maximum elevation measurements for each surface model.

The average slope angle along each of the above intervals was also calculated within excel. First, the SLOPE function was used to get the tangent of the line along each interval. Next, the ATAN function converted this to the slope angle into radians and finally the DEGREES function converted the radians into decimal degrees. This produced 110 different slope measurements for each surface model. An example of both the height and slope measurements using the 0 to 30 m interval, on the 573225 Easting for 2018, can be seen in Figure 5.12.

All of the elevation and slope values can be found in Appendix 2

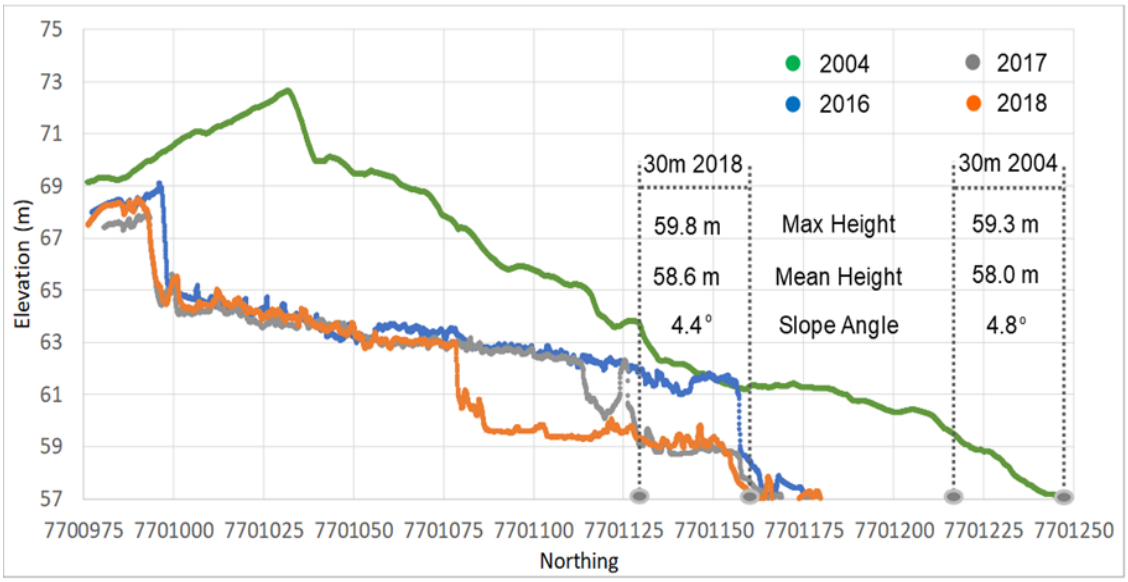

Figure 5.12: Example elevation transects along the 573225 easting with 30m interval measurements for 2018 and 2004

While most of the changes in elevation and slope can be attributed to mass wasting via RTS activity, some of the areas further inland are lower in elevation due to reaching the slope towards the south coast. As such, as the shoreline retreats further back, some regions will naturally see a lowering of the average elevation without the influence of thawing or RTSs. Figure 5.13 displays the elevation for the two profiles that experienced the greatest vertical change averaged over 150 m, located in the large thaw slump on the eastern side of Peninsula Point (Figure 4.14). These two display clear signs of RTS activity, as identified by the headwalls and elevation loss.

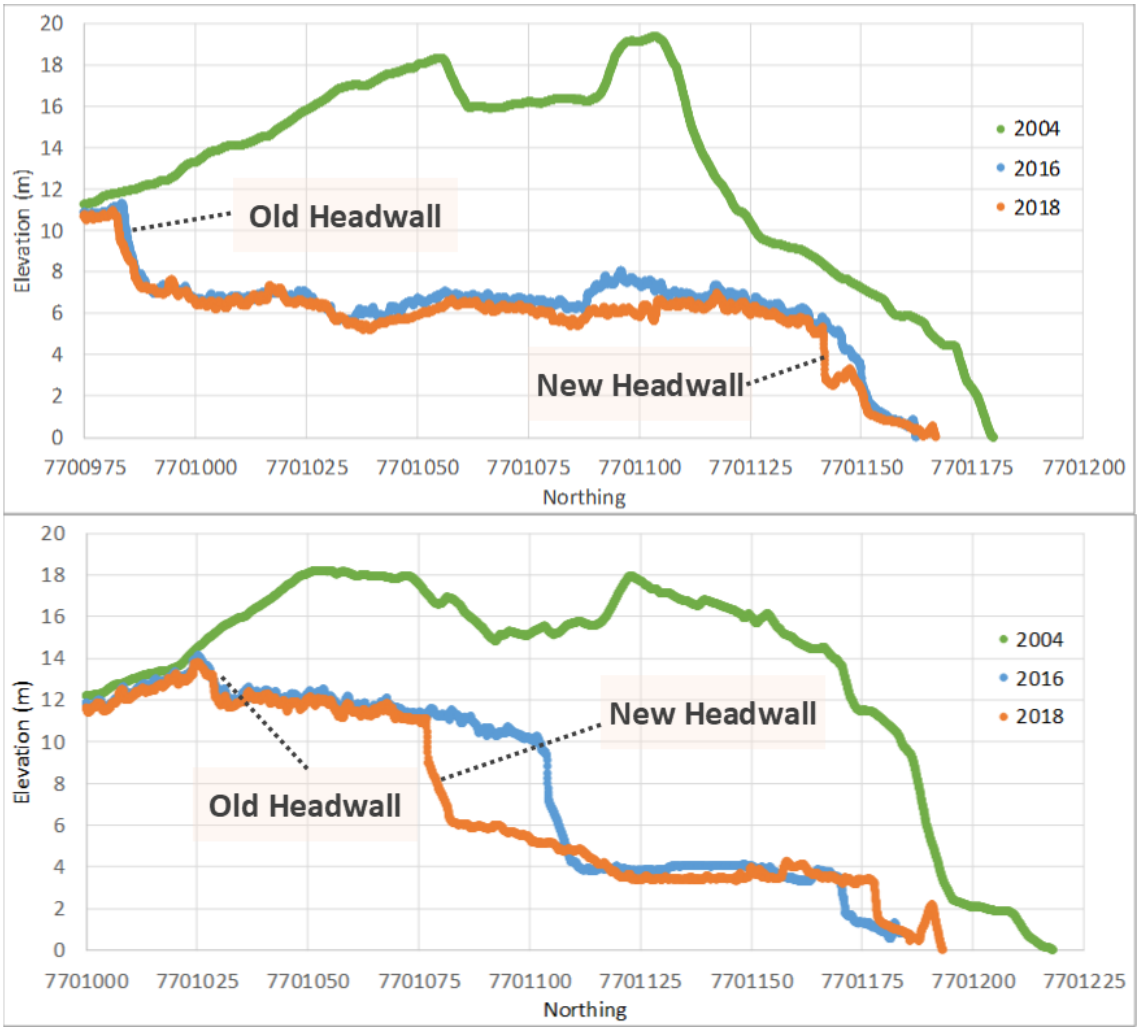

Figure 5.13: Two elevation profiles showing the lowering of elevation through time, likely the result of RTS activity. 57 m elevation is equal to local sea level.

Figure 5.14 demonstrates the effect of the tendency for the landscape to reduce in elevation further south, away from the northern shoreline. Each of the 150 m distances inland, for 2004, 2016 and 2018, incorporated more of the lower elevation sections overtime. While significant HWR and mass loss is apparent along the profiles, the natural elevation reduction of the landscape is also contributing to changes in elevation and slope, primarily as measured over the 150 m distance. While the contribution of the static reduction in ground surface elevation further south appears to be minor compared with mass wasting, it is still worth considering when interpreting the changes in topography, their causes and relationships with the other metrics.

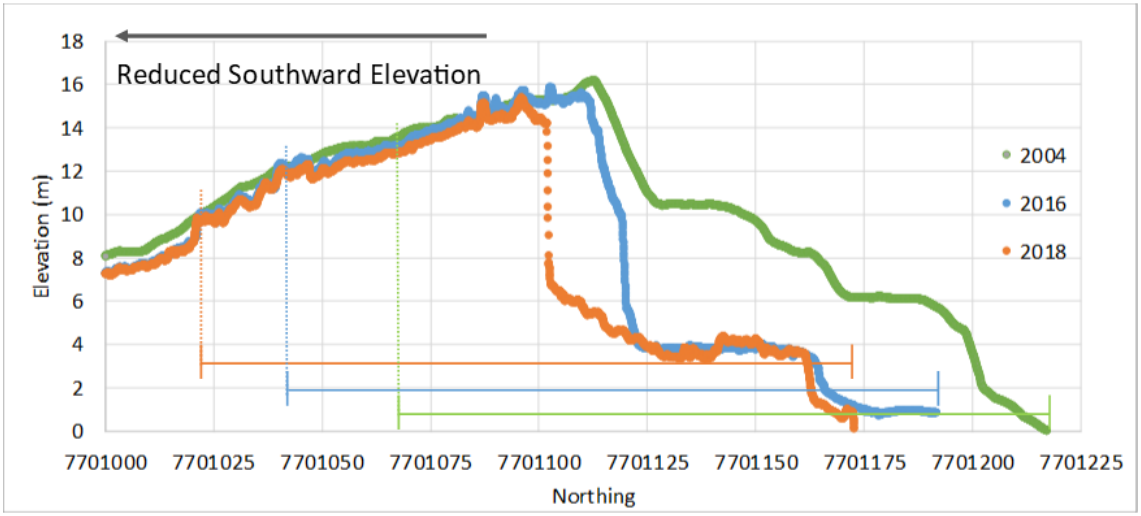

Figure 5.14: Southward lowering of the elevation, influencing the elevation values over 150 m inland

5.4.1.2 Elevation and Slope Monitoring Results

Average Along-shore Change

Between 2004 and 2018, the average longitudinal elevation changed significantly (i.e., change greater than error ranges) at many of the measurement intervals. The largest interval, 150 m, experienced the largest reduction, with an elevation drop of 3.0 m, or -0.21 m a^{-1}. In contrast, the shortest interval, 30 m, experienced an increase in elevation in 2016 and 2017, which reversed back to 2004 levels in 2018 (Figure 5.15A).

The pattern of maximum height changes varied slightly more than the average values, but still displayed significant reductions overall. The largest reduction occurred in the 100 m interval, with a drop of 3.6 m, or -0.26 m a^{-1}. The smallest reduction was in the 30 m interval again, with a 1.2 m drop between 2004 and 2018, or 0.08 m a^{-1} (Figure 5.15B).

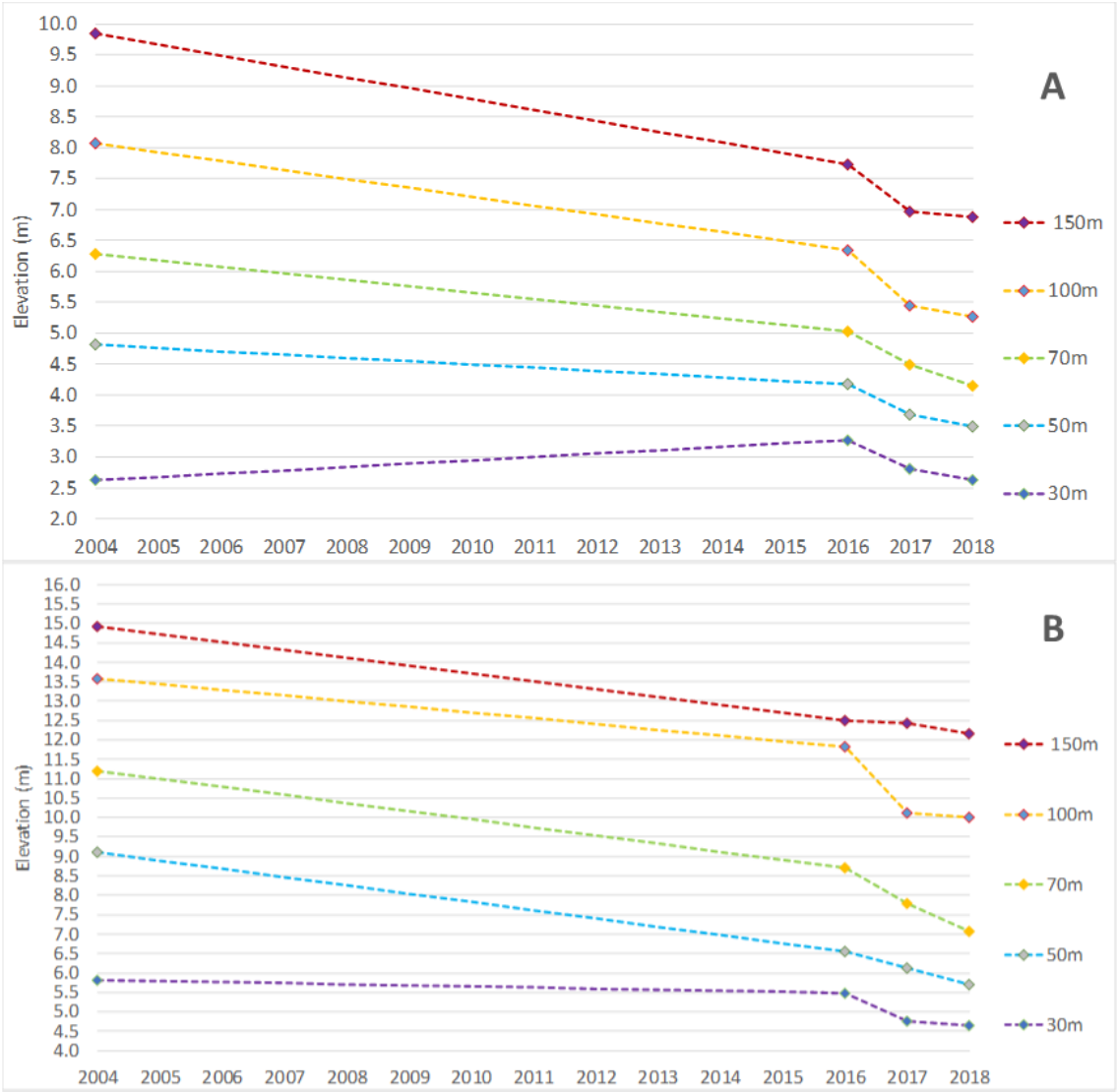

Figure 5.15: These graphs show how both the average (A) and maximum (B) elevation has changed since 2004, along each of the five measurement intervals, 0-30 m, 0-50 m, 0-70 m, 0-100 m and 0-150 m.

The average slope angle has also decreased overall, but with a slightly different pattern to the elevation. The maximum reduction in slope angle occurred on the 50 m interval, with a reduction of 5.5°, or 0.39° a^{-1}. The smallest reduction occurred on the 150 m interval, with a loss of 1.3°, or 0.1° a^{-1} (Figure 5.16). Variability in the last three years was more marked with slope angle, with the 150 m interval increasing since 2016, while both the 100 m and 30 m intervals increased between 2017 and 2018.

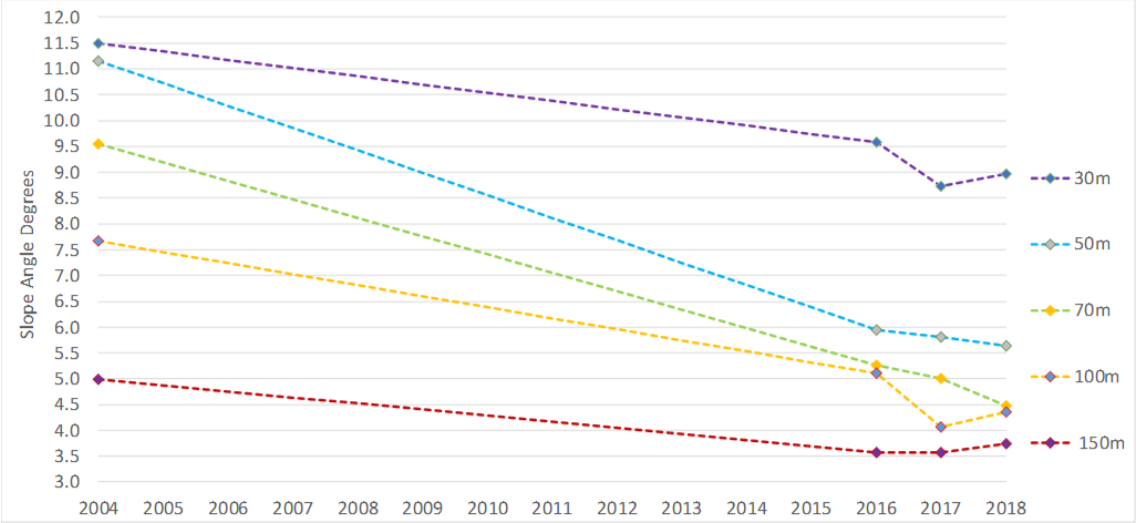

Figure 5.16: Averaged slope angle change since 2004, along each of the five measurement intervals, 0-30 m, 0-50 m, 0-70 m, 0-100 m and 0-150 m

5.4.1.2.1 Along-shore Variability 2004 to 2018: Elevation

Significant along-shore variability exists with both the elevation and slope angle changes. Examining the 150 m average height change between 2004 and 2018 in more detail (as this exhibited the largest reduction) it is evident that the central region was responsible for the vast majority of the reduction. Figure 5.17 shows the average height values across all transect lines (labelled 0 through to 525, representing the 25 m intervals) using the solid lines for 2004 and 2018, with the differences illustrated by the grey bars. It then splits both years into the inner 12 transects (inner segment), represented by the broad dashed line, and the five outer transects for both the western and eastern ends (outer segments), represented by the fine dashed line. The outer western and eastern 150 m elevations changed by +0.7 m and -1.7 m respectively, averaging -0.5 m. The inner 12 dropped by 5.0 m overall. The same overall pattern persists for all measurement intervals. For the 100 m average, the outer segments changed by an average of -0.3 m while the inner segment changed by -4.8 m. For the 70 m interval, the elevation changes were +0.1 m and -4.0 m, 50 m average was +0.2 m and -2.6 m, while the 30 m average was +0.9 m and -0.7 m, respectively.

In 2004, the 150 m average height for the inner segment was 11.8 m while the outer segments averaged 7.5 m. From this, one might assume that the inner segment had more elevation to lose, which may explain the larger elevation drops relative to the outer segments. However, in 2018 the 150 m average elevation for the inner segment was 6.7 m, below the 7.0 m average of the outer segments. This pattern is also repeated across all the other measurement distances (Table 5.2). It is evident that

there has been a levelling out, with signs of a reversal, in the pattern of near shore elevation at Peninsula Point between 2004 and 2018.

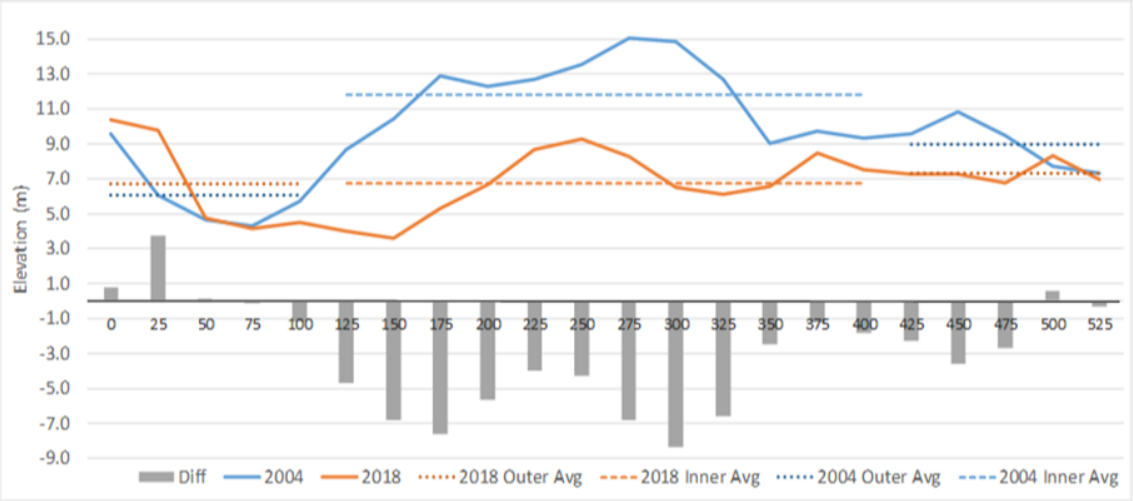

Figure 5.17: Average height 150m inland along all transect lines between 2004 and 2018 (solid lines), the differences (grey bars) and averages for both the inner 12 transects (broad dashed line) and the five outer transects on both the western (left) and eastern (right) ends (fine dashed lines)

Table 5.2: Comparison of the average height across 150m in the inner and outer segments for both 2004 and 2018

Distance	Inner 04	Outer 04	Inner 18	Outer 18
150 m	11.8 m	7.5 m	6.7 m	7.0 m
100 m	9.7 m	6.1 m	4.9 m	5.7 m
70 m	7.5 m	4.8m	3.5 m	4.9 m
50 m	5.4 m	4.1m	2.9 m	4.2 m
30 m	2.9 m	2.3 m	2.1 m	3.3 m

The same pattern is exhibited clearly in the maximum elevation also. The change between the outer and inner segments for the 150 m length is -0.4 m and -4.7 m respectively, +0.3 m and -6.8 m for 100 m (Figure 5.18), -0.2 m and -7.4 m for 70 m, -0.4 m and -5.9 m for 50 m, and +1.3 m and -3.2 m for 30 m, respectively. Similarly, the maximum heights for the inner segments on all measurement lengths were higher in 2004 than the outer segments. By 2018, all but the 150 m measurement length had lower maximum elevations on the inner segment than the outer ones.

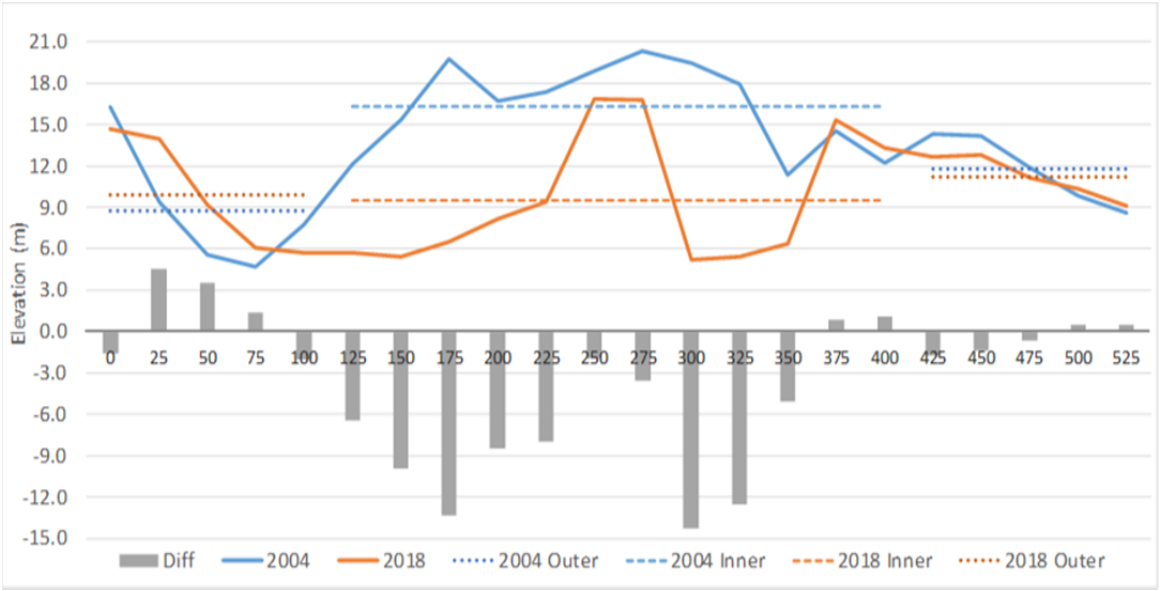

Figure 5.18: Maximum elevation 100m inland along all transect lines between 2004 and 2018 (solid lines), the differences (grey bars) and averages for both the inner 12 transects (broad dashed line) and the five outer transects on both the western (left) and eastern (right) ends (fine dashed lines)

5.4.1.2.2 Along-shore Variability 2004 to 2018: Slope

Significant longitudinal variability also exists in the average slope angle change since 2004. Examining the 100 m interval in detail (Figure 5.19), the average inner slope in 2004 was 9.5° while the outer was 5.4° (4.4° in the west, 6.4° in the east). By 2018, this had changed to 4.8° and 3.9° respectively (4.5° in the west, 3.3° in the east), reducing the difference between the inner and outer segments from 5.1° to 0.9°. A similar pattern exists across the other intervals too. For the 150 m interval, the 2004 inner and outer slope angles were 6.0° and 3.8°, and by 2018 were 4.3° and 3.1° respectively. For 70 m, 2004 was 11.9° and 6.7°, changing in 2018 to 4.2° and 4.8° respectively. For 50 m, 2004 was 13.5° and 8.4°, changing in 2018 to 4.8° and 6.6° respectively. Finally, for 30 m, the 2004 angles were 12.7° and 10.0°, changing in 2018 to 7.1° and 11.2° respectively. While there is not as clear a reversal in the 2004 to 2018 pattern with the slope as there was with the elevation, all measurement intervals have either experienced a reversal (50 m and 30 m) or a significant reduction in the average slope difference between the outer and inner segments (150 m, 100 m and 70 m). This reversed pattern is apparent in 2016 and 2017 also, albeit with large variability in the shorter measurement distances (Table 5.3).

Table 5.3: Comparison of the average slope angle for the inner and outer segments. Dist is the measurement distance in metres

Year	**Inner**	**Outer**	***Inner***	***Outer***	**Inner**	**Outer**	***Inner***	***Outer***	**Inner**	**Outer**
Dist	**150**		***100***		**70**		***50***		**30**	
2004	6.0°	3.8°	*9.5°*	*5.4°*	11.9°	6.7°	*13.5°*	*8.4°*	12.7°	10.0°
2016	3.8°	3.3°	*6.0°*	*4.0°*	6.2°	4.1°	*6.1°*	*5.8°*	8.7°	10.6°
2017	4.0°	3.0°	*4.2°*	*4.0°*	5.0°	5.0°	*5.2°*	*6.5°*	7.0°	10.9°
2018	4.3°	3.1°	*4.8°*	*3.9°*	4.2°	4.8°	*4.8°*	*6.6°*	7.1°	11.2°

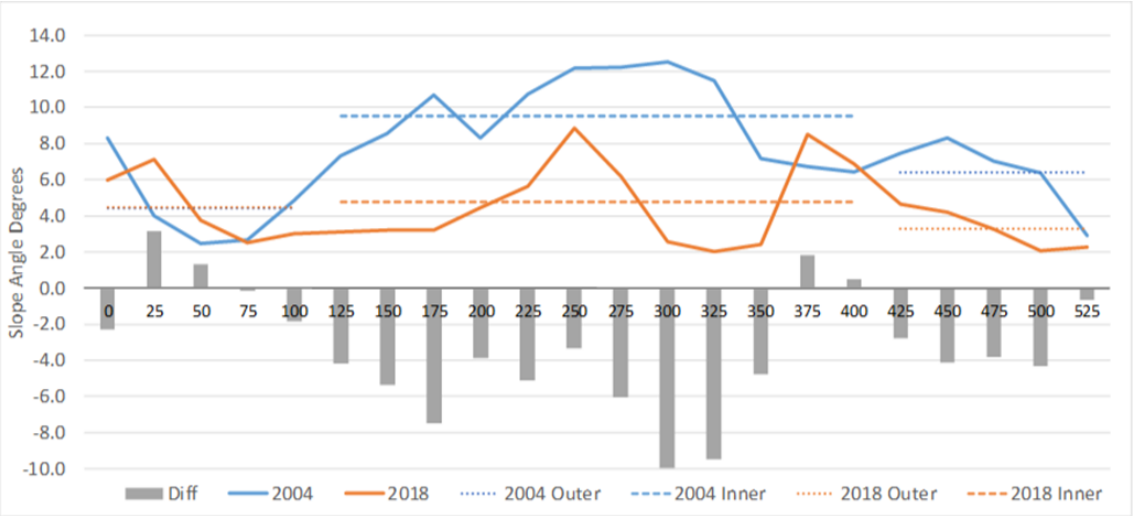

Figure 5.19: Average slope angle 100m inland along all transect lines between 2004 and 2018 (solid lines), the differences (grey bars) and averages for both the inner 12 transects (broad dashed line) and the five outer transects on both the western (left) and eastern (right) ends (fine dashed lines)

The change in slope angle corresponds with the change in height. As the average elevation decreases over time, so too does the slope angle from the shoreline inland. This is evidenced by strong correlations between the two features, although the correlation fails to be statistically significant for the 150m measurement distance (Table 5.4).

*Table 5.4: Correlation coefficients between average elevation and slope angle changes between 2004 and 2018. * Denotes P value below 0.05*

Measurement Distance	150m	100m	70m	50m	30m
Correlation Coefficient	0.20*	0.82	0.92	0.81	0.78

The data on both the elevation and slope angle appear to suggest that the large differences between the inner and outer segments present in 2004 have been eliminated in the period to 2018. Substantial variation from one transect to the next is still apparent, but the broad scale pattern from 2004 is no longer present.

5.4.1.3 HWR Monitoring: Methods

As well as the dates used in the previous section from 2004, 2016, 2017 and 2018, HWR rates were monitored using the 1993/94 SfM-MVS model. While the model proved unreliable for elevation-based measurements, such as height and slope, planimetric accuracy was suitable, with an RMSE in X and Y of 0.23 m and 0.54 m respectively (section 4.2.3.2). The high spatial resolution optical black and white imagery of the SfM-MVS model allowed the headwalls to be easily identified, making it a useful addition. Mapping of the headwalls was carried out manually based on differing criteria in each dataset, depending on the approach that best identifies their positions. For the 1993/94 data, the headwalls were digitised within ArcGIS 10.3 based the visual identification (Figure 5.20). For the 2004 data, the elevation changes in the DEM were used to identify the headwalls. As headwalls are typically near vertical, the sudden change in elevation is useful for identifying their positions. As an extra check, high spatial resolution historical imagery from Google Earth was also used to confirm their positions. The SfM-MVS point clouds were converted to DEMs with 0.5 m cell sizes within QTM, imported into ArcGIS 10.3 where the changes in headwall elevation were used to identify and digitise their positions. These were confirmed through analysis of the orthomosaic visual imagery that are formed as part of the SfM-MVS model construction. To track the changes in position of the headwalls, the same 25 m interval transect lines were used as shown in Figure 5.4. The shapefile representing the 1993/94 headwall was used as a baseline from which HWR rates in the remaining years were measured. These could then be used for calculating rates of change over the entire time period and from one surface model to the next. They could also be used for assessing along-shore variability in these rates and comparing with other measurements taken along the same transect lines. In total, this resulted in 22 headwall position measurements in each year, or 110 measurements in total from 1993/94 to 2018.

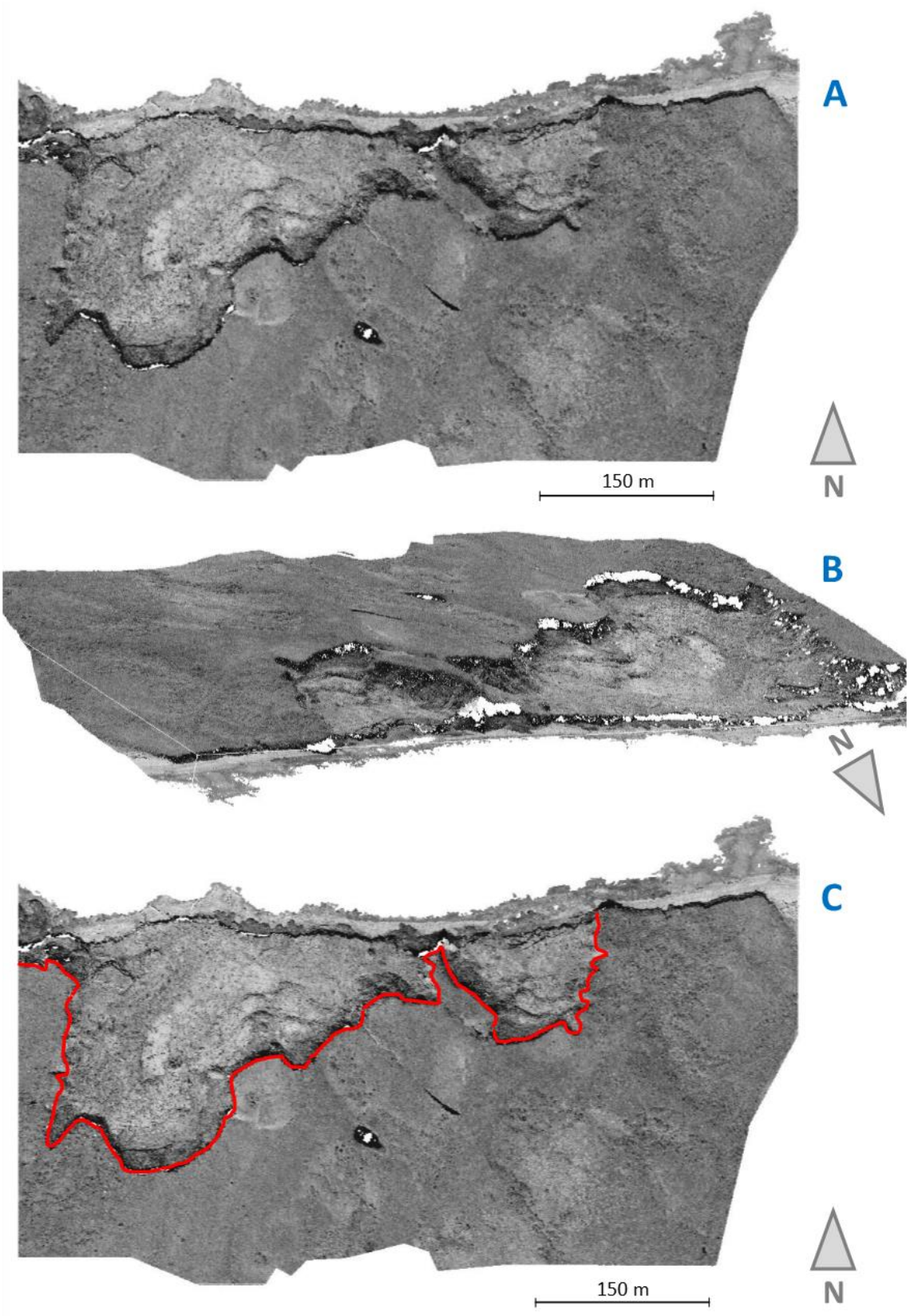

Figure 5.20: SfM Model from 1993/94 in plan view (A), oblique view (B) and plan again with the headwall digitised in red (C)

5.4.1.4 HWR Monitoring: Results

The total HWR between 1994 and 2018, averaged across Peninsula Point, was 110.9 m, a rate of 4.6 ±0.1 m a^{-1} (all HWR data are available in Appendix 2). Retreat across the individual transect lines ranged from 3.2 m to 179.6 m (0.1 m a^{-1} to 7.5 m a^{-1} with a SD of 1.9 m a^{-1}). However, like SLR, the headwall rates have slowed in recent years, from 5.6 ±0.2 m a^{-1} between 1994 and 2004, to 4.1 ±0.2 m a^{-1} between 2004 and 2016, 3.0 ±2.0 m a^{-1} between 2016 and 2017, and 2.7 ±2.0 m a^{-1} between 2017 and 2018 (Figure 5.21).

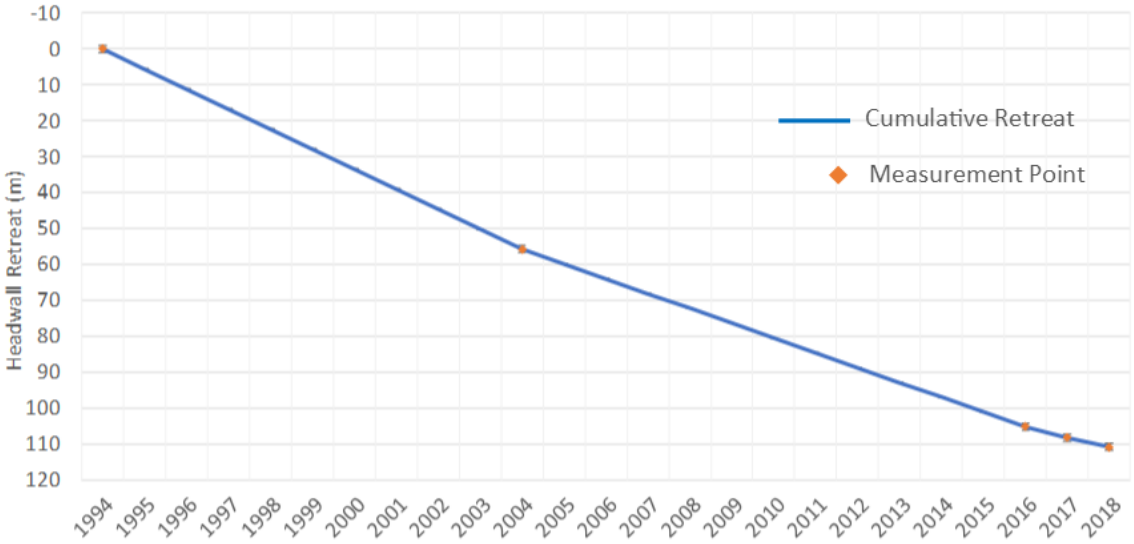

Figure 5.21: Cumulative average along-shore headwall retreat between 1994 and 2018 at Peninsula Point

5.4.1.4.1 HWR Along-shore Variability: Results

Across all time intervals, the smallest (or most negative) HWR rate was -1.3 ±2.0 m a^{-1} (2016 to 2017, transect line 573,475). While this represents an advance in the headwall, it lies within the margin of error when comparing one year with the next and so is unlikely to be truly representative of an advancing headwall, which is physically improbable. The greatest individual HWR rate was +12.6 ±0.2 m a^{-1} (1994 to 2004, also transect line 574,425). 80%, or 70 out of 88, of the measured rates were between 0 m a^{-1} and 8 m a^{-1}, while the seven that were below zero lay within the margin of error. There appears to be little or no temporal consistency in HWR rates along individual transects (Figure 5.22), with some transects displaying both fast and slow headwall rates during different time intervals. This may be related to quickly retreating headwalls eventually moving inland, upslope and stabilising as the exposed massive ice is covered. This results in a period of slower retreat until the massive ice is once more exposed and ablation can drive a new phase of HWR.

The along-shore variability differs from the elevation and slope. HWR rates between 1994 and 2018 proceeded at 5.3 m a^{-1} for the western five transects, 5.2 m a^{-1} for the middle 12 and 2.5 m a^{-1} for the eastern five transects. This is likely related to the large RTS identified in the western segment of Peninsula Point in Figure 5.20. As the headwall was already far advanced inland, retreat would have proceeded at a slower pace than the other regions where the headwalls were in closer proximity to the shoreline.

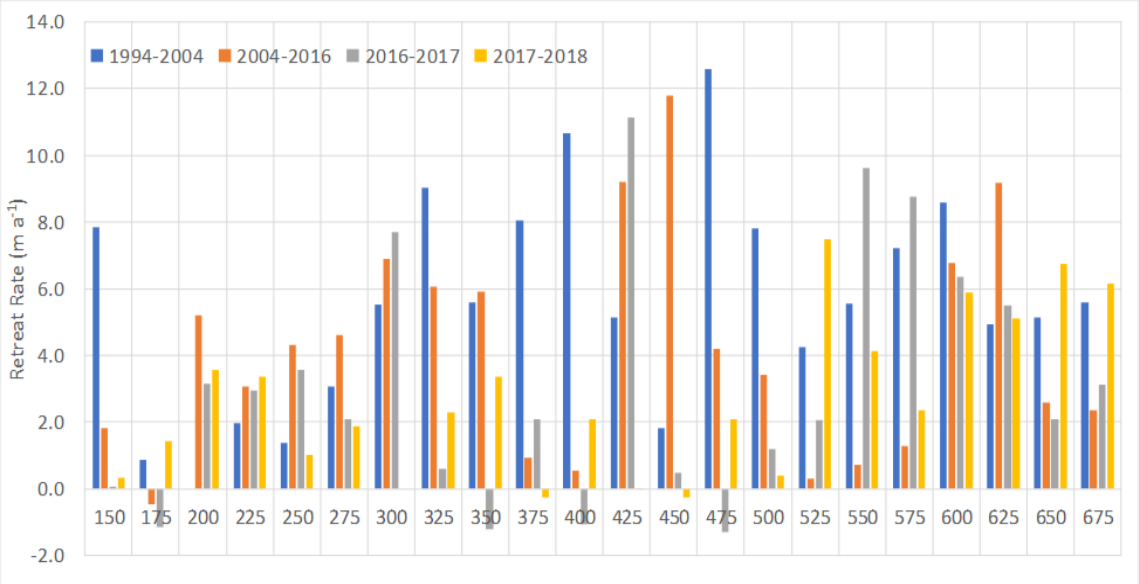

Figure 5.22: Headwall retreat rate differences across the four timespans measured on each transect line.

5.4.1.5 Volume Monitoring: Methodology

To maintain consistency with the other measurements, volume calculations were performed along the same 25 m interval transects as before. As the models used for each year covered slightly different areas, the measurements extended from where the north coast elevation was maintained above 57 m (0 m sea level) as far as the length of the shortest overlapping area, which was an average length of 240 m inland, with a range from 208 m to 267 m. This meant that the end point measurement for an individual transect line was the same for each surface model, allowing for a comparative volumetric change assessment. For each transect the average length was multiplied by the average height above 57 m to create a vertical slice through the landscape. An example, along transect line 573,300W, using the years 2004, 2016 and 2018, can be seen in Figure 5.23. The 2004 volume slice had an area of 2,659 m^2, 2016 had an area of 1,218 m^2 and 2018 had 976 m^2. These measurements were performed on the 22 transect lines for the years 2004, 2016, 2017 and 2018, resulting in 88 discrete volume measurements. Any slice can be multiplied by 25 (the number of

meters between transect lines) to estimate the volume of that section. From this, the sum volume of all 22 slices from a single model can be used as an estimate for overall north coast volume in that year.

For calculating the error margins, the vertical accuracy estimate was used for 2016 (±0.25 m), while the RMSEs derived from the vertical accuracy assessments were used for 2017 and 2018 (0.10 m and 0.20 m, respectively). While the RMSE error for 2004 was 0.52 m, it is likely that thermokarst processes lowered the elevation of the landscape, affecting the RMSE. As such, the vertical accuracy 0.3 m from the metadata were used instead (Table 5.5). The errors for each year were used to generate two additional volume measurements for each profile, creating a likely upper and lower range.

Table 5.5: Values and sources of error range estimates used in volume measurements

	2004	2016	2017	2018
Method	Vertical Accuracy	Vertical Accuracy	RMSE to 2016	RMSE to 2016
Value	0.30 m	0.25 m	0.09 m	0.32 m

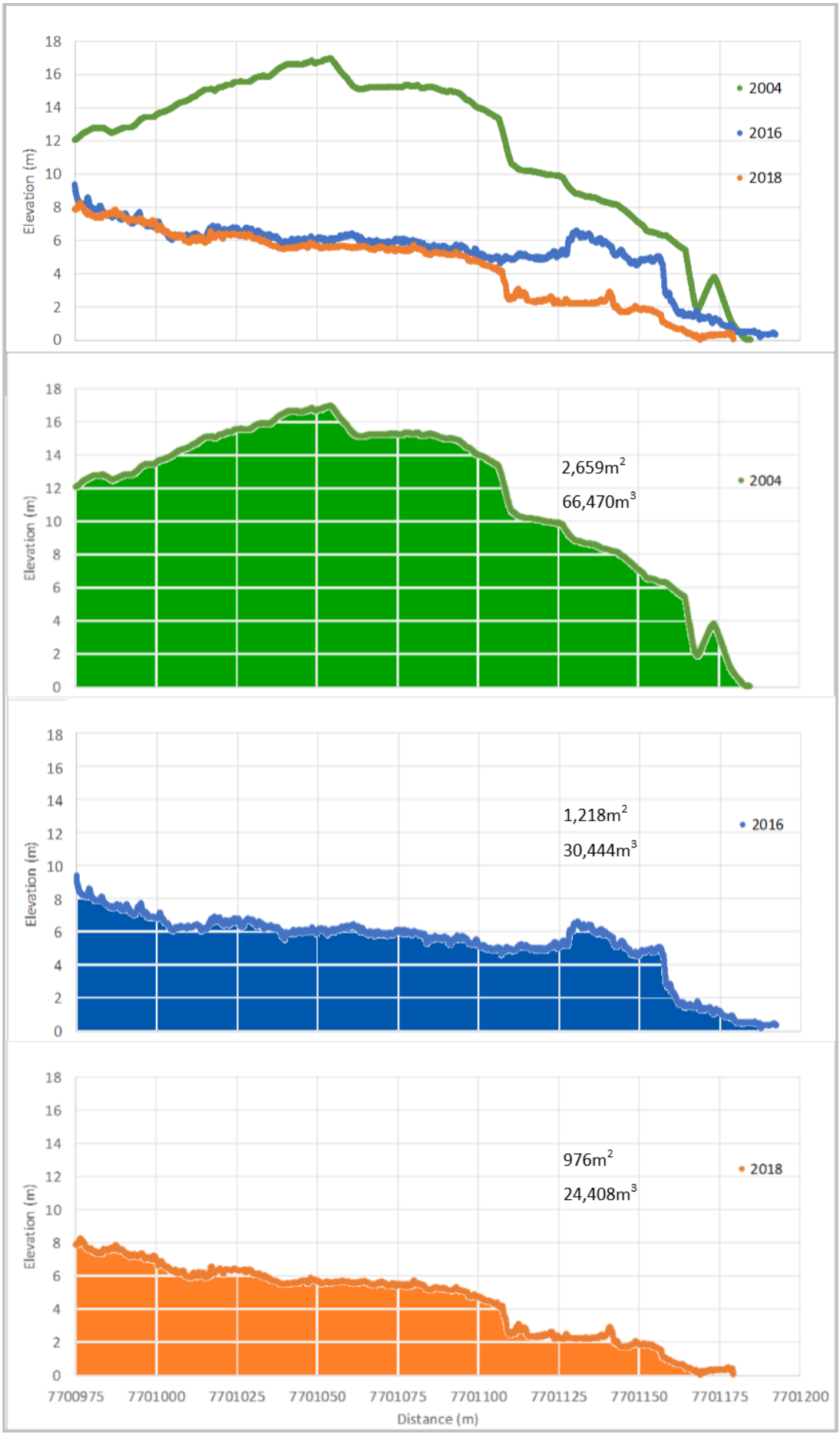

Figure 5.23: Volume slices along the 573,300W profile for 2004, 2018 and 2018.

To ensure that the method of calculating volume based on transect slices was accurate, the total volume for Peninsula Point calculated from the 2004, 2016 and 2017 transect slices were compared to those calculated from the point clouds using the 2.5D volume tool in CC V2.7.0. The volume tool works by setting an arbitrary baseline height, converting the point cloud into a raster grid and calculating the raster volume relative to the baseline. The volumes calculated from both methods and their differences can be seen in Table 5.6.

Table 5.6: Comparison of the total volume calculations from the transects method (TS) and the 2.5D volume tool from CloudCompare (PC). The differences between the two and the % difference relative to the transects method are also presented.

Model	TS	TS Err	PC	Diff	Diff%
2004	1,409,146 m^3	±39,308	1,356,066 m^3	-53,350	-3.79%
2016	911,796 m^3	±28,143	899,492 m^3	-20,670 m^3	-1.35%
2017	852,727 m^3	±32,179	847,330 m^3	6,910 m^3	-0.75%

The volumes calculated from the transects method appear to match the point cloud-based measurements very well. While the difference with the LiDAR is slightly outside the error margins, it is close enough to confirm that the transect method produces realistic volume totals and should be suitable for a more detailed analysis.

5.4.1.6 Volume Monitoring: Results

Between 2004 and 2018, the average volume of the north coast from all transect slices was reduced by 43%, from 1,409,416 m^3 to 805,144 m^3 — a rate of 43,162 (±5,872) m^3 a^{-1} or 3.0% a^{-1}. Unlike coastal and HWR rates, there has been a slight increase the rate of volume loss in 2016 to 2018 vs 2004 to 2016 (Figure 5.24). The rate of change between 2004 and 2016 was 41,459 (±5,621) m^3 a^{-1}, compared to the 2016 to 2018 rate of 50,912 (±35,525) m^3 a^{-1}. Much of this increase came between 2016 and 2017, when there was a loss of 59,497 (±60,322) m^3 a^{-1}. The 2017 to 2018 loss was less, at 42,809 (±75,085) m^3 a^{-1}, but still greater than the 2004 to 2016 rate. However, the losses from 2016 to 2017, and 2017 to 2018, lie within their respective error margins, and so the increase in the average rate of volume loss is not statistically significant (volume data are available in Appendix 2).

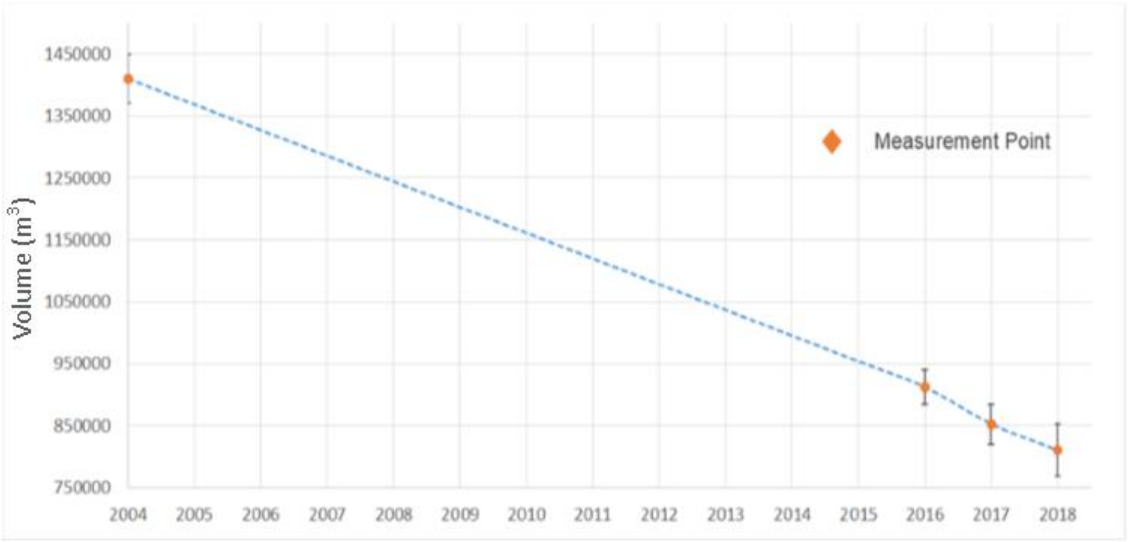

Figure 5.24: Volume measurements in 2004, 2016, 2017 and 2018 with error ranges. Made by combing all the 22 volume slices for each year.

5.4.1.6.1 Along-shore Volume Variability: Results

On individual transects, the rate of volume loss between 2004 and 2018 ranged from 605 m^3 a^{-1} to 3,004 m^3 a^{-1} (Figure 5.25A). As a percentage of the original 2004 volume, losses ranged from 19% to 63% (1.4% to 4.5% a^{-1}), with 15 of the 22 profiles losing between 29% and 50% of their respective volumes (Figure 5.25B). Rates of volume loss between 2016 and 2018 ranged from 518 m^3 a^{-1} to 5,370 m^3 a^{-1} (0.9 to 6.5% per year of the original 2004 volume).

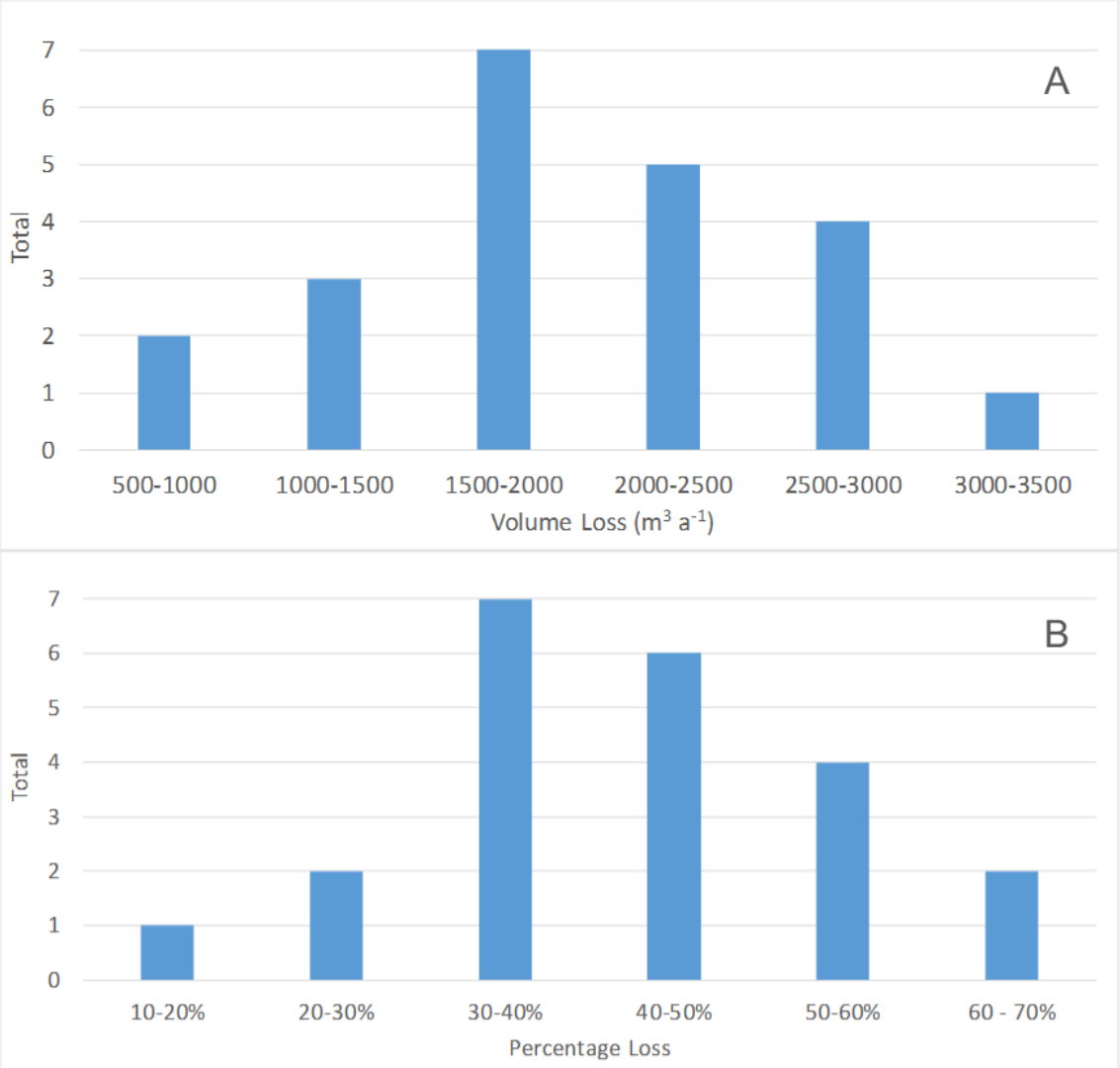

Figure 5.25: Frequency distribution of volume loss rates for each transect between 2004 and 2018 (A), and the percentage of 2004 volume lost between 2004 and 2018 (B)

The spatial pattern of both the volume loss rates and the % loss rates relative to 2004 can be seen in Figure 5.26. Using the inner 12 and outer five segments from each side as before, there is a pattern of greater volume losses in the middle and western segments, and much slower along the eastern segment (Table 5.7).

Table 5.7: Spatial rates and percentages of volume loss on Peninsula Point

Time Period	Western	Middle	Eastern
2004 Avg Volume	58,163 m^3	69,220 m^3	57,591 m^3
2004 to 2018	1,860 m^3 a^{-1} (3.2%)	2,215 m^3 a^{-1} (3.2%)	1,387 m^3 a^{-1} (2.3%)
2004 to 2016	1,739 m^3 a^{-1} (3.0%)	2,143 m^3 a^{-1} (3.1%)	1,409 m^3 a^{-1} (2.3%)
2016 to 2018	2,585 m^3 a^{-1} (4.5%)	2,644 m^3 a^{-1} (3.8%)	1,251 m^3 a^{-1} (2.3%)
2018 Avg Volume	32,129 m^3	38,213 m^3	38,178 m^3

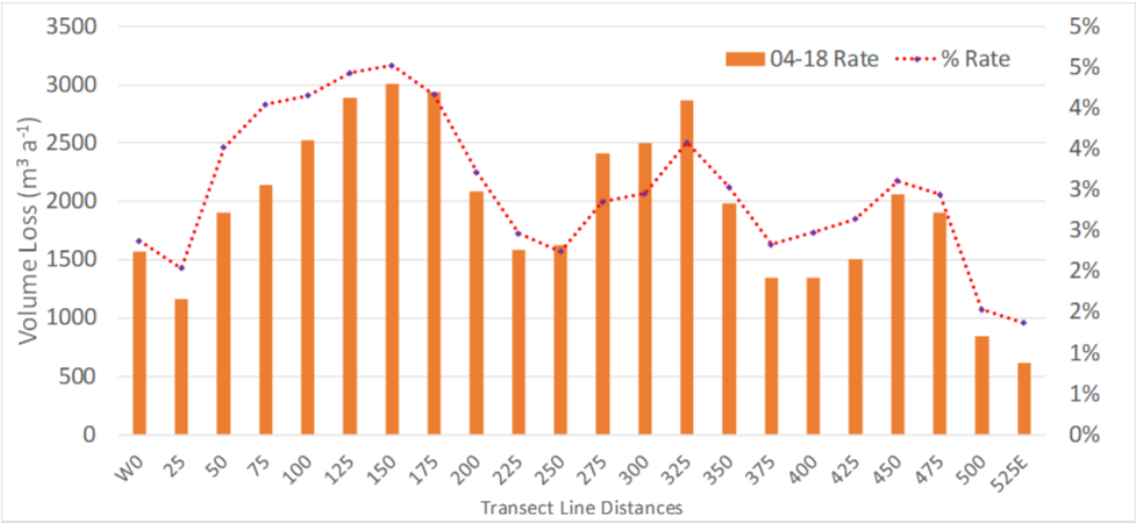

Figure 5.26: Along-shore variations in volume loss rates and percentage loss rates between 2004 and 2018

Starting in 2004, the average transect volume was highest in the middle and lowest in the eastern segment. By 2018, the middle and eastern transects had the same average volume, while the western segment had the lowest. The difference in the rate of volume loss grew in the 2016 to 2018 period, relative to 2004 to 2016.

The difference in the 2004 to 2018 rate of volume loss across all transects can be seen in Figure 5.26. The higher rates along many of the western transects are likely related to the large PRTS noted in the elevation difference in Figure 4.14. The relatively slower retreat of the tall (>15 m) headwall towards the middle of Peninsula Point may also contribute towards the higher volume loss rates there. Of note is the difference in the percentage of volume lost along each transect, with all five of the highest percentage loss rates occurring together in the western half, all associated the largest area of height loss from the PRTS.

The separate rates for 2004 to 2016 and 2016 to 2018 can be seen in Figure 5.27. Here a shift to the middle three transects (250, 275 and 300) is recorded, dominating the volume loss rates in 2016 to 2018 relative to 2004 to 2016. The transects with the highest fraction of volume loss is more evenly distributed between the middle and western segments. A difference is apparent in the variations in absolute and percentage loss rates when comparing the short- and long-term periods. The volume loss rates (percentage rates) for 2004 to 2016 range from 3,228 m^3 a^{-1} to 502 m^3 a^{-1} (4.6% to 1.1%), while the 2016 to 2018 rates range from 5,370 m^3 a^{-1} to 518 m^3 a^{-1} (6.5% to 0.9%).

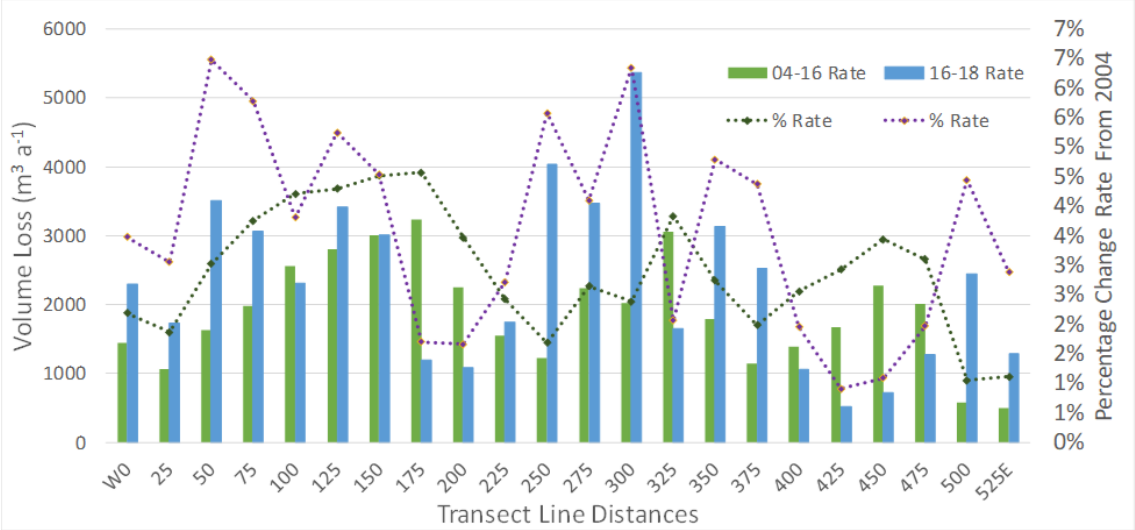

Figure 5.27: Along-shore variations in volume loss rates and percentage loss rates between 2004 and 2018

5.5 2 & 2.5D Monitoring: Shoreline to Headwall Distance

By combining the shoreline mapping from the 2D section, with the headwall mapping from the 2.5D section, it is possible to track changes in the distance between the shoreline and the headwalls. This distance is important for several reasons. For HWR to be maintained, thawed material needs to be easily transported away from the exposed headwall ice. By increasing the distance to the shoreline, there is more time for the muddy mixture to dry out and stabilise before being eroded by sea water. This could further decrease the slope angle from headwall to shoreline, reducing the efficiency of the seaward flow and potentially allow a build-up of material capable of protecting the headwall from further melt. This build-up of material will also affect other features, such as volume, changes to the elevation profile and slope angle. As such, it is a useful metric to monitor.

5.5.1 Shoreline to Headwall Distance: Methods

As both the headwall and the shoreline were digitised as lines for each data set, measuring the distance between the two linear features along each transect line for each year results in a data set capable of tracking changes in shoreline to headwall (SL2HW) distance. Both data sets incorporate 1993/4, 2004, 2016, 2017 and 2018, allowing for changes over two and a half decades to be tracked. Uncertainty values for both headwall and coastal change have already been estimated and can be incorporated into the new data set.

5.5.2 Shoreline to Headwall Distance: Results

The average SL2HW distance has grown substantially over the measurement period (all SL2HW data are available in Appendix 2). Starting with the 1993/94 data, the

average distance was 90.4 ±3 m. This grew to 104.7 ±3 m in 2004, and further to 125 ±2 m in both 2016 and 2018 (Table 5.8). These data appear logical, given that sections 5.3.2.1 and 5.4.1.4 have found that the HWR rate (4.6 m a^{-1}) has been proceeding more quickly than the shoreline retreat rate (3.1 m a^{-1}) since 1994.

Table 5.8: Average maximum (Max), minimum (min) and standard deviation (SD) of the coast to headwall distances in meters for all 22 transect lines in each year.

Year	1993/4	2004	2016	2018
Average	90.4	104.7	125.0	125.0
Max	197.6	198.2	206.8	199.5
Min	0.0	11.4	12.6	12.8
SD	62.0	54.7	53.1	55.3

The changes in the SL2HW distance from 1994 to 2018 display a clear along-shore pattern (Figure 5.28). The western segment underwent a significant reduction of -38.2 m (-1.6 m a^{-1}), which was largely balanced out by a similar level of expansion in the eastern segment of 39.6 m (+1.7 m a^{-1}). However, the middle segment underwent the largest change, expanding by 62.9 m (+2.6 m a^{-1}). This pattern appears consistently within the intervening years.

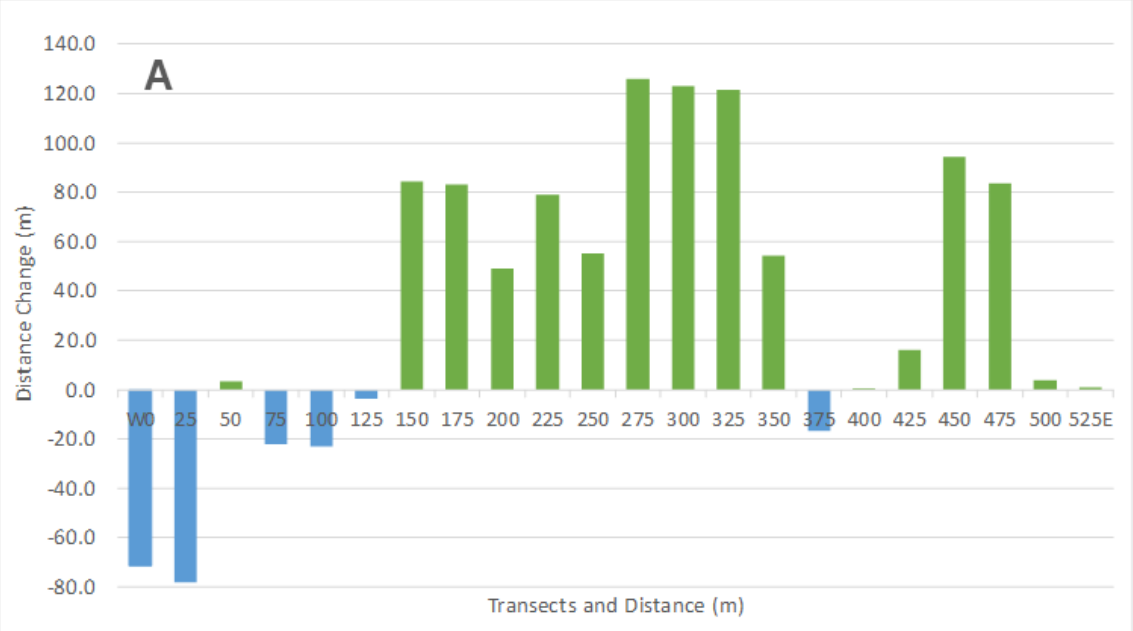

Figure 5.28: Shoreline to headwall distance changes between 1994 and 2018

Between 1993/4 and 2004 the distance from the SL2HW distance grew by 14.3 m, at a rate of 1.4 m a^{-1}. The increase in distance primarily occurred in the middle and eastern sections (Figure 5.29). The western five segments reduced by 1.8 m (-0.2 m a^{-1}), the

middle segment grew by 20.1 m (2.0 m a^{-1}), and the eastern segment averaged +16.3 m (1.6 m a^{-1}).

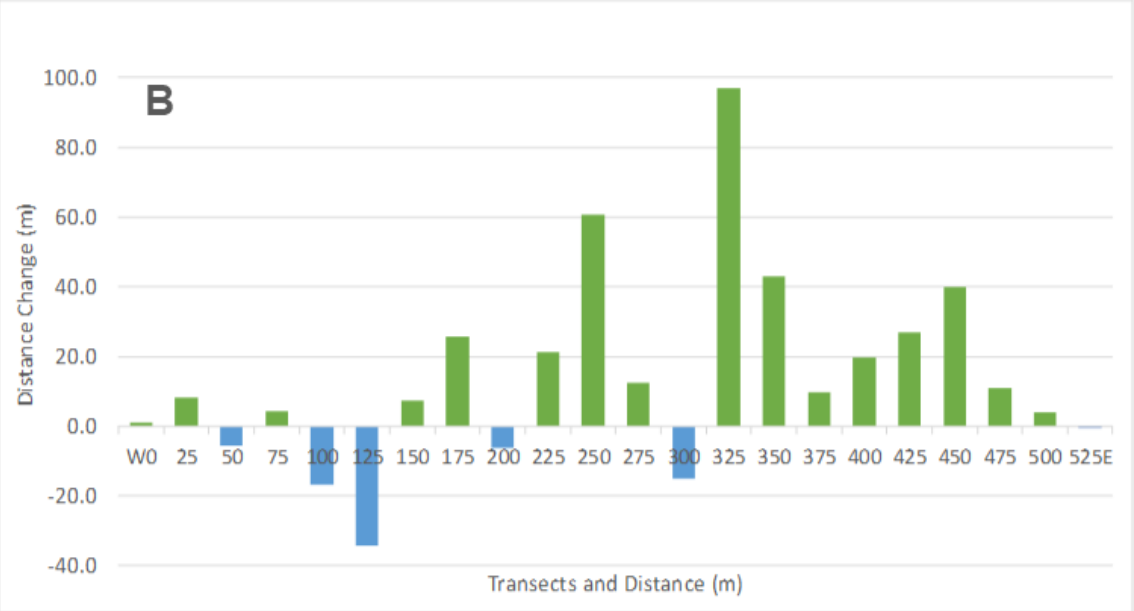

Figure 5.29: Shoreline to headwall distance changes between 1994 and 2004

Between 2004 and 2016 the distance grew by 20.3 m, or 1.7 m a^{-1}. The pattern to this growth shifted slightly, so that the central region began to dominate the expansion (Figure 5.30). The western and eastern segments continued to largely cancel each other out, with changes of -25.6 m (-2.1 m a^{-1}) and 23.0 m (1.9 m a^{-1}) growth respectively, while the central segment underwent an expansion of 38.4 m (3.2 m a^{-1}) on average.

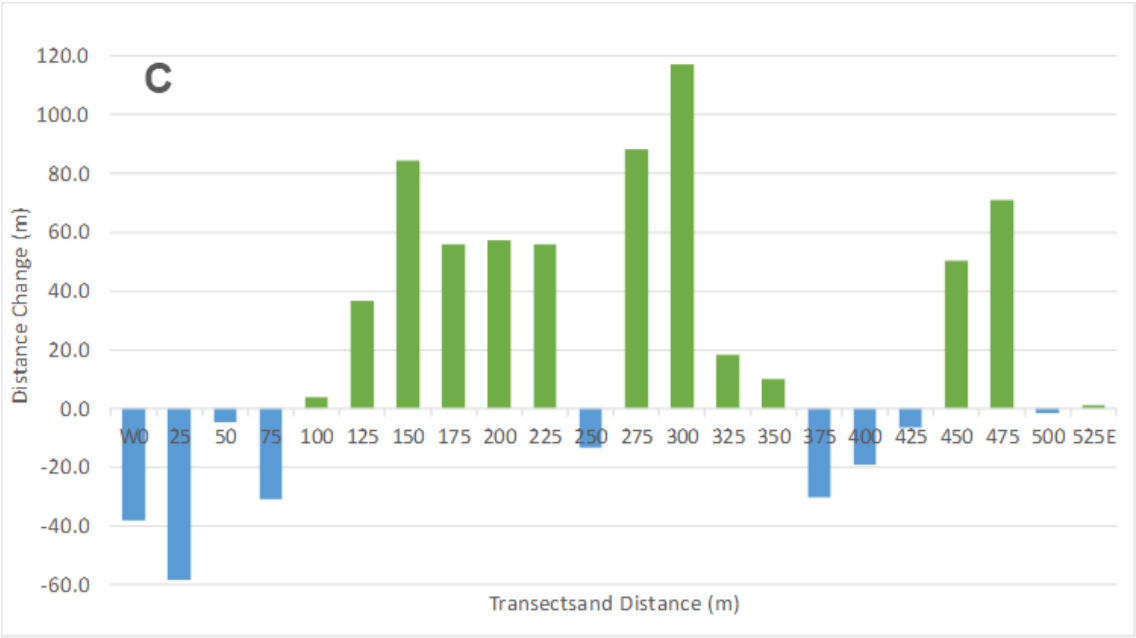

Figure 5.30: Shoreline to headwall distance changes between 2004 and 2016

Between 2016 and 2018, there was no change in the overall SL2HW distance. However, there were some notable differences from west to east between the segments (Figure 5.31). Growth continued fastest in the middle segment and moderate the eastern segment, averaging +4.3 m (2.2 m a^{-1}) and +0.4 m (0.2 m a^{-1}) respectively. However, the western segment underwent a large reduction in the SL2HW distance, -10.8 m (-5.4 m a^{-1}). This was brought about primarily by changes in the first two transects, of -33.9 m and -28.2 m (-16.9 m a^{-1} and -14.1 m a^{-1}) respectively. The changes observed in the first two transect are almost entirely due to a phase of rapid SLR, with negligible changes in headwall position.

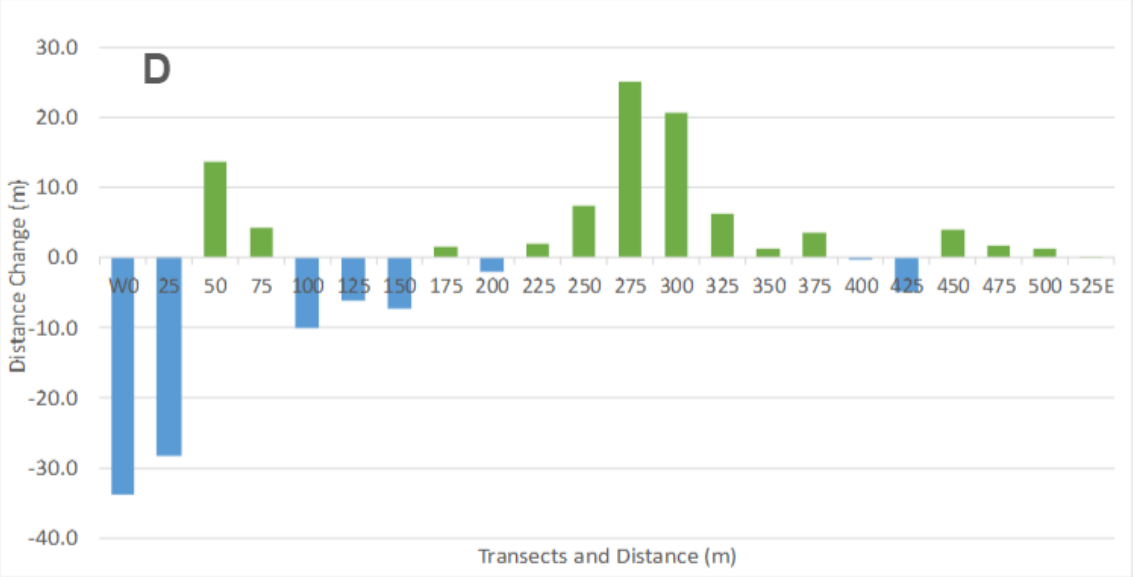

Figure 5.31: Shoreline to headwall distance changes between 1994 and 2018

The lack of SL2HW expansion between 2016 and 2018 does not in itself indicate an end to the growth or an imminent reversal. Despite the large reductions in the first two transects, the SL2HW distance continued to grow along 14 of the remaining 20 transects. However, while the trends are not statistically significant, there has been a slight increase in the rates of SLR between 1994 and 2018, while the HWR rate has slowed during that time, allowing both rates to reach parity between 2016 and 2018. Should this trend continue, there may well be a reversal in the SL2HW growth experienced over the last two decades.

5.6 Summary: Coastal Change

This aim of this chapter has been to analyse the coastal changes occurring on Peninsula Point. To achieve this, it has

- Established a long-term record of SLR from 1935 to 2018
- Established a record of HWR from 1994 to 2018

- Assessed morphological changes through slope and elevation from 2004 to 2018
- Assessed changes in volume from 2004 to 2018

Analysis has revealed a reduction in the rate of SLR, from 5.8 m a^{-1} between 1935 and 1985, to 3.4 m a^{-1} between 1985 and 2018, an average of 4.6 m a^{-1} overall. While the slowdown contrasts with expectations, it falls slightly short of statistical significance. HWR, monitored between 1994 and 2018, averaged 4.6 m a^{-1}, with a non-significant reduction during that time. However, as the headwalls retreated faster than the shoreline between 1994 to 2018, the SL2HW distance grew from 90.4 m to 125 m. Volumetric measurements revealed a 43% reduction averaged 240 m inland between 2004 and 2018. This occurred despite the shoreline retreating by only 36.2 m, illustrating the disconnect between volumetric measurements and those estimated using planimetric data (Figure 5.32).

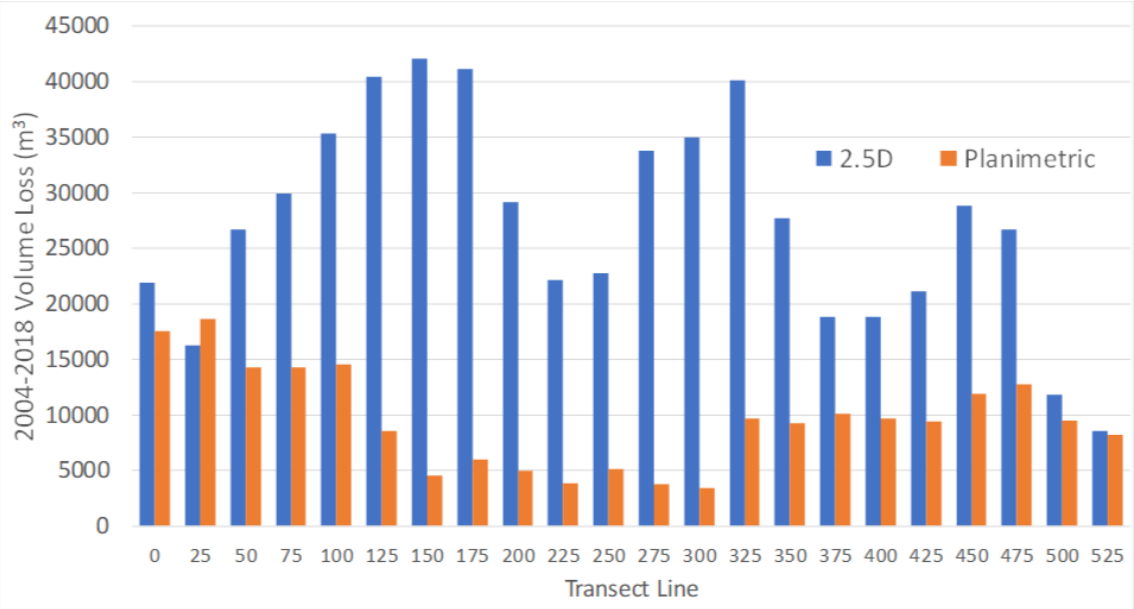

Figure 5.32: A comparison between the 2.5D estimates (blue) of the 2004 to 2018 volume loss, and the planimetric estimates (orange), along the individual transect lines.

Aside from the 30 m average elevation which recorded no change overall, significant reductions in the slope gradient, and both the average and maximum along-shore elevations, were found at all measurement distances. For example, elevation averaged 150 m inland dropped from 9.8 m to 6.9 m, a reduction of 30%, and a 28% reduction was measured in the slope gradient over the same distance, from 5.0° to 3.6°.

Significant along-shore variation was also recorded. During the 1935 to 1985 period, the fastest SLR rates occurred along the central segment of Peninsula Point. The reverse is true for the 1985 to 2018 period. A different trend is observed with HWR

since 1994, with the middle and eastern segments displaying a faster rate of retreat than the western transects. The spatial differences in SLR and HWR contributed to the SL2HW pattern – a moderate growth in the east, moderate reduction in the west and a large growth in the middle. Volume change also displayed a different spatial pattern, undergoing the largest loss in the middle, followed by the western and then eastern segments. This likely influenced the spatial topographic trends. Both elevation and slope started out greater in the central segment in 2004 compared to the outer segments. By 2018, no significant differences remained between the three segments.

However, several questions have arisen for the analysis presented in this chapter. Why have the SLR rates on Peninsula Point slowed since 1985 when most similar shorelines have exhibited faster retreat rates? There is evidence from other regions that RTS activity, via mass transport, can produce more variable SLR rates, but this does not apply to multi-decadal trends (Obu *et al.,* 2016; Obu *et al.,* 2017). Similarly, what drivers and controls are governing the heterogenous temporal and spatial trends observed across various metrics monitored? Furthermore, what influence might massive ice body variability or climate trends exert? To effectively elucidate the coastal dynamics described in this chapter, chapter 6 will provide a more detailed and correlative analysis, including massive ice variability and long-term climate trends.

6 Controls on Coastal Change

6.1 Introduction

Spatial and temporal variability in coastal change metrics such as volume loss, SLR and HWR, have often been linked to local meteorological conditions, such as rain, seasonal heatwaves and storms — with limited success (Heginbottom, 1984; Kokelj *et al.,* 2015; Lantuit *et al.,* 2015; Zwieback *et al.,* 2018). Changes to atmospheric circulation and warming trends are cited as important drivers of retreat and mass loss trends over multi-decadal timespans and are anticipated to continue driving changes over the coming century (Gorokhovich and Leiserowiz, 2012; Forbes, 2011; Lewkowicz and Way, 2019; Segal *et al.,* 2016).

While many studies make mention of the likely importance of landscape morphology and ice content on coastal evolution (Heginbottom, 1984; Irrgang *et al.,* 2018; Lantuit *et al.,* 2008, Lantuit *et al.,* 2011; Novikova *et al.,* 2018), few studies have attempted to assess the role of topographic variability as a control in a quantitative way, especially not over multi-decadal timescales (Ramage *et al.,* 2017; Vasiliev, 2003). As such, this chapter aims to assess the controls on coastal evolution using a combination of old and new approaches. Firstly, the connections and relationships between the change metrics themselves, SLR, HWR, Volume and SL2HW distance, will be analysed. Secondly, air temperature and meridional wind trends during the thaw season (May to September) will be analysed as potential external controls of long-term SLR rates since 1935 (both HWR and volume have too few data points for a similar analysis at this time). Thirdly, morphological controls (elevational and slope) on change metrics will be assessed. Shoreline and HWR controls will be considered over the multi-decadal (1994 to 2018), decadal (1994 to 2004, 2004 to 2016) and short-term (2016 to 2018), while controls on volume loss will only be considered over the decadal (2004 to 2016) and short-term (2016 to 2018), for which the data are available. Finally, the role of massive ice as a control will be considered. This will involve the ice surface model from Chapter 4, observations of massive body variability from the field and the SfM-MVS point clouds, and historical descriptions and images from the published literature. These will be used to assess the contribution of massive ice in controlling the both the spatial and temporal coastal dynamics of Peninsula Point.

6.2 Coastal Change Metrics

Each of the coastal change metrics described in chapter 5 respond to changes in the other, through different means which also vary over time. It will be useful to explore the

interactions and linkages between the change metrics before assessing the role of external controls, like climate trends, and the internal controls of elevation, slope and massive ice.

6.2.1 SLR and HWR

SLR exhibits no significant correlations with HWR over any of the measured time periods. The sign of the correlations also shifted depending on the timeframe analysed, further demonstrating the lack of consistency. This may be due to several factors. In some scenarios, headwalls may extend into areas with a large mass, transporting material towards the shoreline and slowing SLR rates. At other times, the headwall may extend into areas that produces small volumes of material, with no effect on SLR. Where the headwall does not change position significantly, SLR will still vary based on numerous other factors. As such, it appears no simple relationship is apparent between the two metrics.

6.2.2 SLR and Volume

The relationship between volume loss and SLR is more varied than with HWR. No consistent significant relationship is apparent between both metrics, but two correlations are significant ($P<0.05$) and two more come close (P values between 0.05 to 0.10). The strongest correlation is between the 1994 to 2018 SLR rate and the 2018 volume -0.61 (Figure 6.1), suggesting that where volume was highest in 2018, the 1994 to 2018 SLR rate was slower. It may simply be that where SLR was slower, the volume has remained more intact, and that SLR proceeds faster in areas that have a low volume to begin with. The region with the largest volume in 2018, the central five transects, has not gone through the phases of polycyclic thaw slumping that contributed to the large volume losses experienced to the east and west. The gradual retreat of the tall central cliffs, in combination with a lateral flow of mud from transects further east towards the centre, did produce a large prograding mud lobe that persisted into 2018. This has a large effect on the spatial pattern of the SLR rate, much reduced in the centre where volume is greatest and faster either side where volume is lower – partially explaining the correlation observed.

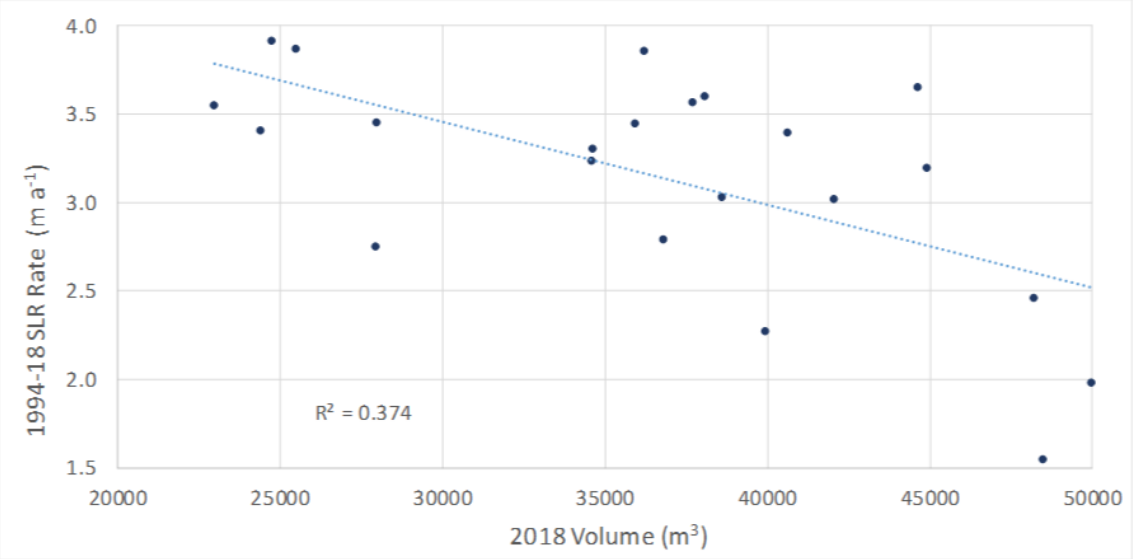

Figure 6.1: Relationship between the 1994 to 2018 SLR rate and the 2018 volume

The other significant correlation was between the rate of both SLR and volume loss from 2016 to 2018, at -0.60 (Figure 6.2). The presence of a strong short-term correlation between volume change and SLR may be related to the ability of the shoreline to rapidly remove the thawed sediment. Where volume loss was largest, coastal progradation was more likely to occur. This relationship is non-linear and complicated by various other factors. Field observations reveal that thawed material can flow in channels laterally along the slump floors before entering the sea. This can reduce the numerical linkage between volume loss along a particular transect line and SLR. This can be seen on the green point in Figure 6.2, with a SLR rate of -3.3 m a^{-1} and volume loss of 1,656 m^3 a^{-1}. Despite a relatively modest volume loss, progradation occurred as material flowed from headwalls to the east forming a mud lobe nearby. The next transect west, 573500 (orange point, Figure 6.2), experienced a volume loss of 3,595 m^3 a^{-1}, yet also recorded a SLR rate of 0.4 m a^{-1}. Despite this, the progradation events are short-lived, and it is likely that this exerts a strong influence on observed retreat rates only over the shorter time periods. As the mud lobe is likely to be removed in the next few years, the correlation between changes in volume and SLR will likely diminish. Evidence for this is seen in the correlation between the 2004 to 2016 rates of volume loss and SLR, which is +0.26.

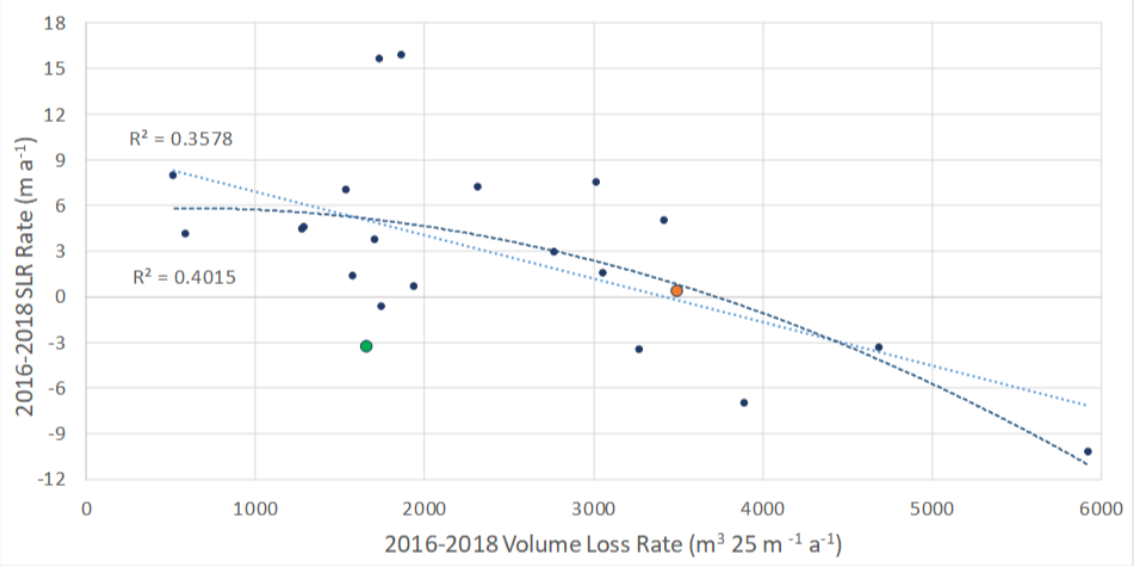

Figure 6.2: Correlation between the 2016-2018 SLR and the volume loss during the same period.

6.2.3 SLR and SL2HW Distance

The SL2HW distance exhibits a more consistent relationship with SLR, than volume or HWR. The rates of change in both metrics produce significant correlations during the 1994 to 2018 (Figure 6.3), 2004 to 2016 and 2016 to 2018 (Figure 6.4) timeframes, of -0.57, -0.56 and -0.93 respectively. While SLR (and HWR) is an inherent part of the SL2HW measurement, and thus a lack of independence is an issue, some elucidating features still appear upon analysis. The correlations between the two metrics during the 1994 to 2018 and 2004 to 2016 periods are significant, but relatively weak. While the 1994 to 2004 correlation is only -0.18. Another metric, most likely HWR, is dominating the relationship over longer time periods. The connection between the HWR and SL2HW distance is presented in section 6.2.5.

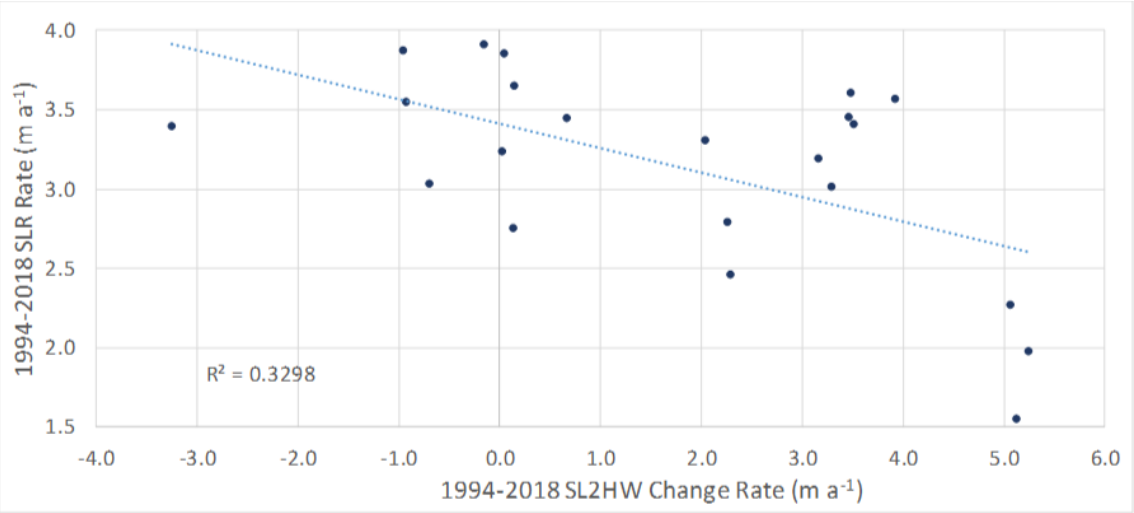

Figure 6.3: Correlation between the 1994-2018 shoreline to headwall distance change rate and the 1994-2018 shoreline retreat rate

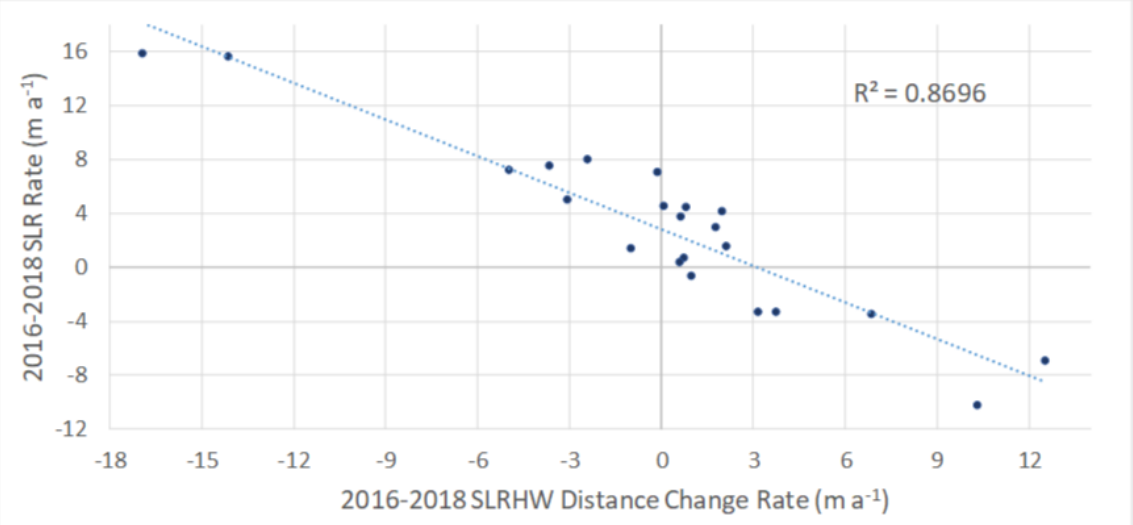

Figure 6.4: Correlation between the 2016 to 2018 rates of change for both SLR and SL2HW distance

6.2.4 HWR and Volume

For all time periods assessed, only 2004 to 2016 produced any significant correlations. These were between the HWR rate and both the 2004 volume (Figure 6.5) and volume loss rate (Figure 6.6) of +0.60 and +0.55 respectively. These indicate that where the volume was largest in 2004, and where the loss rate was greatest between 2004 and 2016, the HWR rate also tended to be faster. This occurs as HWR represents the process of mass wasting extending further inland, with a transfer of volume from the retreating headwall towards the shoreline and eventually into the nearshore and beyond. This relationship breaks down in the short-term, where none of the correlations are close to statistical significance. This is partially explained by the ability of mass transferred from a retreating headwall to get removed over such a short period. This creates scenarios where the HWR occurs on some transects but mass accumulates on the slump floor or in mud lobes, thus not represented as complete volume loss. Furthermore, transient headwalls, which begin near the shoreline and extend along the old slump floors, may also produce losses in volume, without a corresponding retreat in the position of the long-term monitored headwall. These two factors illustrate why the relationship is not clear over the 2016 to 2018 period.

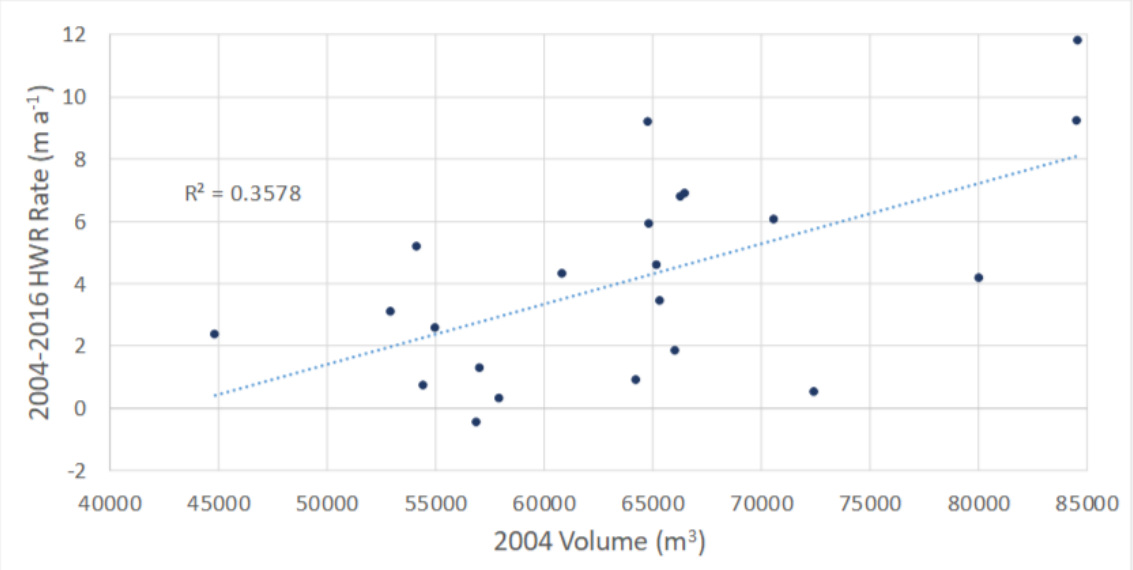

Figure 6.5: Correlation between the 2004 to 2016 HWR rate and the 2004 volume

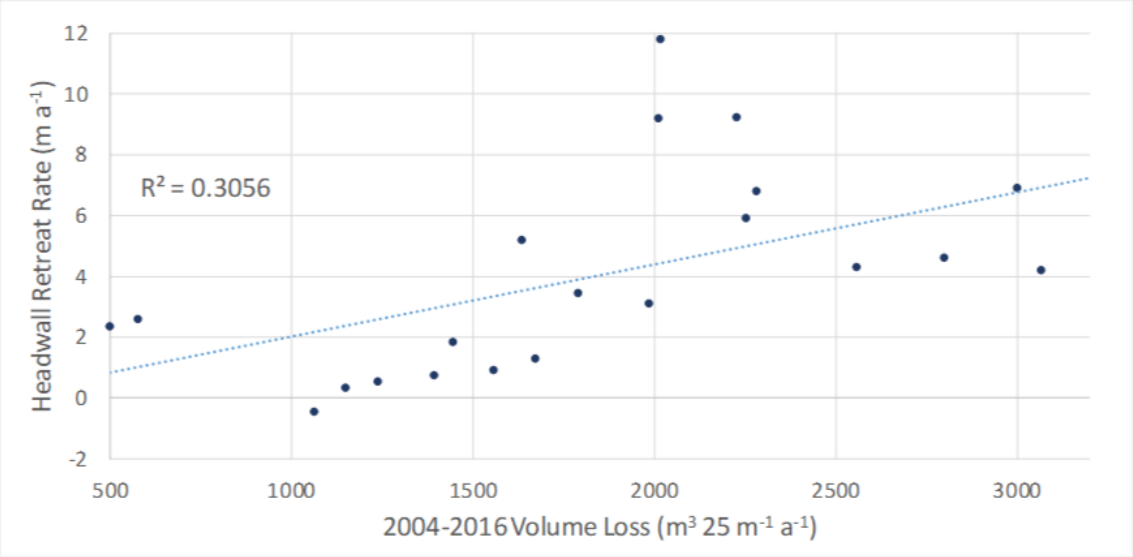

Figure 6.6: Correlation between the 2004 to 2016 rates of change for both HWR and volume

6.2.5 HWR and SL2HW Distance

Significant correlations are found between the HWR and SL2HW distance over all time periods measured (Table 6.1). Like with SLR, there is a lack of independence between the SL2HW distance and HWR rates, but analysis still reveals some interesting items. The SL2HW distance at the start of each measurement is weakly, though relatively consistently, correlated with the proceeding HWR i.e., where the SL2HW distance is greatest, the subsequent rate of HWR is reduced. A large component of this relationship is due to the apparent maximum SL2HW distance. The maximum SL2HW distance in all years measured ranges from 197.6 to 206.8 m, indicating a maximum extent of close to 200 m. It then follows that where the SL2HW distance is near 200 m, the proceeding rate of HWR will be slower, or have a narrower range of possible retreat

rates. Where the SL2HW distance is smaller, the range of possible HWR rates will be larger. This can be seen in Figure 6.7, which displays the relationship between the 1994 SL2HW distance and the 1994 to 2018 HWR rate. Where the SL2HW distance was below 120 m in 1994, the HWR rates were between 2 m a^{-1} and 8 m a^{-1}, while above 120 m the range fell to between 0 m a^{-1} and 4 m a^{-1}.

Table 6.1: Correlation between the HWR rate and SL2HW distance. Values in bold are significant at P<0.05

Metric	1994-2018	1994-2004	2004-2016	2016-2018
SL2HW Distance Change	**0.92**	**0.83**	**0.83**	0.26
Starting SL2HW Distance	**-0.55**	**-0.58**	-0.32	**-0.45**

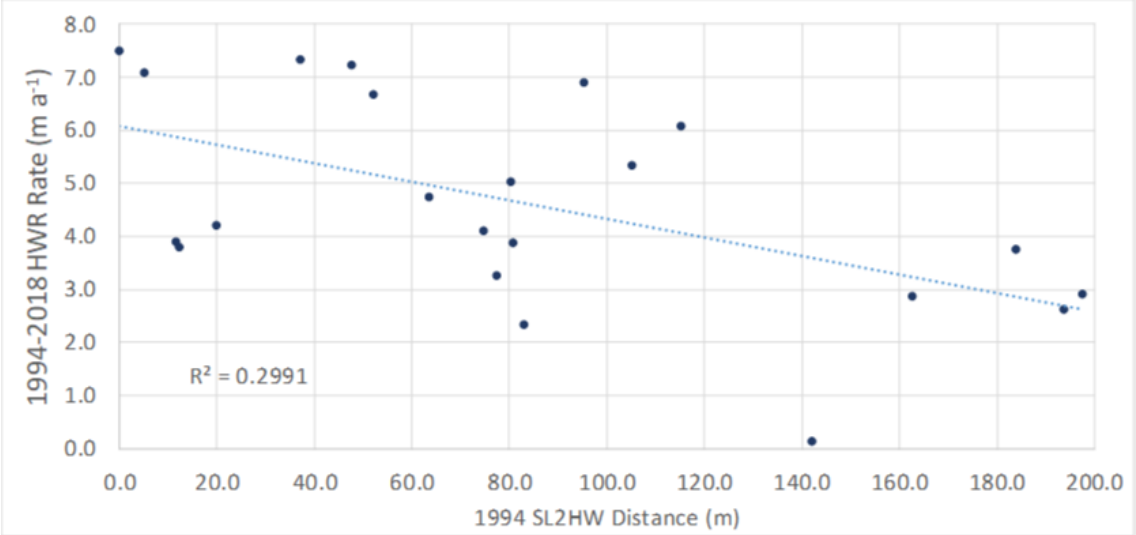

Figure 6.7: 1994-2018 headwall retreat rate vs the 1994 shoreline to headwall distance

The connection between the rates of change in both metrics show a sharp reduction in the short-term relative to all the others (Table 6.1, Figure 6.8A and Figure 6.8B). As discussed in section 6.2.3, SLR typically has a weak relationship with SL2HW distance over decadal and multi-decadal timeframes, with HWR having a much stronger correlation. This relationship completely reverses for the shortest, 2016 to 2018 period, when SLR dominates the relationship over HWR, as seen in Table 6.1

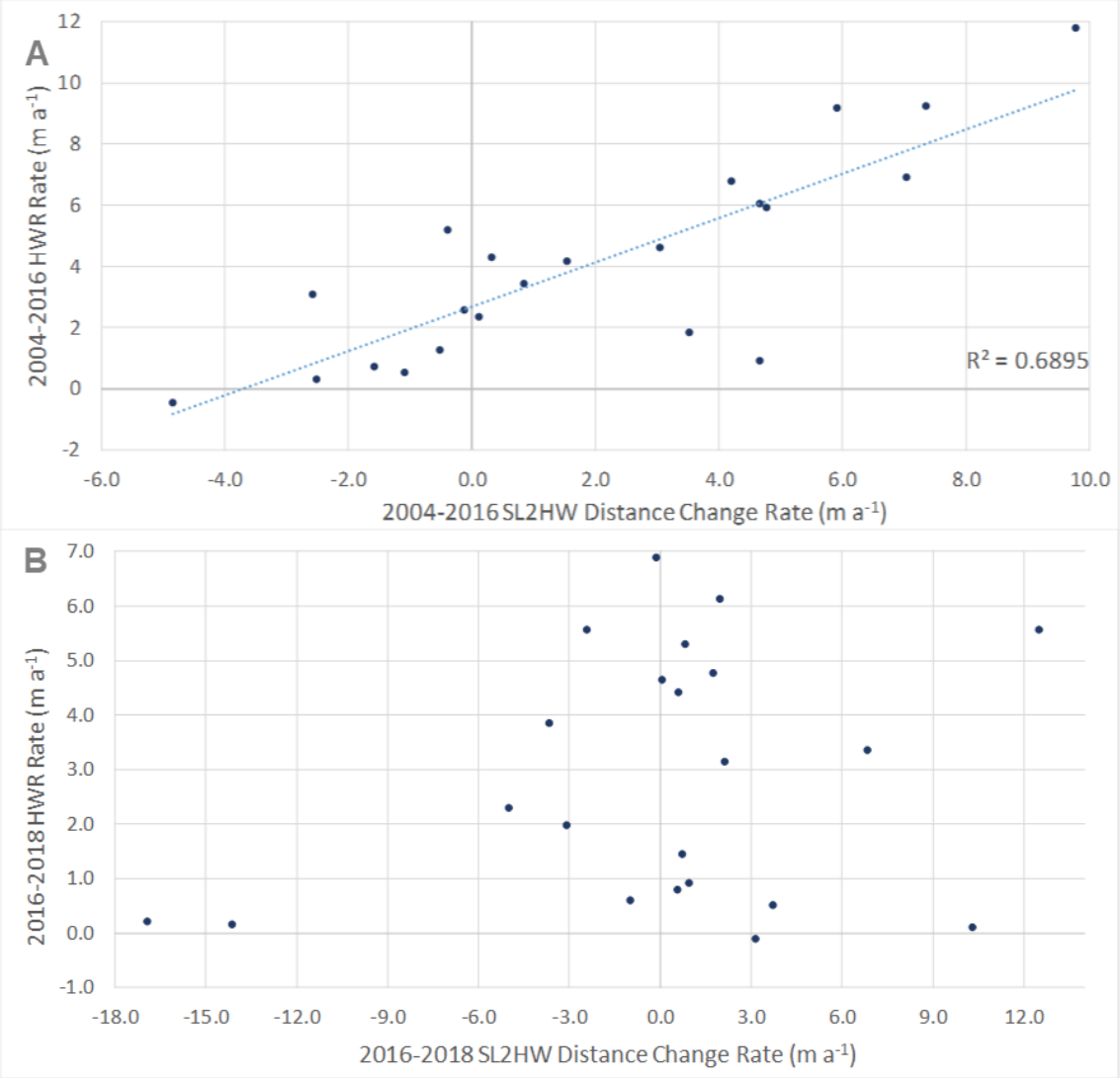

Figure 6.8: Relationship between the rates of change for both the HWR and the SL2HW distance between 2004 and 2016 (A) and 2016 and 2018 (B)

6.2.6 Volume and SL2HW Distance

The 2004 volume is a strong predictor of the 2004 to 2016 SL2HW distance change rate (+0.64, Figure 6.9) and, as logic follows, the 2016 SL2HW distance (+0.48). Where the volume was greatest in 2004, the SL2HW distance grew faster and was subsequently larger in 2016. It follows that the regions with a greater starting volume in 2004 are unlikely to have been affected by large RTSs, meaning the headwalls would be closer to the shoreline. As the headwalls progress along these high-volume transects, material is transported towards the shoreline, slowing the SLR rate and expanding the SL2HW distance. No similar significant relationship between the 2016 volume and the 2016 to 2018 SL2HW change or 2018 distance is apparent. This may be due to several factors, such as incomplete removal of thawed sediment and the larger error ranges in change rates over short time periods.

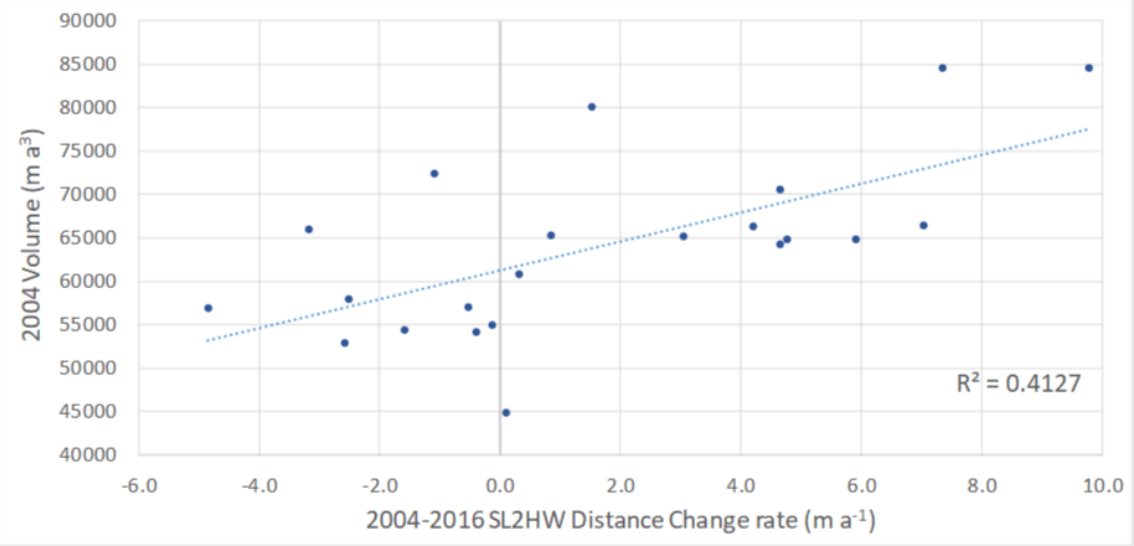

Figure 6.9: Relationship between the 2004 volume and the 2004-2016 SL2HW distance change rate.

The 2004 to 2016 volume loss rate exhibits significant correlations with both the 2004 to 2016 SL2HW distance change rate (+0.55) and the 2016 SL2HW distance (+0.81, Figure 6.10A). This relationship also remains for 2016 to 2018, as the volume loss displays a weak but significant correlation with the 2016 to 2018 SL2HW distance change rate and the 2018 SL2HW distance (Figure 6.10B), +0.46 and +0.49, respectively. Large rates of volume loss imply an inland extension of the slump headwall concurrent with a transfer of material towards the shoreline. This leads to a significantly larger SL2HW distance, even over the shorter 2016 to 2018 timeframe. In this instance for example, for every additional 100 $m^3 a^{-1}$ lost from 2004 to 2016, the 2016 SL2HW distance was 5.9 m wider.

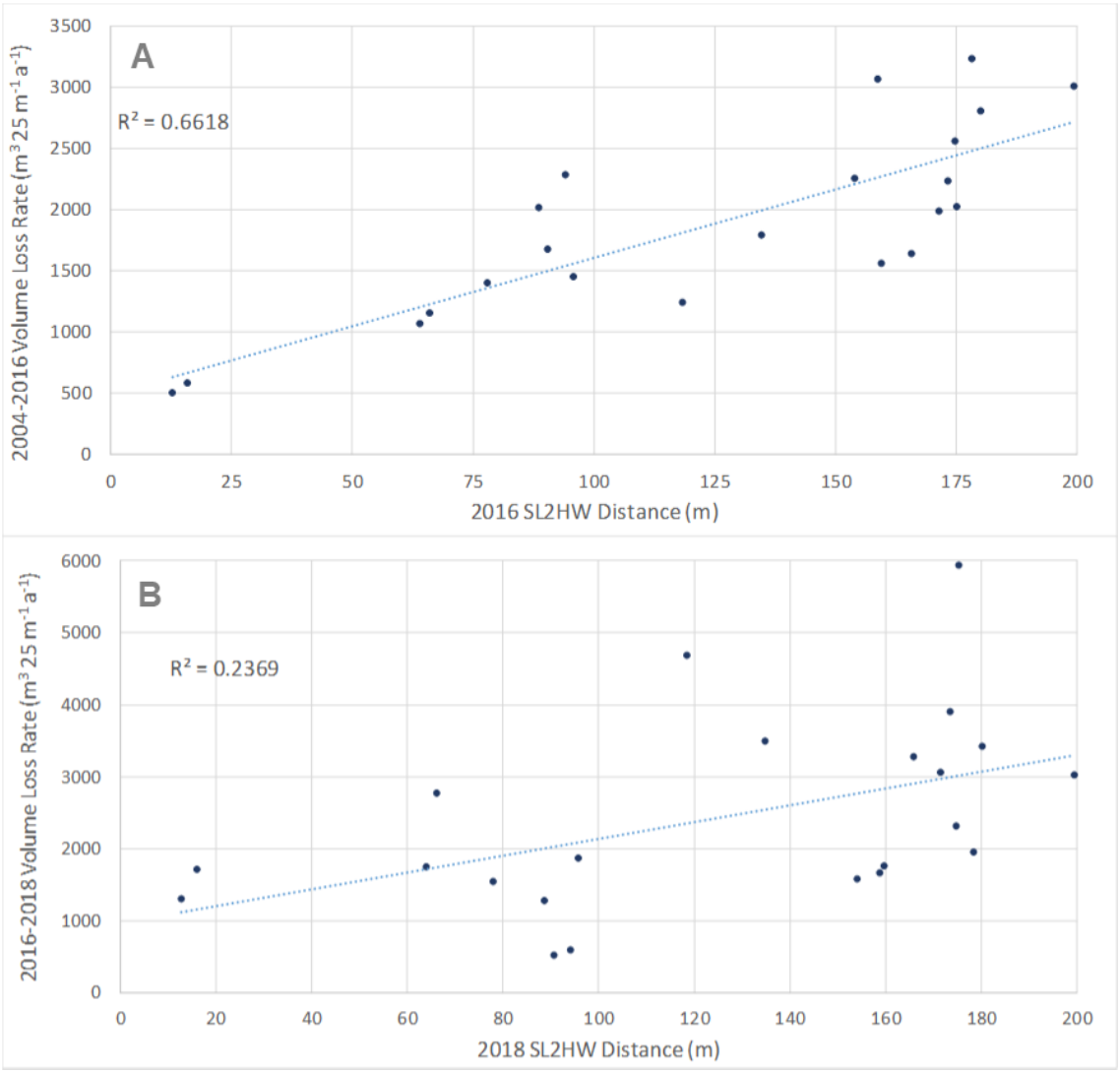

Figure 6.10: Relationship between the 2004-2016 volume loss rate at 2016 SL2HW distance (A) and the 2016-2018 volume loss rate at 2018 SL2HW distance (B)

6.2.7 Summary: Coastal Change Metrics

The SL2HW distance metric appears to produce the most consistent relationship with all other metrics and over all timeframes considered. The SL2HW distance can be representative of several processes at once. Where the distance is close to its maximum it is likely to represent a large polycyclic RTS and an area with substantial volume change. Expansion of the SL2HW distance is governed by the relative rates of SLR and HWR, which appear to change drastically in the short-term monitoring period compared to the longer periods assessed. The cause of this will be explored in section 6.5.

There were no significant correlations found between SLR and HWR over any time considered, which is unexpected. It could be assumed that where HWR is greater, then SLR would be slower due to the shoreward transport of material, but this does not

appear to be the case. The extension of the headwall into low volume regions may not exert a measurable influence on SLR, while lateral transport of thawed headwall material can also complicate the relationship.

Volume and volume loss correlated poorly with SLR overall, with the only significant correlation occurring between the short-term rates of change. This is likely related to the transient shoreline variability produced by volume transport, such as prograding mud lobes and rapid removal of former mud lobes. This lack of a significant relationship over longer timeframes has important implications. The average volume for 2004, measured an average of 240 m inland, was 1,409,416 m^3. This was reduced by 43% by 2018, down to 805,144 m^3. During the same time, the shoreline retreated an average of 36.2 m, representing a 15.1% loss of the 240 m volume measurement distance. This highlights the difficulty in estimating volume changes from planimetric measurements along RTS dominated coasts.

Volume and HWR display a more consistent connection, with significant positive correlations between both the 2004 volume and the 2004 to 2016 volume loss, and the 2004 to 2016 HWR rate. Where volume was largest, HWR tended to be faster, likely due to transects with larger volumes being unlikely to have undergone the mass wasting associated with inland headwall extension. As such, they have a narrower SL2HW distance, and the headwall can extend into these areas faster than areas where it is already closer to 200 m from the shoreline.

Volume and SL2HW distance appeared most closely connected. Areas that both started with a larger volume and those that experienced the largest volume loss also underwent greater increases in the SL2HW distance. Mass loss in RTS coastlines can often be a proxy for HWR (Lantuit *et al.,* 2005; Obu *et al.,* 2016). At the same time as the HWR and volume change, mass can also be transported towards the shoreline, altering the SL2HW distance.

Finally, no significant autocorrelation was recorded among the metrics, aside from the SLR. The strongest predictor of the 2004 to 2016 SLR rates (average of 2.2 m a^{-1}) are the 1994 to 2004 SLR rates (average of 3.9 m a^{-1}), with a correlation coefficient of -0.83 (Figure 6.11). This indicates that areas with the fastest rates of retreat between 1994 and 2004 had slower rates between 2004 and 2016, and vice versa. The relationship represents a 0.6 m a^{-1} drop in the 2004 to 2016 SLR rate for every 1.0 m a^{-1} increase in the 1994 to 2004 SLR rate. The reason for the shift is not immediately apparent, but a clear reversal of the pattern in retreat rates is visible, especially in the western half of the transects (Figure 6.12). This may be cyclic pattern, related to similar factors that

also caused a broad pattern reversal between 1935 to 1985, and 1985 to 2018 (section 5.3.2.1.3). Potential causes of this reversal will be explored later in section 6.5.

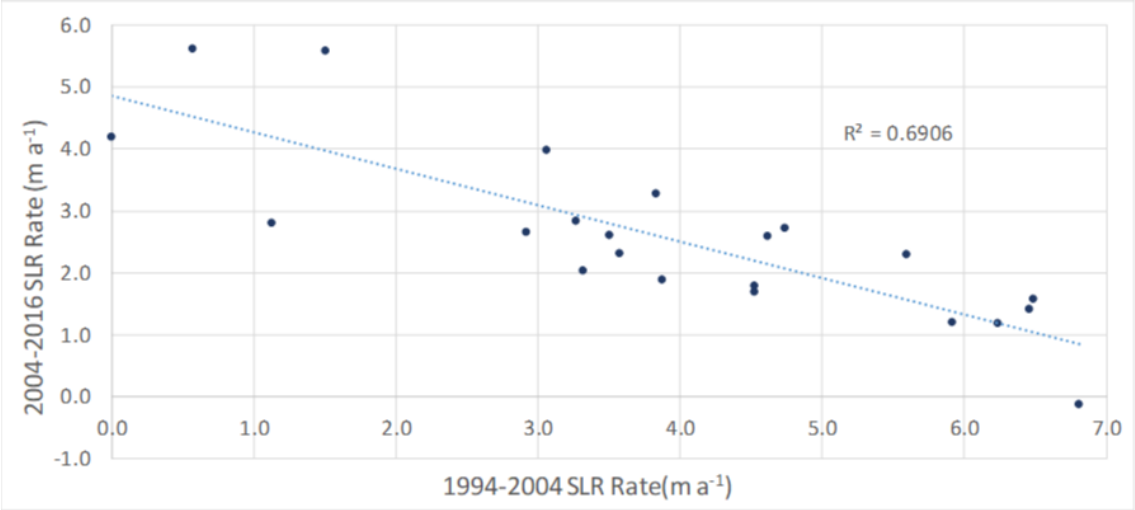

Figure 6.11: 1994-2004 vs 2004-2016 shoreline retreat rates on Peninsula Point

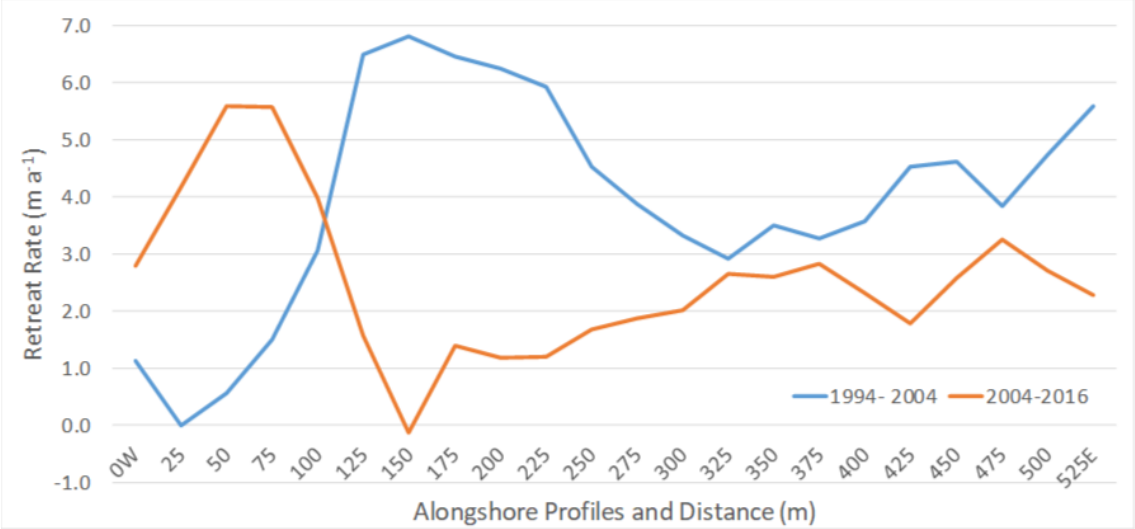

Figure 6.12: Along-shore retreat rates on Peninsula Point, comparison between 1994-2004 and 2004-2016

6.3 Climate Data

6.3.1 Methods and Data

Monthly average temperature data from 1935 to 2014, the most recent available, was acquired from the 20th Century Reanalysis (2CR) V2c project (Compo *et al.,* 2011). Coordinates used were 69.5 to 70N and 226.5 to 227.5E, and the "2 m Air Temperature" variable was selected. The data were downloaded as a text table and added to excel for further analysis. Weather station data were also downloaded for Tuktoyaktuk (Climate and Environments Canada https://climate.weather.gc.ca/historical_data/search_historic_data_e.html, 2019) in

order to compare the trends and variability to ensure the reanalysis data were suitable. The weather station data came from a range of data sets, covering multiple time intervals between 1949 and 2014, and at a range of measurement intervals. Some of the data were provided in the form of monthly averages, but where gaps were present in the daily data, then only daily data were provided. Linear interpolation was used to fill in gaps of one to five days. Where gaps were longer than five days, the averages from the surrounding 10 years were used (maximum of 12 days). As these small gaps had little influence on the average monthly values and would only be used to ensure the long-term trends and variability in the reanalysis data were suitable, these simple gap filling methods were sufficient to create a useful comparative dataset.

The correlation between the 2CR and weather station data for the May to September average temperature, from the overlapping period of 1950 to 2014, was 0.84 ($p < .05$), with an offset of 1.1°C. The correlation coefficients ranged +0.77 in May to +0.92 in August, with the 2CR temperatures ranging from 3.1°C warmer in June to 0.5°C cooler in August and September (Details of the other months can be found in Table 6.2). This makes the longer and more consistent 2CR data appear suitable for long-term trend and variability analysis.

Table 6.2: Correlation coefficients between the station and 2CR temperatures and the temperature offset of the 2CR compared to the station temperatures

Month	May	June	July	August	September	May-Sept
ρ	0.77	0.79	0.80	0.92	0.90	0.87
Offset	+2.5°C	+3.1°C	+0.7°C	-0.5°C	-0.5°C	1.1°C

Monthly average meridional wind values were also sourced from the 2CR. Surface level winds were not available, so 1,000mb level was used. Once more, data were acquired for the 1935 to 2014 timeframe. Meridional winds have a positive value when primarily southerly in direction and negative values when primarily northerly, with the anomaly values (in m s^{-1}) representing the relative strength of the wind directions. On Peninsula Point, northerly winds are onshore and promote coastal inundation, and southerly winds are offshore and encourage low water levels. As wind speed and direction information was not available from the weather station data, the 2CR values are assumed to be accurate enough for the long-term trend analysis. As the north facing coast of Peninsula Point is the focus of study, meridional winds may play a role in the frequency of coastal inundation, and thus erosion and transportation of eroded material. As such, with its potential role as an external control for coastal change, it was included in the analysis.

6.3.2 Thaw Season Temperature Trends

Based on the 2CR, the thaw season average temperature at Peninsula Point has increased at a rate of 0.43°C per decade, from an average of 4.4°C between 1935 and 1964, to 6.6°C between 1985 and 2014. However, the rate of increase has dropped, from +0.62°C per decade in the first half of the record, to +0.27°C per decade in the second half. The pattern of accelerated warming in the first half of the record and slower warming in the second half are repeated throughout all other months except May. Two of the three coldest Mays were measured in 1978 and 1983, contributing to a faster warming rate in the latter half of the record. Both the temperature and SLR rates are presented in Figure 6.13. SLR is represented in terms of annual rates, with resolution much lower earlier in the record than later, but still suitable for long-term trend analysis. SLR exhibits a pattern of variable, but reduced retreat rates over time. Thaw season temperatures are represented as yearly values, and an average that matches the temporal resolution of the SLR data.

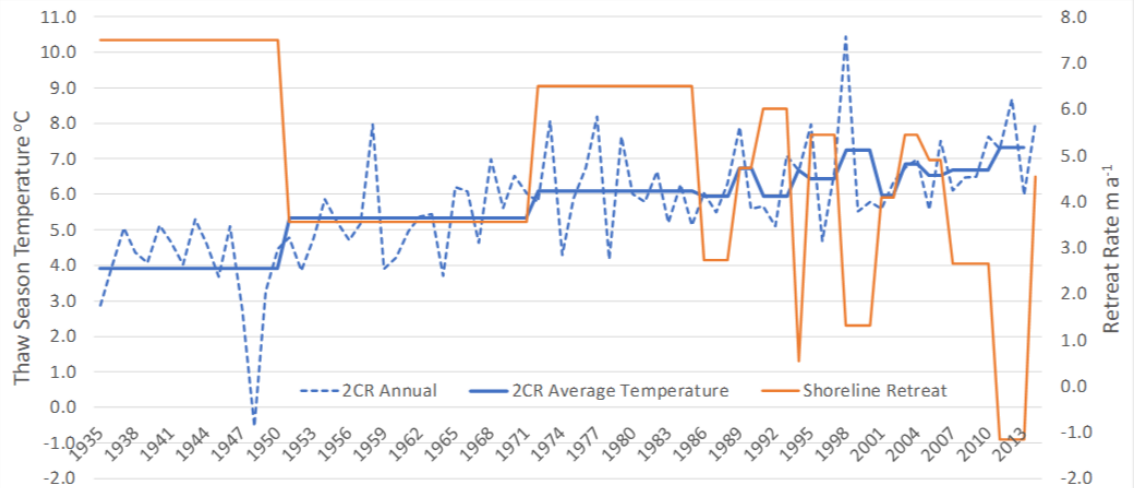

Figure 6.13: Shoreline retreat rates and May to September average surface air temperatures, both annual and averaged to match the retreat rate periods, from 1935 to 2014 for Peninsula Point.

All thaw season months have displayed a warming trend (Appendix 3), which contrasts with the expectation that Arctic warming, and related Arctic Amplification (Serreze and Francis, 2006) should act to increase SLR rates (Forbes, 2011; Jones *et al.,* 2009). However, this may support the studies that suggest an increase in SLR variability in response to warming, although these features have only observed to occur on sub decadal scales, not exerting an influence on multi-decadal trends (Farquharson *et al.,* 2018; Gibbs *et al.,* 2011). As such, the evidence suggests that thaw season temperature trends are not driving the long-term rates of SLR on Peninsula Point.

6.3.3 Thaw Season Meridional Wind Trends

Thaw season meridional winds have displayed a positive trend between 1935 and 2014, increasing at a rate of +0.08 m s^{-1} per decade. However, the wind direction remains predominantly negative (northerly) overall but has weakened from a thaw season average of -1.14 m s^{-1} between 1935 and 1964, to -0.73 m s^{-1} between 1985 and 2014. Both SLR rates and meridional winds are presented in Figure 6.14. Thaw season meridional winds are represented as yearly values, and an average that matches the temporal resolution of the SLR data. The datasets once more display opposing trends. In this instance, a weakening of the dominant northerly winds during the thaw season may reduce the frequency of coastal inundation and thus the removal and transportation of thawed material. Overtime, this may play a role in slowing SLR rates. However, the trend towards more negative value (northerlies) after 1975, during which time SLR rates dropped, means that meridional wind trends are unlikely to act as a significant driver of coastal change

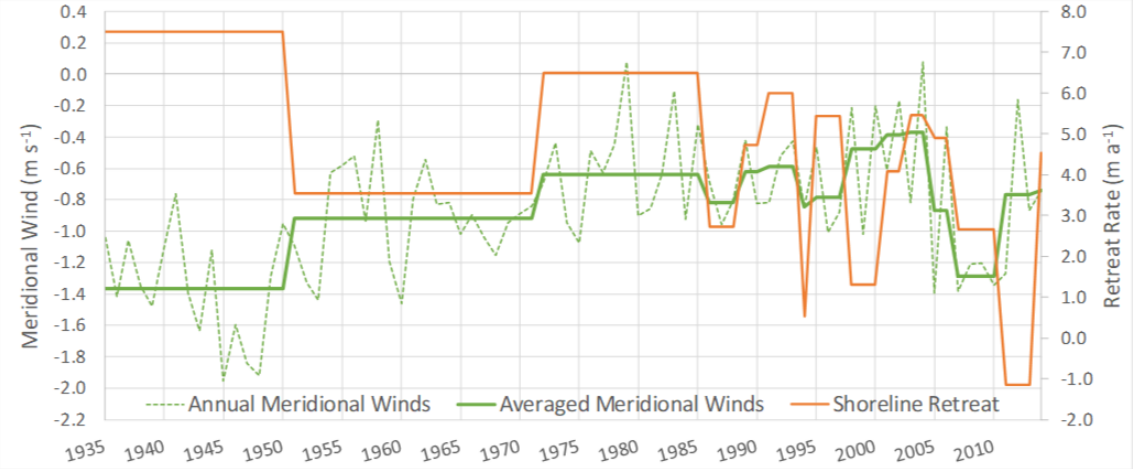

Figure 6.14: Shoreline retreat rates and May to September average meridional temperatures, both annual and averaged to match the retreat rate periods, from 1935 to 2014 for Peninsula Point.

The pattern observed for meridional winds in the thaw season is broadly repeated in the individual months (Appendix 3). Each month displays a positive trend of between 0.12 m s^{-1} and 0.05 m s^{-1} per decade. Despite the positive trends, climatological averages remain negative indicating a continued, though weakening, dominance of northerly winds. As with the temperature record, every month has observed a reduction in the positive trend, or a partial reversal of the trend, in the latter half of the record. Table 6.3 shows these trends, including how four of the five months have seen the meridional wind trend turn negative after 1975, but not enough to negate the long-term positive trend.

Table 6.3: Rate of change of meridional winds for the first half (1935-1975), second half (1975-2014) and full 1935-2014 period in m s^{-1} per decade.

Period	May	June	July	August	September	Average
First Half	+0.26	+0.16	+0.36	+0.06	+0.02	+0.17
Second Half	+0.07	-0.20	-0.04	-0.15	-0.09	-0.08
All	+0.12	+0.09	+0.07	+0.05	+0.08	+0.08

6.3.4 Climate Controls on SLR

Despite an overall positive trend in thaw season temperatures between 1935 and 2014 (with a slower trend after 1975), SLR rates have slowed over Peninsula Point. Two possible causes may help to explain some of this trend. First, the increase in air temperatures may result in a deepened active layer and greater RTS activity. This may have increased the volume of material flowing towards the shoreline. Secondly, despite a partial reversal after 1975, there has been a tendency for meridional winds to become more positive in the long-term. This may reduce the frequency of coastal inundation, hindering the removal and transportation of thawed sediment, further contributing to a reduced rate of SLR. However, detailed analysis of both temperature and meridional winds reveal disparities with the response of SLR over time. For example, between 1971 and 1985, SLR increased relative to the 1950 to 1971 period. This occurred despite meridional winds becoming less negative (i.e., more southerly) during the same period. Similarly, despite a strong trend towards more northerly winds after 2005, SLR rates continued be slower than the long-term averages. While higher temperatures can result in increased variability in short-term shoreline retreat, previous research suggests increased temperatures contribute to faster SLR rates over multi-decadal timescales (Forbes, 2011; Jones, *et al.,* 2009a; Mars and Houseknecht, 2007; Pizhankova, 2016). As such, other factors clearly must play a more dominant role in governing SLR rates on Peninsula Point.

6.4 Topographic Controls

As several studies have noted the importance of terrain variability on coastal evolution (Ramage *et al.,* 2017; Vasiliev, 2003), the following sections will explore the role of topography as a control on coastal change on Peninsula Point using average and maximum elevation values and the slope gradient. These will include both the absolute topographic values in 2004, 2016 and 2018, and the changes between those years too.

6.4.1 Topographic Controls on SLR

6.4.1.1 SLR and Elevation

For both the 2004 to 2016 and 2016 to 2018 periods, the starting average elevation is significantly correlated with the respective rates of SLR. This is also true of the maximum elevation values for the same periods (Table 6.4). This relationship suggests that the higher elevation transects tend to result in a much slower rate of shoreline retreat. For example, the correlation with the 2004 150 m average elevation indicates that from every additional 1 m in elevation, the 2004 to 2016 SLR rate drops by 0.3 m a^{-1}. The broad relationship with elevation is apparent in the short-term correlations too, though it is much weaker and less consistent among the different elevation measures. High elevation coastlines are typically observed to display slower rates of SLR, as the large volume of permafrost requires more energy and time to erode. As such, these results fit broadly with expectations.

Table 6.4: The correlations between the starting average and maximum elevation values, and the rates of SLR, for the 2004-2016 and 2016-2018 periods. Significant values are in bold

Control	2004 to 2016	2016 to 2018
2004 (2016) Average 150 m Elevation	**-0.73**	**(-0.46)**
2004 (2016) Average 100 m Elevation	**-0.66**	**(-0.51)**
2004 (2016) Average 70 m Elevation	**-0.60**	**(-0.48)**
2004 (2016) Average 50 m Elevation	**-0.54**	(-0.29)
2004 (2016) Average 30 m Elevation	**-0.50**	(-0.36)
2004 (2016) Maximum 150 m Elevation	**-0.71**	(-0.35)
2004 (2016) Maximum 100 m Elevation	**-0.74**	(-0.26)
2004 (2016) Maximum 70 m Elevation	**-0.63**	**(-0.50)**
2004 (2016) Maximum 50 m Elevation	**-0.49**	(-0.39)
2004 (2016) Maximum 30 m Elevation	**-0.46**	(-0.09)

The connection between elevation and SLR continues when examining the rates of elevation change also. With the 2004 to 2016 elevation, both the average and maximum elevation changes along the 150 m, 100 m and 70 m distances all correlated significantly. The 150 m average elevation changes displayed the strongest correlation, at +0.77 (Figure 6.15), meaning for every additional metre of elevation dropped between 2004 and 2016, the SLR rate was reduced by 0.4 m a^{-1}. This makes sense since a lowering of the elevation is often associated with RTS activity and a transfer of mass towards the shoreline, slowing SLR.

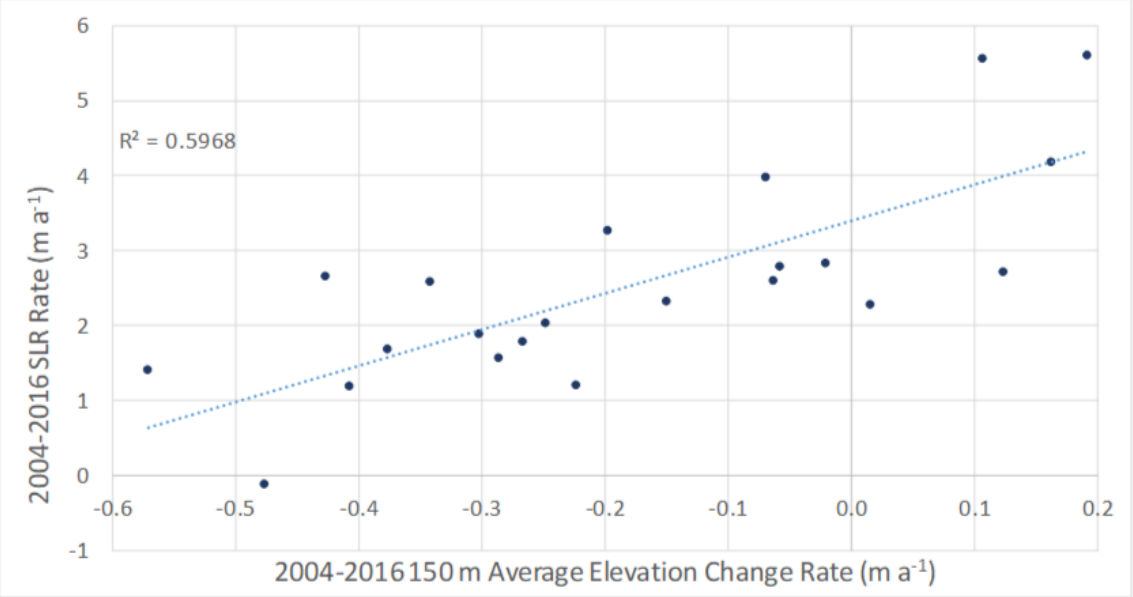

Figure 6.15: 2004-2016 shoreline retreat rate vs 2004-2016 elevation change averaged 150 m inland.

The rate of elevation change maintains a strong connection to SLR for the 2016 to 2018 periods also, with numerous highly significant correlations, as seen in Table 6.5. The strongest, the 100 m average elevation change, is shown in Figure 6.16. Here, for every additional metre dropped, the 2016 to 2018 SLR rate was reduced by 4.5 m a^{-1}. The only exception occurs with the 150 m maximum elevation change, which does not produce a significant correlation. The reason for this is not immediately apparent.

Table 6.5: Correlation coefficients between the 2016-2018 SLR rate and the rate of change in average and maximum elevation. Significant correlations are in bold.

Elevation Distance	Average Elevation	Maximum Elevation
150 m	**+0.84**	+0.21
100 m	**+0.85**	**+0.49**
70 m	**+0.84**	**+0.70**
50 m	**+0.73**	**+0.73**
30 m	**+0.73**	**+0.57**

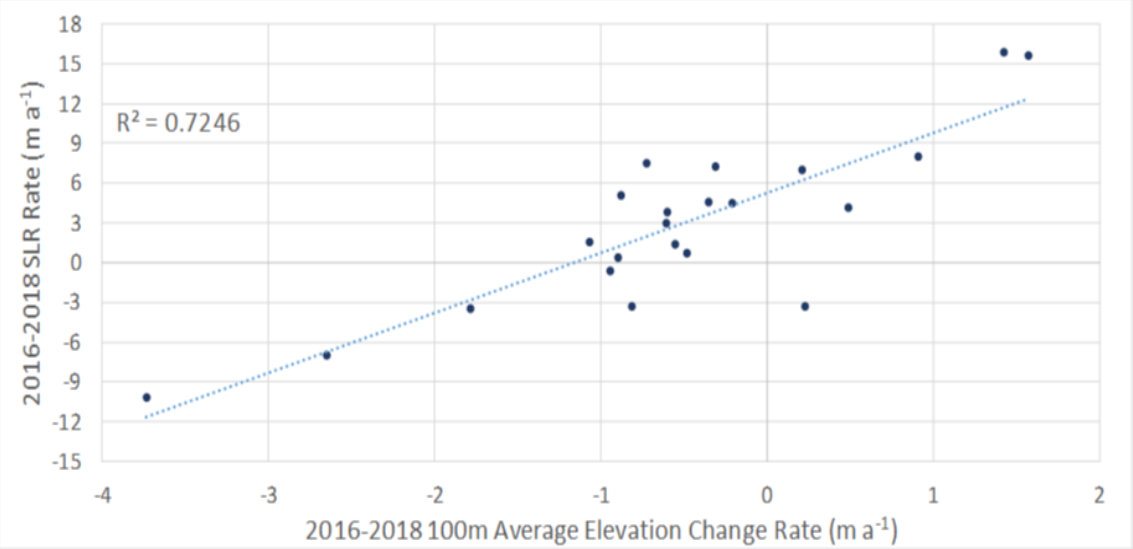

Figure 6.16: Relationship between the 2016 to 2018 SLR rate and the change in the 100m average elevation.

6.4.1.2 SLR and Slope

For the 2004 to 2016 period, the starting slope gradient and the change in slope gradient are significantly correlated with SLR rates. Where the starting slope angle is greatest, the proceeding rate of SLR is slowest. As the slope angle and the average elevation are closely related (r^2 of 0.66 for average elevation and corresponding slope angle in 2004), the processes relating them to SLR are likely similar. This is clear on the slope changes also, where the areas with the least change in slope angle experienced the highest levels of SLR. This relationship appears to break down when comparing with the 2016 to 2018 data, where none of the 2016 slope angles correlate well with the 2016 to 2018 SLR rates. In fact, the relationship between the 150 m average slope angle change and the SLR for 2004 to 2016 reverses for the 2016 to 2018 period, from +0.49 to -0.71. This highlights the complex and time variable relationship between coastal topography and retreat rates (Table 6.6).

Table 6.6: The correlations between the starting slope gradients and their rates of change, and the corresponding SLR rates for the 2004-2016 and 2016-2018 periods. Significant values are in bold

Control	2004-2016	2016-2018
2004 (2016) Slope Angle Average 150 m	**-0.62**	-0.03
2004 (2016) Slope Angle Average 100 m	**-0.67**	-0.25
2004 (2016) Slope Angle Average 70 m	**-0.51**	-0.38
2004 (2016) Slope Angle Average 50 m	-0.41	+0.06
2004 (2016) Slope Angle Average 30 m	**-0.49**	+0.09
Average Slope Angle Difference 150 m 04-16 (16-18)	**+0.49**	**-0.71**
Average Slope Angle Difference 100 m 04-16 (16-18)	**+0.62**	+0.40
Average Slope Angle Difference 70 m 04-16 (16-18)	**+0.44**	**+0.66**
Average Slope Angle Difference 50 m 04-16 (16-18)	+0.23	**+0.47**
Average Slope Angle Difference 300 m 04-16 (16-18)	+0.31	+0.42

6.4.2 Topographic Controls on HWR

While there are more limitations with assessing controls on HWR, such as the influence of short-lived HWR phases on PRTS that occur within the measurement years, it may be possible to still draw some conclusions.

6.4.2.1 HWR and Elevation

For the 1994 to 2004 period, many of the average and maximum elevation values in 2004 displayed a strong correlation with the preceding HWR rates. The average elevation values of 150 m, 100 m and 70 m produced significant correlations from +0.49 to +0.59, and the maximum elevation along 150 m, 100 m and 70 m from +0.57 to +0.61. These indicate that where elevations were higher in 2004, the preceding HWR rates from 1994 tended to be faster. This relationship is not apparent in 2004 to 2016 or 2016 to 2018, where none of the elevation values correlate significantly with their preceding HWR rates. There is no immediate evidence or reasoning that can explain the change.

The 2004 to 2016 HWR rate produced a few significant, but weak, correlations with elevation. The average 2004 elevation at 70 m and 50 m both produced correlations of +0.46, while the maximum elevation at 50 m (Figure 6.17) and 30 m were +0.60 and +0.53, respectively. There were also significant correlations with the change in 50 m average and both 50m and 30 m maximum elevations (from -0.47 to -0.53). The change relationship suggests that where the elevation reductions are largest, HWR is faster. The Figure 6.17 scatter plot shows that the relationship is neither strong nor

linear. The two outlier points, with both high elevation and HWR, dominate the relationship. When both are removed, the correlation coefficient drops to +0.23. This also applies to all the other correlations within this period, where removal of the two outlier points breaks the relationship with HWR.

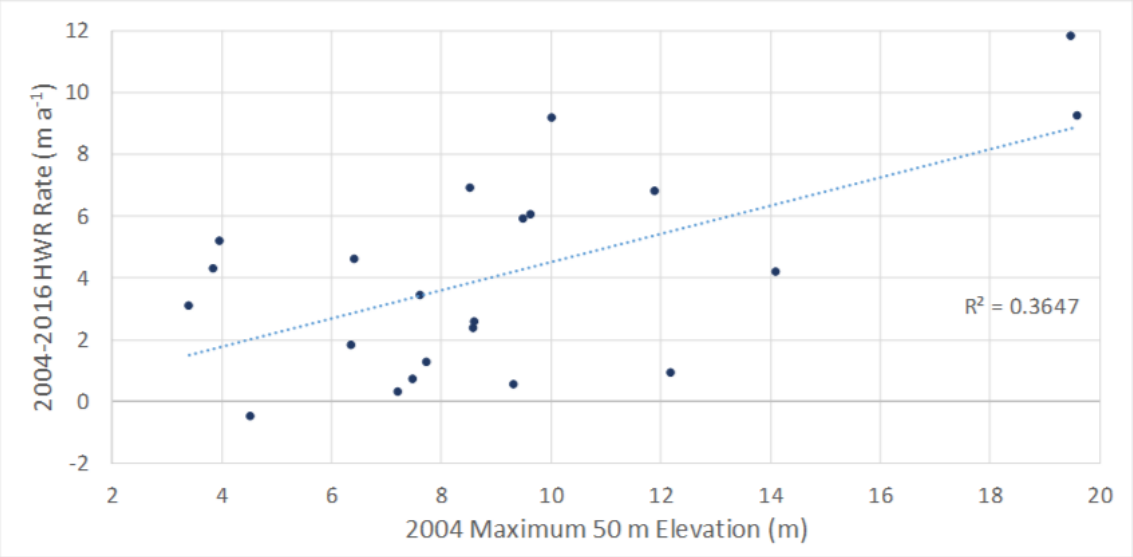

Figure 6.17: Relationship between the 2004-2016 HWR rate and the 2004 maximum elevation 50 m inland of the shoreline.

For the 2016 to 2018 period, none of the elevation values produce any significant correlations. This further highlights the lack of a strong connection between the two variables after 2004.

6.4.2.2 HWR and Slope

The relationship between HWR and slope follows much the same pattern as with elevation. The 2004 slope values along 150 m, 100 m and 70 m produced correlations of +0.47, +0.61 and +0.47, respectively, with the 1994 to 2004 HWR. For the 2004 to 2016 period, there were significant correlations with the 2004 slope angle along 50 m (+0.48) and 70 m (+0.62), and the slope angle change along 50 m (-0.65, Figure 6.18). This suggests that where the slope angle was greatest in 2004, the subsequent HWR rate was also fastest. Similarly, where the slope angle was reduced most, the corresponding HWR rates were also typically faster. Their influence on HWR may be related to the steeper slope allowing for more efficient transport and removal of thawed material from the headwall and slump floor. This transport of material increases the likelihood of massive ice remaining exposed, continuing to ablate and HWR being maintained. However, the 2016 to 2018 HWR rate exhibits a weak, but significant, relationship with two values, the 50 m slope angle in 2016 (-0.46) and the 70 m slope angle in 2018 (-0.49). Here, it appears that where the slope angle was greatest in

2016, the HWR was slower – the opposite of the 2004 to 2016 period. It also suggests that where the slope angle was greatest in 2018, the preceding HWR rate was slower, the opposite to the relationship between the 2004 slope angle the 1994 to 2004 HWR rate. As such, it appears there is little consistency between the slope angle and HWR rates.

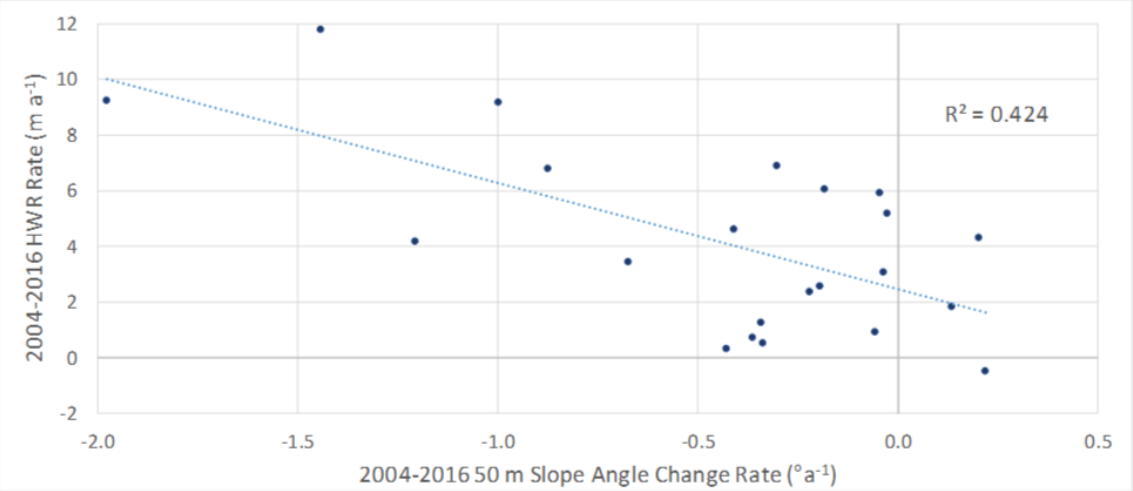

Figure 6.18: Relationship between the 2014-2016 HWR rate and the 50 m slope angle change rate

6.4.3 Topographic Controls on Volume Change

6.4.3.1 Volume and Elevation

For 2004 to 2016, none of the 2004 elevation values appear to offer any guidance to the proceeding volume loss. One value from 2016 showed a weak, but significant, correlation, the 150 m average elevation (-0.44, Figure 6.19). A similar, but weaker, correlation is found with the other 2016 elevation values too, from -0.39 to -0.41. This consistency suggests a genuine, but weak connection with volume loss — where elevation was higher in 2016, the preceding volume loss was lower. This can be explained by the fact that areas of higher average elevation are less likely to have experienced large degrees of mass wasting, such as through RTSs, and thus will likely have experienced slower rates of volume loss in the preceding years. Figure 6.19 reveals that the relationship is not linear, with some high elevation points also experiencing high volume losses.

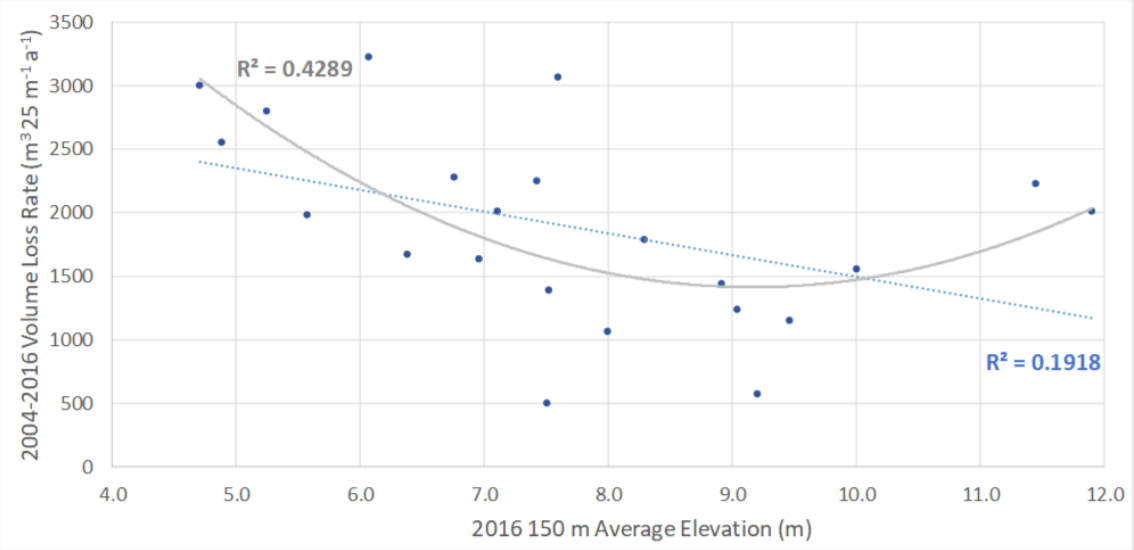

Figure 6.19: Relationship between the 2004-2016 volume loss and the 2016 elevation averaged 150 m inland

The 2004 to 2016 change in average (maximum) elevation produces significant correlations with volume loss along the 150 m, 100 m and 70 m measurement intervals, of -0.70 (-0.75, Figure 6.20), -0.54 (-0.64) and -0.44 (-0.45). Where elevation dropped the fastest beyond 70 m inland, the volume losses were greater.

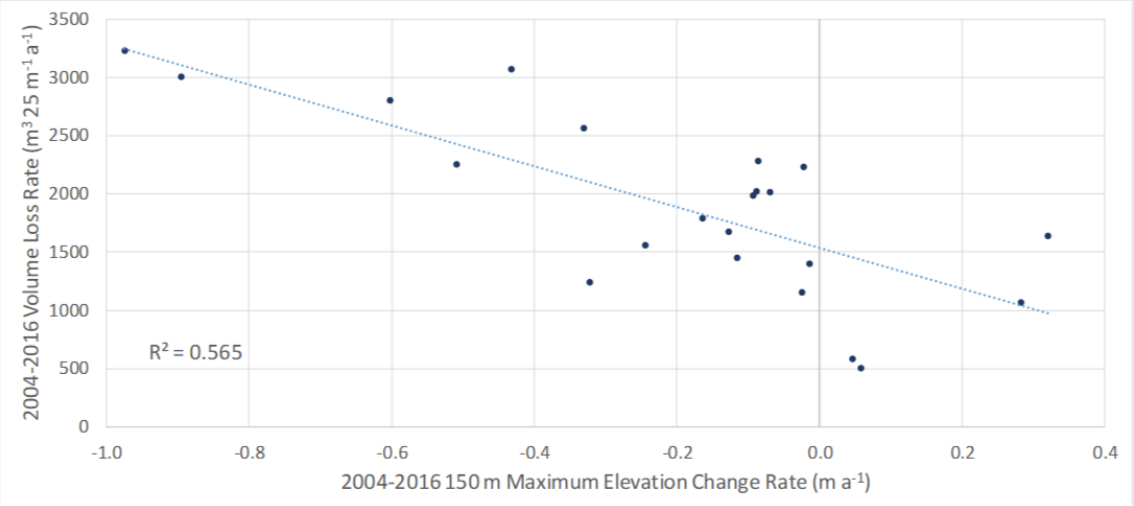

Figure 6.20: Relationship between the volume loss rate and the 150 m maximum elevation change rate for 2004-2016

For 2016 to 2018, one value each from the 2016 average elevation (100 m, +0.49) and 2016 maximum elevation (70 m, +0.63) have significant correlations with the rate of volume loss. This indicates that where the elevation was highest along those specific intervals, the volume loss rate was greatest. The other elevation correlations are weak and variable, which casts doubt on the utility of elevation for predicting short-term volume losses. Correlations with the 2018 elevations values were also poor, with only the 30 m (-0.53) and 50 m (-0.48) averages and the 30 m (-0.44) maximum elevation

being significant. These suggest that where the elevation within 50 m of the shoreline was higher in 2018, the preceding volume loss was smaller.

Many of the 2016 to 2018 changes in elevations produced significant correlations with the volume loss (Table 6.7). The contrast between the relatively strong correlations with average values along 150 m (Figure 6.21) and 100 m and the lack of any significant correlation with the corresponding maximum values is perplexing, with no immediate explanation apparent. However, the overall pattern suggests that transects where the elevation reductions were largest from 2016 to 2018 also tended to produce the fastest rates of volume loss.

Table 6.7: Correlation coefficients between the 2016-2018 volume loss rate and the average and maximum elevation change. Bold values are statistically significant.

Measurement Distance	Average	Maximum
150 m	**-0.70**	+0.05
100 m	**-0.69**	-0.33
70 m	**-0.64**	**-0.62**
50 m	**-0.47**	**-0.68**
30 m	-0.40	-0.34

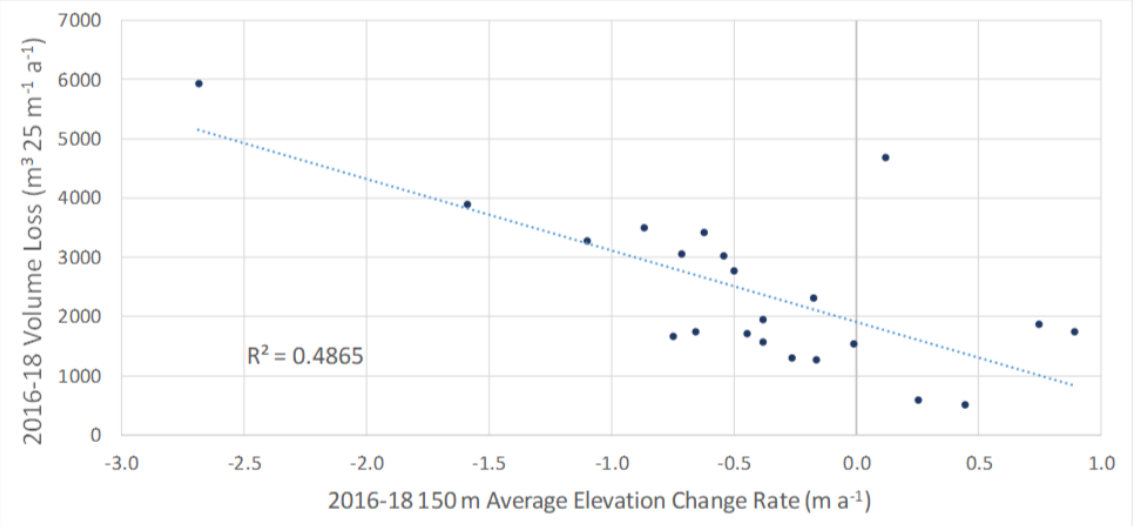

Figure 6.21: Relationship between the change in volume and 150 m average elevation from 2016-2018

6.4.3.2 Volume and Slope

For 2004 to 2016, only the 2004 150 m slope angle (+0.53, Figure 6.22) and the and the change in the 150 m (-0.54) and 100 m (-0.48) slope angle correlated significantly with volume loss. Much like elevation, where the slope angle in 2004 was steepest, and where the slope angle was reduced the most, the volume losses were greater.

Additionally, none of the 2016 slope values displayed significant relationships with the 2004 to 2016 volume loss.

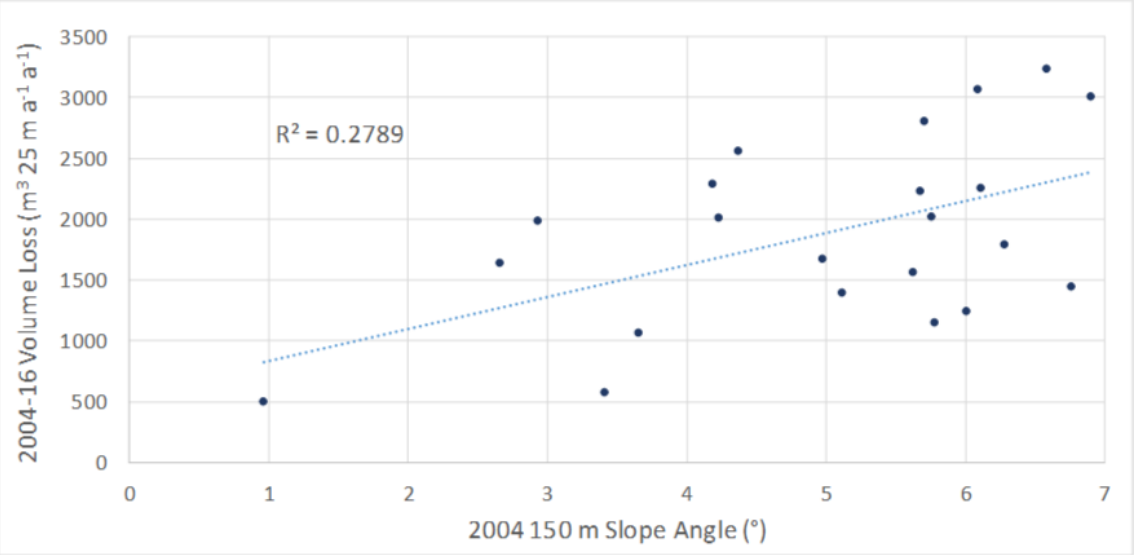

Figure 6.22: Relationship between the 2004-2016 volume loss rate and the 2004 slope angle averaged 150 m inland

For the 2016 to 2018 period, both the 100 m and 70 m slope angles in 2016 correlate significantly with volume loss, at +0.47 and +0.66, respectively. However, the connection between the rate of slope change and volume is puzzling. Significant relationships are found with the 150 m, 100 m and 70 m slope angle change. Both the 100 m and 70 m values produce negative correlations of -0.47 and -0.67 (Figure 6.23A), respectively, but the 150 m slope change produces a correlation of +0.46 (Figure 6.23B). This suggests that where the slope angle was most reduced along the 70 m and 100 m distances, volume loss tended to be greater. The opposite trend is apparent with the 150 m slope angle, where a greater reduction is associated with less mass loss.

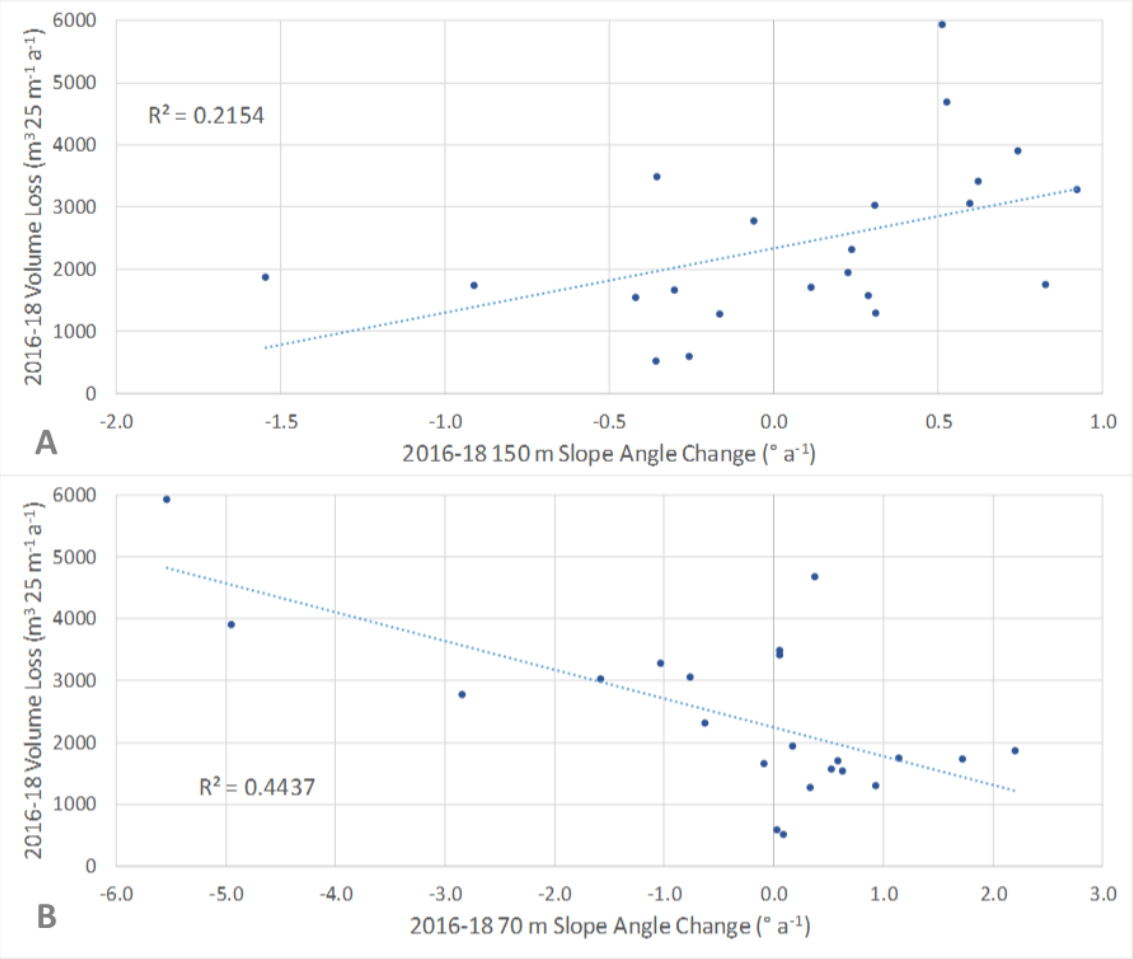

Figure 6.23: Relationship between the 2016-2018 volume change rate and the (A) 150 m slope angle change and (B) the 70 m slope angle change

6.4.4 Topographic Controls on Coastal Change: Overall

Elevation and slope angle appear to influence the response of the three analysed processes. The significant correlations make intuitive sense, bar one notable exception. With SLR, areas with higher elevations and steep slopes have typically experienced slower proceeding retreat rates. The measurement distances over which the elevation and slope values generate significant correlations with SLR depend on the timeframe used; longer distances (like 150 m) are more effective with longer timeframes, while shorter measurement distances correlate better with narrow timeframes, but the relationships generally hold up and make sense. This is also true with changes in elevation and slope — large reductions in elevation and slope result in slower shoreline retreat, likely due to the transfer of mass seaward, acting as a buffer. This relationship is borne out in volume changes too, as reductions in elevation and slope are strongly associated with variations in volume loss. However, when using the 2018 150 m slope value and looking at the SLR and volume rates from 2016 to 2018,

the correlation reverses. What contributed to this reversal? This element will be analysed further in section 6.5.

Elevation and slope are very weakly linked with HWR. Where they are greater, there is a very slight tendency for the proceeding HWR rates to be faster. When looking in the opposing direction (what can elevation and slope now say about past HWR rates?) a split occurs in the relationship. In 2004, many of the slope and elevation values exhibited strong, negative correlations with the 1994 to 2004 HWR, yet none of the 2016 or 2018 values correlate with their preceding HWR rates. This may be related to the pattern reversal in elevation and slope from 2004 (section 5.4.1.2), when the centre of Peninsula Point had the highest elevation and slope values, to 2018, where the outer edges had greater or at least equal elevation and slope values. Understanding what drives these pattern shifts is another element that will require further exploration in the next section.

High elevation and steep slopes tended to promote slower SLR rates across all time spans measured. This would suggest that if the average elevation and slope values decreased overtime, then the SLR rate should increase. However, the evidence for this occurring on Peninsula Point is weak. This is another area that requires further assessment.

6.5 Massive Ice Body Controls

This section will assess the influence of massive ice thickness and surface elevation variability on the coastal evolution of Peninsula Point. To achieve this, massive ice variability will be considered over three timescales, short-term (one to three years), inter-decadal and historical (1935 to present). This will involve the use of the massive ice body surface model described in section 4.5, modern high-resolution observations of massive ice exposures and historical observations of massive ice described in published literature. In addition, this section will attempt to answer the questions which have arisen from the analysis in this chapter so far, which are summarised below.

1. Why does the HWR and SL2HW distance relationship break down during the 2016 to 2018 period?
2. Why did the correlation between the 150 m slope angle and other metrics reverse after 2016?
3. What drove the reversal in the pattern of elevation and slope across Peninsula Point between 2004 and 2018?

4. Why was there a reversal in the spatial pattern of SLR after 2004?
5. Why has the overall reduction in elevation and slope angle not resulted in increased SLR rates?

6.5.1 Short-Term Massive Ice Controls

6.5.1.1 Short-Term Massive Ice Controls Methods

To effectively analyse the influence of massive ice variability on short-term processes, active headwalls along the 2016, 2017 and 2018 SfM-MVS models have been measured for three metrics — massive ice thickness (IT), overburden (OB) thickness and the proportion of ice (PI). The headwalls digitised in this section are separate to those used in section 5.4.1.3, which followed the headwalls furthest from the shoreline in order to track changes over a longer time period. Here, the more active (seaward) headwalls with ice exposures are analysed.

The three metrics are represented by colour coded, digitised lines along the top of each headwall. This resulted in three coloured lines for each year and nine in total. The headwall positions across the three years have been used to assess each metrics influence on HWR rates and related features, such as shoreline variability and volume change. The categories used for each metric can be seen Table 6.8.

Table 6.8: Peninsula Point headwall metrics and values: Ice Thickness (IT), Overburden Thickness (OB) and Proportion of Ice (PI)

Feature	**1**	**2**	**3**	**4**	**5**	**6**	**7**
IT	None	0-2 m	2-4 m	4-6 m	6-8 m	8-10 m	>10 m
OB	None	0-2 m	2-4 m	4-6 m	6-8 m	8-10 m	>10 m
PI	None	0-15%	15-30%	30-45%	45-60%	60-75%	75-90%

The measurements were carried out using the profile analysis tool in QTM. Where massive ice was present, the lowest point on which the ice was exposed was considered the base of the headwall. For the top of the headwall, the ground surface above the vertical part of the headwall was used, to exclude the influence of any drooping overhangs. An example of the exposed IT measurements line for 2016 and additional detail on the other measurements on a small section is provided in Figure 6.24. The organisation of the metrics using grouped values made it easier to both categorise their variance along the headwall and analyse their potential influence. The colour coded categories for each metric then allowed for comparisons with retreat rates, while also ensuring measurement points could be generated for each metric value.

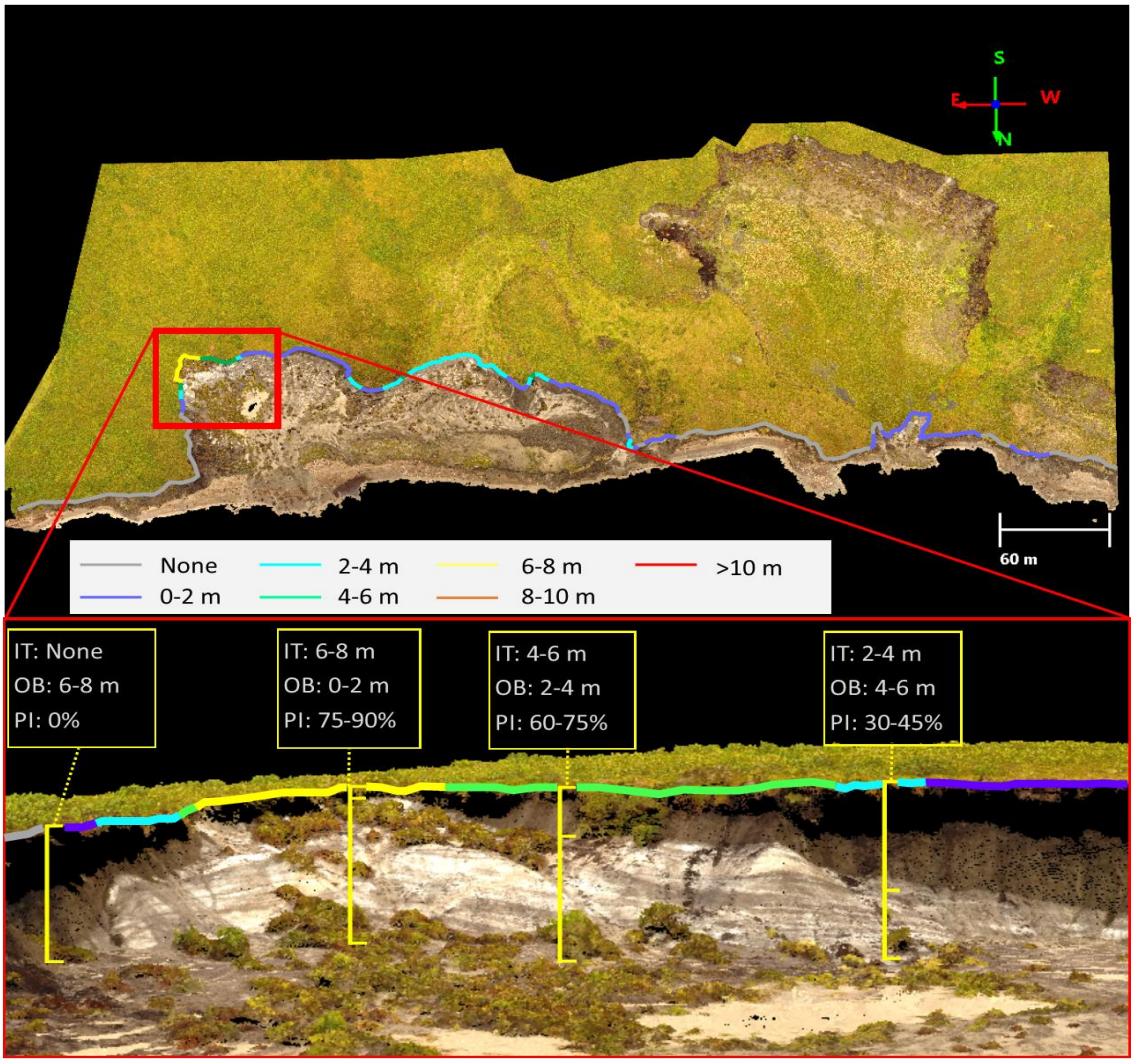

Figure 6.24: An example of the ice thickness (IT) colour coded line and the details of the on a small section where the metric values varied significantly

A total of 54 transects across the three headwall lines (Figure 6.25) were used. The transects positions are arranged to capture as much headwall constituent variability as possible based on the 2016 data, while still having a broad spatial coverage. This results in some clusters of transects in areas where the headwall constituents vary rapidly over short distances, and isolated transects where there is little variance in the headwall metrics. The number of measurements in each category also varied across the years as the proportions of ice and soil changed. The only categories that were not present in any year were 6 and 7 for IT, and 1 for OB thickness. The transects were further split into east, middle and west (Figure 6.25), with 25, 16 and 13 transects respectively. These categories align with the overall elevation variations of the headwalls, which are lowest to the west, highest in the middle and average in the east.

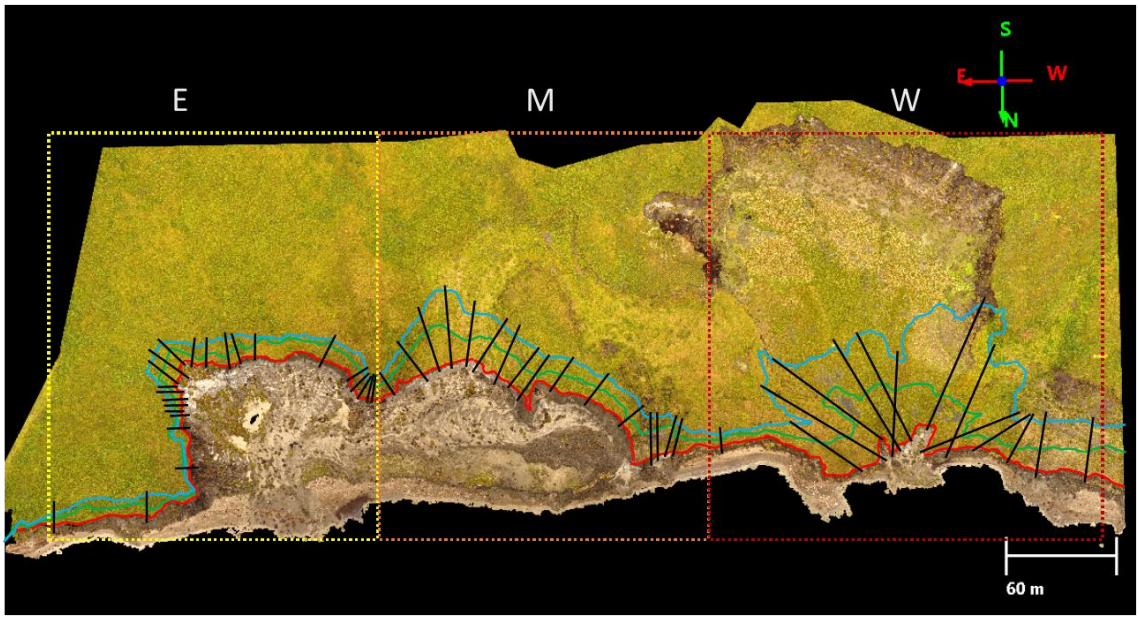

Figure 6.25: Measurement transects used for Peninsula Point headwall metrics, with separation into East (E), Middle (M) and West (W) transects

6.5.1.2 Short-Term Results

The number of observations for each category is shown in Table 6.9 and the full dataset is available in Appendix 3. There were significant changes across each of the metrics over the course of the three years. The number of measurements of massive ice thickness greater than 4 m dropped from eight (15%) in 2016, to four (7%) in 2017 and zero in 2018. For OB thickness greater than 4 m, the change was from 21 (39%), to 29 (54%) and 32 (59%) in 2018. This resulted in the number of headwall observations with a proportion of ice below 30% increasing from 28 (52%) in 2016, to 37 (69%) in 2017 and 41 (76%) in 2018. Using the middle value from each category, the average IT exposure dropped from 2.0 m in 2016 to 1.2 m in 2017 and 0.6 m in 2018, while the average OB thickness grew from 4.1 m in 2016 to 5.4 m in 2017, remaining at 5.4 m in 2018. This resulted in the average PI dropping from 31.7% in 2016, to 20.7% in 2017 and 14.4% in 2018.

Despite the large changes in ice and OB thickness, the average HWR remained relatively consistent, averaging 11.9 m from 2016 to 2017, and 11.4 m from 2017 to 2018. However, there are marked differences in the absolute values and trends in the three broad locational categories. Both the east and the middle recorded relatively slow HWR between 2016 and 2017, of 6.6 m and 11.8 m respectively, which then decreased to 4.1 m and 9.4 m respectively between 2017 and 2018. Conversely, from 2016 to 2017 the western headwall retreated by 22.1 m, increasing to 28.0 m for 2017 to 2018. The maximum HWR occurred here between 2016 and 2017, of 54 m, the

second largest retreat known, after a measurement of 79 m in the Canadian High Arctic (Jones *et al.,* 2019).

Metric	2016	Number	2017	Number	2018	Number
	None	10	None	23	None	36
	0-15%	9	0-15%	9	0-15%	1
	15-30%	9	15-30%	5	15-30%	4
PI	30-45%	8	30-45%	3	30-45%	5
	45-60%	9	45-60%	8	45-60%	3
	60-70%	5	60-70%	6	60-70%	4
	75-90%	4	75-90%	0	75-90%	1
	None	10	None	23	None	36
	0-2 m	24	0-2 m	19	0-2 m	12
	2-4 m	12	2-4 m	8	2-4 m	6
IT	4-6 m	3	4-6 m	4	4-6 m	0
	6-8 m	5	6-8 m	0	6-8 m	0
	8-10 m	0	8-10 m	0	8-10 m	0
	>10 m	0	>10 m	0	>10 m	0
	None	0	None	0	None	0
	0-2 m	14	0-2 m	10	0-2 m	16
	2-4 m	19	2-4 m	15	2-4 m	6
OB	4-6 m	9	4-6 m	10	4-6 m	9
	6-8 m	5	6-8 m	6	6-8 m	7
	8-10 m	5	8-10 m	4	8-10 m	10
	>10 m	2	>10 m	9	>10 m	6

Table 6.9: Headwall metrics, categories and the number of measurements in each for 2016, 2017 and 2018

6.5.1.3 Short-Term Results: Ice Thickness

The IT along each of the three model headwalls can be seen in Figure 6.26. There does not appear to be a clear pattern in the rates of retreat and IT. Where there is no ice visible, retreat appears mostly slow, but with some notable exceptions towards the west. The purple (0-2 m) visible IT also appears to be linked with relatively slow rates, except for the west, where it appears to be associated with the largest HWR. For the IT categories above that, there are fewer observations, but these also appear quite mixed. When split into east, middle and west, the average IT was 3.0 m, 1.6 m and 0.7 m respectively for 2016, 0.5 m, 2.4 m and 1.0 m for 2017, while 2018 averages 0.3 m, 0.4

m and 1.3 m respectively. Both the east and middle saw reductions in the average IT, while the west experienced an increase. This trend is broadly similar to the average HWR in the three regions over time, suggesting that IT may be an important factor.

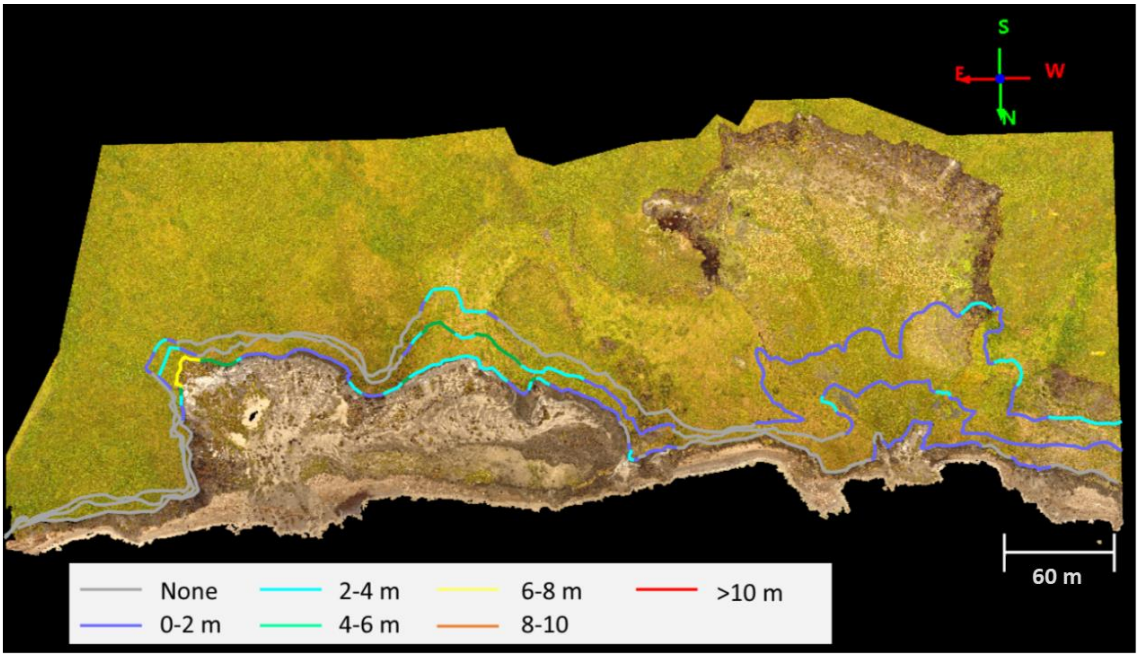

Figure 6.26: Headwall lines from 2016, 2017 and 2018 digitised and colour coded to the thickness of exposed massive ice. 2016 drone based orthomosaic used as a base image

Figure 6.27 displays the IT categories in each year, and the average HWR for each period associated with them, highlighting the complexity of the relationship. It appears that in 2016 (A), the ice free and lowest IT categories are associated with the largest HWR. The ice-free category becomes associated with the smallest retreat in the following two years, while the 0-2 m IT remains associated with the largest retreat. The one ice metric that has a consistent strong association with HWR is the IT in 2018, with correlation coefficients +0.49 and +0.52 with the total retreat (2016 to 2018) and 2017 to 2018 retreat, respectively. However, using the average IT of 2017 *and* 2018 for the same correlation, instead of just the 2018 thickness, weakens the relationship. Similarly, using the average IT across all years completely removes any significant correlation. This suggests that ice present further behind the headwall is a better predictor of HWR, even than currently exposed levels of massive ice. To explore this relationship further, retreat rates were split into two groups, where an ice exposure is present in 2018 and not present in 2018. The resulting box and whisker plot can be seen in Figure 6.28. The average HWR rate *without* ice in 2018 was 7.3 m a^{-1}, with an interquartile range of 4.9 m a^{-1} to 9.4 m a^{-1}. The transects with ice in 2018 had an average HWR rate of 21.3 m a^{-1} and an interquartile range of 12.5 m a^{-1} to 31 m a^{-1}.

From this analysis, it is evident that the presence of a massive ice body, rather than its thickness, is an important factor for HWR rates. Furthermore, the presence of ice inland from the headwall is a key factor. This can be seen in both Figure 6.28 and by the high rates of HWR from 2016 to 2018 towards the west of Peninsula Point (Figure 6.26), even in regions where ice was not yet visible in the headwall in 2016.

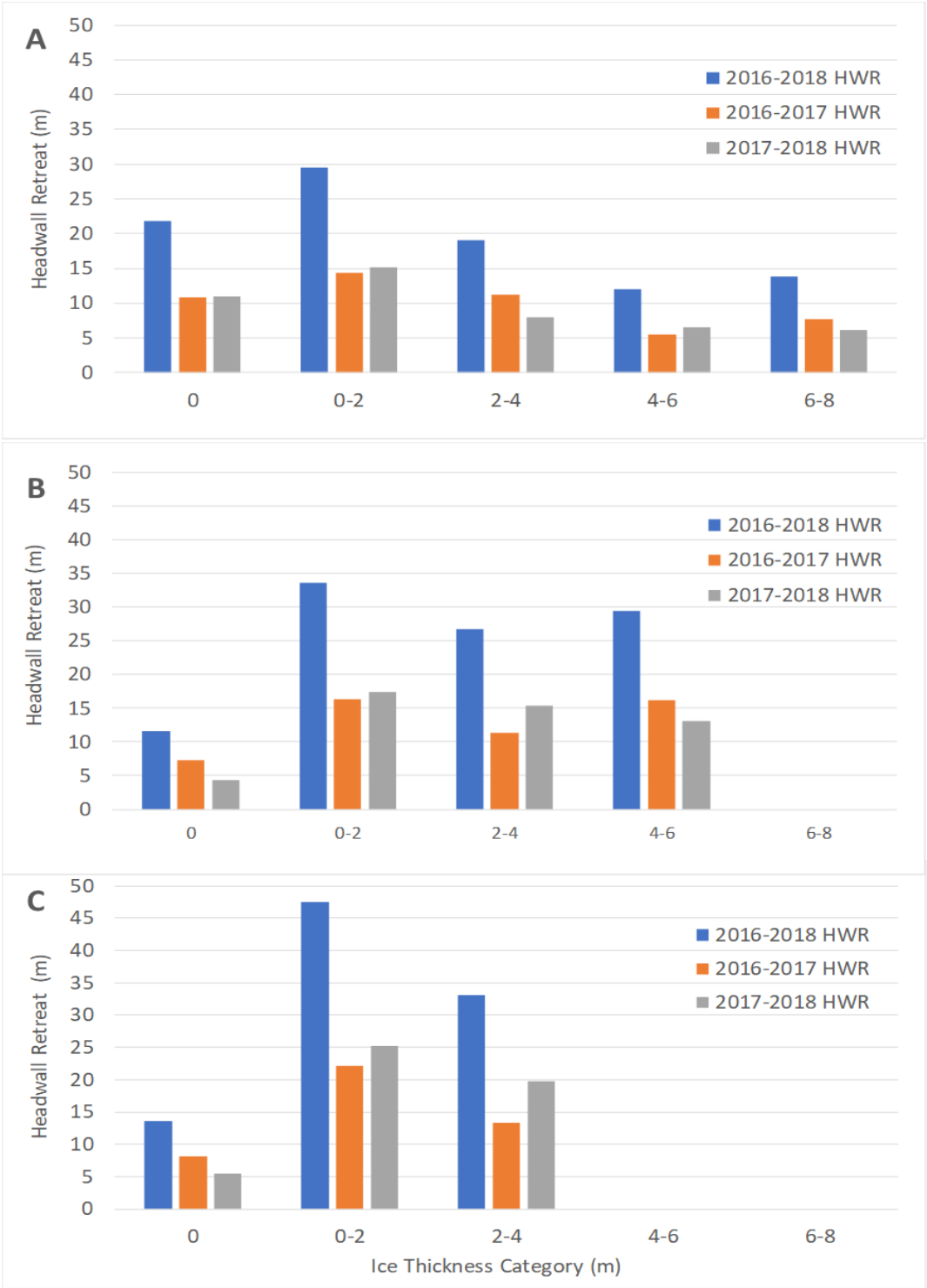

Figure 6.27: Ice thickness categories for the years 2016 (A), 2017 (B) and 2018 (C) and their association with levels of HWR between 2016 and 2017 (orange), 2017 and 2018 (grey) and the total retreat from 2016 to 2018 (blue)

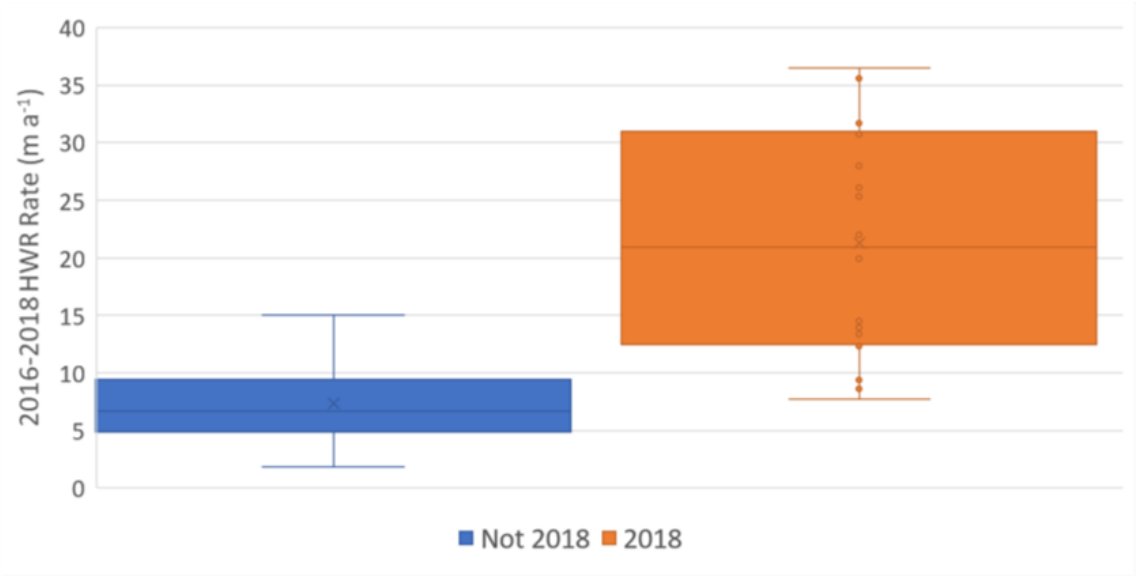

Figure 6.28: Comparison of HWR rates between transects with ice present in 2018 and those without

6.5.1.4 Short-Term Results: Proportion of Ice

The proportion of ice along each of the three headwalls can be seen in Figure 6.29. it demonstrates that anywhere after 2016 where the proportion of ice drops to 0%, the rate of HWR is significantly lower than areas where ice remains visible, supporting the results from the previous section. However, it also appears that areas that maintain an ice exposure *and* have a large PI (>45%) experience faster rates of retreat, such as in the thaw slump near the middle, and the large slump towards the west (Figure 6.29). When split into east, middle and west, the averages were 38.1%, 31.9% and 19.0% respectively for 2016, 9.0%, 28.1% and 34.0% for 2017, while 2018 averages 8.1%, 7.5% and 36.3%, respectively. Like both the IT and retreat rates, there was a reduction in the PI in the east and middle from 2016 to 2018, with an increase in the west during the same time. This adds further evidence that exposed IT and the PI relative to OB thickness are important controls on HWR rates.

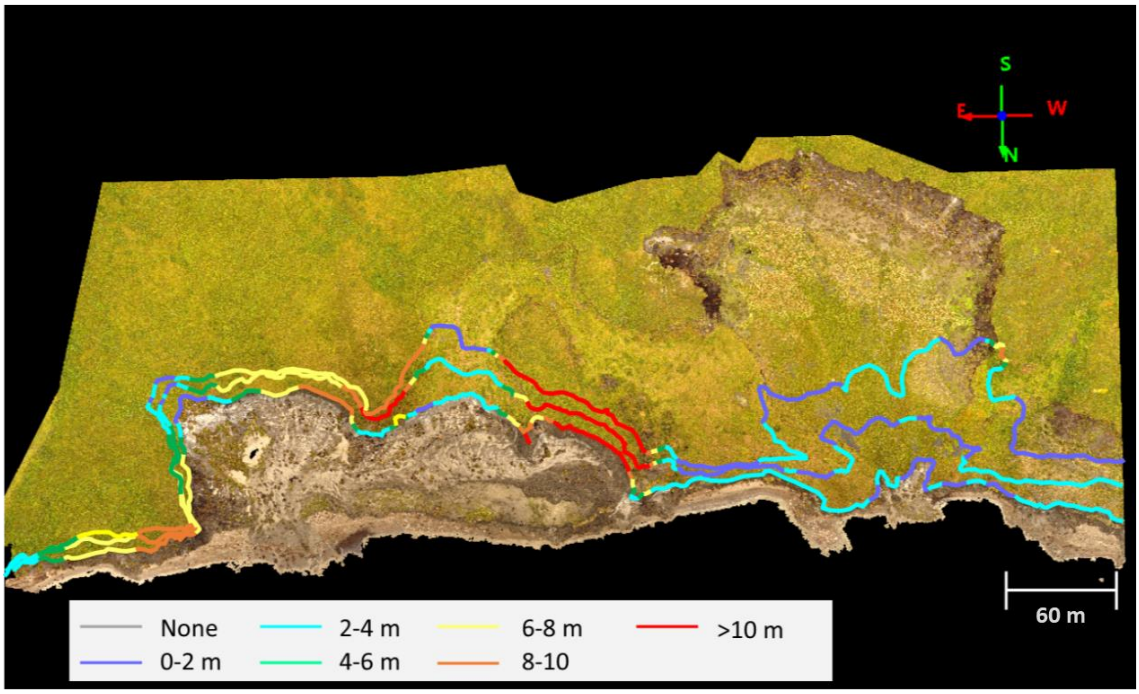

Figure 6.29: Headwall lines from 2016, 2017 and 2018 digitised and colour coded to the proportion of exposed ice thickness relative to overburden thickness. 2016 drone based orthomosaic used as a base image

Figure 6.30 displays the PI categories in each year, and the average HWR for each period associated with them. Interpreting the bar charts is made difficult by the extent of changes in the PI categories overtime (Table 6.9). In 2016, measurements were well distributed through each PI category, with no ice having the most observations, at 10 (18%), and at the lower end was 75-90% with four observations (7%). By 2018, the no ice category had 66% of the total observations with 36, leaving just 18 observations for the other categories. In 2016, the PI from none present through to 60% experience similar HWR rates, while the PI above 60% coincided with slower HWR rates. Figure 6.30B, 2017, produced the opposite trend to 2016. Here the two lowest PI categories were associated with the smallest HWR, while the remaining four PI categories displayed a large degree of variability. For 2018, the greatest HWR was associated with the middle PI category, 30-45%, with HWR reducing as the PI both increased and decreased away from this value.

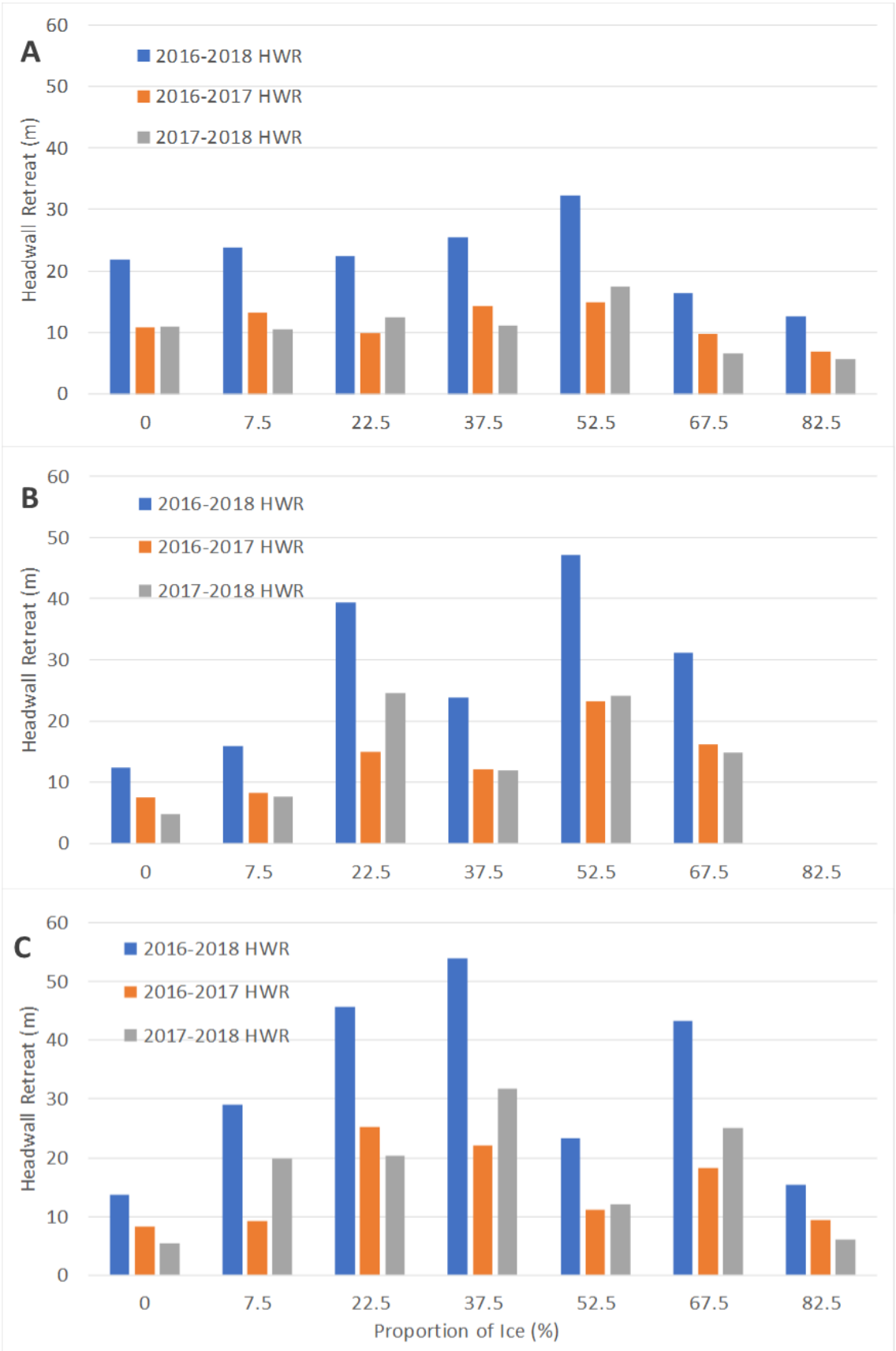

Figure 6.30: Proportion of ice categories for the years 2016 (A), 2017 (B) and 2018 (C) and their association with levels of HWR between 2016 and 2017 (orange), 2017 and 2018 (grey) and the total retreat (blue)

From Figure 6.30 it is evident that the presence of a massive ice exposure after 2016, regardless of what proportion of the headwall exposure it accounts for, is an important feature for producing greater levels of HWR.

6.5.1.5 Short-Term Results: Overburden Thickness

OB thickness displays much more consistency between 2016 and 2018 than the IT and PI. This can also be seen in the colour coded headwall lines in Figure 6.31. It reveals that in the three main areas with a thin OB (<4 m), HWR is much greater than in other regions. When split into east, middle and west, the averages are 4.4 m, 5.4 m and 1.9 m respectively for 2016, 6.6 m, 6.3 m and 2.1 m for 2017, while 2018 averages 6.0 m, 7.6 m and 1.5 m, respectively. This supports the general pattern of greater and increasing HWR in the western segment corresponding to lower and decreasing OB thickness. The slower and decreasing HWR in the middle and east correspond with a thicker and increasing OB in these regions also.

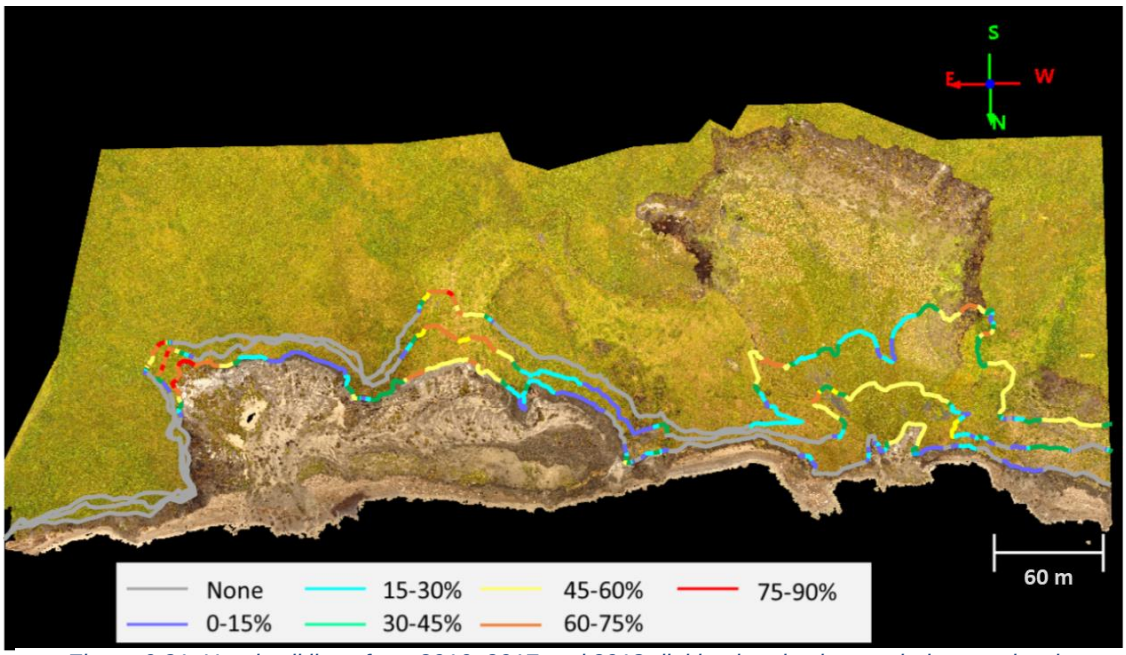

Figure 6.31: Headwall lines from 2016, 2017 and 2018 digitised and colour coded to overburden thickness. 2016 drone based orthomosaics used as a base image

The average HWR associated with the OB categories in each year can be seen in Figure 6.32. There is a very clear link between the low OB values and greater HWR. For 2016, the average total retreat for the two lowest OB categories (0-2 m and 2-4 m) is 30.7 m. This is over twice the retreat of the average of the other categories. These differences are even greater for the OB categories in 2017 and 2018. Together, this strongly suggests that an OB below 4 m is strongly associated with faster rates of HWR. To explore this relationship further, retreat rates were split into two groups, where an OB less than 4 m is present in all years and where it is not. The resulting box

and whisker plot can be seen in Figure 6.33. The average HWR rate without a persistently thin OB was 6.9 m a^{-1}, with an interquartile range of 4.7 m a^{-1} to 9.0 m a^{-1}. The transects that did feature an OB below 4 m in all years had an average HWR rate of 18.6 m a^{-1} and an interquartile range of 9.2 m a^{-1} to 28.7 m a^{-1}. It is evident that a persistently thin (<4 m) OB is strongly associated with faster active HWR rates.

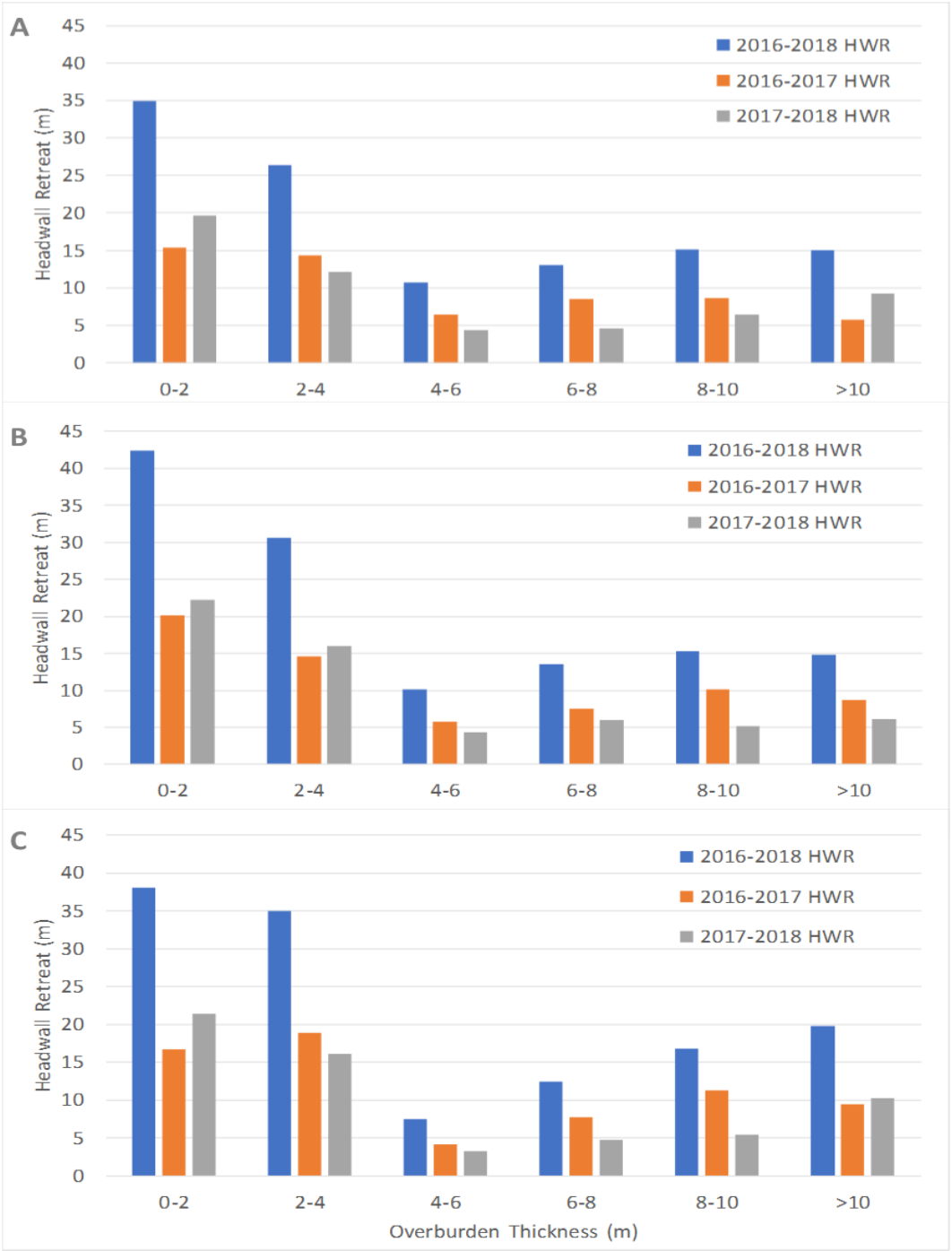

Figure 6.32: Overburden thickness categories for the years 2016 (A), 2017 (B) and 2018 (C) and their association with levels of HWR between 2016 and 2017 (orange), 2017 and 2018 (grey) and the total retreat (blue)

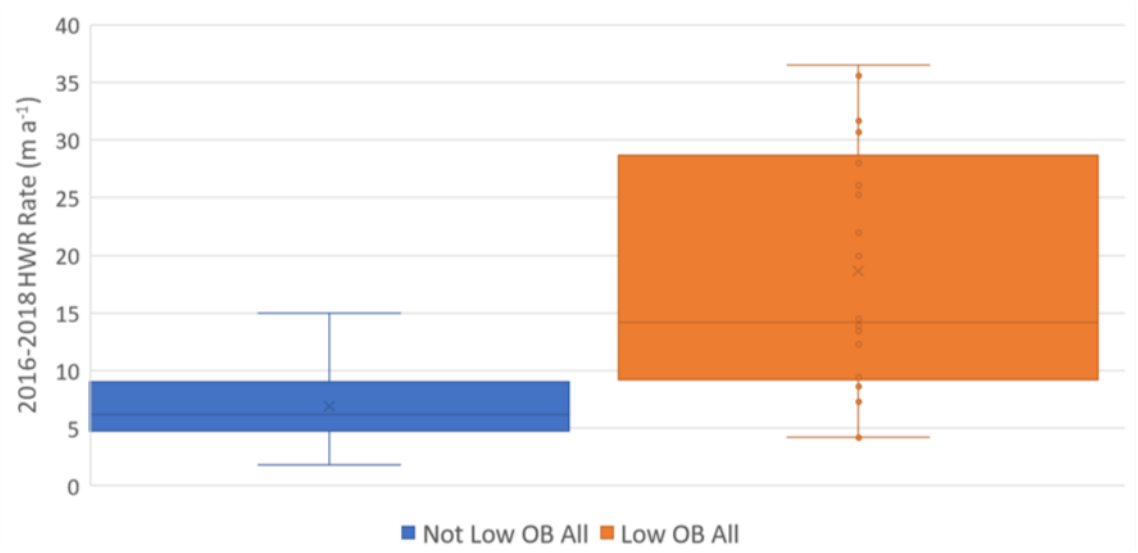

Figure 6.33: Comparison of HWR rates between transects with an OB below 4 m in all three years, and those without

6.5.1.6 Short-Term Results: Collation

The short-term analysis has revealed that there are two factors dominant in driving HWR: the presence of ice inland of the headwall, regardless of how thick it is, and a thin OB layer (<4 m). Where the OB thickness was below 4 m in all three years, and ice was present in 2018, the average HWR rate was 21.3 m a^{-1}, while the average of all other transects was 6.8 m a^{-1} (Figure 6.34). However, there are some exceptions to these rules and analysis of their causes may reveal some interesting features of the headwall and general coastal dynamics.

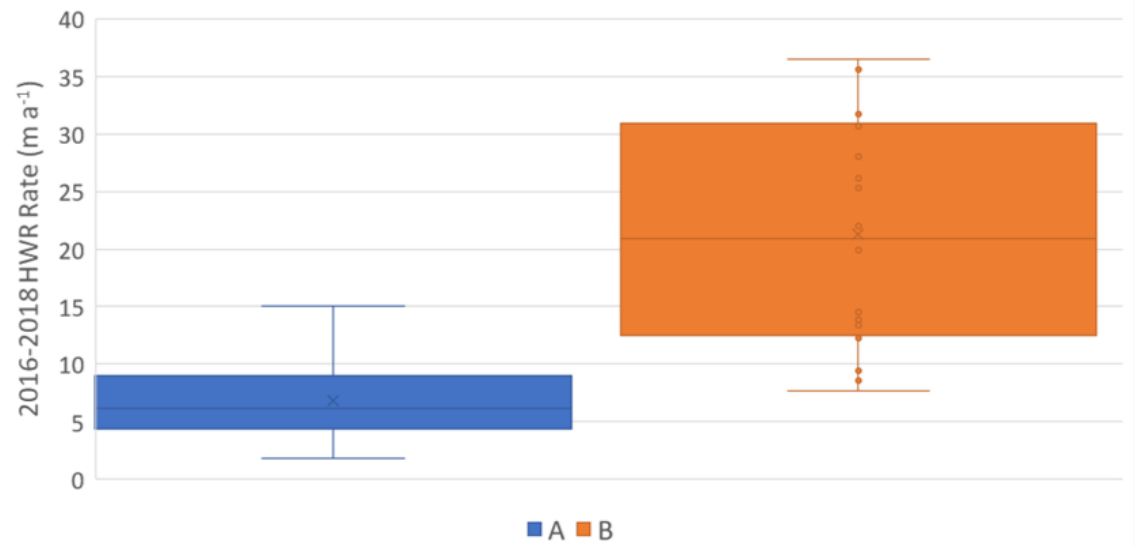

Figure 6.34: Comparison of HWR rates between the transects with persistent OB under 4 m and ice present in the headwall in 2018.

Some transects cross headwalls that appear to have the metrics suited to fast HWR rates but have slower rates than expected. Four of these are associated with a headwall in the east of Peninsula Point. In 2016, there was an area 55 m across, with

an IT of 4 m to 8 m and OB of 0 m to 4 m (Figure 6.24). Along all four transects the OB remained below 4 m, while three of the four transects maintained an exposure of ice. Despite this, the retreat rates were 7.5 m a^{-1} from 2016 to 2018, slower than expected. The length of headwall with exposed ice and the thickness of the ice rapidly diminished between 2016 and 2017, dropping to 24 m across and 0 m to 4 m thick. This continued into 2018, to 18 m across and most of the IT below 2 m (Figure 6.35). During the three years, less ice become exposed to ablation, reducing the volume of thawed water and allowing material to accumulate at the foot of the headwall (Figure 6.36). This allowed for a stabilisation of material on the slump floor (vegetation in Figure 6.35C), and a build-up of material at the base of the exposed headwall ice, further protecting it from ablation. A large part of the build-up in material was due to the ice surface dipping steeply inland from its elevation visible in the headwall in 2016. The changing ice elevation and stabilisation of the slump floor played important roles in reducing the HWR rates relative to those observed in other similar areas.

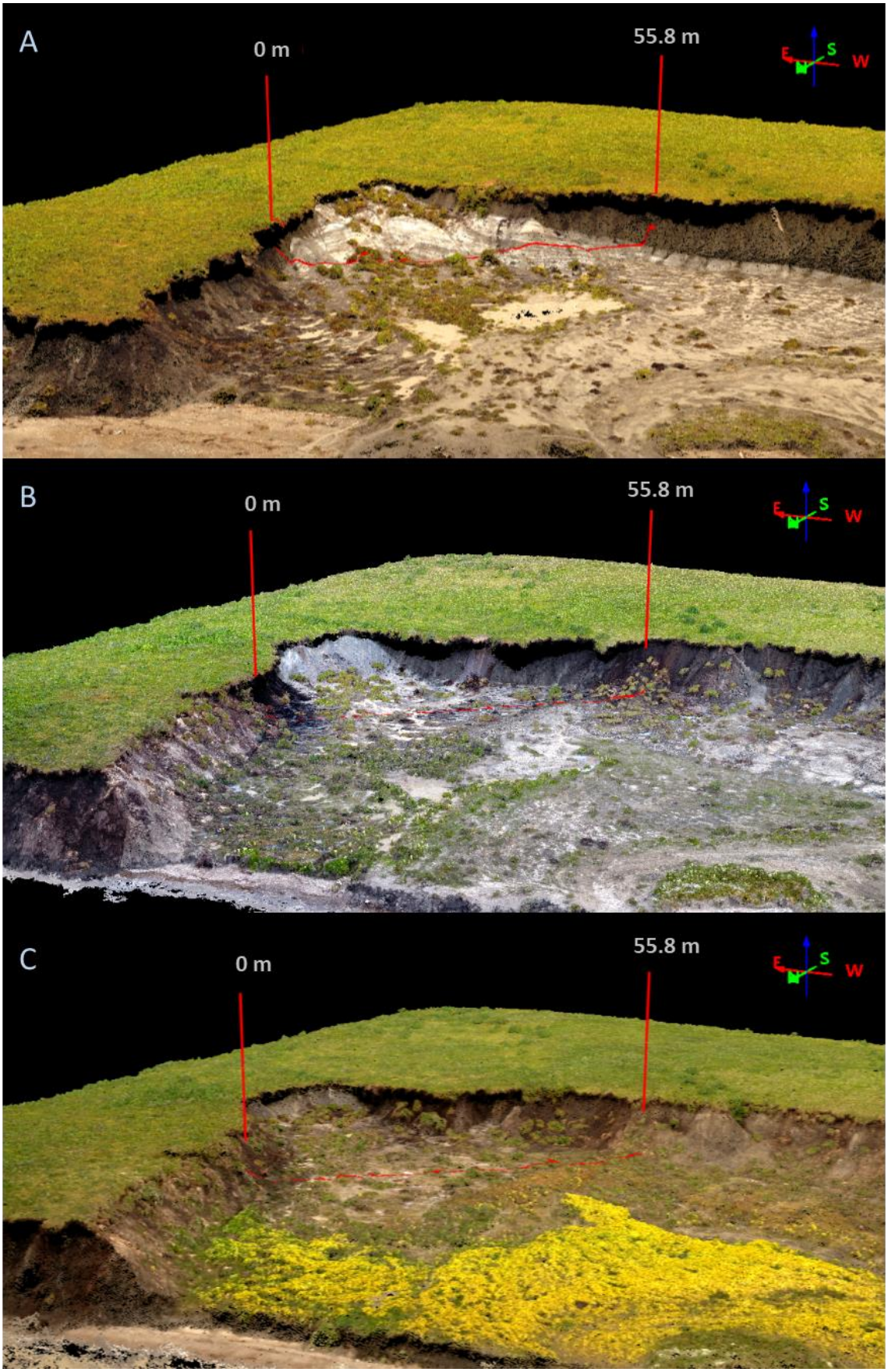

Figure 6.35: Progression of a headwall section from 2016 (A), the 2017 (B) and 2018 (C).

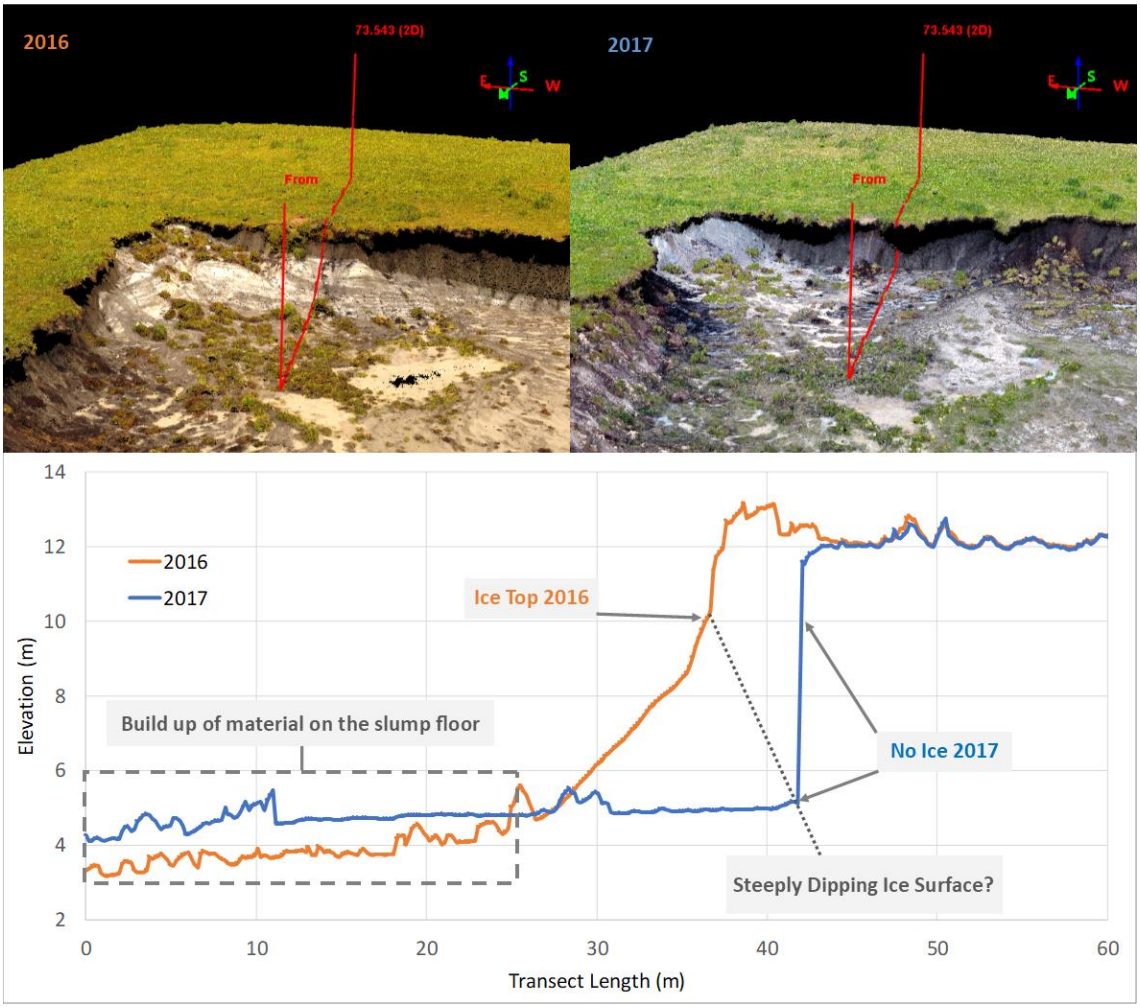

Figure 6.36: Example of headwall stabilisation from 2016 to 2017 from ice body variability

On the western end of Peninsula Point no ice was visible in 2016 and the OB was 2-4 m – headwall constituents which did not appear conducive to rapid HWR. However, by 2017 the headwall had retreated by 6.5 m and an IT of under 2 m was visible, still with a slightly reduced OB. The headwall retreated a further 7.4 m by 2018, exposing an IT of 2-4 m with the OB reduced to under 2 m (Figure 6.37). The rapid change in the IT suggests that 20 m from the shoreline in 2016, massive ice was less than 2 m under the ground surface. As the headwall base was less than 2 m above sea level, the exposure of ice and rapid retreat of the headwall also contributed to this area experiencing the fastest rate of SLR from 2016 to 2017. It is also possible that the ice is thicker still further inland, as there appears to be an older headwall present 25 m inland from the 2018 headwall position.

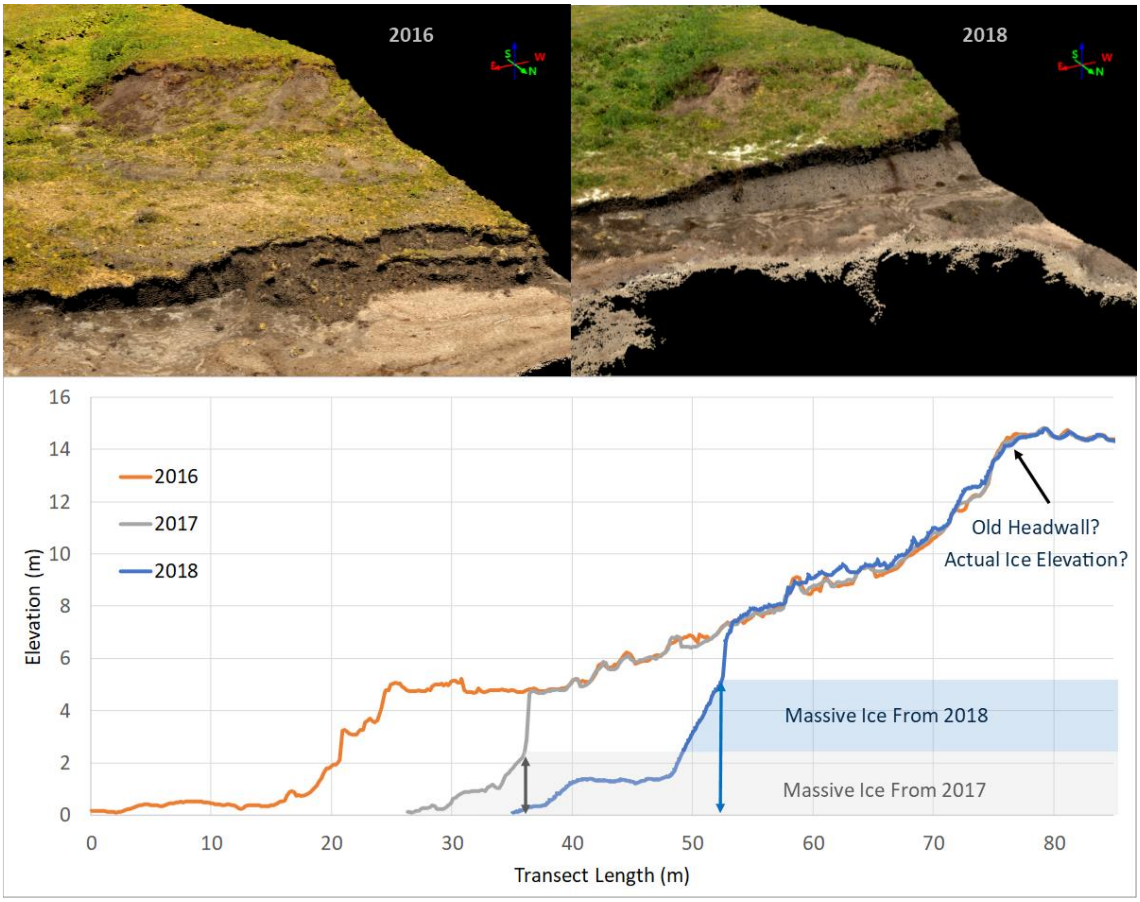

Figure 6.37: The western edge of Peninsula Point from 2016 and 2018, showing the rapid change in headwall characteristics after retreating. Bottom shows an elevation profile through the after for 2016, 2017 and 2018. The height of the massive ice, estimated from the visible exposures, are also displayed

These examples illustrate the degree of cross-shore massive ice variability and the importance it plays in headwall dynamics. In the middle of Peninsula Point, there is an area that spans 80 m that displays a large range of IT and OB variations, from an IT of none to 5.9 m and an OB from 2 m to 12.2 m (Figure 6.38).

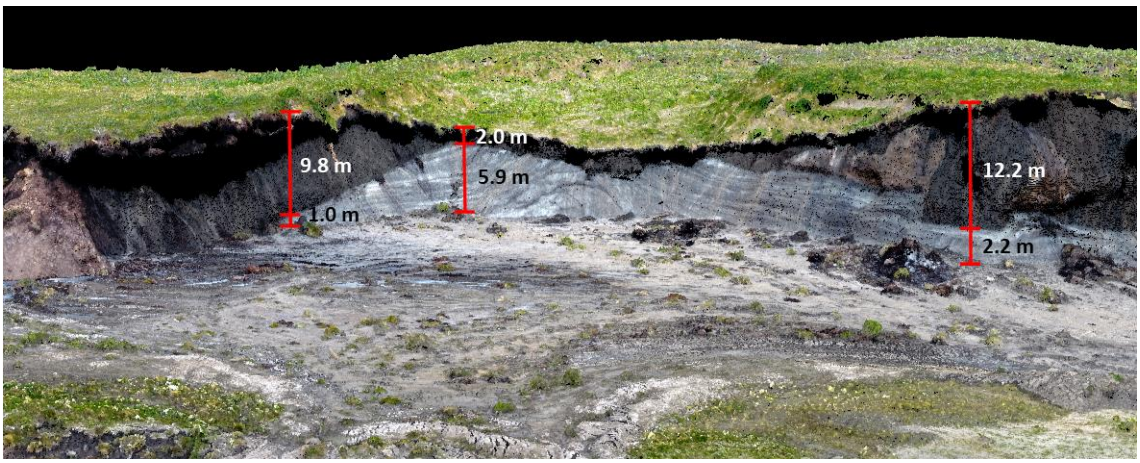

Figure 6.38: Range of 2017 IT and OB values in the middle regions of Peninsula Point where the passive seismic measurements were taken and ice surface model generated

This area is the focus of the 2017 ice surface model, described in section 4.5. Figure 6.39 shows the ice surface model in 2D positioned over the 2017 orthomosaic, with a colour scale representing the surface elevation of the ice above local sea level. A greater level of HWR is expected where the ice surface is higher, at a sustained elevation further inland from the headwall and the OB is less than 4 m. This coincides with the central dome region of the ice model (defined in section 4.5.3.3). The highest massive ice elevation is circled in red. A slower rate of HWR can be expected where the exposed ice is lower in elevation, reducing inland from the headwall and the OB is greater than 4 m. This coincides with the areas to the east and west of the dome (defined as massive ice east and massive ice west from section 4.5.3.3). Here, the lowest massive ice elevation is highlighted in blue.

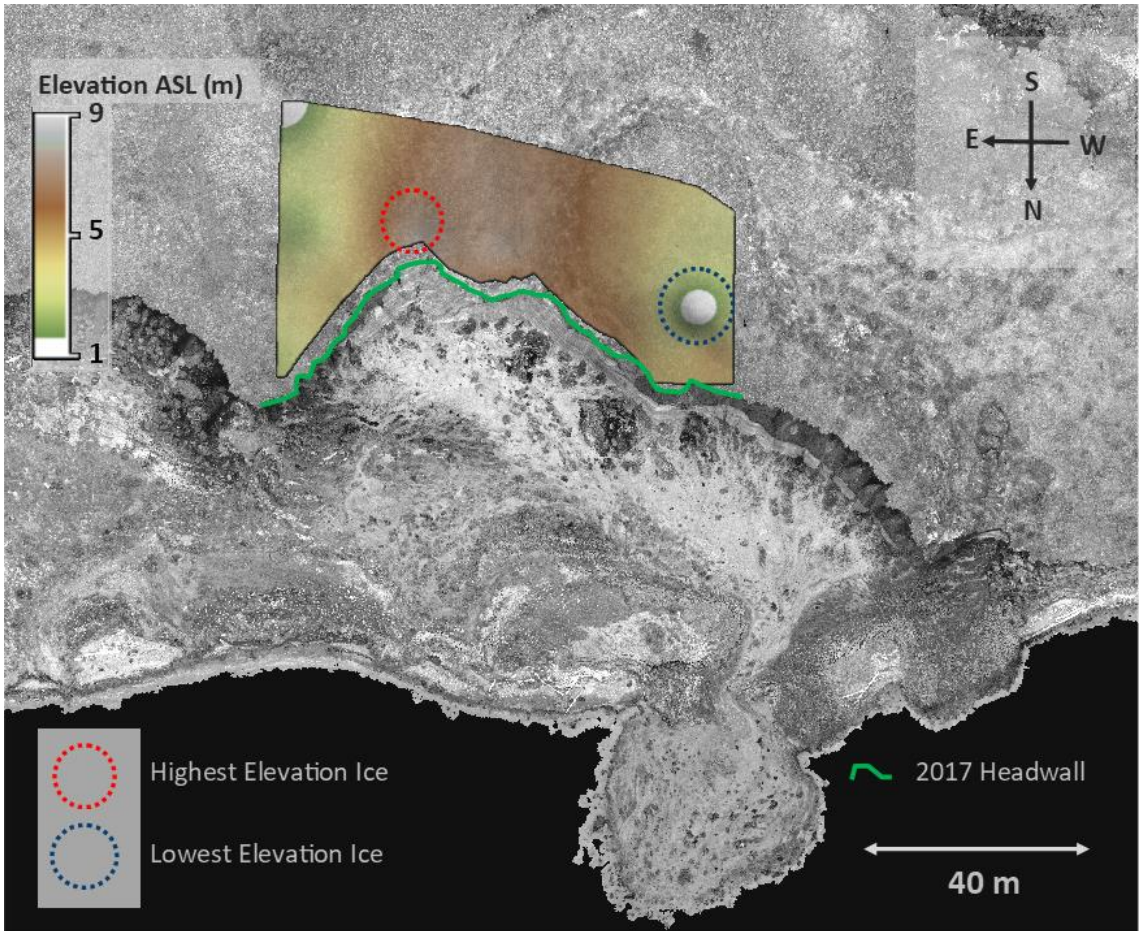

Figure 6.39: 2017 orthomosaic in grey scale with the ice surface model positioned over and set 25% transparent. The ice surface elevation is in metres above sea level (ASL). The areas of highest elevation and lowest elevation ice are highlighted with blue and red circles, respectively

Based on analysis of the IT and OB controls it can be expected that the slowest rate of retreat will be concentrated towards the east, fastest rates would occur in the middle, and a moderate rate of retreat in the west where the ice surface is modelled to steeply

dip towards the topographic low point highlighted in Figure 6.39. Figure 6.40 and Figure 6.41 present the changes that occurred by 2018.

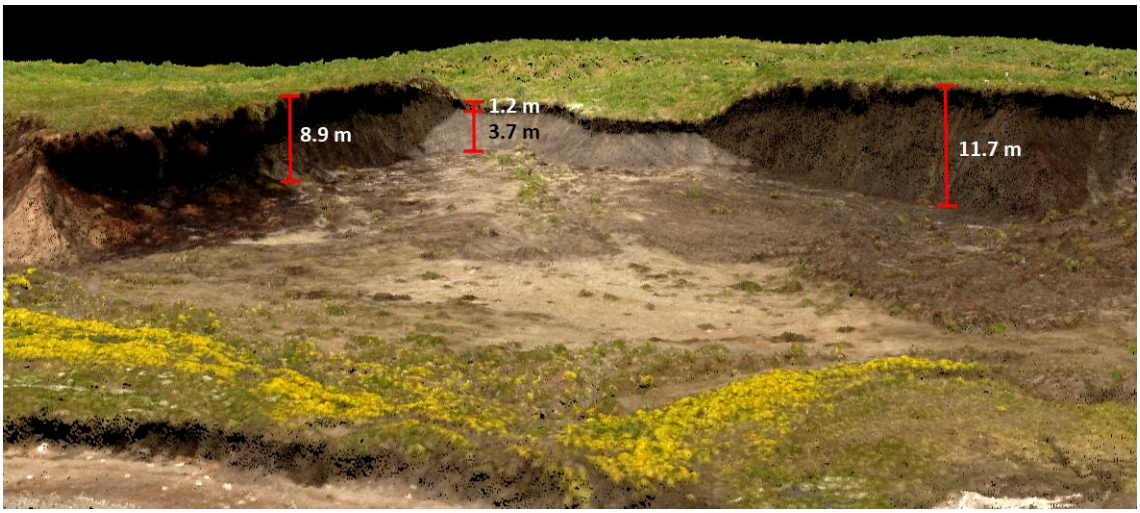

Figure 6.40: Range of 2018 IT and OB values in the middle of Peninsula Point

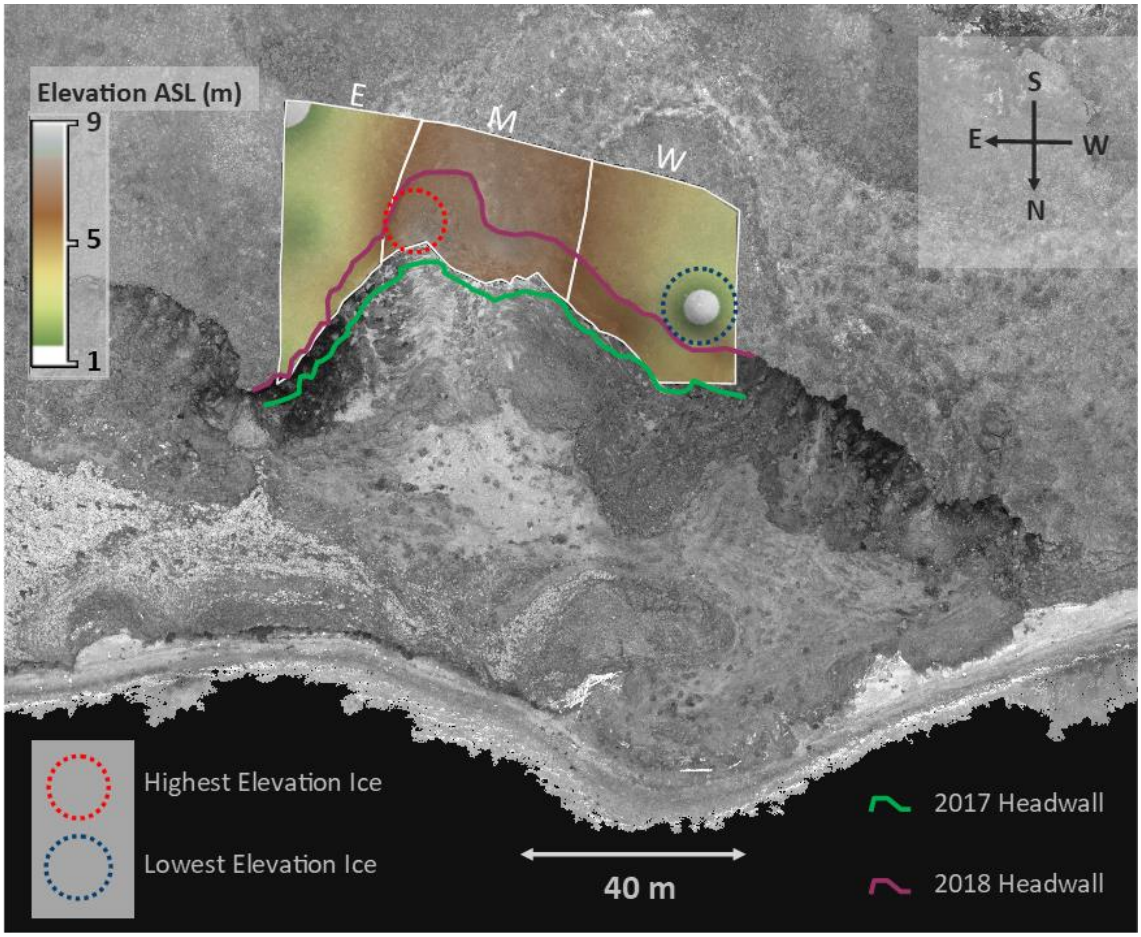

Figure 6.41: 2018 orthomosaic in grey scale with the ice surface model positioned over and set 25% transparent. The ice surface elevation is in metres above sea level (ASL). The areas of highest elevation and lowest elevation ice are highlighted with blue and red circles, while the headwall positions for 2017 and 2018 are shown in green and purple respectively. The separation into east (E), middle or central dome (M) and west (W) are also shown

Measurements were made every 5 metres perpendicular to the 2017 headwall, producing an average HWR of 11.1 m. The eastern section retreated by 5.8 m, the west by 10.0 m and the middle by 15.4 m. The retreat patterns contradict simple extrapolations from exposed headwall ice but are explained well by the massive ice surface model. Focusing on the eastern segment, the headwall was mainly free of exposed ice in 2017 and contained only thin ice in a small section where it was exposed. The ice surface model indicated that ice remained below the elevation of the base of the headwall further east. This was largely confirmed in 2018, when the HWR both removed the remaining ice exposure and produced no new ice exposures. For the western segment, the exposed ice in 2017 was between 5.9 m thick, near the central dome, and 2 m thick near the western edge. This was modelled to dip in elevation as the headwall retreated, resulting in a mainly thin IT of under 1.3 m down to ice free near the western edge. However, the ice elevation dipped more steeply than modelled, resulting in a lack of exposed massive ice along the entire headwall section by 2018. This suggests that the massive ice surface was dipping at between 10 and 30° away from its position in 2017, compared to the modelled values of 2° to 18°. The central dome in the middle retreated at over twice the rate of the eastern segment, and more than 50% faster than the western segment. The greatest retreat occurred where the highest ice elevation was modelled, and the overall pattern of the massive ice elevation matched the modelled elevation.

Finally, elevation transects across the area also highlight different dynamics operating along the slump floor elevation (Figure 6.42). These changes appear to be related to the ability of the slump floor to efficiently transport material away from the headwall, which is related to the melt water input from the immediate and the nearby retreating headwalls (Figure 6.43). In 2016, there was an average of 2 m IT (highlighted in blue), but thawed material was blocked from spilling seaward, causing a slight increase in the slump floor elevation. In 2017, the average IT had increased to 3.2 m, increasing the meltwater volume and allowing material to flow away from the slump floor, dropping the elevation slightly. By 2018 the IT averaged 1 m and the thawed material accumulated, resulting in a large elevation increase on the slump floor. As the ice surface model predicts no high elevation ice behind the east and west headwall, this area is likely to become more stable, with significant HWR becoming increasingly restricted within the domed ice section.

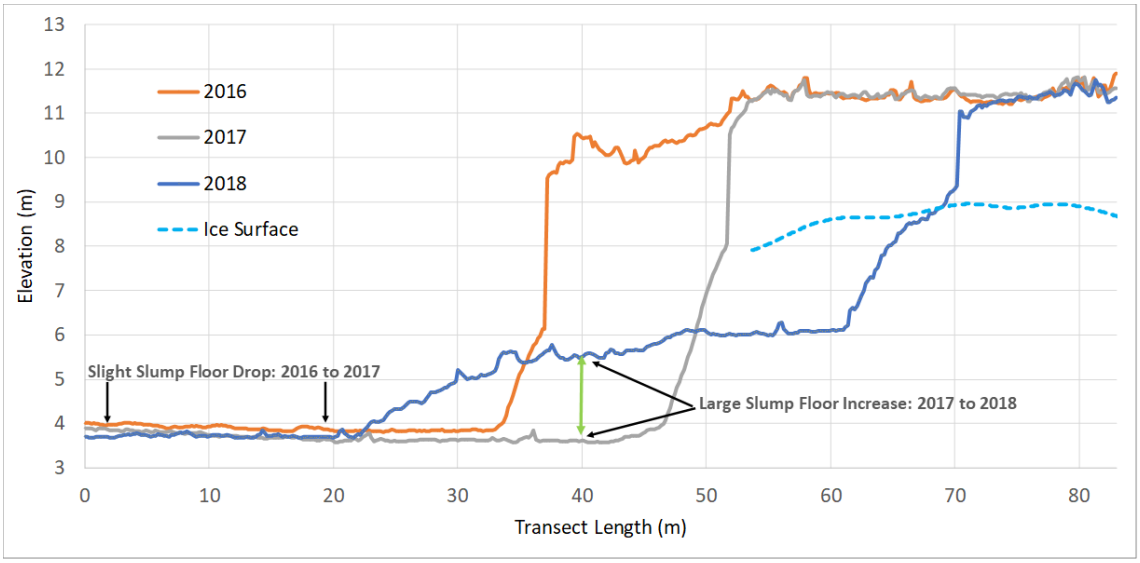

Figure 6.42: Elevation profiles for 2016, 2017, 2018 and the ice surface model going through the middle of the central PRTS perpendicular to the shoreline. Slump floor elevation drop from 2016 to 2017, and an increase from 2017 to 2018 are depicted.

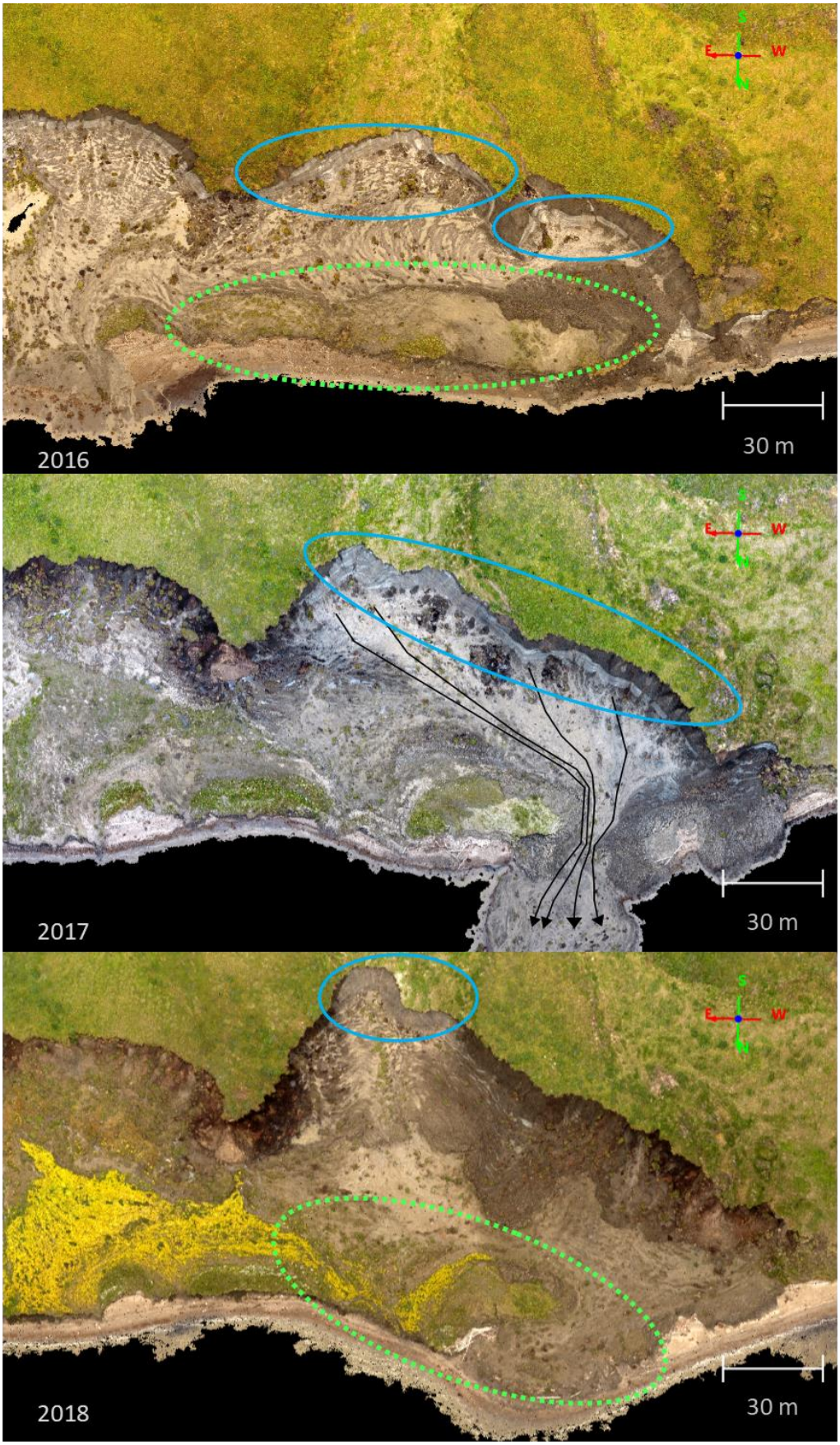

Figure 6.43: Slump flow dynamics with ablating ice in blue and flow blockages in green for 2016, 2017 and 2018

The ice surface model has proven useful in refining estimates of relative HWR (Figure 6.44). It was particularly effective for the western segment of the model. The average maximum elevation of the massive ice in 2017 was between 0.6 and 2.7 m higher than in 2016, with the average IT increasing from 2 m to 3.2 m. Despite this, the model showed the ice elevation dipping steeply inland, going against the observed trend between 2016 and 2017. This prediction was validated, although the ice surface dipped more steeply inland than was modelled. The minor discrepancy is likely a feature of the interpolation method. Away from the ice exposures, there were only six passive seismic measurement points covering an area of approximately 3,500 m^2. The expected and actual IT in 2018 near the four closest measurement points were in agreement — two suggesting the ice was below the base of the headwall in the east and west, and the others showing less than 0.1 m difference in the middle. This suggests that the measurement density needs to be increased to accurately capture the variability in massive ice surface elevation.

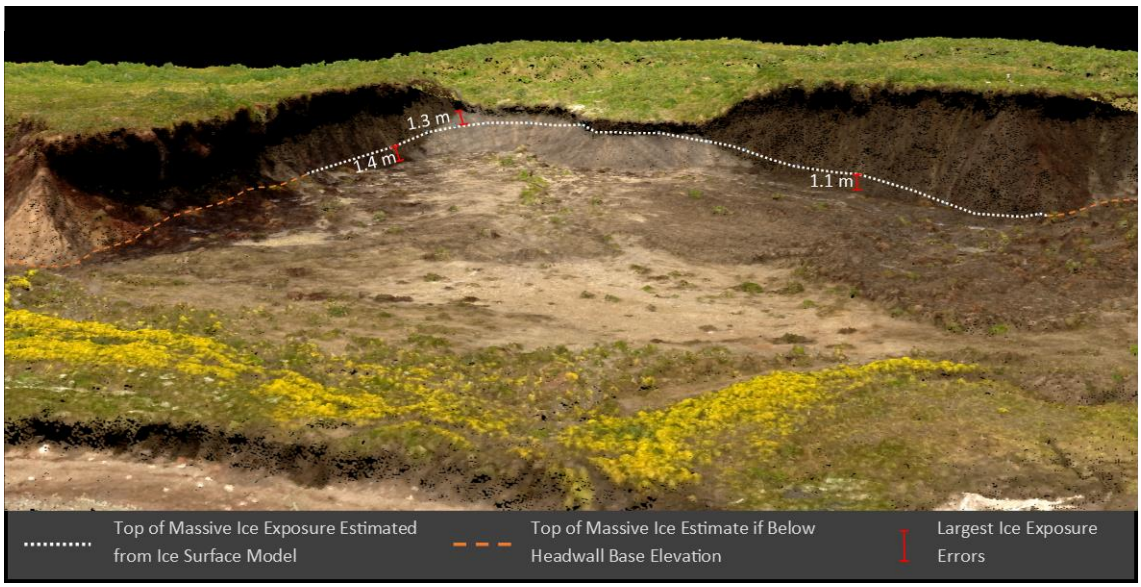

Figure 6.44: Actual and estimated headwall ice elevation from the ice surface model in 2018

6.5.1.7 Short-Term Results: Explanations

With some insights into the short-term RTS dynamics gained through analysing the influence of ice bodies, two of the five of the questions raised from the topographic controls sections can now be answered.

1. Why does the HWR and SL2HW distance relationship break down during the 2016-2018 period?
2. Why did the correlation between the 150 m slope angle and other metrics reverse after 2016?

1) The correlation between the SL2HW distance change rates and the HWR rates for 1994 to 2004, 2004 to 2016 and 2016 to 2018 were 0.83, 0.83 and 0.26 respectively. The same correlations with SLR were -0.18, -0.56 and -0.93, respectively. Why such a reversal in the pattern? The answer is twofold. Firstly, the rate of HWR (from section 5.4.1.4) has slowed at a faster rate than the SLR. HWR and SLR were 5.6 m a^{-1} and 3.9 m a^{-1} respectively, from 1994 to 2004, before matching each other at 2.8 m a^{-1} during the 2016 to 2018 period. There has also been a large increase in the variability of SLR rates for 2016 to 2018. For 1994 to 2004, 2004 to 2016 and 2016 to 2018, the SD of HWR was, 3.3 m a^{-1}, 3.3 m a^{-1} and 2.3 m a^{-1}. The corresponding deviations for SLR were 1.9 m a^{-1}, 1.4 m a^{-1}, and 6.3 m a^{-1}. The SLR and progradation rates during the 2016 to 2018 period can be linked with headwall dynamics described in the previous section. Firstly, the exposure of the massive ice on the western edge, less than 1 m above sea level and close to the shoreline, allowed for rapid HWR, efficient removal of thawed material and rapid SLR (Figure 6.37). Secondly, the thick massive ice exposures and OB in the central region produced large volumes of muddy run-off resulting in a mud lobe protruding from the shoreline and coastal progradation in 2017 and 2018 (Figure 6.43). The gradual trends in SLR and HWR, combined with the large volatility in recent shoreline position (driven by massive ice and OB variability) explains why SLR dominated the relationship with SL2HW distance for 2016 to 2018.

2) The correlation between the 150 m slope angle change and both SLR rate and volume loss rate has reversed from the 2004 to 2016 (+0.49 and +0.54) period compared with 2016 to 2018 (-0.71 and -0.43). For 2004 to 2016, a lowering of the slope angle was associated with greater volume losses and a slower SLR rate. This was due to slope angle reductions being associated with large PRTS which transport thawed material seaward, reducing the total volume and slowing SLR rates. Between 2004 and 2018 there was a significant reduction in slope angles measured across all distance intervals. This is largely true for the slope angle changes between 2016 and 2018 also, except for the 150 m measurement interval. In this instance 13 of the 22 transects recorded an increase in the average slope angle (Figure 6.45).

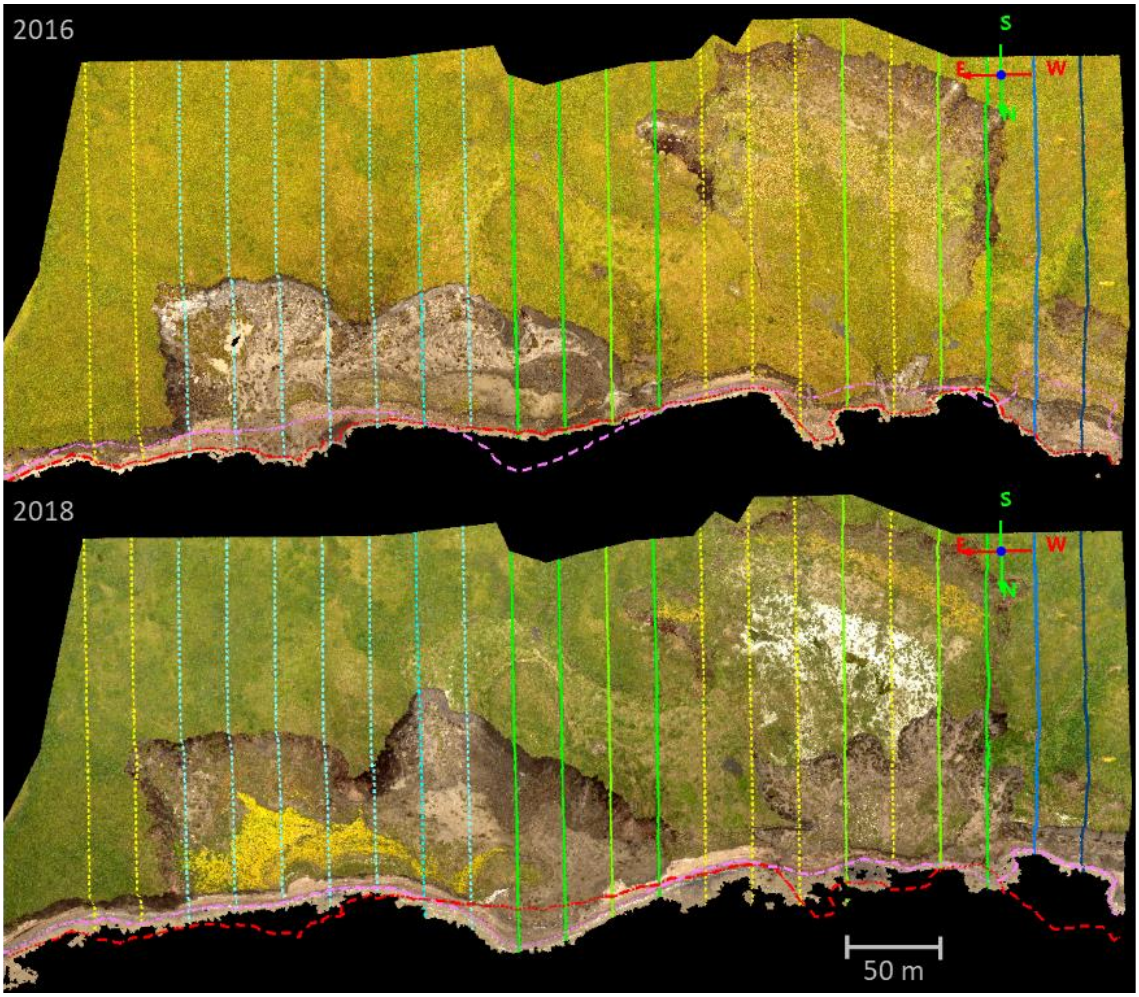

Figure 6.45: Transects and shorelines in 2016 and 2018. Solid blue represents 150 m slope angle decreases of more than 1°, dashed light blue of less than one. Solid green represents slope increases of greater than 1° and dashed yellow less than one. The 2016 and 2018 shorelines are represented by red and pink dashed lines respectively.

Aside from the two transects furthest east and west, all areas where the slope increased or decreased are grouped together. The seven transects where the slope decreased by less than 1° (dashed blue) exhibit a HWR of between 50 and 110 m from the shoreline (lowering the elevation further inland) with transport of volume from the headwall to the slump floor, where an accumulation of material and subsequent increase in elevation occurred. The cause of this is discussed in section 6.5.1.6. These processes resulted in a lowering of the slope angle, reduced volume loss and a faster rate of SLR. Conversely, the areas that have experienced an increase in the slope angle have undergone two distinct changes. Firstly, in the middle, a high elevation headwall retreated inland. The headwall had a widespread and typically thin ice exposure with a thick OB, generating a large loss of volume and causing coastal progradation in 2017. In 2018, the headwall had retreated to a region with lower elevation ice mostly below the base of the headwall. This reduced the volume of

meltwater, causing a stabilisation of the thaw slump and an increase in the elevation at the foot of the headwall. In combination with the progradation, these features enhanced the slope gradients, increasing the average slope angle. In the west, the development and progression of a new phase of HWR within the old RTS began in 2016. The new headwall was 5-20 m from the shoreline in 2016, extending inland by up to 73 m by 2018. This process produced large volume losses and reduced the elevation near the shoreline, without significant changes further inland behind the headwall. This has also increased the slope gradient inland. However, the headwall in the region was low in elevation. With an average OB thickness dropping from 1.8 m to 1.5 m, while the IT increased from 0.7 m to 1.3 m from 2016 to 2018. That meant that a large and increasing proportion of the volume loss was accounted for by water, allowing the SLR to proceed at a faster rate than the 2016 to 2018 along-shore average.

As such, in the 2016 to 2018 period, variations in along-shore RTS dynamics resulted in significant differences in the relationships between elevation, slope, volume loss and HWR, compared to those that were found in the 2004 to 2016 period. This explains the reversal in correlations with the 150 m slope angle from question 2.

6.5.1.8 Summary: Short-Term Massive Ice Controls

While massive ice body variability has been noted as a key factor in understanding the workings of RTS (Ramage *et al.,* 2017), the analysis here highlights the critical importance of fine scale data on massive ice thickness, OB thickness and their trends and variations both along and cross-shore. It also explored the complex interplay between RTS dynamics and topography that exists both spatially and temporally. Finally, passive seismic surveying was proven to be successful in detecting subsurface massive ice body elevation, contributing to both an improved understanding of short-term processes and an enhanced predictive capability of these processes. The next section will examine how this knowledge of massive ice variations can also play a key role in the coastal dynamics at Peninsula Point over decadal timescales.

6.5.2 Decadal

6.5.2.1 Decadal Methods

In this section results from the short-term massive ice body analysis and observations of massive ice exposures from the published literature will be used to re-examine the patterns of variability in topographic and shoreline changes since 1985. This analysis will provide fresh insights into the connection between massive ice variability and decadal coastal change, and attempt to answer three of the remaining questions presented in section 6.5:

3. What drove the reversal in the pattern of elevation and slope across Peninsula Point between 2004 and 2018?
4. Why was there a reversal in the spatial pattern of SLR after 2004?
5. Why did the overall reduction in elevation and slope angle not result in increased SLR rates?

6.5.2.2 Massive Ice Variability and Shoreline Change

Within the published literature, photographic and descriptive massive ice thickness observations of Peninsula Point in recent decades indicate that massive ice exposures of between 5 m and 10 m, and OB of 1 m to 10 m, are common (Gilbert *et al.,* 2016; Mackay and Dallimore, 1992; Moorman *et al.,* 1998; Murton, 2009). However, the average ice thickness exposure in 2018 was 0.6 m, with a maximum of 3.9 m. The average OB thickness was 5.4 m, with maximum of over 11 m. A clear reduction in the thickness of exposed massive is evident. The short-term results can help to highlight the contrasting influence of ice and OB thickness on SLR. Figure 6.37 presents how an area near the shoreline with a thin OB and thin ice can experience rapid changes. The exposure of the massive ice resulted in an average SLR of 30 m and HWR of 12.5 m along the two western-most transects from 2016 to 2017. The HWR grew to 15.5 m from 2017 to 2018, while the SLR dropped back to 1.5 m. This contrasts with the two transects east of the large slump in Figure 6.46. Here there is an area close to the shoreline where no exposed ice is observed, which experienced slight shoreline progradation of 1.2 m and HWR of 4.6 m from 2016 to 2017. Between 2017 and 2018 SLR and HWR were 3.3 m and 2.3 m respectively, much slower and relatively consistent compared to the two sections in the west. The influence of ground ice content on SLR extends well beyond Peninsula Point. For the Beaufort Sea coastline, numerous studies have noted the association between high ground ice content, especially massive ice bodies, and greater rates of SLR (Hequette and Barnes, 1990: Irrgang *et al.,* 2018; Obu *et al.,* 2017; Solomon, 2005). This trend is also apparent across the entire Arctic, with ground ice content offering the best, although weak, correlation with long-term coastal retreat rates (Lantuit *et al.,* 2012a). Massive ice and RTSs are also linked for the greatest inter-annual variability in SLR rates, with Obu *et al.,* (2017) noting that RTSs were "*responsible for the most extreme values of erosion, accumulation and coastline movements among the geomorphic units*" (p.341). Together, this highlights the fact that massive ice and high ground ice content in general is associated with faster long-term SLR, but greater short-term variability.

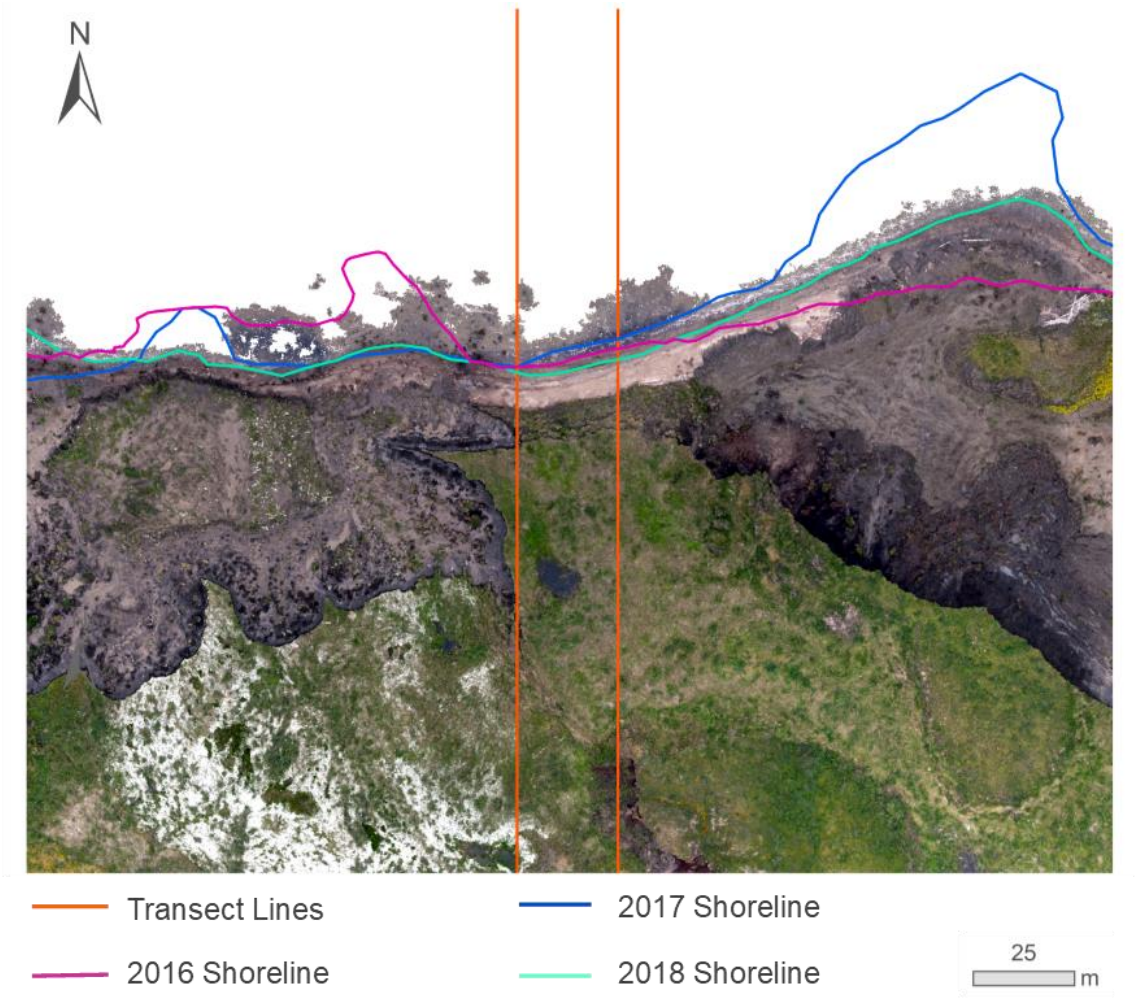

Figure 6.46: Transect lines (orange) for the region with no exposed ice, with the 2016 (purple) 2017 (blue) and 2018 (turquoise) shorelines over the 2018 orthomosaic

There were 15 years (from 1985 to 2018: The time periods are 1985-88, 1988-90, 1990-93, 1993-94, 1994-97, 1997-00, 2000-02, 2002-04, 2004-06, 2006-10, 2010-13, 2013-16, 2016-17 and 2017-18.) with shoreline positions mapped and measured along 22 transect lines allowing for 308 discrete SLR rate values (section 5.3). 5.5% of these underwent no change, 69.8% retreated and 24.7% prograded. The average correlation from one time period to the next is -0.43, indicating that fast retreat rates along transects in one period tend to be followed be slow rates in the next. Of the 13 comparisons made, six of these were statistically significant ($p < 0.05$), with the strongest being between 2017 and 2018, at -0.81. While annual resolution data would be more ideal for this analysis, the evidence derived from the available time periods make a compelling case for a quasi-cyclic pattern of SLR. When examining patterns over individual transects or small groups, progradation events appeared to occur at semi regular intervals, possibly representing cycles of material flow towards the shoreline due to retrogressive thaw slump activity, followed by accelerated SLR before another phase of progradation occurs. Figure 6.47 shows the 1985 shoreline in pink,

the 2018 shoreline in red, and highlights the transects that are used in Figure 6.48, Figure 6.49 and Figure 6.50.

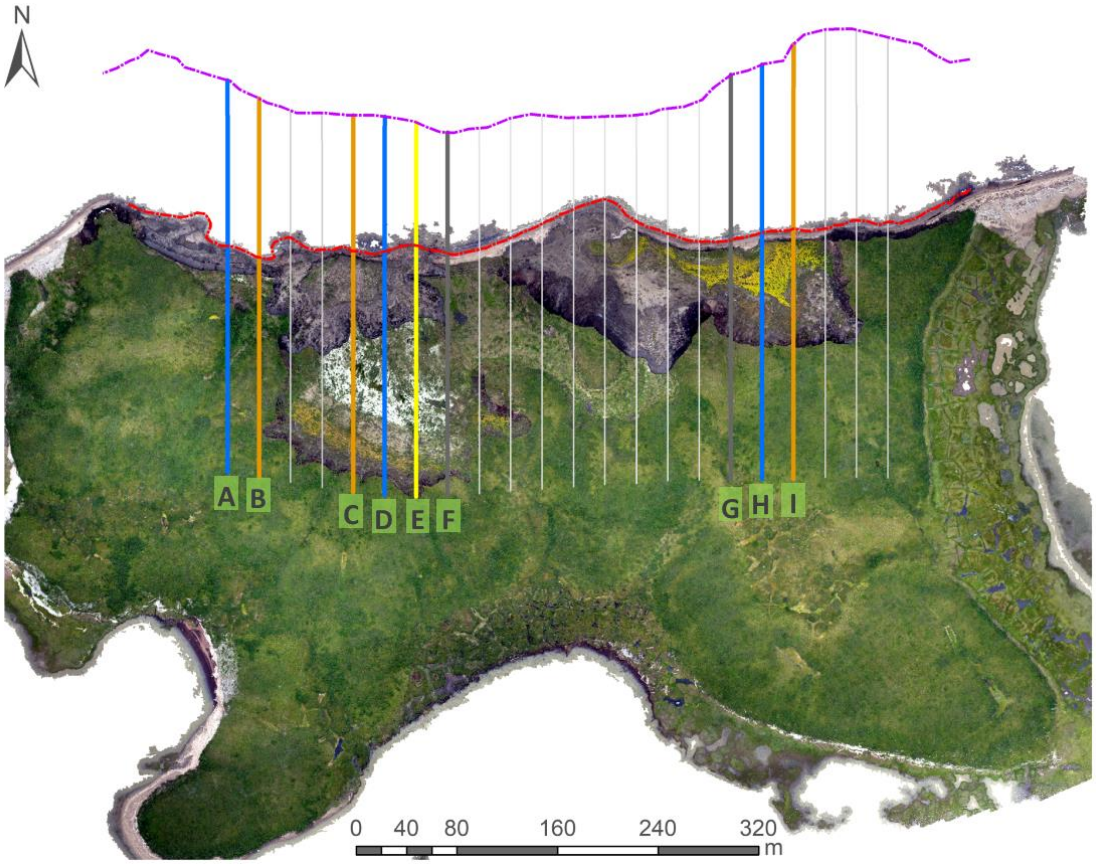

Figure 6.47: Transect lines, with the groups of transects used in Figures 6.48, 6.49 and 6.50 highlighted and labelled

Figure 6.48 presents an example of shoreline variability along two neighbouring transects (A and B, Figure 6.47), with a cycle repeating approximately every nine years. The phases and amplitudes are relatively consistent and there is no significant trend in the SLR rates for the time period analysed.

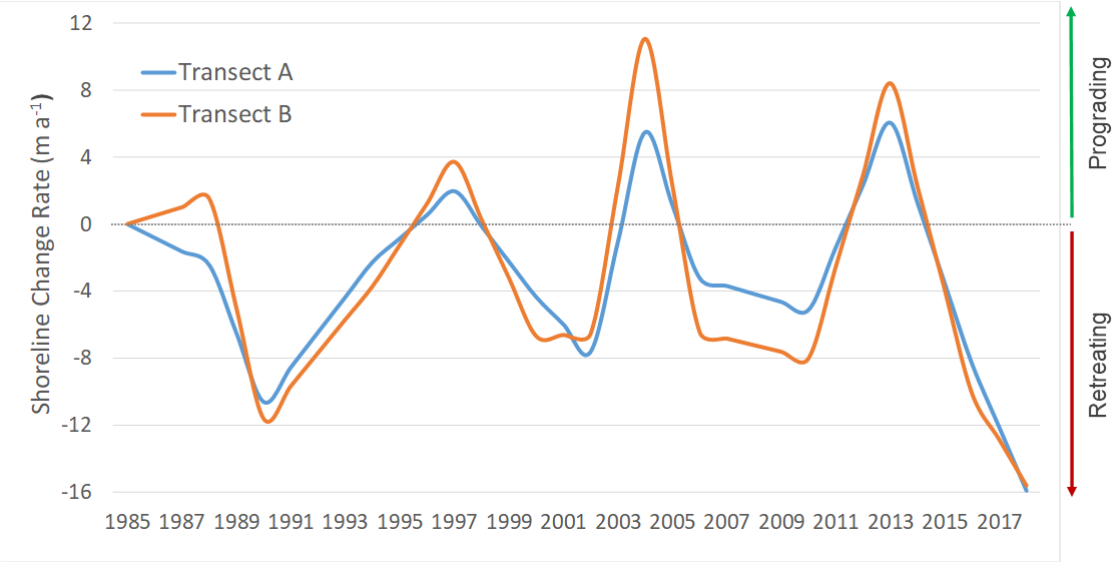

Figure 6.48: Pattern of shoreline retreat and progradation between 1985 and 2018 for transects following the northing 573150 (A) and 573175 (B), the two most westerly transects.

Other areas display a different pattern. Figure 6.49 represents four transects that pass through the large PRTS present on the western side of Peninsula Point, labelled C, D, E and F in Figure 6.47. SLR rates here appeared relatively stable until the year 2002, when variability increased markedly. The switch from retreat to progradation between 2000 and 2002 was present across five adjacent transects. The most likely explanation is the development of an active phase of thaw slumping and the formation of a massive mud lobe. After this time, the shoreline along the transects in Figure 6.49 display a marked increase in variability. This increased variability also coincided with an increase in the overall SLR retreat rate for these transects, with a rise from 1.3 m a^{-1} between 1985 and 2002, to 3.3 m a^{-1} between 2002 and 2018.

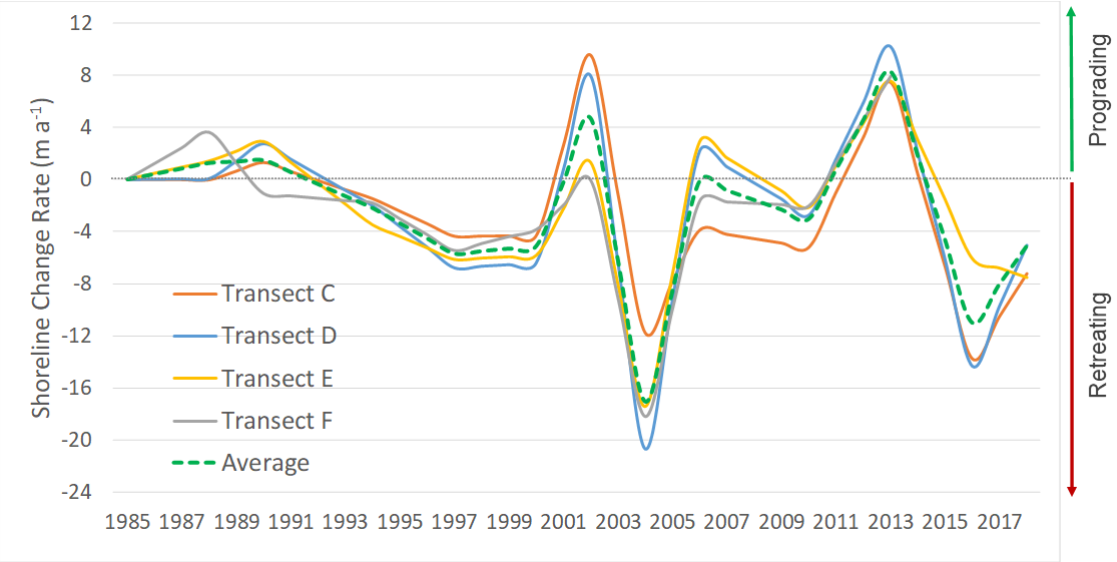

Figure 6.49: Pattern of shoreline retreat and progradation between 1985 and 2018 for transects following the northing 573250 (C) 573275 (D), 573300 (E), 573325 (F) and the average of all four

Figure 6.50 shows the shoreline change rates along three transects towards the eastern end of Peninsula Point. Here, the amplitude of the wave pattern is smaller and more irregular than in Figure 6.48, especially after 2000. The same effect on retreat rates are also apparent, with the more variable phase before 2000 averaging 4.5 m a^{-1}, while the period after averaged 3.2 m a^{-1}.

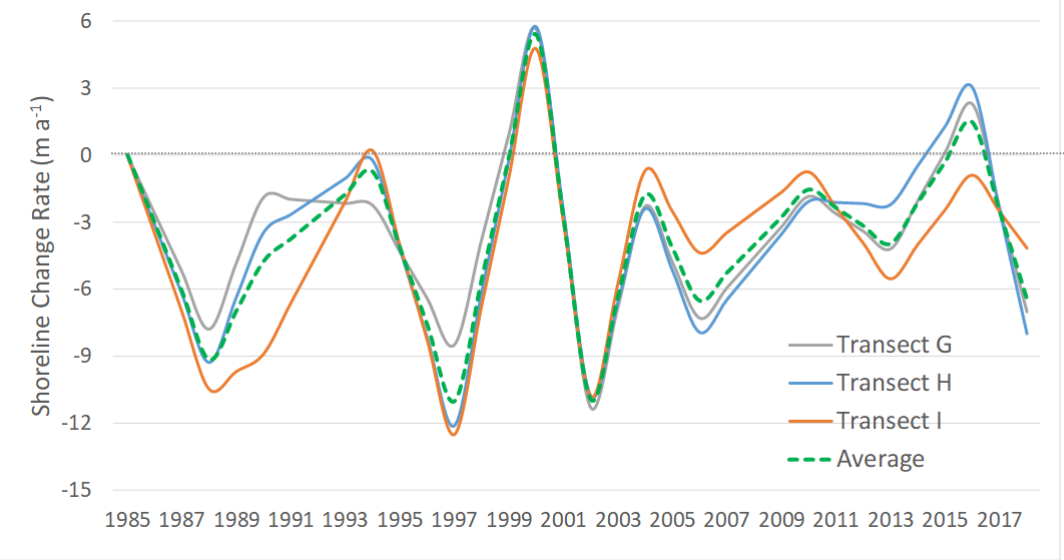

Figure 6.50: Pattern of shoreline retreat and progradation between 1985 and 2018 for transects following the northing 573550 (G) 573575 (H), 573600 (I), and the average of all three

Examination of the changes in the frequency and amplitude of SLR and progradation from 1985 to 2018, a clear pattern of a peak is apparent between 2000 and 2006, with minor peaks around 1990 and at the end of the period (Figure 6.51). The phase from 2000 to 2006 is associated with the fastest retreat rate of 4.8 m a^{-1}. The period before and after averaging 3.8 m a^{-1} and 2.2 m a^{-1} respectively. The shorter periods of increased variability, from 1987 to 1991 and 2012 to 2018, produced average SLR rates of 4.7 m a^{-1} and 3.0 m a^{-1} respectively. This strengthens the link between the presence and thickness of massive ice and greater rates of shoreline retreat, as despite eight years where variability in SLR rates have increased, there has not been a corresponding increase in the average SLR. This also allows question number 5 to be answered

5. Why did the overall reduction in elevation and slope angle not result in increased SLR rates?

Despite a link between reduced elevation and slope angles, and increased SLR across individual time periods discussed in section 6.4.1, the overall reduction in elevation and slope from 2004 to 2018 did not produce an increase in SLR. From observations in the published literature, SLR is closely related to ground ice content such as massive ice.

Additionally, from the analysis in this chapter, the reduced SLR appears to be related to the reduction in massive ice thickness, as evidenced by the much thinner exposures along the headwalls of Peninsula Point (section 6.5.1.3). This is likely due to decrease the input of meltwater into the slump floor, diminishing the water content of the mud flow and slowing the transporting of material into the sea. It also results in a build-up of material on the slump floor providing increased protection against waves and swells, further reducing SLR rates (Figure 6.36, Figure 6.42 and Figure 6.43). Another aspect is that thick bodies of massive ice can produced large PRTSs, such as the west of Peninsula Point. These PRTSs can rapidly remove volume, resulting in pulse of volume transport towards the shoreline, enhancing short-term variability. Over time, the volume loss lowers the elevation and slope of the landscape, leaving a thin base of massive ice along the old slump floor and promoting faster SLR rates. As such, the reduction in massive ice exposure has slowed the rates of SLR. This is likely to be part of the long-term trend, but enhanced by recent variability, such as with the mud lobe that formed in 2017.

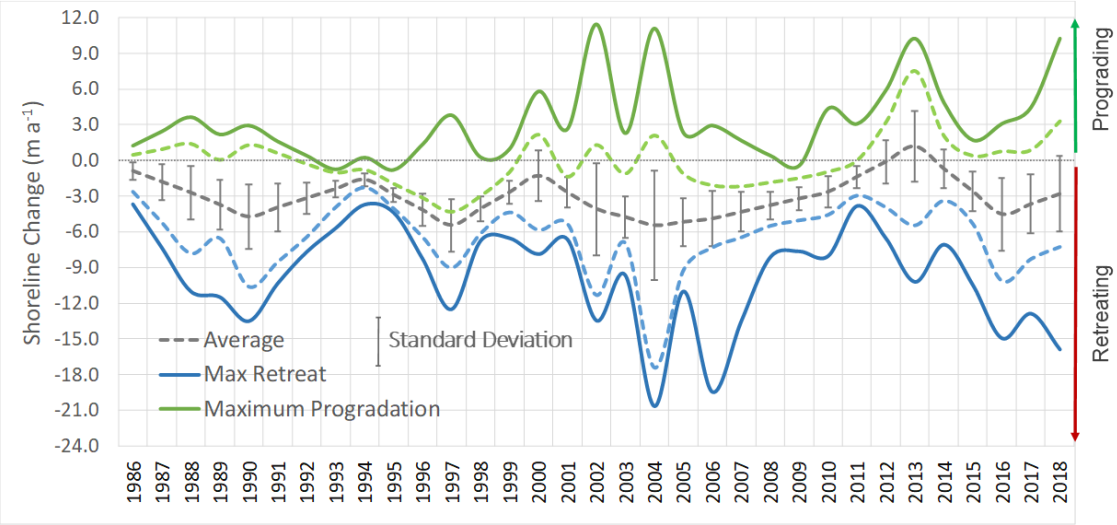

Figure 6.51: Variations in the shoreline change rate between 1985 and 2018. The average rate is shown by a grey dashed line with bars representation the standard deviation. Blue represents the maximum retreat and dashed blue the fifth highest retreat. Green shows the maximum progradation rate and dashed green the fifth highest

6.5.2.3 Massive Ice variability and Topographic Change

Two questions remain to be answered. These are:

3. What drove the reversal in the pattern of elevation and slope across Peninsula Point between 2004 and 2018?

4. Why was there a reversal in the spatial pattern of SLR after 2004?

From the analysis thus far, it appears likely that these two observations are related to each other, and that massive ice variability plays a key role.

6.5.2.3.1 The 2004 SLR Reversal

It was established in section 6.2.7 that the along-shore SLR rates for 2004 to 2016 were most closely correlated with the rates during 1994 and 2004, with an r of -0.83. The reason for this reversal was unclear. The 2004 to 2016 SLR rate was also negatively correlated with the 150 m elevation and slope variations, meaning that where elevation was highest in 2004, and the rate of elevation change the greatest, the SLR rate was slower (Figure 6.52). The starkest changes occurred in the western transects so this will be the primary area of focus.

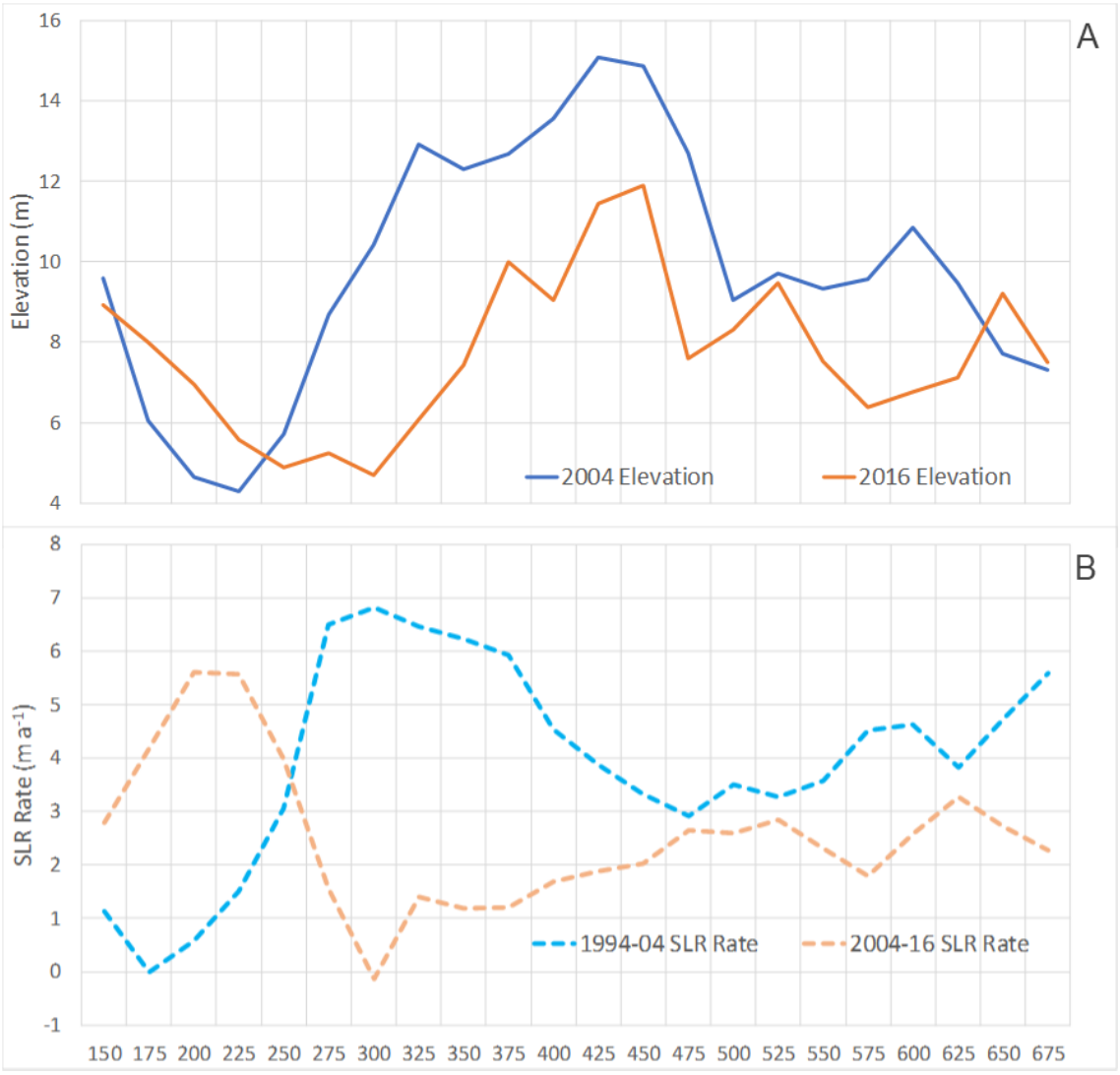

Figure 6.52: Elevation averaged 150 m inland (A) and SLR rates (B) across all transect lines

The highlighted region “A” in Figure 6.53I indicated the path where thawed material likely flowed towards the shoreline, acting as a buffer against SLR, as evidenced by the close proximity of both the 1994 (blue) and 2004 (pink) shoreline positions. The flow direction is largely confirmed by analysis of the drainage patterns, displayed as white lines in Figure 6.53II, using the hydrology spatial analyst toolset in ArcGIS 10.3. Region “B” also appears favourable for the flow of thawed material, with a clear HWR since 1994 and a steep slope. However, the drainage pattern here suggests a reduced supply compared to section “A”. Instead, region “B” experienced one of the fastest rates of SLR for 1994 to 2004. Analysis of the SLR for section “A” (B) in the periods 1994-1997, 1997-2000, 2000-2002, and 2002-2004 reveal a highly dynamic situation, with rates of -0.8 (5.7) m a^{-1}, 6.5 (4.9) m a^{-1}, -4.7 (-2.4) m a^{-1} and 2.6 (-19.0) m a^{-1} (negative values representing retreat, and vice versa). Both exhibit phases of progradation and retreat, but only section “B” experienced a large retreat in the last time period.

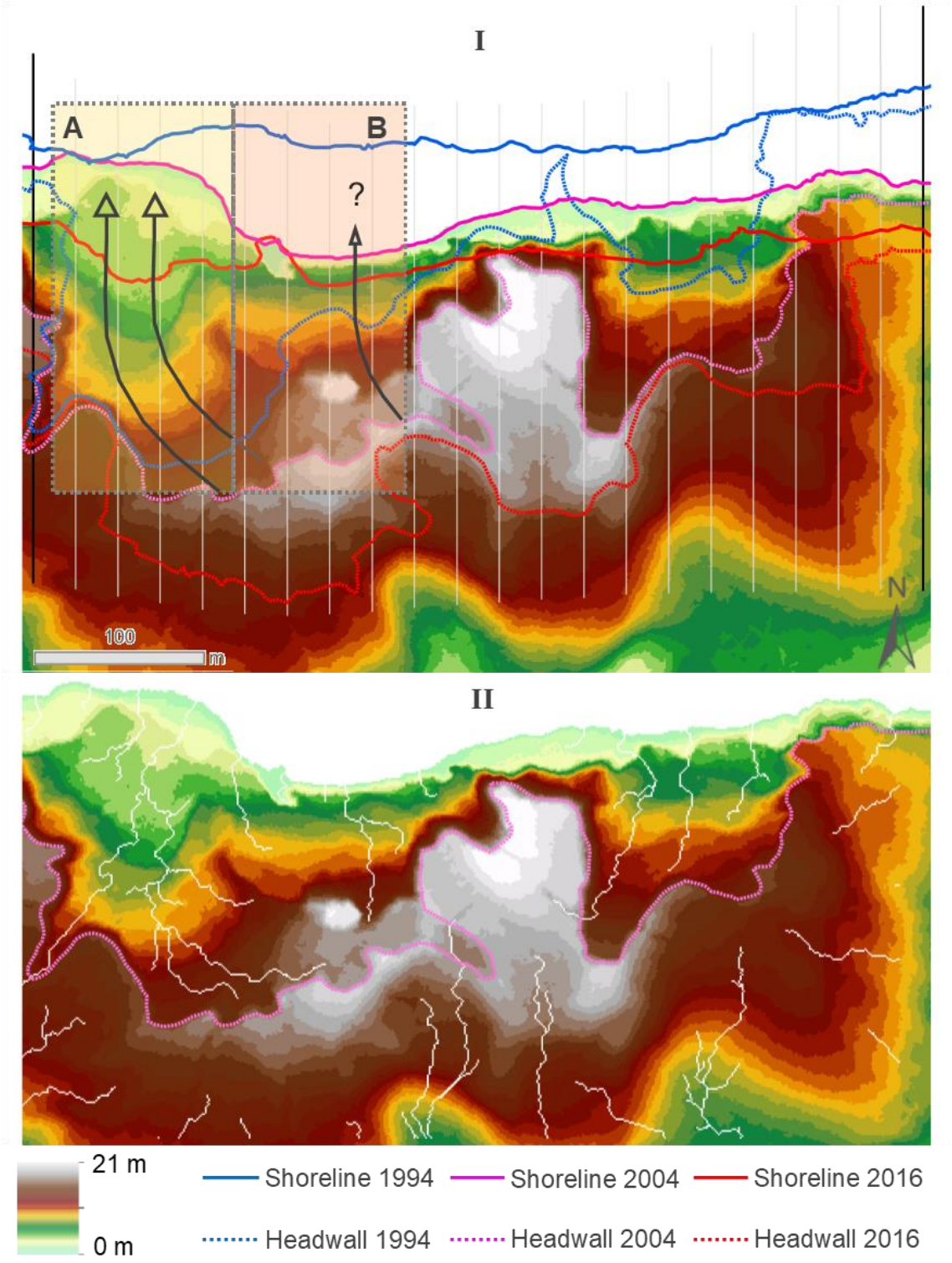

Figure 6.53: 2004 DEM displaying the shoreline position and inland headwalls from 1994, 2004 and 2016 (I) and the watershed slow lines, likely to represent the thawed material flow paths

Figure 6.54 has the same features as Figure 6.53, but with the 2016 DEM on top (I) and the elevation change between 2004 and 2016 on the bottom (II). Here opposite trends are found in sections “A” and “B”. Once more, there is evidence of a large retreat in the slump headwall and a corresponding lowering of elevation within the

slump floor of up to 13 m. All this is indicative of large quantities of thawed material being transported towards the shoreline in section “A”, which should, in theory, result in a slower SLR rate. However, drainage analysis this time suggests only a weak tendency for material flow in this region (thin white lines, difficult to see), possible due to the reduction in slope gradient along the slump floor, from an average of 5.0° in 2004 to 1.6° in 2016. Instead, the area sees the fastest SLR of the 2004 to 2016 period. Looking at the SLR for the 2004-2006, 2006-2010, 2010-2013 and 2013-2016 periods for “A” (B), rates of 4.5 (-0.3) m a^{-1}, 5.5 (2.4) m a^{-1}, -4.2 (-7.0) m a^{-1} and 13.3 (8.1) m a^{-1} are found, the pattern of progradation being followed by rapid retreat once again evident.

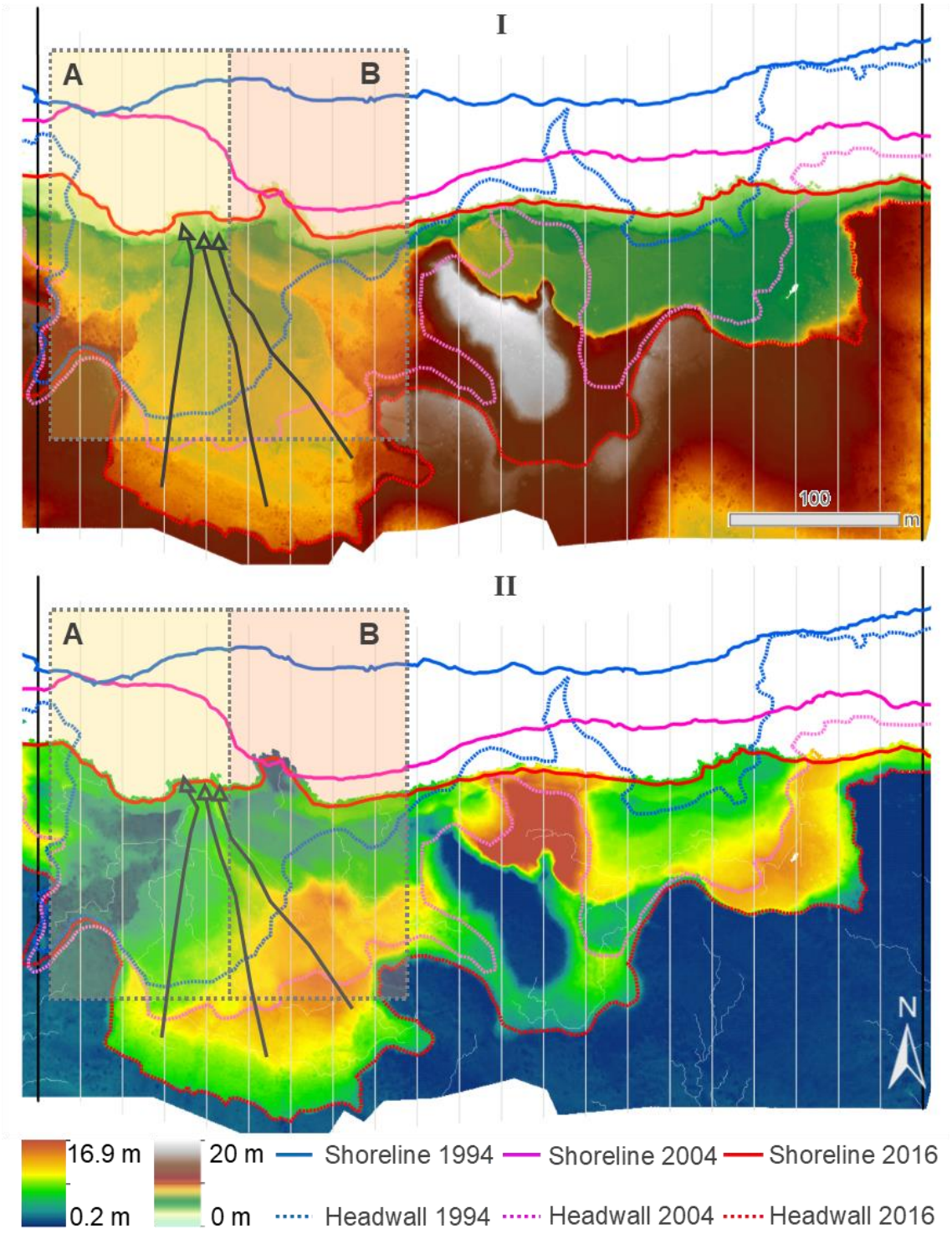

Figure 6.54: 2016 DEM displaying the shoreline position and inland headwalls from 1994, 2004 and 2016 (I) and the watershed slow lines, likely to represent the thawed material flow paths displayed over the elevation change between 2004 and 2016 (II)

The patterns appear complex, but a few processes are apparent that provide coherent and therefore potentially predictable responses. Firstly, the cycle of progradation and retreat exists in both section A and B. However, between 2000 and 2002, section A continued to be supplied by material from a larger catchment area, even from over 150 m inland, as suggested by the drainage patterns. This resupplied sediment, slowing the

SLR between 2002 and 2004, while section B, with less input material, underwent rapid SLR during the same period. After 2004, section A had a large, low angled and low-lying mud lobe (average 100 m elevation of 3.2 m and slope angle of 2.6°) which would be open to rapid removal once the flow of thawed material weakened. Section B had a steep, high elevation area behind it after 2004 (100 m averages of 8.7 m and 8.6°), offering more protection from rapid SLR. The variability for section A rapidly increased after 2004. A total of 31 m retreat between 2004 and 2010 in section A, with only 9 m in section B. Progradation then occurred in both areas between 2010 and 2013, with totals of 12.7 m and 21.0 m, respectively, before both regions underwent retreat in the following three years totalling 39.8 m in section A and 24.3 m in section B. By 2016, the 100 m elevation and slope angle had been largely equalised in both sections. Massive ice dynamics acts as a key control throughout these processes. The large slump in the west, present in all years, extends inland up to 200 m from the shoreline and has undergone multiple phases of HWR. This is only possible where a thick massive ice body is present. Re-exposure of the ice and rapid ablation has contributed to the pulses of shoreline progradation in the western half of Peninsula Point. The alterations to sediment supply, elevation, slope (driven by massive ice variations) therefor play a critical role in the apparent switch in rates of SLR between 1994 to 2004 and 2004 to 2016.

6.5.2.3.2 The 2004 to 2018 Topographic Changes

From section 5.4.1.2, it was noted that the elevation switched from a high centre relative to the edges in 2004, to a lower, more broadly similar average elevation in 2018. The overall pattern of change in Figure 6.55 is notable. The outer transects are highlighted by darker lines, while the inner transects are highlighted by the lighter lines.

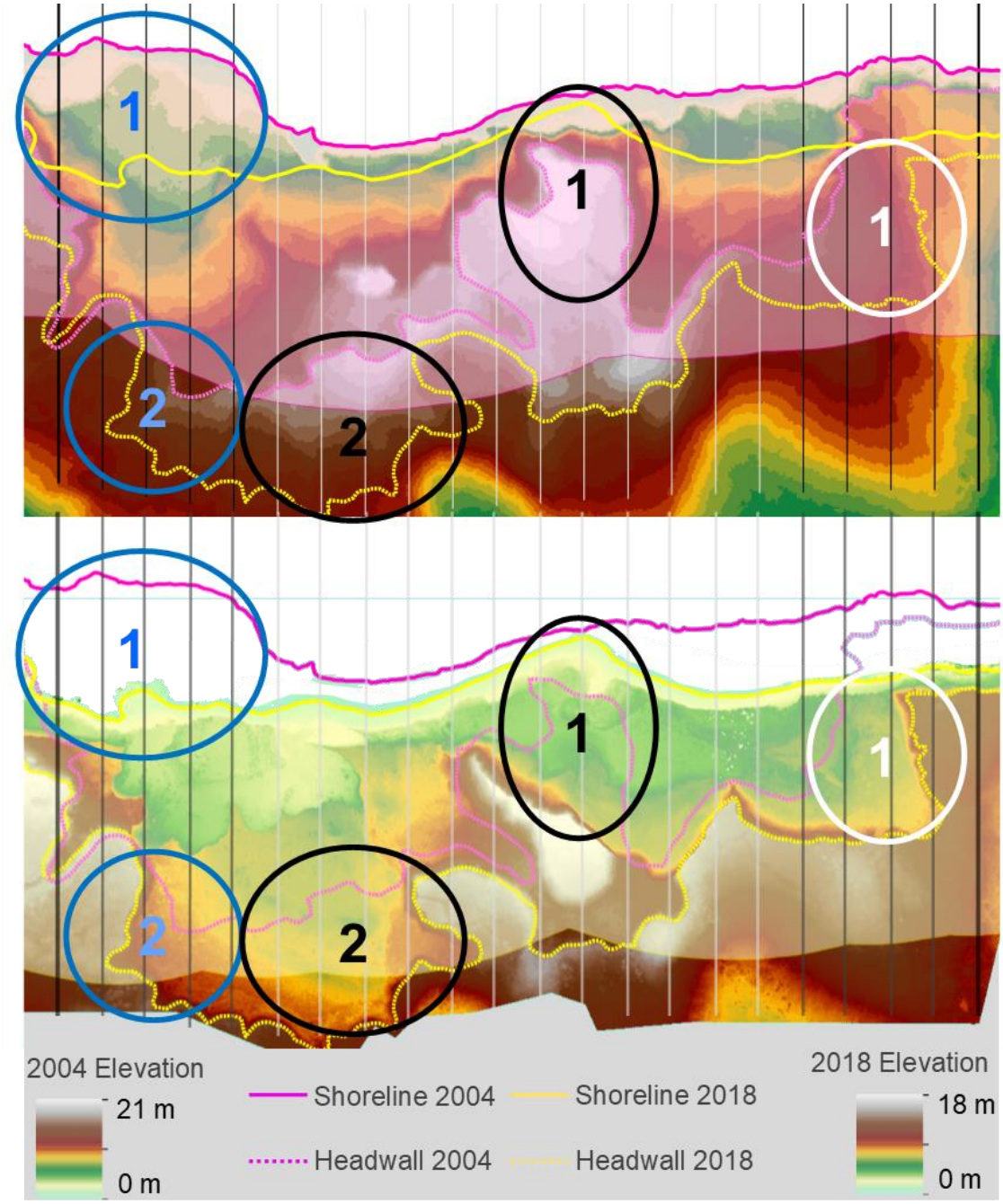

Figure 6.55: Elevation in both 2004 (top) and 2018 (bottom) along with the shoreline position with a 150 m inland buffers and headwall positions. Key areas are highlighted to explain the pattern shift in elevation for the west (blue), middle (black) and east (white).

One of the most evident changes is the distance between the shoreline and the back headwall. The average SL2HW distance increased from 104.7 m to 125 m from 2004 to 2018. This change was highly variable across the different regions. The changes between the west, middle and east SL2HW (elevation) distances were -36.5 m (+0.7 m), +42.8 m (-5.0 m) and +23.4 m (-1.7 m) respectively. The overall correlation between the SL2HW distance and 150 m average elevation change was -0.84 (Figure 6.56). It appears that the change in the pattern of elevation is linked to the changes in

SL2HW distance. Which, in turn, is largely governed by HWR rates and variability — all tied with massive ice body variability.

The large elevation reduction in the middle 12 transects is a result of several factors. Due to a combination of a thin IT exposure and a thick OB, the headwall is retreating as a tall whole instead of gradually decreasing overtime through multiple phases of HWR. The large volume loss has also produced a mud lobe, creating an area of low elevation, removing the highest elevation on the site and increasing the SL2HW distance (black oval 1 in Figure 6.55). The three transects affected by this process produced an average elevation drop of 7.3 m. On the western side of the middle section there is an area of four transects that experienced slow SLR but a large HWR, increasing the SL2HW distance and mass wasting, resulting in a drop in elevation of over 10 m across a wide area (black oval 2 in Figure 6.55 and Figure 6.54II). These four transects experienced an average elevation drop of 6.2 m.

The eastern five transects recorded a more moderate reduction in elevation overall. This is due to the headwall extending inland by 107 m along two transects (white oval 1 in Figure 6.55), while the SLR averaged 44 m. This increased the SL2HW distance, producing an average elevation drop of 3.1 m.

Counter to expectations, the western five transects recorded an overall increase in elevation, for two reasons. Firstly, as highlighted by blue oval 1 in Figure 6.55, a large area of low elevation ground was removed by SLR. This resulted in a large reduction in the SL2HW distance, meaning more high elevation ground is incorporated when calculating the average elevation over 150 m, producing a 1.5 m increase. On the inner most two transects, HWR and mass loss between the shoreline and headwall produced a slight drop in elevation of -0.7 m (blue oval 2 in Figure 6.55), not enough to counter the elevation gain on the outer transects.

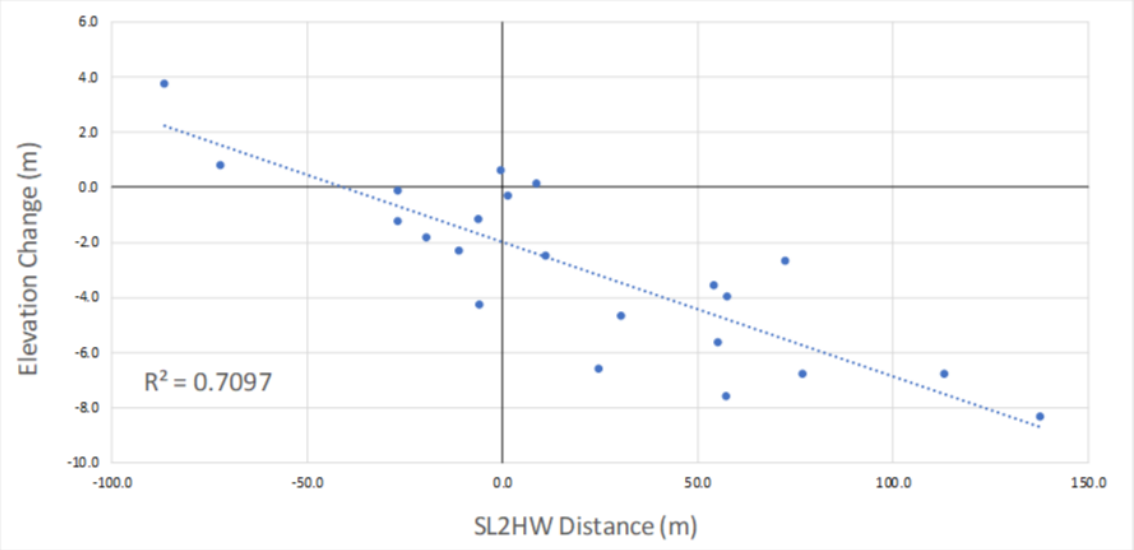

Figure 6.56: Relationship between the shore to headwall distance and the change in the 150 m average elevation between 2004 and 2018

The variations described are all tied to massive ice variability. The thin ice exposure in the middle causing the retreat of a tall elevation headwall (~10 m). The massive ice in the west producing a large PRTS with extension of the headwall and lowering of slump floor elevation through multiple phases of HWR. The variability in ice on the eastern side, causing steady SLR and HWR where massive ice was absent and fast HWR and elevation loss where it was present. This variability is largely responsible for equalisation the along-shore elevation and slope values from 2004 to 2018.

6.5.2.4 Summary: Decadal Massive Ice Controls

It has been revealed that many the significant changes on Peninsula Point are directly or indirectly tied to massive ice body variability. Many of the connections are complex and time varying, with a mix of quantitative and qualitative analysis required for their identification. However, variability in slope and elevation patterns, reversals in the spatial and temporal SLR rates, SL2HW distance variations and even decadal trends in overall SLR rates — all can be linked to variations in massive ice thickness and surface elevation.

6.5.3 Massive Ice Body Controls: 1935-2018

6.5.3.1 Massive Ice changes

Thick massive ice exposures were present in the earliest recorded observations of Peninsula Point. Mackay (1986) provides field-based images from 1954 (Figure 6.57A) and oblique aerial imagery from 1975 (Figure 6.57B), while field photos from 1989 (Murton, 2009; Figure 6.57C) demonstrate that the thick, widespread massive ice exposures have been present for over half a century at least. The topography of

Peninsula Point has been described within the literature as a flat-topped hill and slightly domed towards the middle, with a topographic pattern suggesting a high likelihood that the thick massive ice apparent from field observations underlie the majority of the site (Mackay 1971; Mackay 1986; Mackay and Dallimore, 1992). This appears at odds with recent observations, where large variations in topography are apparent and a reduction in the average massive ice thickness exposures has been observed. As such, there appears to have been a widespread change in both the topography and thickness of exposed massive ice on Peninsula Point.

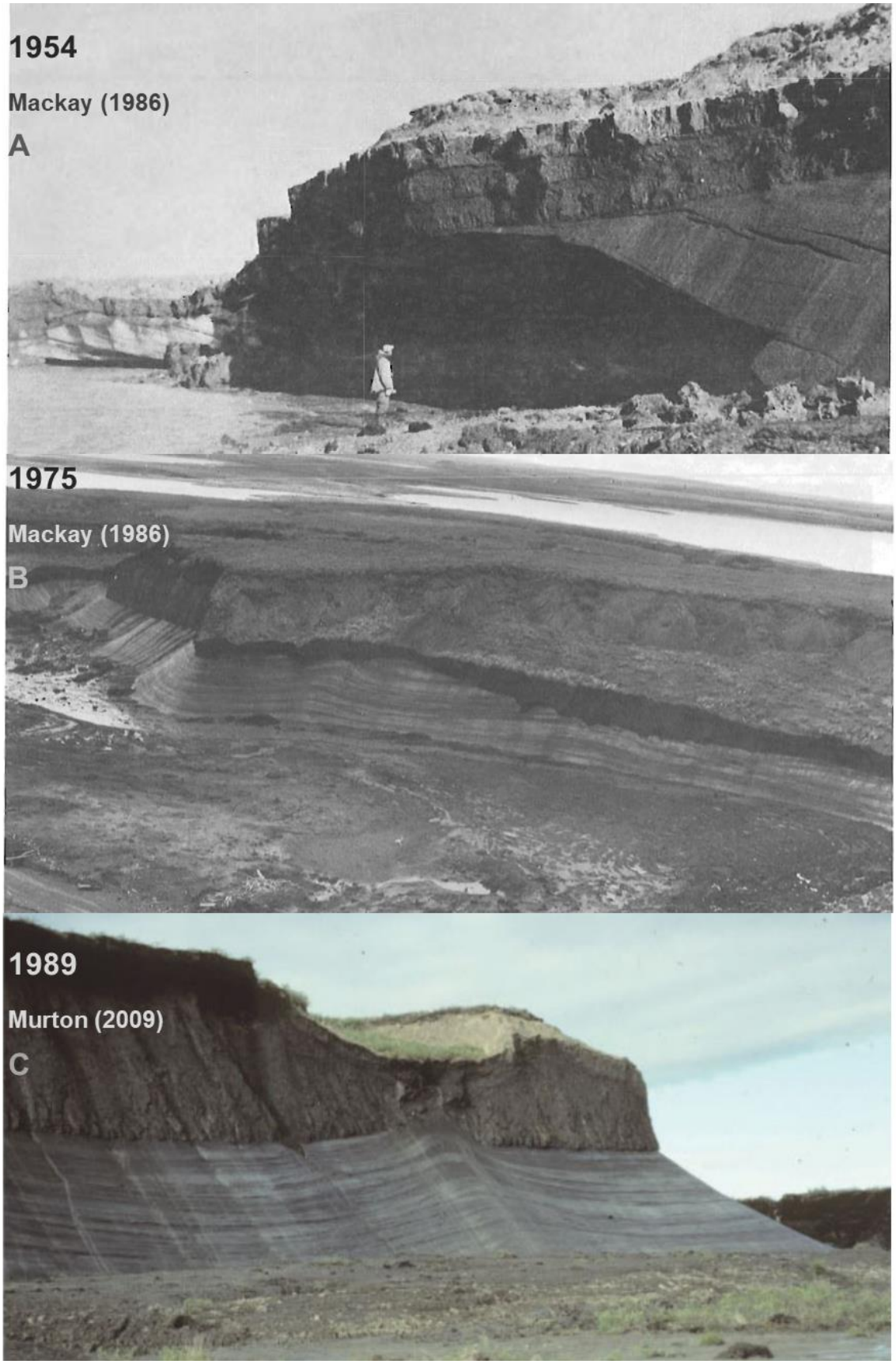

Figure 6.57: Photographic evidence of widespread thick massive ice exposures. First two images are from Mackay (1986) while the bottom image is from Murton (2009).

6.5.3.2 SLR Variations

It was noted in section 5.3.2.1 that between 1935 and 1985, the fastest SLR rates occurred in the middle of Peninsula Point with slower rates on both sides. This pattern then reversed from 1985 to 2018. SLR calculations from section 5.3.1 were performed along 11 transects due to the low resolution of the imagery, rather than the 22 used for 1985 to 2018. To make both comparable, the 1985-2018 measurements were averaged to produce 11 equivalent lines of measurements (Figure 6.58). The correlation between the two rates is -0.89.

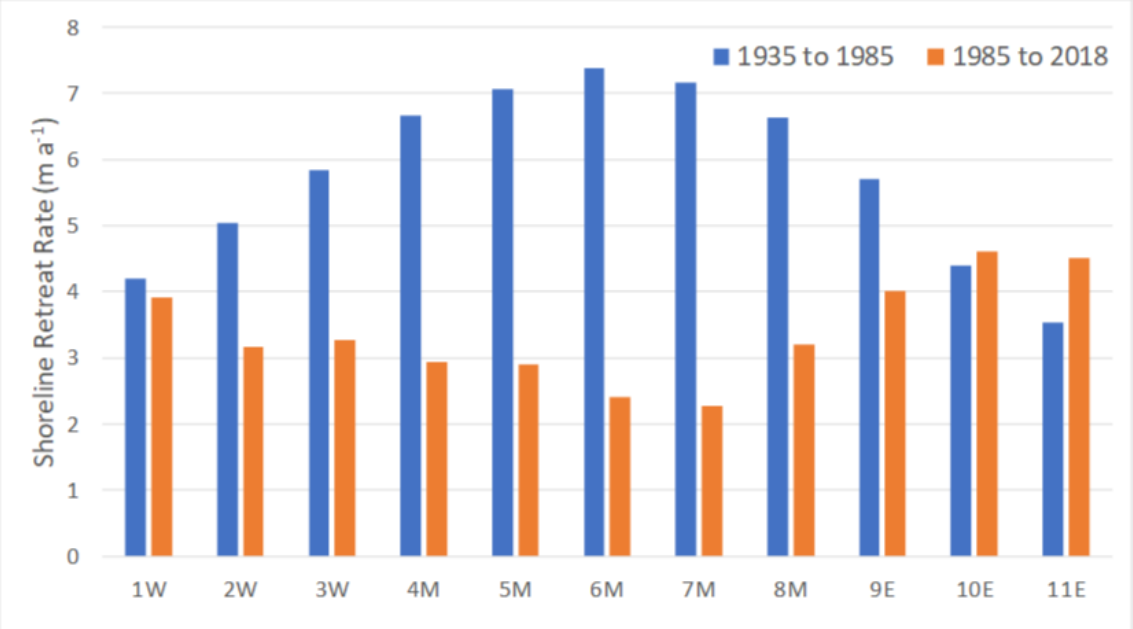

Figure 6.58: SLR rates for the 1935 to 1985 period (blue) and 1985 to 2018 (orange) along 11 transects, three in west, five in the middle and three in the east.

The slowdown in SLR rates and the increasingly large rate differences towards the middle are also apparent in Figure 6.58. Another notable feature from the historical aerial imagery is the shape of the north shoreline. In 1935 the middle extended out seaward relative to the sides in a convex pattern, switching to a concave form by 1985

before flattening out in 2018 (Figure 6.59; Figure 6.60). From the analysis of massive ice, several features can help to explain the trends and patterns observed since 1935:

- SLR rates increase in the presence of massive ice
- SLR rates on Peninsula Point have slowed between 1935 and 2018
- Reports of massive ice on Peninsula Point through the 20th century are illustrative of widespread thick ice exposures
- The thickness of massive ice exposures has been greatly reduced on Peninsula Point in recent years
- Observations reveal that the massive ice can undergo significant shifts in elevation and slope over distances of a few meters, which can alter headwall and SLR rates
- The spatial pattern of SLR since 1935 has displayed both short- and long-term variations

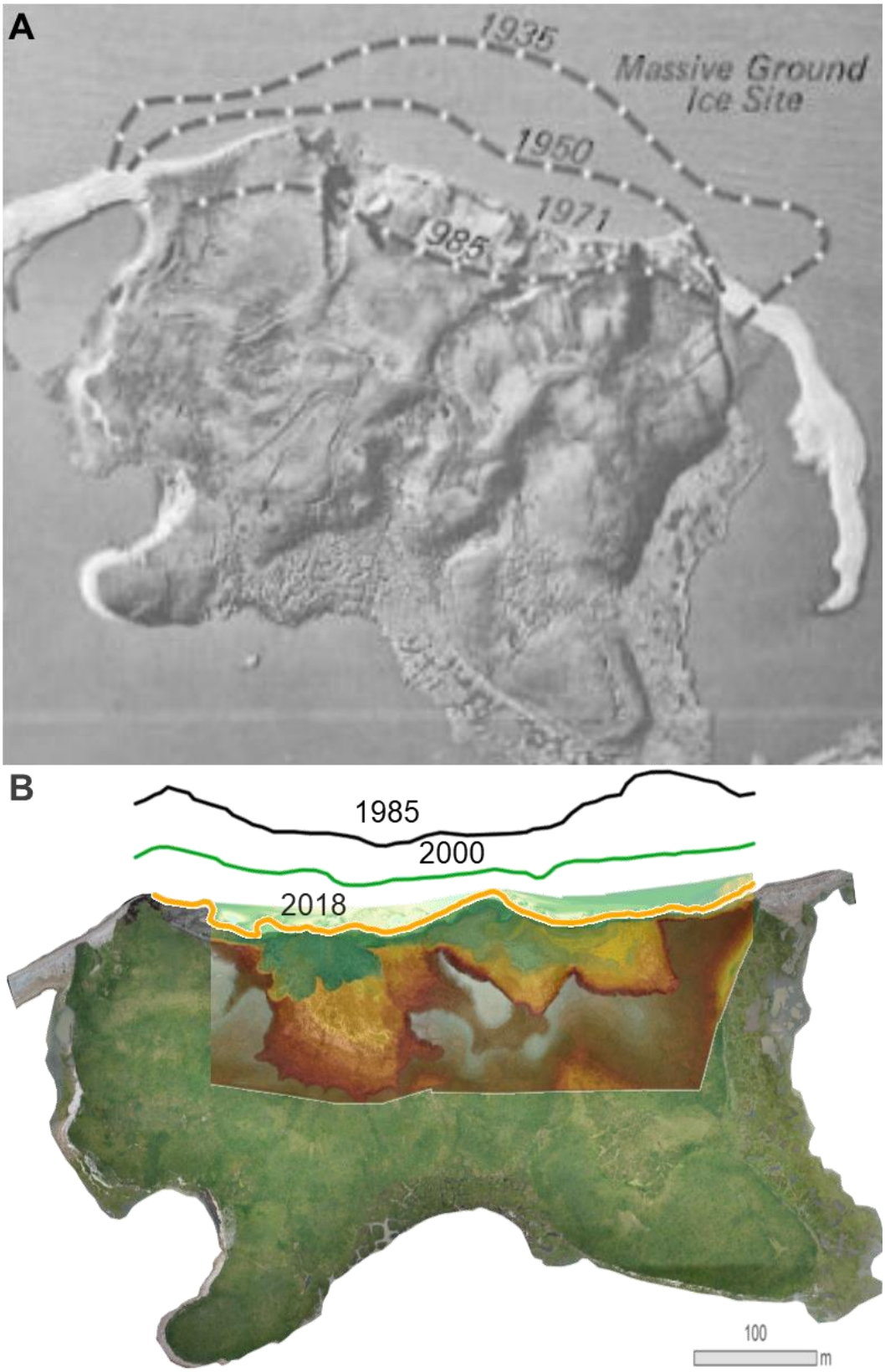

Figure 6.59: Aerial imagery from 1971 (A), with the shorelines from 1935, 1950 and 1985 (Mackay 1986). 2018 orthomosaic (B) with DEM overlay and shorelines from 1985, 2000 and 2018.

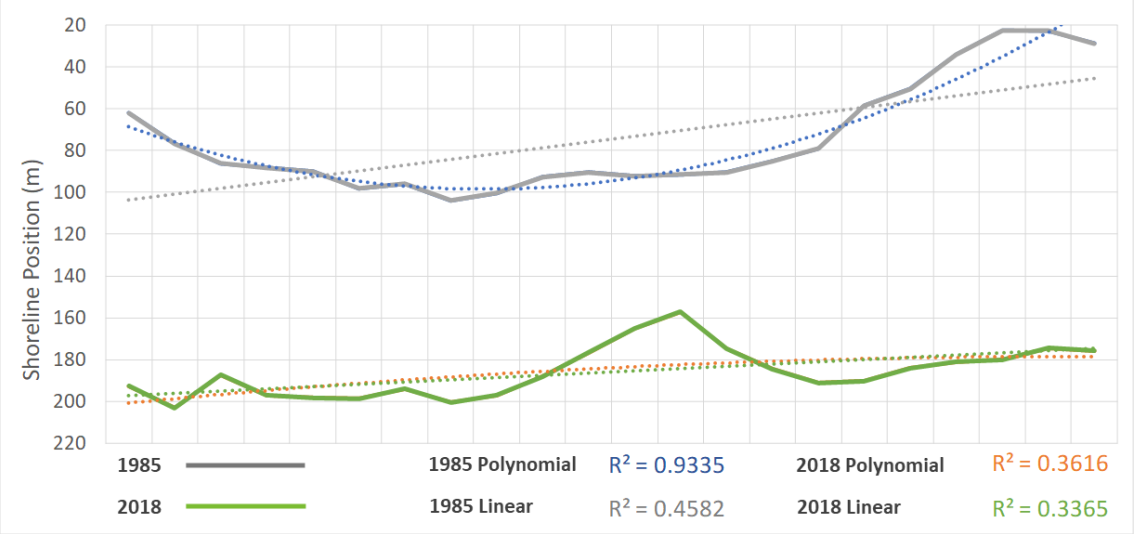

Figure 6.60: Shoreline positions in 1985 (grey) and 2018 (green) relative to arbitrary straight line 20 m from 1985. Comparison of first order polynomial trends and linear trends are used too assess the convexity of the shoreline.

It appears that SLR patterns, both spatial and temporal, are closely related to massive ice variability. This relationship is also evident throughout the Arctic, as described in section 6.5.2.2. The spatial pattern of SLR from 1935 to 1985, and the subsequent reversal towards 2018 should be no different. Observational evidence supports a widespread massive ice body along much of Peninsula Point, especially across the middle during the 20th century. Both aerial, satellite and drone-based imagery and DEMs also suggest less evidence of recent mass wasting towards both the eastern and western ends of Peninsula Point, which suggests that massive ice may not be as thick or as prevalent. This all points towards a large-scale pattern of high elevation ice towards the centre of Peninsula Point around 1935, with a gradual reduction in surface elevation further south, east and west (Figure 6.61). Between 1935 and 1985, repeated exposure of this thick ice allowed for a pattern of fast SLR rates across the middle of Peninsula Point relative to the sides, (average rates of 7.0 m a^{-1} in the middle, 5.0 m a^{-1} in the west and 4.5 m a^{-1} in the east) This resulted in the convex shoreline of 1935 switching to a concave pattern by 1985. From 1985 to 2018, as the ice exposure gradually reduced in elevation, so too did the SLR rates across the middle of Peninsula Point, to 3.2 m a^{-1} from 1985 to 2002, and 2.5 m a^{-1} from 2002 to 2018. At the same time the east and west edges, now more exposed and vulnerable to retreat, maintained a relatively faster rate of SLR (2.7 m a^{-1} and 4.1 m a^{-1} for 1985 to 2002, and 4.4 m a^{-1}

and 2.6 m a^{-1} respectively for 2002 to 2018). This resulted in a gradual flattening out the of the north shore profile (Figure 6.60).

Superimposed on the broad scale ice dome from Figure 6.61 are small scale undulations. These may be related to mass wasting during the early Holocene which allowed for differential uplift of the massive ice, more recent thermokarst activity resulting in ablation of the ice surface, or elevation differences where the massive ice originally formed between lower deltaic sands and overlying diamicton (Lacelle *et al.,* 2004; Mackay and Dallimore, 1992; Murton, 2009). These small-scale features contribute to the massive ice thickness variations noted from field surveys and the resulting patterns of RTS activity, mass wasting and SLR variations seen since 1935.

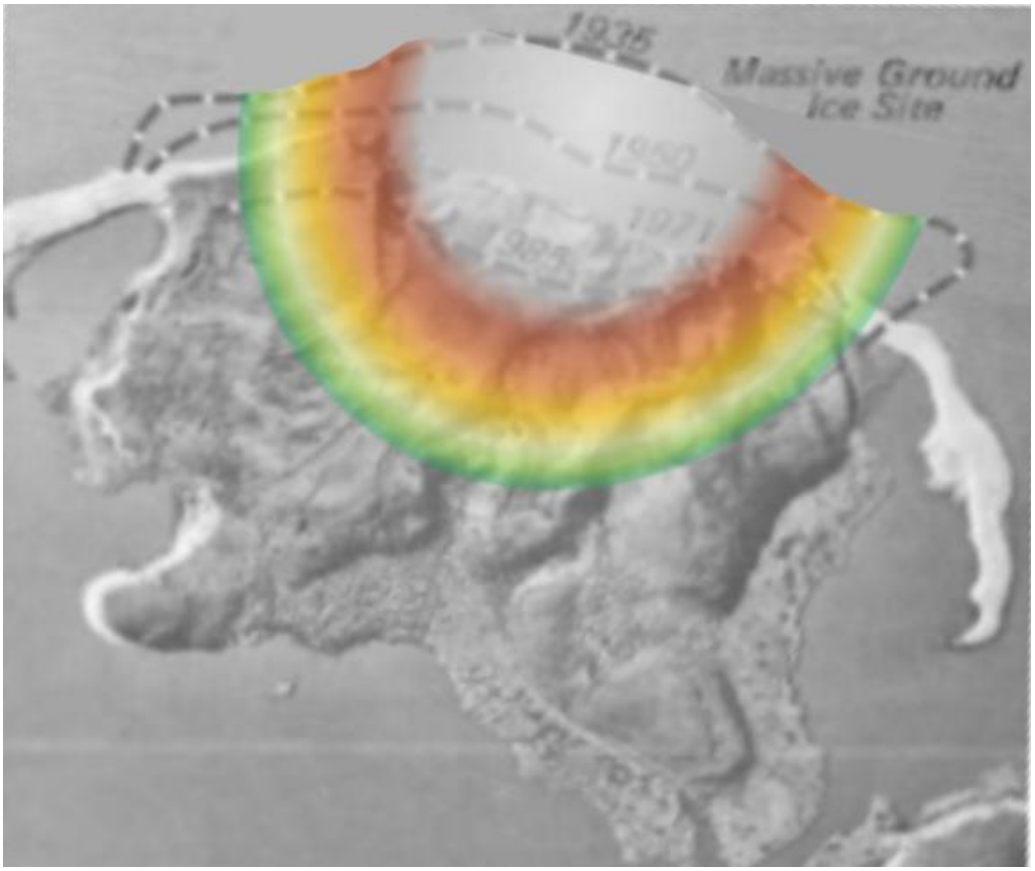

Figure 6.61: Estimate of the broad scale massive ice elevation pattern draped over the 1971 aerial image from Mackay (1986). White represents massive ice thickness over 10 m above sea level, gradually tapering off to a few meters along the green edge

6.5.4 Summary: Massive Ice Body Controls

Spatial and temporal differences in massive ice thickness on Peninsula Point have been shown exert a strong influence on coastal dynamics from inter-annual to multi-decadal time spans. This ranges from significant controls on inter-annual HWR rates, to decadal topographic variations, quasi-cyclic SLR variability and historical SLR trends.

Passive seismic monitoring was demonstrated to be an effective method for accurately detecting and mapping massive ice surface elevations. This offers a new means of improving predictions and analysis of RTS dynamics and assessing the future local and regional landscape response to changes in external forcing.

6.6 Summary: Controls on Coastal Change

This chapter set out to examine the controls on coastal permafrost dynamics on Peninsula Point. For SLR, areas with high elevation and slope tended to be more resistant and were associated with slower SLR rates. This is especially true for areas that underwent large reductions in slope and elevation, likely due to the buffering from thawed material transported towards the shoreline. This relationship is partially borne out in volume changes too, as reductions in elevation and slope are strongly associated with volume loss. HWR and SL2HW distance are also shown to linked with volume, due to their association with thaw slumps and related mass wasting processes. Indeed, the distance from the shoreline to the headwall appeared to be limited to approximately 200 m. As such, the SL2HW distance acted as a strong control on HWR rates.

The incorporation of massive ice further elucidated the coastal dynamics and provided explanations for the exceptions and anomalies discovered within the topographic and climate controls sections (sections 6.3 and 6.4). The effects of the IT and OB variations, both along and cross-shore, were examined in detail at key areas on Peninsula Point. A thin OB and a persistent ice exposure were found to be critical in promoting fast rates of retreat in active headwalls, exemplified by a maximum HWR observation of 54 m between 2017 and 2018. Furthermore, decadal trends in elevation, slope, HWR and volume can be linked directly or indirectly to massive ice body variability. Both fast SLR rates and increased short-term shoreline variability occur on Peninsula Point in connection with massive ice exposures, manifesting as quasi-cyclic SLR oscillations between 1985 and 2018.

From analysis of historical climate data, a long-term increase in the thaw season temperature and a weak positive trend for meridional winds were revealed. Warming temperatures are typically associated with increased SLR, but on Peninsula Point the retreat rates have slowed from 5.8 m a^{-1} between 1935 and 1985, to 3.4 m a^{-1} from 1985 to 2018. Meridional wind changes also failed to explain the SLR trends. However, published observations provide strong evidence of widespread massive ice exposures on Peninsula Point of up to 10 m during the 20th century (Gilbert *et al.,* 2016; Mackay and Dallimore, 1992; Moorman *et al.,* 1998; Murton, 1999), a feature that has become

largely absent in recent years. Indeed, the historical decline in SLR rate is attributed to the reduction in the massive ice thickness and distribution. This is a feature not previously described within the academic literature.

Finally, headwall exposures of massive ice in 2018 demonstrated the accuracy and effectiveness of passive seismic data in measuring the massive ice surface. The passive seismic data accurately reflected ice surface elevation changes that were the reverse of those predicted from headwall exposures, both improving estimates of relative HWR rates and illustrating the weakness of extrapolation massive ice thickness and surface elevation from visual observations alone.

7 Discussion

7.1 Introduction

This research has explored the role of massive ice and topography as controls on the evolution of RTS dominated coasts, using the type locality for intra-sedimental massive ice: Peninsula Point. This was achieved by analysing the influence of massive ice thickness and surface elevation variability on internal controls, such as ALD, elevation and slope, and external controls, such as climate trends. This required analyses over a range of spatial and temporal scales, from grain size variability, to high resolution surface modelling and multi-decadal SLR trends. It also required the use of emerging technology and novel applications, such as SfM-MVS point cloud generation and passive seismic detection of massive ice depths. By integrating these data and results gained from this multi-scale approach, a coherent model of the long-term evolution of Peninsula Point has emerged – one that stands in contrast to other ice-rich Arctic coastlines. The significant warming trend during the thaw season, which contributed to increases in SLR in many similar areas, appeared to have no influence on SLR trends on Peninsula Point. Topographic features such as elevation and slope were found to exert a weak, but significant, influence on coastal dynamics from annual to decadal time spans. However, massive ice was found to play a pivotal role across all timescales from inter-annual headwall dynamics to historical SLR trends.

This chapter will briefly discuss the main observations and results, comparing and contrasting them with similar observations within the published literatures. These will be separated into:

- Fine scale data – ALD, grain size, CTS, ice surface modelling
- Multi-temporal trends – SLR, HWR, volume, slope and elevation
- Controls on the coastal dynamics with a focus on massive ice

A series of conceptual models will then be presented. These will aim to collate and distil the results of this research into focused advances in coastal permafrost science, highlighting the influence of massive ice variations on coastal dynamics. Finally, the summary will discuss the importance of the results, the implications and limitations.

7.2 Fine Scale Characterisation

Field work and lab analysis provided information on ALD, soil grain size and CTS values across a section of Peninsula Point containing a thaw slump affected low ground with undisturbed high ground either side to the east and west. Massive ice

surface and overburden thickness variations were also assessed through the novel application of passive seismic monitoring.

Substantial differences in some soil characteristics are associated with the topographic features. The high ground contained an average ALD of 0.39 m while the low ground active layer extended an average of 2.5 m to the surface of the ice dome, due to previous RTS phases. This distribution was in agreement with previous research which demonstrated that the ground thermal regime becomes disturbed during thaw slumping, causing a reduction or elimination of the near surface permafrost which requires decades or more to regain thermal equilibrium (Burn, 2000; Burn and Friel, 1989). This elimination of the permafrost also leaves the buried massive ice subject to surface energy fluxes, increasing the risk of future thaw slumps being triggered and allowing ground surface subsidence to occur as the buried ice continues to melt (Farquharson *et al.,* 2019).

Grain size distributions were not significantly different between the active low ground and undisturbed high ground, averaging 17.5% clay, 73% silt and 9.5% sand, with a slight increase in the coarser grains and decrease in the finer grains in the low ground soil. This is also in agreement with grain size comparisons on similar features on Herschel Island where a similar, non-significant, difference was noted (Lantuit *et al.,* 2012b). A combination of the topographic features and hydrological interactions appear to explain small differences. The active ground area sits as a depression between the two high ground segments. It also contained no permafrost between the ground surface and massive ice, allowing melt water to flow into and through the soil. This flow may cause finer grains to be washed out and transported towards the sea. Additionally, coarse grains may be added through thawing headwall permafrost and from grains embedded within the massive ice that are deposited upon ablation. These factors may contribute to measured grain size differences. Grain size does not, however, appear to explain the variances in RTS activity on Peninsula Point.

CTS values were significantly higher and more variable in the active, low ground than the stable high ground. While there was no directly observable cause, it is possible that salt frozen within the local permafrost was leached into the low ground soil during thaw slumping. Alterations to soil salinity have been observed elsewhere in the Canadian Arctic, resulting from similar forms of soil disturbances (Kokelj and Lewcowicz, 1999). In regions where salt leaching can occur, its presence in the soil may act as a proxy for previous soil and terrain disturbances, offering a means of detecting previous RTSs in stabilised terrain.

The mapped massive ice surface displayed variability not apparent from field observations. Small scale wave-like undulations were observed approximately 20 m apart with a 5 m amplitude. These were super imposed over a dome like structure approximately 100 m wide with a base to peak height difference of approximately 8 m. The ground surface topography was the inverse of the ice surface, with the lowest ground surface elevation situated over the ice dome resulting in thin OB averaging 2.5 m. The high ground surface to either side contained lower elevation massive ice and a much thicker OB, averaging 10 m but with a maximum of 14.7 m. Elevation data from previous years indicate that the current low ground was the highest elevation area on Peninsula Point in 1994. By 2004, it had become a slight depression, due to the first phase of HWR and reached its modern low elevation state by 2016. This highlights the time-varying relationship between topography and massive ice, which is an important consideration when assessing topographic variability and associated volume losses in recent decades. For example, when analysing a current RTS, one might need to consider whether the current low-ground section was previously low-ground, even before being altered by RTS activity? Or might it have had a similar topographic relief or even greater than the surrounding terrain? Simple interpolations may fail to accurately represent historic topographic variability in these dynamic landscapes. These are important considerations when assessing past carbon and sediment loss. Knowledge of this time-variable relationship can also be of benefit in planetary remote sensing, such as on Mars. Here, features suggestive of widespread thermokarst have been identified across the mid-latitude plains (Balme and Gallagher, 2009; Orgel *et al.,* 2019; Séjourné *et al.,* 2012; Ulrich *et al.,* 2010; Warner *et al.,* 2010), with the Tuktoyaktuk coastlands considered a wet periglacial equivalent of the Utopia Planitia (Soare *et al.,* 2011). An improved understanding of the evolution of terrestrial thermokarst features may allow for identification of more similar features on other planetary bodies, provide insight into their formational history and associated environmental conditions.

The massive ice model improved the prediction of the HWR rates from 2017 to 2018, relative to simple extrapolation of retreat lines or ice exposures. The resulting massive ice exposures largely confirmed the accuracy of the passive seismic methods, with the overall surface topography of the massive ice modelled accurately. Some small differences did occur, but these were typically in the interpolated areas between measurement points. This suggests that a higher density of recordings can improve accuracy in regions with a highly variable massive ice surface. The subsurface variations in ice and overburden thickness also demonstrates that extrapolation inland

based on massive ice exposures may produce inaccurate results, illustrating the importance of high-density measurements on local scales.

7.3 Long term Trends

A record of topographic and volumetric change was created for 2004 to 2018 using a combination of LiDAR and SfM-MVS models, with HWR rates extended to 1994 through the addition of aerial imagery. Using both previously published rates (Mackay, 1986) and historical satellite imagery, SLR rates were extended back to 1935. In addition, the overall trends in massive ice thickness were extended through modern high-resolution observations and both historical photos and descriptions found throughout the literature.

The total volume measured 240 m inland of the shoreline in 2004 was 1,409,416 m^3. By 2018, 43% of that volume had been lost, with a slight increase in loss rates from 2016 to 2018 relative to 2004 to 2016. While several studies have calculated volume losses from individual thaw slumps (Lantuit *et al.,* 2005; Ramage *et al.,* 2018) or details of volume changes on sub-annual timescales (Cunliffe *et al.,* 2019) few studies have examined the broad scale or temporal trends in volume loss. Obu *et al.,* (2017), using LiDAR data for 2012 and 2013, calculated volume losses along the Yukon coast. For actively slumping areas, the volume losses ranged from 2,699 m^3 to 17,573 m^3 per 100 m. When broken down to a volume loss per metre (27 m^3 to 176 m^3 m^{-1}), it compares well with the rates calculated on Peninsula Point, with an average rate of 78 m^3 m^{-1} a^{-1} and a range of 24.6 to 120.2 m^3 m^{-1} a^{-1}. On Herschel Island, volume loss from 2004 to 2013 were 6.9, 73.1, and 23.6 m^3 m^{-1} a^{-1} for the east, north and west sides of the island respectively (Obu *et al.,* 2017). These values appear broadly in line with the results from Peninsula Point.

There were significant reductions in average elevation, maximum elevation and slope angle between 2004 and 2018. For example, the elevation averaged 150 m inland dropped from 9.8 m to 6.9 m, a reduction of 30%, and the average 150 m inland slope angle dropped from 5.0° to 3.7°, a reduction of 26%. A feature of the 2004 along-shore topography was a central segment with high elevation and steep slopes, with lower elevation and shallower slopes on both the eastern and western sides. This broad scale pattern was largely eliminated by 2018, replaced with a more uniform topography, reduced elevation and more shallow slope gradients. This appears to be the first analysis of decadal scale changes in slope and elevation on RTS dominated coasts.

Long term HWR rates of 4.6 m a^{-1} have slowed from 5.6 m a^{-1} between 1994 and 2004, to 2.9 m a^{-1} between 2016 and 2018. The long-term HWR rates are significantly faster than the rates of 50 headwalls monitored by Lantz and Kokelj (2008), with average retreat rates of 0.6 m a^{-1} from 1950 to 1973, and 1.1 m a^{-1} from 1973 to 2004. The difference is likely related to the coastal setting of Peninsula Point, allowing the massive ice to become exposed more frequently through SLR, promoting more frequent phases of ablation and HWR.

Retreat rates along active headwalls in 2016, 2017 and 2018 on Peninsula Point averaged 11.7 m a^{-1}, with two transects recording maximum annual rates of over 50 m. Burn and Lewkowicz (1990) compiled a list of published maximum annual HWR rates from numerous sites throughout Canada. These ranges were typically between 7 m a^{-1} and 15 m a^{-1}, with a low in the Mackenzie Delta of 1.5 to 4.5 m a^{-1} (Mackay, 1966), and a high of 14 to 16 m a^{-1} at Mayo, Yukon (Burn and Friele, 1989). On Herschel Island, typical active HWR rates of up to 9.6 m a^{-1} are common, but 30 m of retreat is possible in exceptional years (Lantuit *et al.,* 2005). On Peninsula Point, Mackay (1986) noted that active headwalls typically experienced average retreat rates >7 m a^{-1}, which appear to agree with modern observations at the site. Active HWR rates on Peninsula Point appear close to regional averages. However, the maximum rates are significantly greater than those published elsewhere in the literature for the western Canadian Arctic. This emphasises the extreme rates of change possible with active RTSs.

The long-term SLR decreased from 5.8 m a^{-1} between 1935 and 1985 down to 3.4 m a^{-1} from 1985 to 2018, with rates averaged over a decade or more ranging from 1.9 m a^{-1} (2006 to 2017) to 7.7 m a^{-1} (1935 to 1950). The majority of studies examining the rates of SLR in specific sites or regions along the Beaufort Sea coast have provided evidence of an overall increase in rates in recent decades (Jones *et al.,* 2008; Mars and Houseknecht, 2007; Ping *et al.,* 2011), with many noting an acceleration in the last decade (Arp *et al.,*2010; Jones *et al.,* 2009b; Jones *et al.,* 2018). Peninsula Point contrasts with these trends, an unexpected finding given it's ice-rich permafrost that should be most susceptible to Arctic warming.

7.4 Controls on Coastal Change

With long-term records established, both the drivers and controls on the coastal evolution on Peninsula Point have been analysed.

7.4.1 Topography and Coastal Change

Headwalls appear to have a maximum inland extent of approximately 200 m. While there was no clear explanation for this, maximum inland extents have also been noted elsewhere, such as an unexplained 500 m maximum on Herschel Island (Lantuit *et al.,* 2008).

Elevation and slope have been noted as significant controls of coastal dynamics in across the Arctic (Heginbottom, 1984; Irrgang *et al.,* 2018; Lantuit *et al.,* 2008, Lantuit *et al.,* 2012a; Novikova *et al.,* 2018; Ramage *et al.,* 2017), but this study was the first to assess the relationship over both decadal and annual timescales, and to include the effect of changes in topography on coastal permafrost dynamics. Analysis revealed that headwalls typically retreat faster along areas with high elevation and steep slopes. The opposite is true of SLR, which is slower in areas with higher relief, especially those undergoing reductions in elevation and slope. This is typically a sign of mass transfer from inland towards the shoreline, providing a link between volume loss and SLR variability. However, the relationships between many change metrics and topography are typically weak and time-variable, with little consistency observed. For example, variations in the SL2HW distance is primarily driven my SLR variations on an inter-annual timescale, but primarily by HWR rates on longer timescales. Similarly, the correlations between coastal change and the slope angle averaged 150 m inland reversed in the 2016 to 2018 period, relative to 2004 to 2016. The timeframes over which these topographic and metrics are compared requires particular consideration.

7.4.2 Massive ice and Inter-annual Coastal Dynamics

Consideration of massive ice allowed many of the weaknesses, anomalies and reversals in the other causal relationships to be explained. Massive ice has been observed to act as a key control across all timescales considered, influencing the topographic variations and changes across Peninsula Point and modifying their relationship with SLR, HWR and volumetric changes. Over inter-annual time periods:

- where massive ice exposures and a consistent OB of under 4 m was present in active slump headwalls, their retreat rate was over three times faster than other retreating headwalls.
- Where subsurface ice was mapped, relative HWR rates could be accurately predicted.
- Short-lived mass transfer from RTSs had significant influence over the shoreline position, causing transient progradation followed by rapid SLR – a potential problem for accurate estimates of SLR trends

The large spatial variations in the 2016 to 2018 SLR rates were closely linked with volumetric losses associated with RTS activity. This agrees with similar results found by Obu *et al.,* (2016), supporting the idea that RTS activity can drive significant inter-annual changes in shoreline position, an important consideration when calculating SLR rates and trends along RTS dominated coasts.

Attempts at modelling HWR rates have previously incorporated factors such as headwall geometry, orientation, heat flux and thawing indices (Heginbottom, 1984; Lewkowicz, 1987A; Robinson, 2000) but these typically resulted in inconsistent, site specific results. Ice and OB thickness variations are cited as problems affecting the models and mentioned throughout the literature as important considerations in determining the initiation, activity and stabilisation of HWR (Burn and Lewkowicz 1990; Heginbottom, 1984; Kokelj and Jorgenson, 2013; Lantuit and Pollard, 2005; Lantuit *et al.,* 2012b; Lewkowicz, 1987A; Lewkowicz, 1987B; Robinson, 2000). It appears that this research is the first to quantify the response of annual HWR rates to exposed massive ice and OB thickness variations. The combination of these simple headwall constituent metrics and the ability to detect massive ice surface variability through passive seismic monitoring may provide a substantial improvement to our ability to predict interannual HWRs and thus RTS activity.

7.4.3 Massive ice and Decadal Coastal Dynamics

Significant intra- and inter-decadal controls were also observed:

- Where thick massive ice is found, mass transfer from thaw slumps slows or reverses shoreline retreat, while also lowering the topographic relief of the nearshore through mass wasting. This creates a strong disconnected between actual volume losses and those derived from planimetric analysis. SLR eventually accelerates along the low relief coast, eroding the material cover over the massive ice and triggering HWR and further thaw slumping. This causes a quasi-cyclic pattern of SLR related to massive ice.
- The spatial pattern of slope and elevation present in 2004 was erased by 2018. The causes were all directly or indirectly tied to massive ice variability.

It has been observed that RTS activity can result in large transient variations in shoreline position over inter-annual timescales (Obu et al., 2016). However, this research is the first to analyse the quasi-cyclic patterns of SLR and relate these to RTS activity. As massive ice is exposed and rapid HWR is initiated, large volumes of material are mobilised and transported towards the shoreline, buffering against SLR. This temporarily reduces the rate of SLR, but also reduces the topographic relief of the

nearshore coast, making it vulnerable to rapid SLR once the RTS activity slows or stops. These cycles introduce spatial variability in shoreline position related to alongshore RTS activity levels, resulting in quasi-cyclic SLR variations than can be identified through repeat shoreline measurements over several decades. While many of the cycles identified appeared to correlate with shoreline positions from Google Earth and Google Earth Engine time-lapse data (Gorelick *et al.,* 2017), the decametre resolution of the Landsat imagery casts some doubt on the source and accuracy of the cycles. However, while they have the potential to be used as a proxy for periods of enhanced mass loss, further research will be needed, including the use of higher temporal and spatial resolution shoreline data. Furthermore, the frequency of these quasi-cyclic patterns may also change over the coming decades, as sea ice loss continues and open-water fetch grows (Markus *et al.,* 2009; Stroeve *et al.,* 2014) and relative sea level rise proceeds at a faster rate in the Canadian Beaufort Sea than elsewhere in the Arctic (James *et al.,* 2014, Manson and Solomon, 2007, Yin *et al.,* 2010). These trends may act to both trigger more frequent phases of active thaw slumping by inundating the shoreline and exposing massive ice more frequently, but also act to increase SLR rates by more easily removing deposited slump material via enhanced storm activity, waves and swells.

7.4.4 Massive Ice and Historical Coastal Dynamics

The long-term reduction in SLR was also linked to massive ice. Descriptive and photographic evidence from the 20th century indicates widespread exposures of massive ice 5 m to 10 m thick, in contrast to the typically thin (<3 m) and limited ice exposures observed from 2016 to 2018. It can now be hypothesised that the historical changes to massive ice have overridden the expected coastal response to the changing Arctic environment on Peninsula Point, slowing rather than accelerating SLR rates. This has important implications for other ice-cored coastal settings, whereby analysis of the massive ice variability may provide information vital for anticipating future changes in SLR and volume loss. This research is the first to relate multi-decadal SLR trends with changes in massive ice thickness and distribution, and therefore highlights the critical role of massive ice in controlling multi-decadal SLR trends.

7.4.5 Summary: Topographic and Massive Ice Controls on Coastal Change

While there is no coherent, pan-Arctic accepted agreement on the strengths, weaknesses and interactions between the controls and drivers of coastal permafrost change, there have been numerous factors cited as important, to varying degrees, throughout the literature. These are highlighted in the top image of Figure 7.1, and

contrasted with the findings from this research in the bottom image of Figure 7.1. While not all factors previously assessed were included in this research, several factors can be compared. For example, topographic relief, considered important in driving HWR, exerted only a weak influence on Peninsula Point. Conversely, topographic relief was frequently cited as a variable and weak influence on SLR throughout the literature, but was shown to be a highly important factor in this research. New factors, such as headwall ice content and long-term massive ice thickness and distribution, are also shown to be important controls on coastal change. The conceptual models presented in the following section will further illustrate to combined influence of massive ice and topographic variability on permafrost coastal evolution.

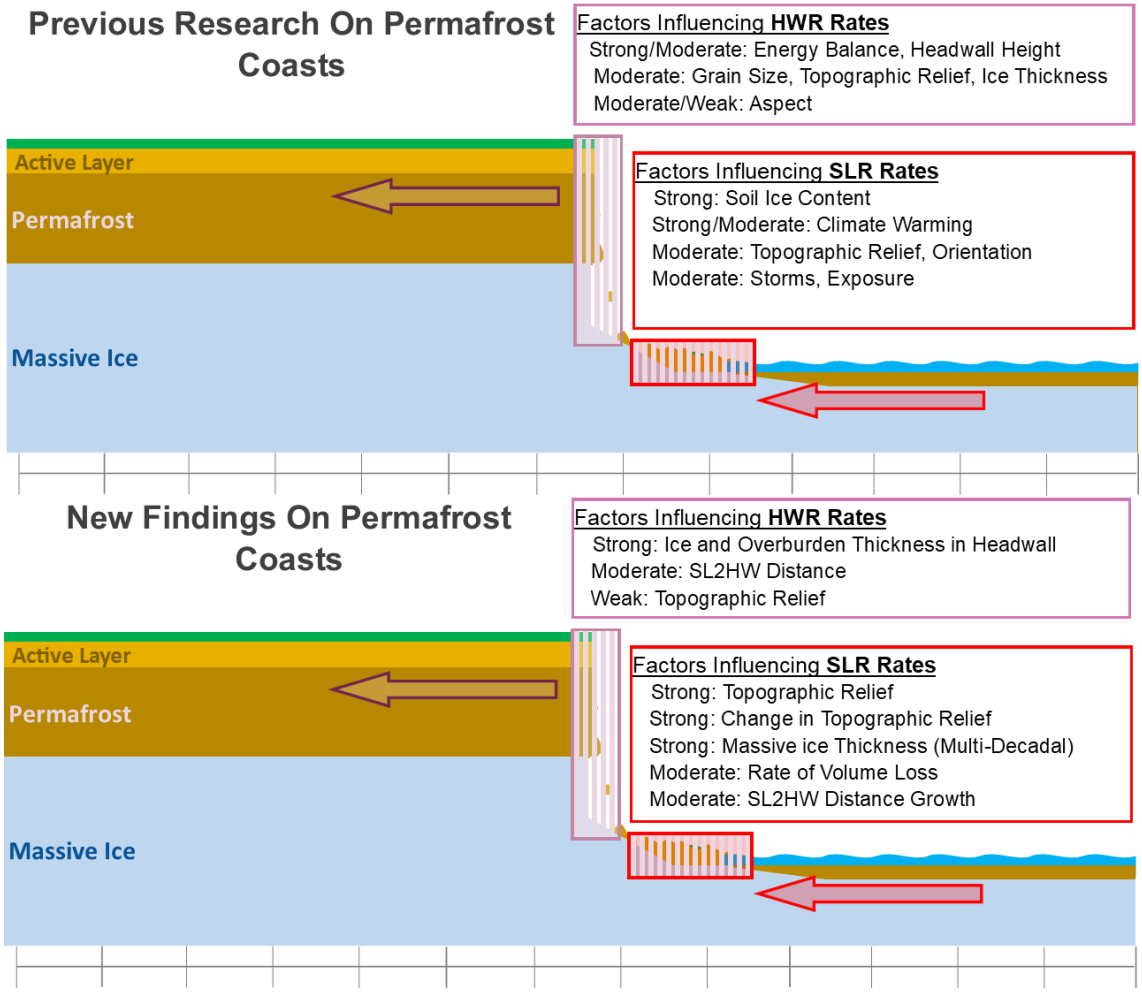

Figure 7.1: Previous factors considered important in determining the rates of HWR and SLR, compared to similar findings from the research presented in this thesis

7.5 Conceptual Models

The conceptual models will start with an ice-free version, before moving on to a simple massive ice model, followed by more complex models. Each will be explained using analysis from previous chapters and examples from the both Peninsula Point and the

published literature. Underneath each model is a scale bar with intervals representing 2.5 m steps. Each panel represents an advancement of approximately one year, however, many of the patterns and process illustrated can operate over much shorter and much longer timeframes and spatial scales. Headwall positions are marked by red circles and the shoreline position is marked by black vertical arrows, with coloured horizontal arrows indicating the direction of shoreline movement.

7.5.1 Simple Models: Massive Ice Free

The simplest SLR model involves a relatively low ice permafrost, free of massive ice bodies or ice wedges (Figure 7.2). In the absence of high ice content permafrost, thermoerosional niche development is unlikely and SLR can proceed in a more uniform matter over years to decades, with the gradual thaw and crumbling of the cliff face. This is represented by the narrow annual range and slow SLR average of -1.9 m a^{-1} in Figure 7.2. This type of SLR was observed on the eastern side of Peninsula Point, where a near vertical cliff between 4 m and 6 m retreated at a steady rate from 2016 to 2018, with no signs of thermoerosional niche development or ice wedges visible (Figure 7.3).

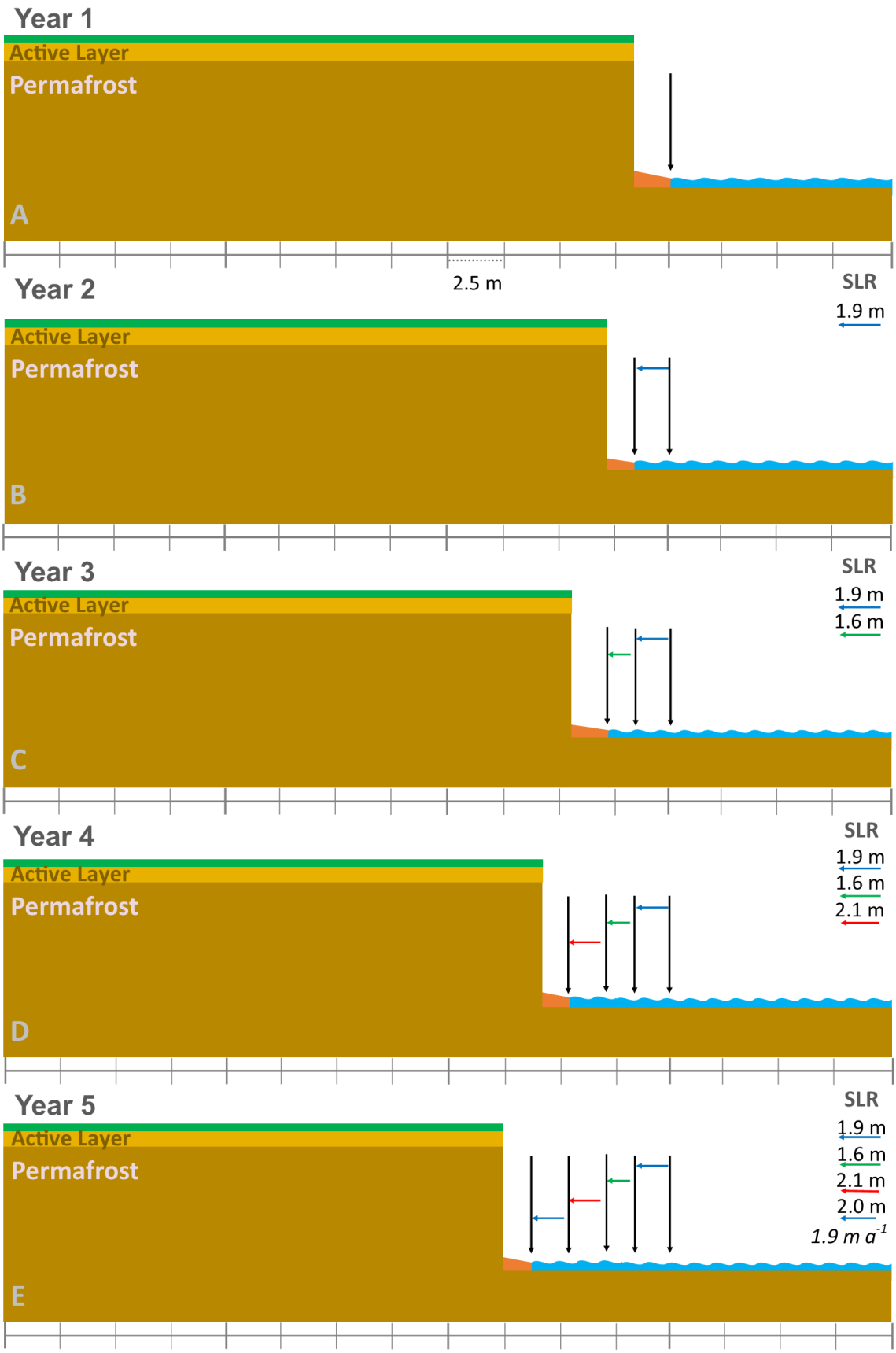

Figure 7.2: Simple low ice permafrost coastline retreat model.

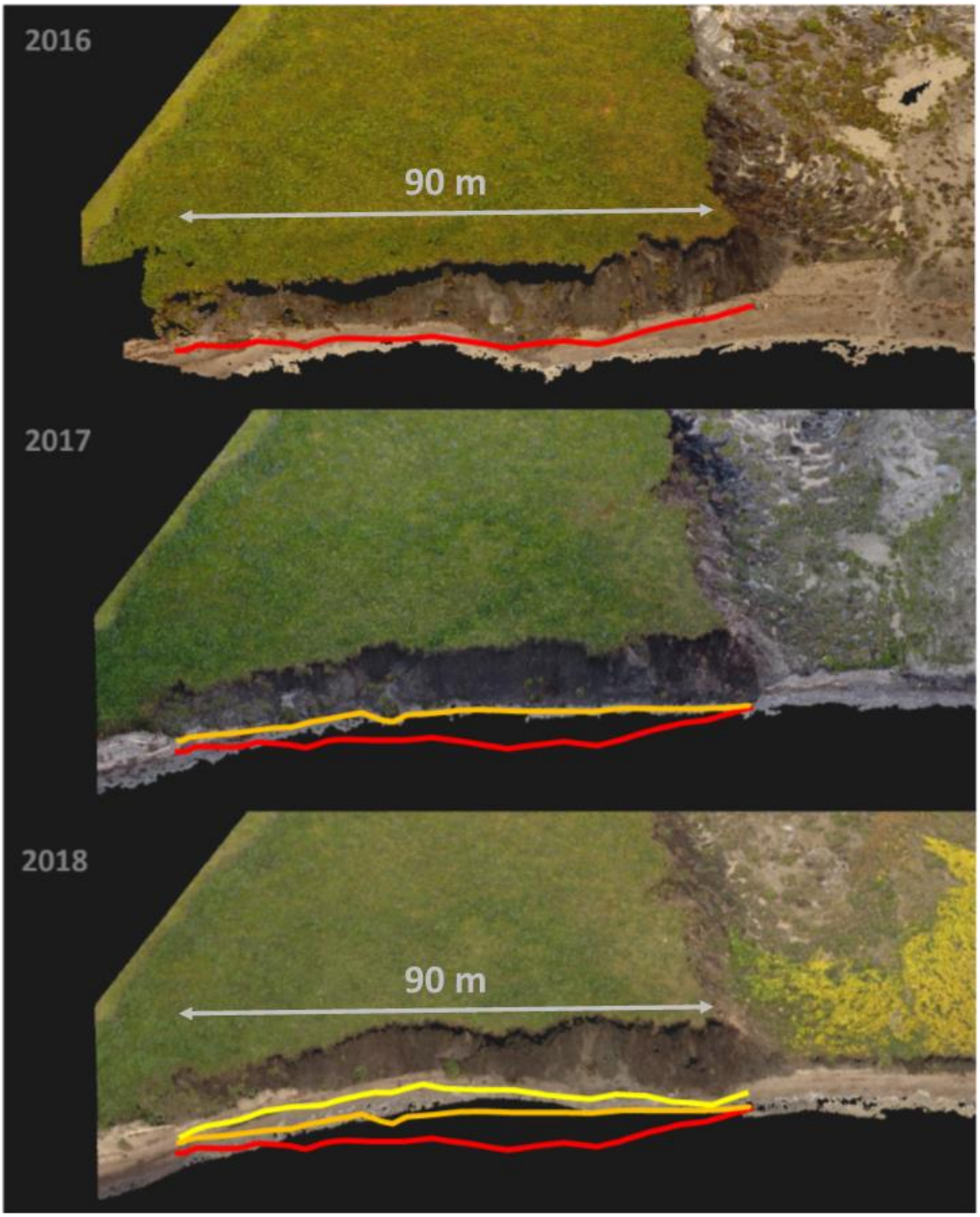

Figure 7.3: Example from Peninsula Point of simple shoreline retreat in a low ice permafrost with no ice bodies

Where the permafrost is ice rich, and often where ice wedges are prevalent, thermoerosional niche development is common and retreat takes the form of block collapse (Figure 7.4). Here, submarine erosion is once more dominant, but in the form of thermal abrasion. Coastal retreat in these settings tend to occur in short pulses. The shoreline position appears relatively stable as the niche proceeds inland, undercutting the permafrost (Figure 7.4B). Once the block collapses the shoreline loses several metres (Figure 7.4C) and remains relatively stable until the next phase of niche development and collapse (Figure 7.4D and Figure 7.4E). Regions dominated by block collapse have some of the fastest SLR rates in the Arctic (Barnhart *et al.,* 2014a; Hoque and Pollard, 2016; Ravens *et al.,* 2016). Niche development and SLR can be rapid during high water phases, such as in storms, resulting in rates that can be measured in terms of metres per hour. Figure 7.5A highlights the effect of a storm on coastal erosion over the course of two hours. The rate of block failure and the failure planes are also strongly influenced by the presence of ice wedges. Blocks often collapse as solid units in the shape of the ice wedge polygons (Figure 7.5B). Thermoerosional niche development can also occur in the presence of massive ice bodies, where waves and swells melt the base of the ice, forming a niche which extends inland under the ice (Figure 7.5C). This can eventually lead to the collapse of the overhanging segment. However, modelling and understanding of the processes involved in coastlines undergoing block collapse is more advanced than those where massive ice bodies are present and RTSs dominate changes.

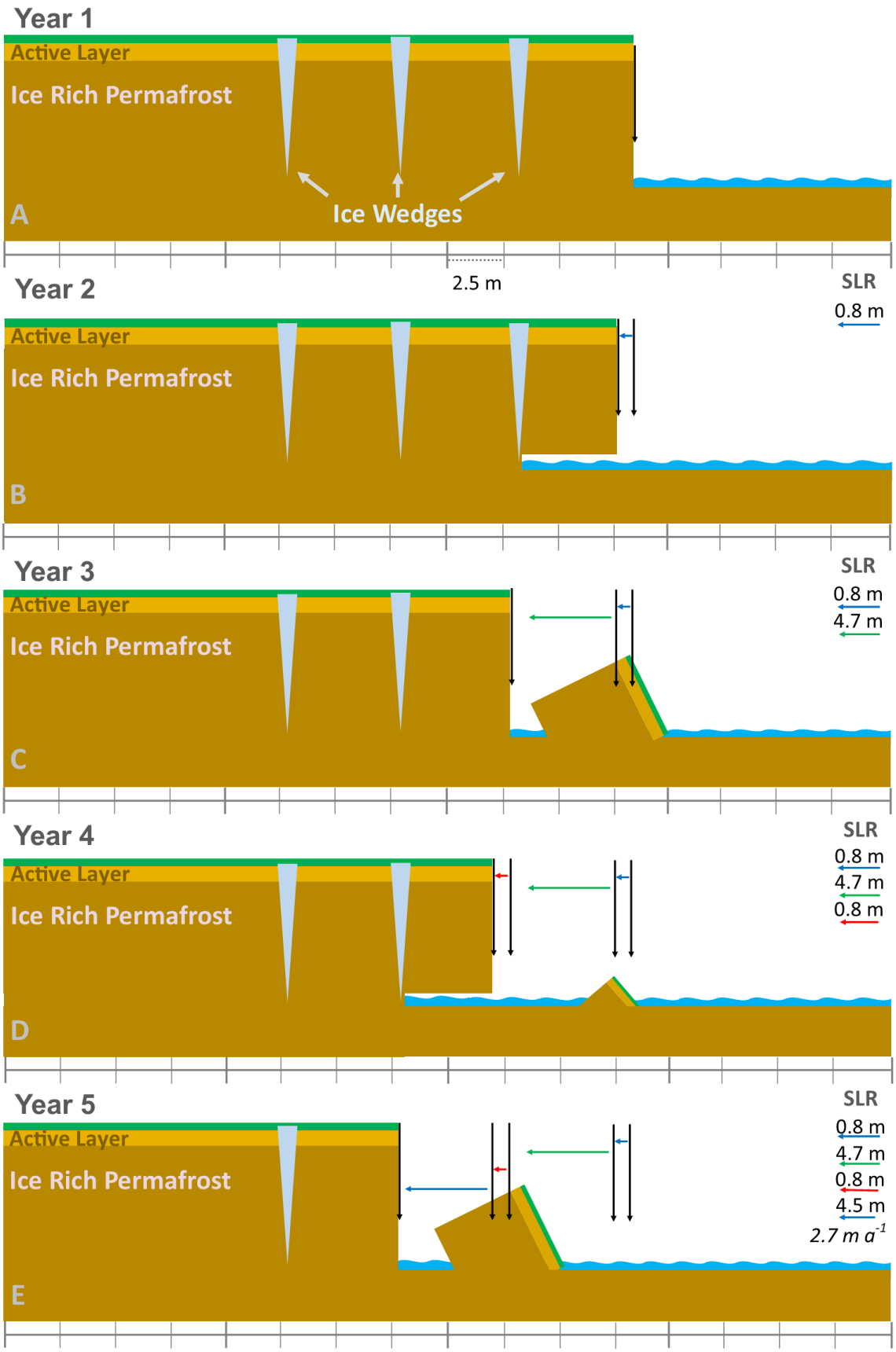

Figure 7.4: SLR in an ice rich permafrost with ice wedges and thermoerosional niche development

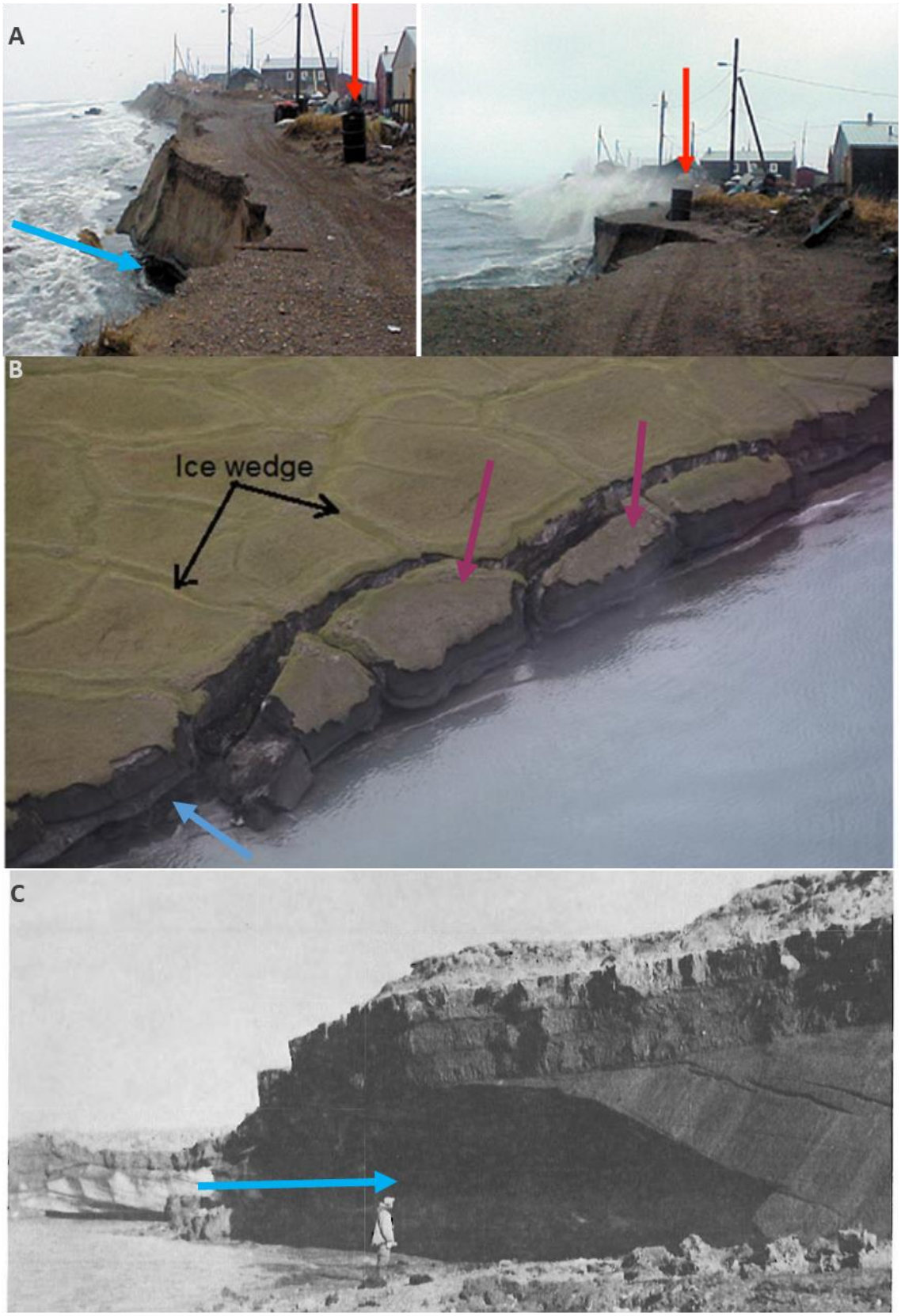

Figure 7.5: Examples of thermoerosional niche and block collapse. A shows the coastal change in two hours during a moderate storm in Shishmaref, Alaska (https://nsidc.org/cryosphere/sotc/permafrost.html). B is from the Alaskan Beaufort Sea Coast (adapted from Hoque and Pollard, 2016). C is from Peninsula Point, (adapted from Mackay, 1986). Blue arrows indicate thermoerosional niches, while wine arrows show collapsed blocks.

7.5.2 Simple Models: Massive Ice

This first massive ice conceptual model will deal a simple, homogenous ice body and uniform OB thickness (Figure 7.6). Panel A shows the massive ice being protected by a thin soil cover on the headwall. The massive ice extends below sea level and remains (at least temporarily) even when the shoreline has retreated over it. Panel A is analogous to the western side of Peninsula Point in 2016, where a thick massive ice layer was hidden underneath a thin covering (Figure 7.7A).

Panel B reveals the initial massive ice exposure and HWR of 3.2 m, with SLR of 2.3 m. This scenario ties in with western Peninsula Point in 2017 (Figure 7.7B), which experienced both headwall and SLR after ice exposure.

Panel C displays a phase of rapid HWR (13.8 m), which mobilised large volumes of material, transferring it downslope and resulting in a prograding shoreline of 3.5 m. Examples of progradation can be seen in Figure 7.7C, where the shoreline extended in small pockets where the volume of thawed material was greatest. Section 6.2.2 revealed similar features for the 2016 to 2018 period on Peninsula Point, where volume loss was negatively correlated with SLR.

In panel D of Figure 7.6 an abrupt slowdown in the rate of HWR (0.8 m) is visible, with a corresponding rapid retreat of the shoreline of 12.3 m. The expansion, followed by rapid retreat of the shoreline, appeared as a quasi-cyclic occurrence on most transects between 1985 and 2018 (section 6.5.2.2). A very clear example of this process in action can be seen in Figure 7.8. Here, a mud lobe extended up to 40 m in 2017, from the 2016 shoreline position. The lobe then retreats by over 20 m in 2018. Similar levels of progradation have also been reported by Obu *et al.,* (2016) at Sabine point on the western Canadian Beaufort Sea.

Finally, in panel E the SLR reaches a point with greater elevation and a steeper slope angle. A new smaller headwall is beginning to extend inland along former slump floor, transporting additional material towards the shoreline. These features cause a reduction in the SLR, down to 2.5 m, while the headwall continues to retreat less than 1 m a^{-1}. Panel E has similarities with the left side of Figure 7.7, where a new headwall formed and began expanding into the floor of an older RTS.

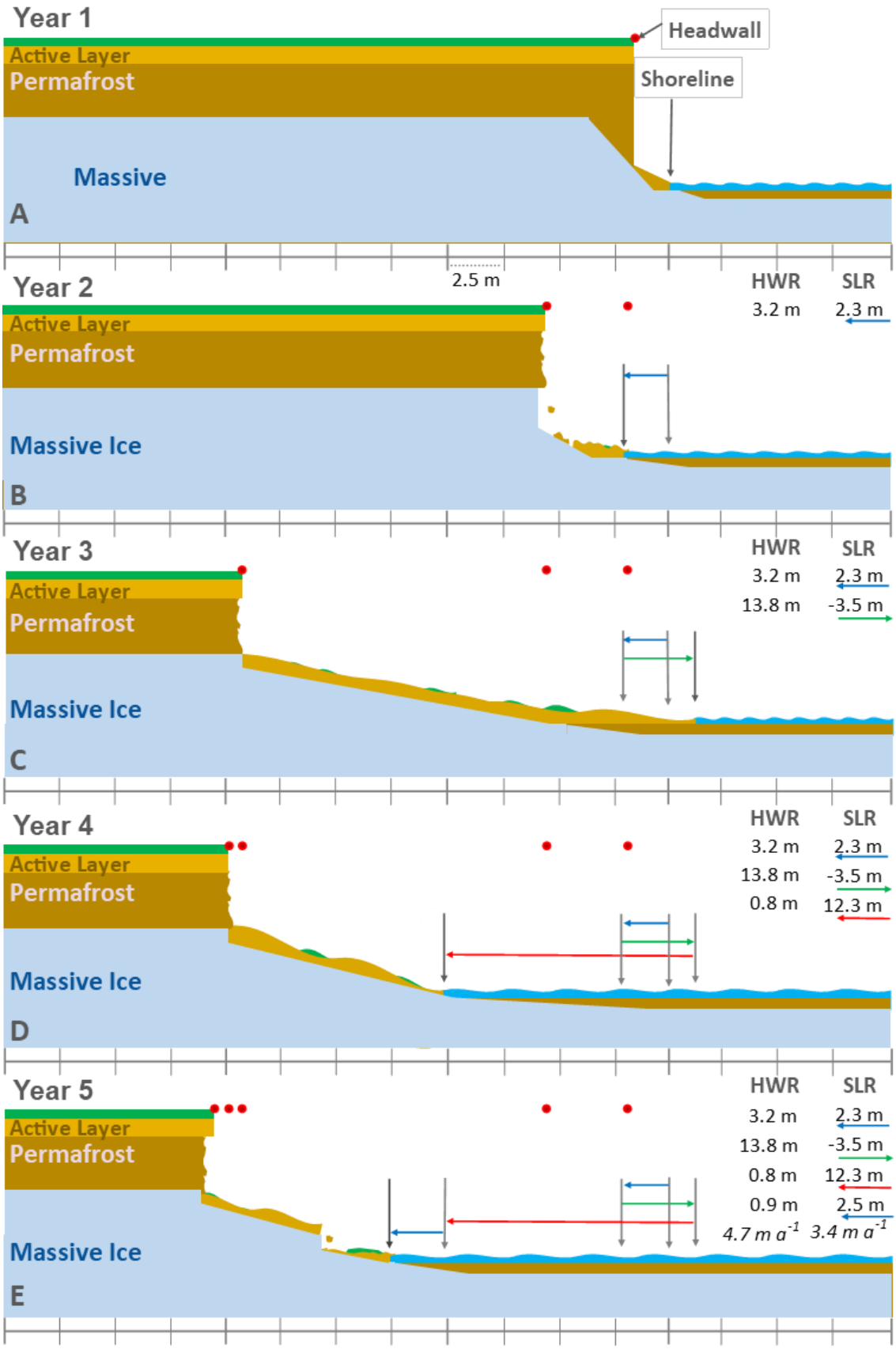

Figure 7.6: The coastal changes in the presence of a simple, uniform, massive ice body

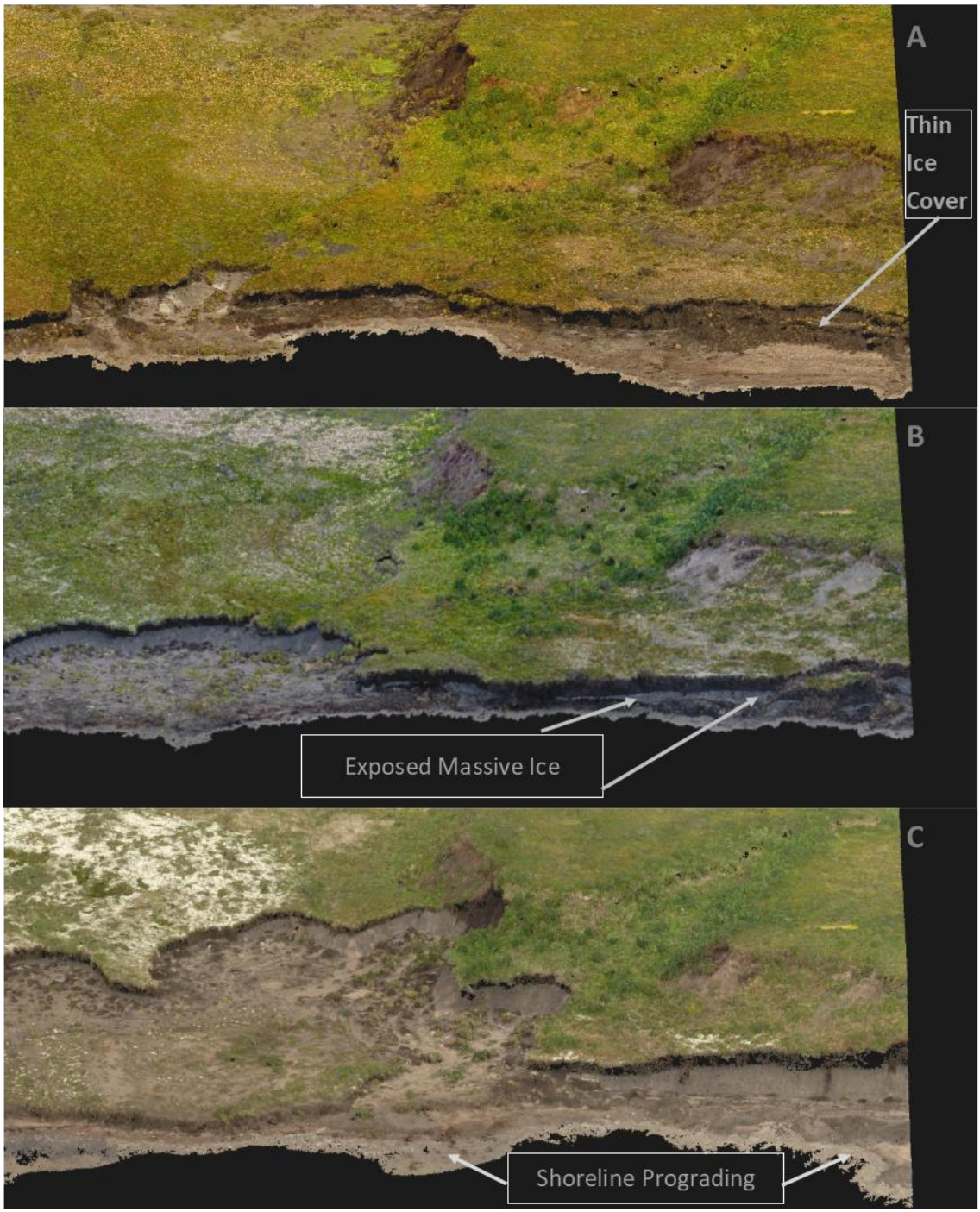

Figure 7.7: Progression from hidden massive ice (A), the exposure and beginning of HWR (B) and mass transfer resulting in slight prograding (C).

Figure 7.8: An example of shoreline prograding through a mud lobe (2017) followed by a phase of rapid shoreline retreat (2018).

Despite a HWR of 4.7 m a^{-1} and an SLR of 3.4 m a^{-1} overall, large annual variances in both headwall and SLR occurred as a consequence of mass transfer, a feature not present in the previous two conceptual models. These variances, when occurring in the field, would make an accurate assessment of the overall trends and rates of the shoreline and HWR highly difficult without consistent, annual monitoring or knowledge of long-term trends. The rates of both headwall and SLR in Figure 7.6 are much greater than in the ice free model in Figure 7.2, and marginally faster than the rates in Figure

7.4. This also ties in well previous findings from section 6.5.2.2, where regions that displayed the greatest degrees of variability in SLR rates also recorded the fastest retreat rates overall. The processes from one panel to the next are supported by the findings of this research, specifically the controls on coastal change and the links between the three dynamic forms of change, SLR, HWR and volume loss. Panel A and B show a steep slope and high elevation, which is associated with slower proceeding SLR rates and faster rates of HWR. From section 6.4.1.1, it was noted that for every additional metre in the 2004 elevation the resulting 2004 to 2016 SLR rate was slower by 0.3 m a^{-1}, with a much weaker and opposing correlation with HWR rates (section 6.4.2). Furthermore, in sections 6.2.2 and 6.2.4, it was observed that enhanced volume losses produced significantly slower SLR rates on inter-annual timescales, while greater starting volume and volume loss produced greater HWR rates on interdecadal timescales. Panel C begins to bare out these relationships as rapid HWR results in a significant mass loss and coastal progradation. This mass loss also has the effect of reducing the elevation and slope angle. In Panel D, the reduction in volume transport from the headwall allows the shoreline to progress rapidly inland along the low relief slump floor. In Panel E the rate of SLR slows as the elevation and slope angle steepen, and a new headwall is formed which begins the transfer of mass towards the shoreline once more, albeit a much-reduced volume. Should the new headwall extend into the old headwall, the resulting fresh exposure of massive ice would likely trigger a new phase of activity.

7.5.3 Complex Model: Variable Massive Ice A

The first conceptual model with non-uniform massive ice can be seen in Figure 7.9. It presents the ice surface gradually lowering as it progresses inland, with a concordant increase in the OB thickness. This results in the HWR rate gradually reducing over time, from 7.0 m a^{-1} in panel B down to 0.9 m a^{-1} in panel E. The SLR displays a more complex pattern, with mass loss associated with the retreating steep angled, high elevation headwall in panel B producing a temporary progradation of the shoreline. The SLR pattern is reversed in panel C, with fast retreat rates continuing in D and E as the shoreline advances inland along the shallow gradient of the slump floor. Diminishing input material from the headwall as the retreat rate slows also allows the SLR to continue unhindered.

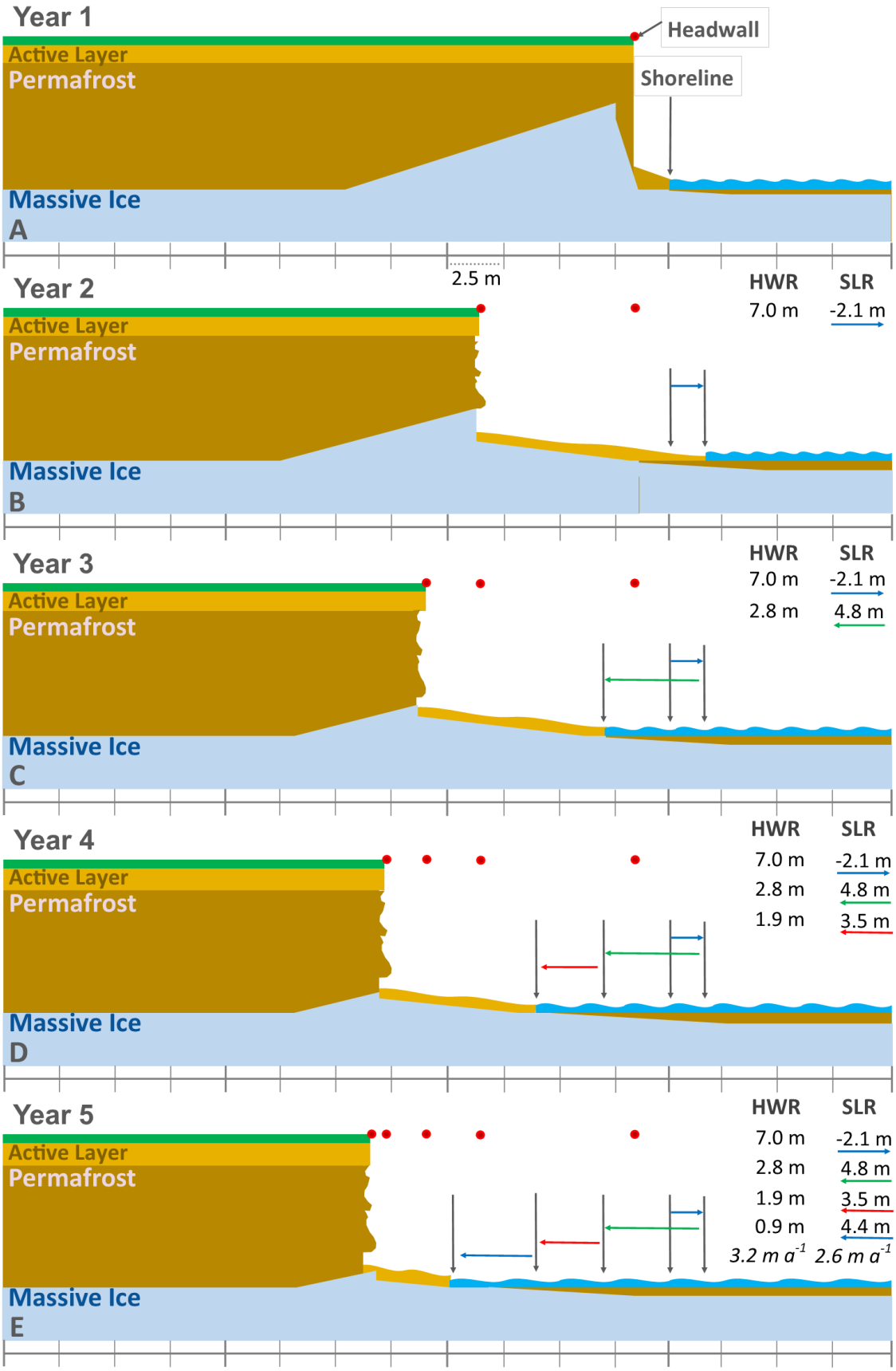

Figure 7.9: Conceptual model showing the influence of declining massive ice thickness on coastal evolution

Figure 7.10 illustrates the influence of similar diminishing headwall ice on coastal dynamics on Peninsula Point. The 2016 image at the top shows a small mud lobe extending out beyond the slump floor, being fed by back-wasting of the headwall at the bottom of the image. The exposed massive ice is visible across most of the headwall, analogous to Panel B in Figure 7.9.

In Figure 7.10, as the massive ice surface dips inland, exposed headwall ice has become limited to the bottom right headwall in 2017. This causes a large reduction in the flow of thawed material into the slump floor, allowing the protruding mud lobe from 2016 to be removed and shoreline to retreat over the low relief of the slump floor. This is similar to Panel C, Figure 7.9.

By 2018 in Figure 7.10, HWR has slowed further as massive ice is no longer exposed and ablating along the majority of the headwall. This cuts off the supply of sediment and meltwater to the slump floor, allowing it to stabilise and vegetation growth to occur. SLR continues at a steady pace while HWR slows quickly as the ice becomes buried, similar to Panel D in Figure 7.9.

The overall rate of SLR and HWR in Figure 7.9 are 2.6 m a^{-1} and 3.2 m a^{-1}, respectively, which is slower than the simple massive ice model in Figure 7.6, and similar to the block collapse model in Figure 7.4. However, the shoreline is beginning to reach the headwall in Panel E of Figure 7.9, after which SLR would proceed at a slower and steady rate, as it did in Figure 7.2.

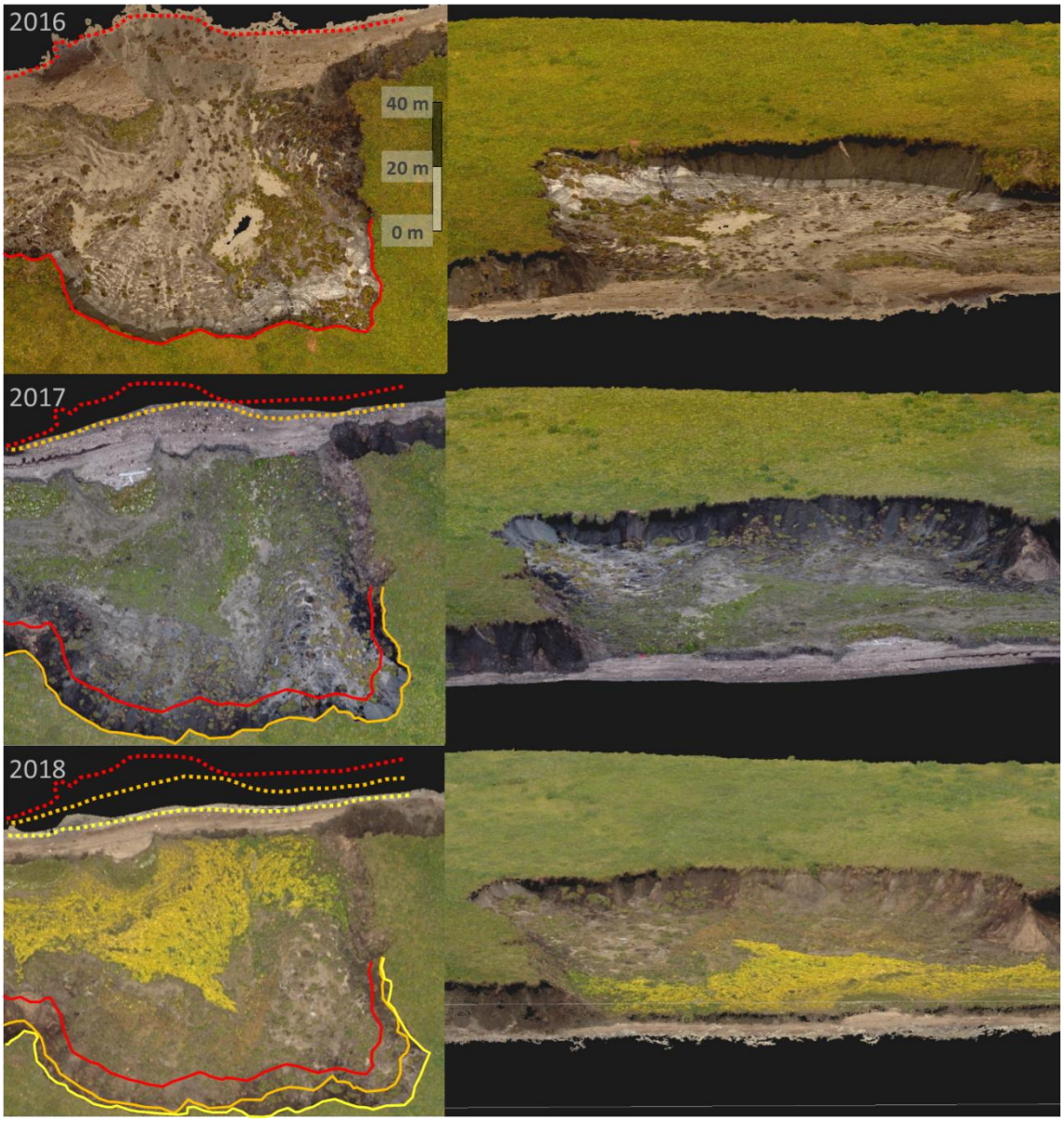

Figure 7.10: Examples of the effect a reduction in headwall ice on both headwall and shoreline position

7.5.4 Complex Model: Variable Massive Ice B

The second conceptual model using variable massive ice thickness is presented in Figure 7.11. Panel A presents the overall features at first, immediately before HWR is initiated. The massive ice has a wave-like surface elevation pattern consisting of two peaks and a trough. In panel B there is the initial exposure of the ice and HWR of 3.2 m along the along the thickening massive ice dome. The transport of thawed material along the steep slope buffers against SLR, slowing it to 1.3 m. In Panel C, HWR increases to 7.2 m a as it extends over the ice dome. However, the HWR is much less than that in Panel C, Figure 7.6. This is due to the headwall reaching a section with lower elevation massive ice, reducing ablation and putting a halt on the rapid inland progression. As much of the volume lost from the HWR is in the form of ice, SLR is less

impeded, advancing by a moderate amount, 2.1 m, along the lowering topographic relief. From panel C to D, the massive ice exposure rapidly thins and becomes entirely covered, resulting in a large reduction in the HWR, from 7.2 m down to 2.3 m. The shoreline retreats by 2.2 m, a slight increase, helped by the reduced slope gradient and reduced sediment supply to the shoreline. The HWR from panel D to E is further reduced to 1.0 m. This further curtails the transport of thawed material towards the shoreline, allowing a SLR of 4.7 m to occur along the shallow slump floor. The overall rates of SLR and HWR from Figure 7.11 are 2.6 m a^{-1} and 3.5 m a^{-1}, respectively. These are similar to those in Figure 7.9, but the progression of both models after panel E differs. While Figure 7.9 would continue with slower and less variable headwall and SLR, Figure 7.11 would experience only a temporary slowdown. Once ice from the second dome is exposed, a new phase of fast HWR would be initiated with a transfer of mass towards the shoreline. This would increase the variability in SLR rates but also increase the overall rates when averaged over multiple years, as evidenced by the association between increased SLR variability and greater overall retreat rates from section 6.5.2.2.

Panels C to E reveal a continued reduction in the elevation and slope gradient of the massive ice within the slump floor. The processes of HWR has removed the near surface permafrost between the ice and the ground surface. This allows the massive ice to remain subject to surface energy fluxes and to continue thawing despite burial. This feature was noted on the slump affected low ground Peninsula Point (section 4.4.2) and has also been described in other locations (Burn, 2000; Burn and Friel, 1989). The large reduction in elevation and slope near the shoreline from panel A to C is associated with a slower than average SLR in Figure 7.11 due to the transfer of mass and the still, relatively, high topographic relief. Evidence for this is derived from section 6.4.1, where for every additional metre lost between 2004 and 2016 (averaged 150 m inland) the resulting SLR rate was reduced by 0.4 m a^{-1}. However, the low topographic relief and much slower reduction in relief from panel C to E, due to thawing massive ice, contributes to an accelerating rate of SLR.

The variations in the thickness of exposed massive ice, from thin in panel A and B, to thick in panel C and absent in D and E, is similar to that observed in the middle of Peninsula Point. The blue oval in Figure 7.12 highlights a region where the massive ice exposure changed from 3 m thick in 2016, to nearly 5 m in 2017 and was reduced to nothing by 2018. The resultant HWR was reduced from 19 m from 2016 to 2017, down to 8 m between 2017 and 2018, despite the thick ice exposure observed in 2017. These wave like variations in massive ice also appear to continue inland beyond the

headwall. This is visible on the fence diagram from section 4.6.4, presented in Figure 7.13. Section A displays a region of massive ice with 17 m distance between the ice peak at the headwall edge and the trough near the middle. The region highlighted in yellow is displayed in section B. Here a broad, gently sloping dome of massive ice occurs over a distance of 98 m. These examples highlight the variable nature of massive ice over 10s to 100s of metres.

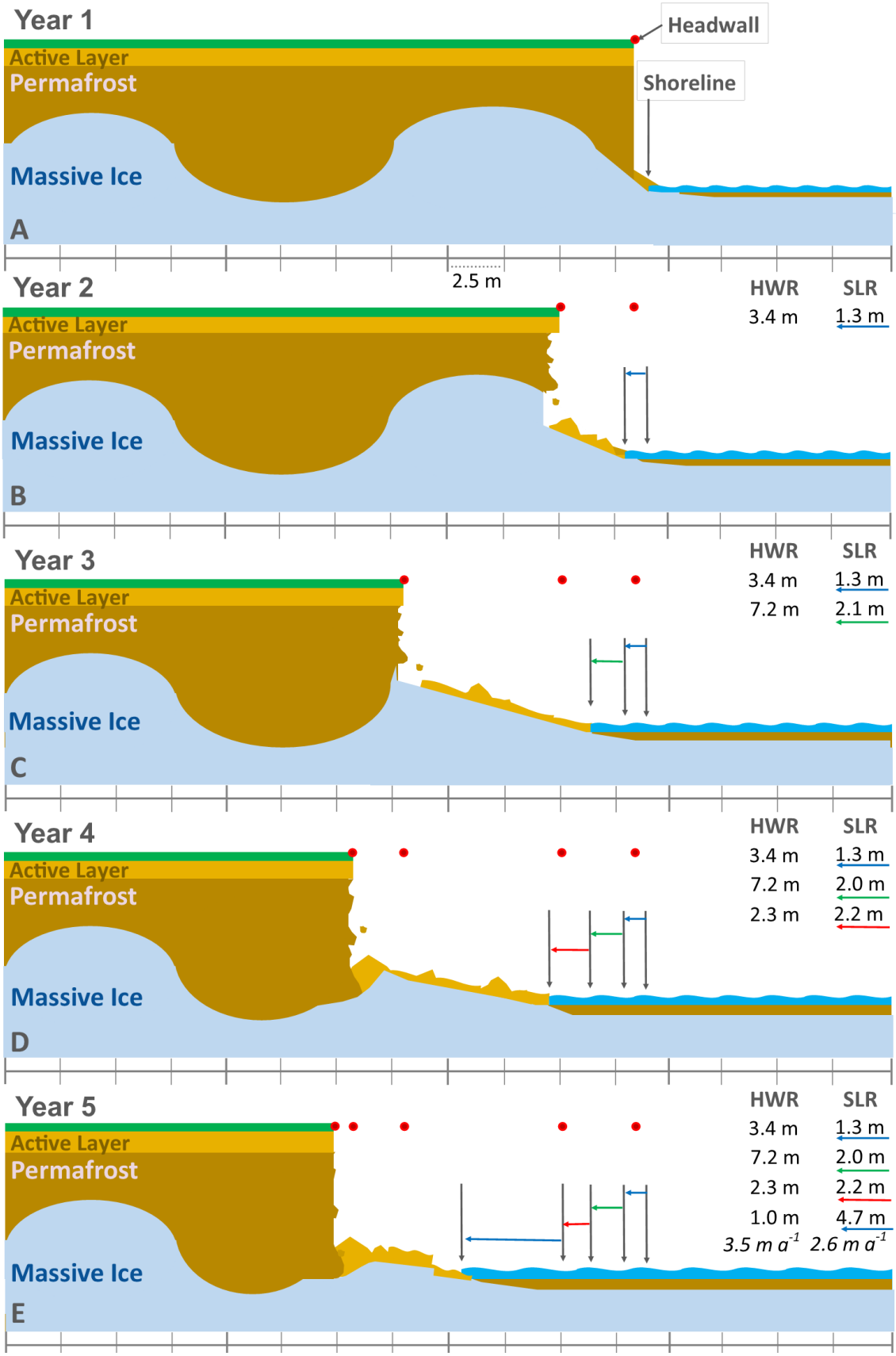

Figure 7.11: Conceptual model demonstrating the effect of variable massive ice thickness on coastal evolution

Figure 7.12: An example of the rapid transition from thin ice, to thick ice and absent ice over three years.

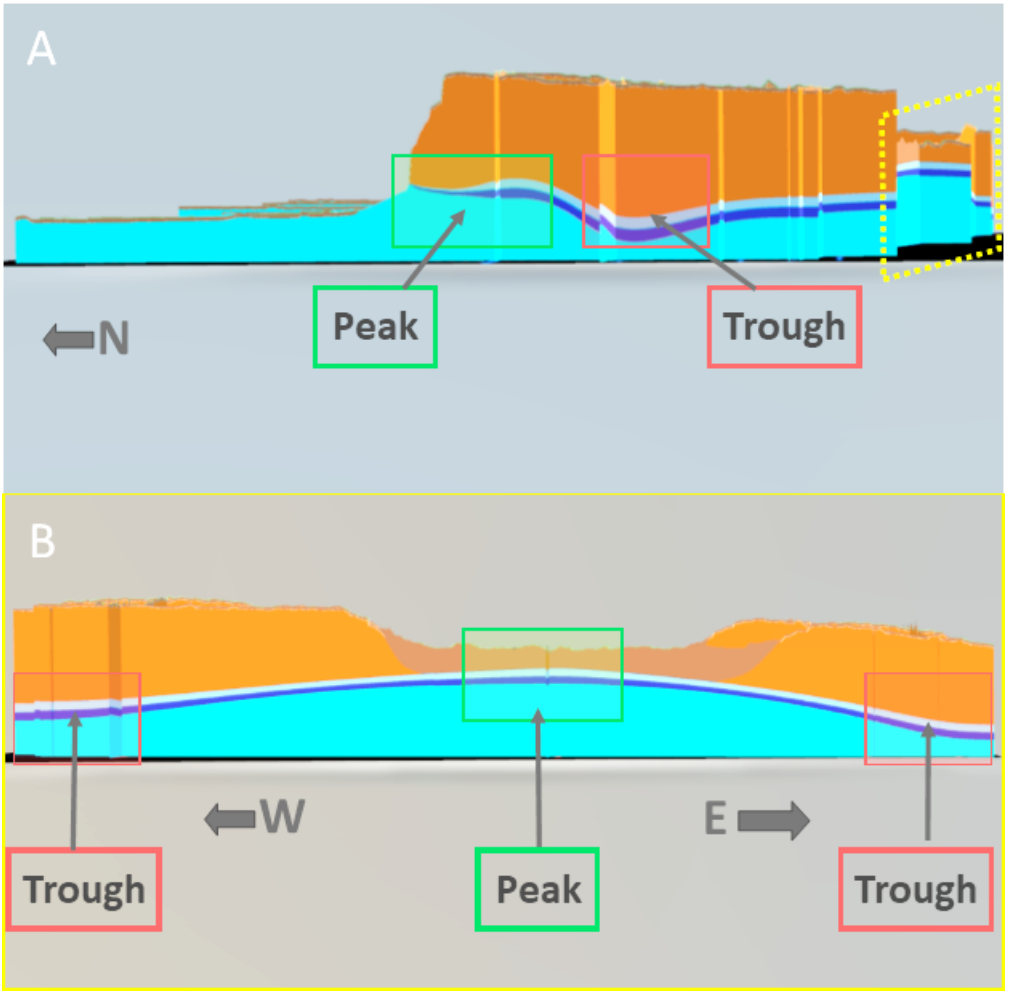

Figure 7.13: Peninsula Point fence diagram illustrating the wave-like pattern in the massive ice surface variability. A is from an east facing perspective. The areas highlighted in yellow is shown in section B, facing north.

7.6 Summary

It is evident that variability in massive ice body thickness and elevation acts as a significant control on coastal dynamics over multiple spatial and temporal scales. The extent and thickness acts as the dominant control over multi-decadal SLR trends. Along-shore differences in the surface elevation of massive ice drives inter-decadal topographic variations and produces quasi-cyclic SLR patterns through its control over RTS activity. Inter-annual variability in shoreline position and HWR rates are both strongly tied to massive ice, and OB thickness.

The conceptual models presented in this chapter highlight the considerable variability in coastal dynamics that can result simply through the addition of massive ice and differences in ice surface topography. Estimates of shoreline and HWR trends could differ by orders of magnitude based on the timing and frequency of observations. SLR rates can slow, accelerate and even reverse over the course of a few years. This depends on coastal elevation, slope angle and volumetric change, over which massive

ice acts as a dominant control. Similar is true of HWR, which can range from dozens of metres in a single year to several years with little or no retreat. Phases of rapid HWR over a thick massive ice body can remove most of the volume for hundreds of metres inland, while also reducing the rate of SLR, such as panel C in Figure 7.6. Using traditional planimetric observations, the slow SLR would suggest a reduction in mass loss or even an accumulation of mass — if observations were taken during a transient progradation event. This is exemplified by the findings that between 2004 and 2018, volume loss derived from planimetric analysis was only 35% of that calculated from the 2.5D data. Along individual transect lines, 2.5D estimates of volume loss ranged from 0.9 times that of planimetric estimates, up to 26.7 times greater. These results highlight the need for high spatial and temporal resolution monitoring and 2.5D data, to better constrain shoreline and HWR rates and variability, and to generate accurate estimates of volumetric changes.

Section 6.5 provides the details on how massive ice variability acts as a control on coastal dynamics on Peninsula Point across a wide range of timescales. This includes reducing the multi-decadal SLR rates and altering their spatial patterns, to decadal changes in coastal topography and control over annual HWR rates — including the maximum annual HWR observation of 54 m. An acceleration in thaw slumping has been noted across the western Canadian Arctic (Lantz and Kokelj, 2008; Ramage *et al.,* 2018; Segal *et al.,* 2016) and in other parts of the world with permafrost soils (Luo *et al.,* 2019). Furthermore, observations of Banks Island found that 4,000 RTSs were recently triggered, representing a 60-fold increase between 1984 and 2015 (Lewkowicz and Way, 2019). The authors suggest that under the moderate RPC 4.5 climate projection, RTS occurrence will continue to accelerate, reaching over 10,000 new thaw slumps per decade by 2076, highlighting the potential for further dramatic landscape changes in regions underlain by massive ice bodies. The control of massive ice over RTS dynamics and the dramatic increase in their occurrences highlights the need for accurate data on the distribution of massive ice bodies and locally detailed maps of their variability.

Another consideration is the ability to map variations in the thickness of buried massive ice. Evidence from section 6.5 and the conceptual models demonstrate that extrapolation of massive ice and OB thicknesses from headwall exposures may be inadequate, especially on local spatial scales, due to the variability in the ice surface. This demonstrates the importance of employing new techniques that allow for the detection and mapping of massive ice. Here, passive seismic monitoring (section 4.5) has proven effective and useful, allowing for the modelling of massive ice variations

and more accurate HWR predictions. To ensure the efficacy of this tool, future work should apply it within a broad range of permafrost environments, containing different soil types, ice volumes and temperatures profiles, for example. The combination of data on subsurface variability and climate projections may allow for greater accuracy in forecasting regional and local coastal changes, resulting in more effective planning and safeguarding of coastal communities, infrastructure and heritage sites, as well as improved estimates of coastal permafrost contributions to regional and global carbon budgets. This has particular important implications for hazard and risk mapping in ice-cored terrains. For example, the village of Tuktoyaktuk is partially protected from erosion by the presence of Tuktoyaktuk island. Current linear rates of shoreline retreat suggest the island may be breached in 30 years (Figure 7.14). However, the island contains a massive ice body also, which could be accurately mapped using passive seismic monitoring. This may allow for areas susceptible to RTS formation, which may allow the island to be breached in under 30 years, to be detected and hazard/risk maps generated. This type of information could prove vital for the planning and protection of the village and its citizens.

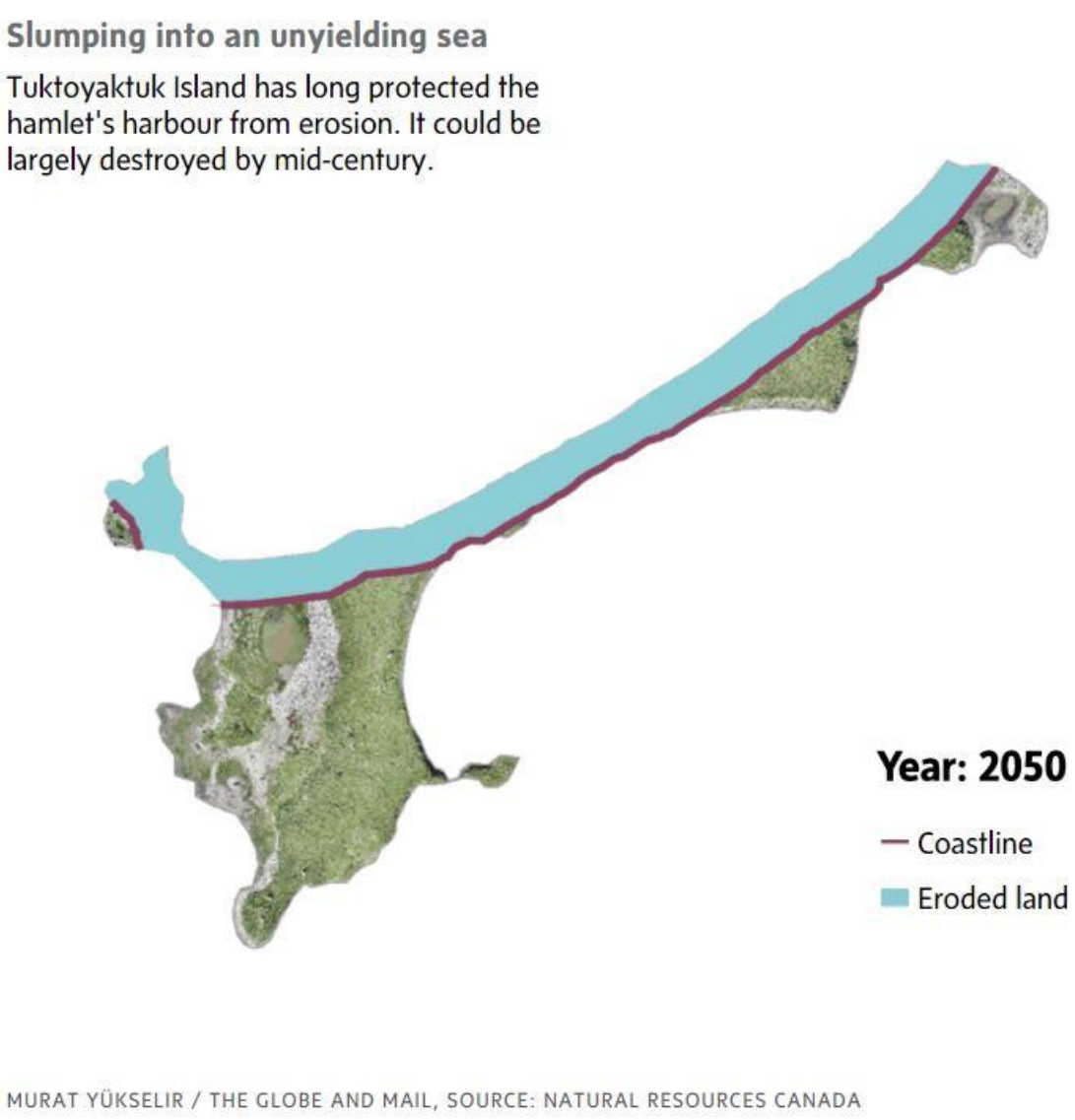

Figure 7.14: Estimated position of the northern shoreline of Tuktoyaktuk based on retreat rates. The blue area represents eroded land, while the maroon represents the shoreline position in 2050 (McClearn, 2019)

8 Conclusions

8.1 Introduction

The overall aim of this research was to:

Quantify the role of massive ice and topographic variability on the dynamics of RTS dominated coasts

This was achieved through a multi-scale analysis of Peninsula Point, the type-locality for intra-sedimental massive ice. More specifically, the research aim was achieved by addressing three primary objectives.

1. Investigate the influence of fine scale, topographic characteristics and internal layering on seasonal and inter-annual RTS dynamics.
2. Explore the interaction between massive ice, decadal changes in terrain morphology and RTS activity.
3. Investigate the role of massive ice variability on the historical (1935 to 2018) evolution of RTS dominated coasts

This chapter will examine the key results produced through addressing the three listed objectives, highlighting their contribution to knowledge, limitations and potential avenues for future research. This will be followed by closing remarks.

8.2 Fine Scale Inter-annual RTS Dynamics

8.2.1 Key Findings and Implications

Massive ice and topographic variability were found to play an important role in inter-annual RTS activity and coastal dynamics. Contained within this finding are three key results.

1. HWR rates are heavily influenced by the absolute thickness and relative proportions of massive ice and soil OB.
2. Annual SLR rates display a large range of variability related to mass transport and RTS activity.
3. Massive ice surface variability can be detected and mapped using passive seismic monitoring.

1) Numerous previous studies have made mention of the potential role of massive ice and topography on the retreat rates of active headwalls, but none had systematically assessed their impact (Burn and Lewkowicz 1990; Heginbottom, 1984; Kokelj and

Jorgenson, 2013; Lantuit and Pollard, 2005; Lantuit *et al.,* 2012b; Lewkowicz, 1987A; Lewkowicz, 1987B; Robinson, 2000). Attempts to understand and model HWR involved simple thawing indices and geometric models, with inconsistent results (Heginbottom, 1984; Jones *et al.,* 2019; Lewkowicz, 1987A; Robinson, 2000). This research followed a different approach, to quantitatively analyse the absolute and relative headwall exposures of massive ice and soil OB and assess their influence on HWR rates in 2016, 2017 and 2018. It was discovered that where massive ice was present *behind* the headwall, and where the OB thickness was consistently less than 4 m, HWR rates were over three times faster than otherwise, up to a maximum recorded annual retreat of 54 m. These simple metrics have a profound effect on HWR rates, independent of slope, elevation and weather. Furthermore, these headwall metrics can be gathered from visual observations and, in combination with data on subsurface layering, can provide a simple and effective means of improving estimates of HWR in other locations, enhancing the understanding of RTS dynamics and improving the planning and preparation for coastal changes in vulnerable areas.

2) Only recently has the relationship between planimetric shoreline change and volume loss been investigated, with RTS activity associated with enhanced short-term shoreline variability (Obu *et al.,* 2016; Obu *et al.,* 2017). Using high resolution SfM-MVS derived topographic data, this research investigated this relationship in finer detail. The largest annual retreat and progradation measured was 32.0 m and 51.4 m, respectively, highlighting the large short-term variability that can exist. An r^2 of 0.4 was found between the rates of volume loss and SLR between 2016 and 2018, confirming the connection with volume change and thus RTS dynamics. This large degree of variability can introduce significant uncertainties in estimating SLR rates if shorelines are digitised infrequently and volumetric changes are not assessed, especially in RTS dominated regions.

3) Previous methods for determining massive ice variability were primarily limited to extrapolation of coastal and headwall exposures, inferred massive ice presence from surface features or spatially isolated borehole measurements (Couture and Pollard, 2017; Couture *et al.,* 2018; Ramage *et al.,* 2017). This research employed the novel application of passive seismic monitoring to the problem. The massive ice surface model revealed levels of ice variability not apparent in the headwall exposures. The accuracy of the model was verified through comparison with the massive ice elevation present in the headwalls after a year of retreat in 2018. Ice-cored terrain is highly vulnerable to RTS intensification, especially in a warming climate, as evidenced by the 60-fold increase in their occurrence on Banks Island (Lewkowicz and Way, 2019). The

ability to map massive ice surface variability through a quick, inexpensive and non-intrusive means, is a significant advance for anticipating the local and regional landscape response to climate change and other anthropogenic disturbances, such as infrastructure works.

8.2.2 Limitations and Future Work

While the strong relationships between the massive ice and short-term coastal and RTS dynamics are clear on Peninsula Point, further testing is necessary to ensure these processes operate similarly in other locations. The influence of headwall constituents on short-term HWR rates should be assessed at different sites covering a variety of geographic locations, terrains and environments to ensure its robustness as a predictive tool. Furthermore, incorporation and testing of the previous thawing indices, headwall geometry models, high-resolution topographic data and buried massive ice has the potential to further improve predictions, not only of HWR rates, but also the initiation and cessation of active RTS phases. Accurate estimates of these features will also improve predictions of transient shoreline variation, mass loss, nutrient and carbon fluxes.

Passive seismic monitoring has proven accurate in modelling massive ice surface variability and improving HWR rate predictions, but only in the narrow range of conditions on Peninsula Point. To explore it's broad-scale efficacy, this approach needs to be tested in other environments, such as those with different permafrost temperatures, ground ice contents, grain types/sizes, active layer depths and surface vegetation. Each of these factors will alter the shear wave velocity and resonance frequencies, introducing complexities and errors where they are not fully accounted for. Testing in winter may also be useful, as this minimises the influence of the active layer variability, such as depth, temperature and water content. For more inland locations, or others where exposures of massive ice are not available for calibration, multiple Tromino™ devices, or other geophones, can be used in combination with an active seismic source in order to measure the shear wave velocity of the soil. A further consideration is the density of measurements needed to accurately model massive ice surface variability. While the overall ice surface elevation was modelled well, the finer scale details that lay between the measurement points were not as well represented on Peninsula Point. The measurement density and interpolation methods required are dependent of the variability within individual sites and the level of detail required. Additionally, further development of the seismic signal processing and analysis may allow for the detecting of other subsurface layers, including measurement of the absolute thickness of massive ice. These methods may be used to improve current

models of massive ice distribution and thickness across the western Canadian Arctic and elsewhere, and to generate decametre-scale resolution maps locally around key vulnerable site, such as villages, heritage sites and infrastructure. These massive ice maps can then contribute to hazard planning. Assessing the thickness of the massive ice and the overburden, and other features, such as the rate of growth in the active layer depth (as a risk of reaching the ice surface and triggering RTS activity), river or coastal retreat rates, the risk of RTS development may be assessed. These can be further expanded by projecting coastal change rates and ALD growth in the 21st century through the use of climate models, creating hazards maps extending decades or more into the future. Seismic monitoring has the potential to vastly improve the predictions of ice-cored landscape response to climate change and other disturbances, but a comprehensive testing plan is first required to ensure its accuracy in a wide range of environments.

8.3 Decadal Coastal Dynamics

8.3.1 Key Findings and Implications

Massive ice and topographic variability were found to exert significant control over coastal and RTS dynamics on decadal timescales. The key findings are:

1. Phases of enhanced RTS activity may be recorded in quasi-cyclic patterns of SLR rates.
2. Topography exerts a statistically significant, but typically weak, control over metrics of coastal change and RTS activity.
3. Estimates of mass loss from planimetric analysis can be several times smaller than actual volume losses.

1) Previous studies have noted the large degree of short-term shoreline variability associated with active RTSs, with mass transport towards the shoreline causing progradation or slowing SLR (Obu *et al.,* 2016; Obu *et al.,* 2017). Fast retreat rates are also associated with RTSs, other coasts with excess ground ice and areas of low elevation (Hequette and Barnes, 1990: Irrgang *et al.,* 2018; Lantuit *et al.,* 2012a; Obu *et al.,* 2017; Solomon, 2005). This research examined rates of shoreline change from 1985 to 2018, finding quasi-cyclic phases of slow SLR or progradation followed by rapid SLR. These are attributed to mass transfer from thaw slumps slowing or reversing shoreline retreat. The same process also lowers the elevation and slope of the slump floor through mass wasting, resulting in faster rates of SLR, which then erode the protective covering over massive ice and initiate the next phase of activity.

These quasi-cyclic patterns could potentially be identified in other RTS dominated regions and used as a proxy for past RTS activity.

2) Higher elevation permafrost coasts have typically been found to exhibit slower SLR rates than those of lower elevation (Lantuit *et al.,* 2012a; Novikova *et al.,* 2018), while steep slope gradients are thought to promote faster rates of HWR (Lewkowicz, 1987a; Robinson, 2000). This study examined these relationships across both 12 years, 2004 to 2016, and two years, 2016 to 2018. Elevation exerted a strong and significant control over the 12-year period. For every additional 1 m in the elevation averaged 150 m inland in 2004, SLR was reduced by 0.3 m a^{-1} up to 2016. This relationship continued for the 2016 to 2018 period but was weaker and more variable. No consistent, strong correlations were found between slope angle and HWR over any timeframe, although greater relief was weakly linked to faster rates of HWR. However, the headwall appears to have a maximum inland extent of close to 200 m, which acts as a significant control over its potential rates of retreat. The links between SLR, HWR and topography appear to be spatially and temporally variable. These factors require consideration before determining the associations between coastal change and topographic variability.

3) Research has suggested that planimetric estimates of volume loss using average cliff heights (Ping *et al.,* 2011) and SLR yield typically accurate results. This is less clear on RTS dominated coastlands (Jorgenson and Brown, 2005; Obu *et al.,* 2016). On Peninsula Point between 2004 and 2018, estimates of mass loss from SLR were 35% of the loss derived from high resolution topographic data, with much greater disparities noted along individual transects, with 2.5D volume loss up to 26.7 times greater than planimetric estimates. These are important considerations when estimating volume losses on RTS dominated coastland, as well and nearshore carbon, nutrient and sediment budgets, from annual to multi-decadal timeframes.

8.3.2 Limitations and Future Work

The quasi-cyclic SLR patterns appeared to be related to phases of RTS activity, and many of the progradation events aligned with analysis of high-resolution imagery on Google Earth and Google Earth Engine time lapses. However, the satellite imagery used was mostly of decametre resolution, which casts doubt on the validity of the cycles identified and determination of their cause. Further analysis using both higher spatial and temporal resolution data, and at a range of differing locations, may allow the quasi-cyclic patterns to be more clearly defined. If validated, this method may also be applied to other ice-cored regions, allowing for a multi-decadal proxy measurement of RTS activity.

Elevation and slope exhibited a significant and strong control over SLR rates from 2004 to 2016 but was weaker for 2016 to 2018. This relationship is generally true across the Arctic, but is often overridden by other local factors, such as ice content and exposure (Irrgang *et al.,* 2018; Novikova *et al.,* 2018; Vasiliev, 2003). As such, with many competing drivers and controls on local scales, coastal elevation may not be an effective metric for predicting SLR rates. However, taking a multi-faceted approach and including factors such as coastal elevation, exposure, ground ice content and type, and nearshore bathymetry, may allow for more accurate predictions of SLR.

It was demonstrated that planimetric analysis of volume loss significantly underestimated actual volume losses on Peninsula Point. This is primarily due to large RTSs mobilising material from up to 200 m inland and transporting it offshore, decades before SLR can reach the same points. Results of a similar analysis from Herschel Island, where RTSs are common, produced inconclusive results (Obu *et al*., 2016). It is possible that the disconnect between the two methods on Peninsula Point is an anomaly, or equally that many areas relying on planimetric volume estimates have consistently underestimated mass loss. The application of high-resolution topographic change data to other regions will help to answer this question, and better constrain estimates of mass loss and variability, especially on RTS dominated coasts. Furthermore, the quasi-cyclic SLR variability is also a sign of RTS activity, and thus rates of enhanced volumetric loss. Combining this, with knowledge of the disconnect between planimetric and 2.5D volumetric change measurements, may further improve our ability to constrain volume, carbon and related mass losses in recent decades.

8.4 Historical Evolution

8.4.1 Key Findings and Implications

For Peninsula Point, SLR rates have slowed between 1935 and 2018, in stark contrast with SLR rates measured in other parts of the Arctic, especially ice rich coasts. This is due to one key finding:

- Massive ice variability has the capacity to override the effects of a warming climate on multi-decadal SLR trends

An acceleration in SLR rates has been observed over the last two decades in sites across the Arctic, especially along coasts with high ground ice contents (Arp *et al.,* 2010; Günther *et al.,* 2013, Günther *et al.,* 2015; Jones *et al.,* 2008; Jones *et al.,* 2009a; Mars and Houseknecht, 2007; Novikova *et al.,* 2018; Ping *et al.,* 2011; Pizhankova *et al.,* 2016). It is thought that these ice rich coasts are most vulnerable to

climate warming, with an enhanced risk of experiencing faster retreat and mass loss rates over the coming century. However, SLR rates on Peninsula Point have decreased in recent decades, from a 1935 to 1985 average of 5.8 m a^{-1}, down to 3.4 m a^{-1} for 1985 to 2018. This has occurred despite a significant local warming trend of +0.46°C per decade and high ground ice content. By comparing previously published photos and descriptions of massive ice exposures on Peninsula Point during the 20th century, with modern observations between 2016 and 2018, a significant reduction in the spatial extent of thick ice exposures and the absolute thickness of those exposures is evident. It is likely that this change in massive ice thickness and distribution is responsible for the observed reduction in SLR rates. This finding has significant implications for other coastal regions containing massive ice bodies. If these massive ice bodies are contributing to current fast rates of SLR, future warming would be expected to increase the SLR rates. However, if the massive ice thins or becomes exhausted, it may counteract the warming climate, maintaining current SLR rates or even reducing them.

8.4.2 Limitations and Future Work

Despite the evidence suggesting that the massive ice on Peninsula Point has thinned, and that SLR rates have slowed, there exists a number of limitations in attributing the SLR trends to massive ice. The first comes from the method of determining massive ice variability over time. Peninsula Point is considered the type locality for intra-sedimental massive ice due to its reputation of having consistent, thick exposures of ice dating as far back as 1935. Quantitative descriptions and photographic evidence are supportive of widespread massive ice exposures of 5 m to 10 m thick. Observations between 2016 and 2018 reveal a different picture, with typically thin (<1.0 m) and patchy exposures, with a maximum thickness of 3.9 m in 2018. The nature of the massive ice thickness reduction is not clear. It may have been an abrupt change in recent years, or a gradual reduction occurring over multiple decades – published observations are insufficient for gaining a clear picture. In combination with this, the lack of long-term volumetric data adds a minor element of uncertainty. It is possible, though unlikely, that the warming trend has triggered in increase in RTS activity on Peninsula Point, accelerating mass transfer towards the shoreline and slowing retreat rates. However, as RTS activity is associated with faster rates of SLR overall, this proposition appears unlikely.

The influence of long-term changes in massive ice and SLR trends has not been explored before in the published literature. As it appears the reduction in massive ice has overridden the influence of a warming climate, it is a consideration that should be

applied to other regions. While it is likely that most coasts will see an acceleration of SLR rates, other regions may also react in a counterintuitive way. By mapping the thickness and distribution of massive ice inland of current exposures, it may be possible to more accurately predict SLR trends over the coming century, enabling more informed planning and adaptation measures.

8.5 Closing Remarks

The Arctic is undergoing an accelerated rate of environmental change relative to the global average (Serreze and Francis, 2006; Overland *et al.,* 2019). This is especially true of the ice marginal landscape of the western Canadian Arctic, where RTS activity is becoming the dominant driver of geomorphic change (Segal *et al.,* 2016). The dramatic increase in RTS numbers and activity highlights how susceptible ice-cored landscapes are to Arctic climate change (Kokelj *et al.,* 2017; Lewkowicz and Way, 2019; Ramage *et al.,* 2018; Segal *et al.,* 2016). It also brings into focus the need for accurate maps of subsurface massive ice variability and a thorough understanding of RTS dynamics across multiple timescales. This research is focused on contributing towards addressing these challenges.

Through the research described in this thesis, new insights have been made on the interactions between massive ice variability, topography, RTS dynamics and coastal change. Many of the findings represent new contributions to knowledge, such as the influence of headwall constituents on annual retreat rates, and the role of massive ice in multi-decadal SLR trends. The utility of passive seismic monitoring has also been demonstrated, a novel, non-intrusive means of detecting and mapping massive ice surface variability. These findings have the potential to provide positive contributions to many areas, from more accurate estimates of nearshore carbon and sediment fluxes, to assessing the susceptibility of local landscapes to rapid geomorphic changes.

Appendices

Appendix 1

The grain size distribution from the undisturbed (U) and active (A) areas are displayed below as percentages in Table 0.1. Table 0.2 and Table 0.3 describe the points used and accuracy from the horizontal accuracy assessment from section 4.2.3.2.

Table 0.1: Grain size percentages for the undisturbed and active sample regions

Size (µm)	**U1**	**U2**	**A1**	**A2**	**A3**
0.01	0.00	0.00	0.00	0.00	0.00
0.0114	0.00	0.00	0.00	0.00	0.00
0.0129	0.00	0.00	0.00	0.00	0.00
0.0147	0.00	0.00	0.00	0.00	0.00
0.0167	0.00	0.00	0.00	0.00	0.00
0.0189	0.00	0.00	0.00	0.00	0.00
0.0215	0.00	0.00	0.00	0.00	0.00
0.0244	0.00	0.00	0.00	0.00	0.00
0.0278	0.00	0.00	0.00	0.00	0.00
0.0315	0.00	0.00	0.00	0.00	0.00
0.0358	0.00	0.00	0.00	0.00	0.00
0.0407	0.00	0.00	0.00	0.00	0.00
0.0463	0.00	0.00	0.00	0.00	0.00
0.0526	0.00	0.00	0.00	0.00	0.00
0.0597	0.00	0.00	0.00	0.00	0.00
0.0679	0.00	0.00	0.00	0.00	0.00
0.0771	0.00	0.00	0.00	0.00	0.00
0.0876	0.00	0.00	0.00	0.00	0.00
0.0995	0.00	0.00	0.00	0.00	0.00
0.113	0.00	0.00	0.00	0.00	0.00
0.128	0.00	0.00	0.00	0.00	0.00
0.146	0.00	0.00	0.00	0.00	0.00
0.166	0.00	0.00	0.00	0.00	0.00
0.188	0.00	0.00	0.00	0.00	0.00
0.214	0.00	0.00	0.00	0.00	0.00
0.243	0.00	0.00	0.00	0.00	0.00
0.276	0.00	0.00	0.00	0.00	0.00
0.314	0.00	0.00	0.00	0.00	0.00
0.357	0.00	0.00	0.00	0.00	0.00
0.405	0.00	0.00	0.00	0.01	0.00
0.46	0.16	0.16	0.27	0.39	0.34
0.523	0.52	0.52	0.74	0.95	0.84
0.594	1.13	1.13	1.25	1.53	1.37
0.675	1.60	1.60	1.61	1.93	1.74

0.767	1.71	1.71	1.72	2.04	1.84
0.872	1.77	1.77	1.61	1.90	1.73
0.991	1.59	1.59	1.41	1.66	1.52
1.13	1.56	1.56	1.27	1.50	1.37
1.28	1.44	1.44	1.27	1.51	1.38
1.45	1.58	1.58	1.43	1.68	1.54
1.65	1.97	1.97	1.68	1.96	1.79
1.88	2.19	2.19	1.96	2.25	2.05
2.13	2.49	2.49	2.20	2.49	2.27
2.42	2.98	2.98	2.37	2.66	2.42
2.75	3.29	3.29	2.49	2.76	2.52
3.12	3.44	3.44	2.55	2.81	2.56
3.55	3.56	3.56	2.59	2.85	2.60
4.03	3.63	3.63	2.60	2.88	2.63
4.58	3.63	3.63	2.61	2.93	2.68
5.21	3.59	3.59	2.60	2.97	2.72
5.92	3.57	3.57	2.57	3.00	2.77
6.72	3.54	3.54	2.52	3.02	2.79
7.64	3.52	3.52	2.44	2.99	2.78
8.68	3.39	3.39	2.35	2.94	2.75
9.86	3.18	3.18	2.25	2.87	2.70
11.2	3.12	3.12	2.16	2.79	2.64
12.7	2.99	2.99	2.09	2.73	2.60
14.5	2.85	2.85	2.04	2.69	2.58
16.4	2.92	2.92	2.01	2.69	2.60
18.7	2.95	2.95	1.99	2.72	2.65
21.2	2.96	2.96	1.98	2.77	2.71
24.1	3.02	3.02	1.96	2.80	2.77
27.4	2.87	2.87	1.92	2.79	2.81
31.1	2.62	2.62	1.85	2.72	2.80
35.3	2.55	2.55	1.77	2.57	2.74
40.1	2.26	2.26	1.69	2.34	2.60
45.6	1.64	1.64	1.62	2.03	2.38
51.8	1.28	1.28	1.57	1.67	2.11
58.9	1.01	1.01	1.54	1.28	1.79
66.9	0.76	0.76	1.53	0.99	1.46
76	0.52	0.52	1.53	0.76	1.18
86.4	0.44	0.44	1.53	0.61	1.03
98.1	0.35	0.35	1.52	0.53	0.90
111	0.34	0.34	1.50	0.46	0.79
127	0.34	0.34	1.45	0.43	0.70
144	0.32	0.32	1.39	0.42	0.62
163	0.27	0.27	1.32	0.42	0.57
186	0.18	0.18	1.25	0.43	0.54
211	0.14	0.14	1.20	0.44	0.52
240	0.11	0.11	1.17	0.44	0.52

272	0.09	0.09	1.17	0.44	0.53
310	0.06	0.06	1.19	0.42	0.53
352	0.02	0.02	1.23	0.38	0.52
400	0.01	0.01	1.25	0.32	0.49
454	0.00	0.00	1.24	0.25	0.43
516	0.00	0.00	1.16	0.18	0.35
586	0.00	0.00	1.01	0.11	0.26
666	0.00	0.00	0.80	0.08	0.17
756	0.00	0.00	0.56	0.07	0.12
859	0.00	0.00	0.32	0.06	0.09
976	0.00	0.00	0.14	0.06	0.07
1110	0.00	0.00	0.03	0.07	0.05
1260	0.00	0.00	0.00	0.08	0.04
1430	0.00	0.00	0.00	0.09	0.03
1630	0.00	0.00	0.00	0.09	0.02
1850	0.00	0.00	0.00	0.08	0.02
2100	0.00	0.00	0.00	0.07	0.01
2390	0.00	0.00	0.00	0.06	0.01
2710	0.00	0.00	0.00	0.04	0.01
3080	0.00	0.00	0.00	0.02	0.00
3500	0.00	0.00	0.00	0.00	0.00

Table 0.2: Description and XY co-ordinated of the 10 assessment points

	2016		2017		2018	
Description	X	Y	X	Y	X	Y
1. Light colour bare patch, left edge - Dark Corner	573142.09	7701109.83	573142.27	7701109.67	573142.09	7701109.65
2. Yellow patch bottom left map - top left corner	573159.51	7701034.20	573159.42	7701034.01	573159.56	7701034.06
3. Box in old slump centre	573284.08	7701099.63	573284.14	7701099.44	573284.11	7701099.64
4. Dark Patch wedge line right of slump - left middle	573396.76	7701034.49	573396.90	7701034.48	573396.88	7701034.47
5. Round green shrub centre - middle	573388.00	7701086.91	573388.05	7701086.79	573388.37	7701087.02
6. Shrub high ground middle - lower white patch	573442.03	7701086.51	573442.16	7701086.50	573442.13	7701086.50
7. Round green shrub centre back - middle	573482.47	7701006.94	573482.62	7701006.84	573482.51	7701006.71
8. Round green shrub near HW edge - middle	573587.94	7701083.42	573588.13	7701083.41	573588.01	7701083.39
9. White patch bottom right - middle	573599.87	7701011.18	573599.79	7701011.17	573599.71	7701011.11
10. Light round shrub, right near HW - middle	573661.20	7701161.50	573661.21	7701161.77	573661.06	7701161.50

Table 0.3: Description and XY co-ordinated of the five assessment points

	2016		1993/4	
	X	Y	X	Y
1. Light patch to the west - centre	573140.09	7701109.09	573139.91	7701109.71
2. East of old slump - bend in ice wedge polygon	573370.83	7701051.67	573370.49	7701051.53
3. Light veg patch high ground - centre	573445.67	7701086.88	573445.92	7701087.29
4. Drained pond back east - centre	573666.67	7700993.49	573666.52	7700993.95
5. Drained pond near eastern HW edge - centre	573619.94	7701095.02	573620.14	7701095.75

Appendix 2

Table 0.4 and Table 0.5 display the shoreline change data from section 5.3. Table 0.6 displays the HWR relative to 1994 from section 5.4.1.3. Table 0.7 displays the volume data as calculated from the transects in section 5.4.1.5. Table 0.8, Table 0.9, Table 0.10 and Table 0.11 display the elevation and slope data from 2018, 2017, 2016 and 2004, respectively. Table 0.12 displays the SL2HW distance data.

Table 0.4: Shoreline change in metres, calculated from aerial imagery in Mackay (1986)

1935	**0**	**0**	**0**	**0**	**0**	**0**	**0**	**0**	**0**	**0**	**0**
1950	75	104	107	119	135	169	160	142	117	83	65
1971	25	38	75	102	93	66	80	100	96	82	52
1985	110	110	110	112	125	134	118	90	72	55	60

Table 0.5: Shoreline change in metres from the individual measurement periods from 1985 to 2018. Negative values represent progradation

	150	175	200	225	250	275	300	325	350	375	400	425	450	475	500	525	550	575	600	625	650	675
1985	0.0	0.0	0.0	0.0	0.0	0.0	0.0	0.0	0.0	0.0	0.0	0.0	0.0	0.0	0.0	0.0	0.0	0.0	0.0	0.0	0.0	0.0
1988	7.3	-4.5	-6.7	4.1	0.1	-0.2	-4.2	-10.8	-10.5	1.4	5.4	3.3	4.3	4.6	11.6	8.7	23.4	27.8	31.4	33.0	27.2	22.9
1990	21.2	23.3	14.2	-2.9	-2.6	-5.5	-5.8	2.2	18.1	16.5	12.4	7.5	5.8	5.1	-4.3	-1.6	3.8	6.9	17.8	23.9	27.0	25.1
1993	26.7	16.8	19.8	24.1	17.8	16.4	18.5	22.0	9.5	5.0	9.5	14.6	18.5	20.2	25.1	31.9	27.0	22.7	19.1	14.8	9.5	6.3
1994	0.0	9.2	7.8	-1.8	0.0	2.6	7.8	0.0	0.0	0.0	0.0	0.0	0.0	0.0	0.0	0.0	0.0	-6.7	-7.2	0.0	0.0	0.0
1997	-5.9	-11.1	-11.3	0.0	13.1	20.3	18.4	16.4	13.0	17.3	15.9	16.8	16.5	17.6	20.0	20.2	25.5	36.3	37.5	27.5	28.0	27.0
2000	13.0	20.1	23.6	20.7	13.0	19.2	17.5	11.6	10.8	6.9	4.3	0.5	-6.0	-3.9	2.4	-12.9	-16.9	-17.3	-14.3	-6.5	-0.4	1.2
2002	15.2	13.1	-9.0	-22.8	-19.1	-15.9	-2.6	0.2	-1.2	-2.4	2.6	9.6	26.9	23.8	8.1	19.1	22.6	21.5	21.6	24.9	23.8	19.7
2004	-11.0	-22.1	2.4	17.2	23.6	41.3	34.8	36.4	39.8	37.4	22.5	11.9	-4.2	-8.3	4.5	6.3	4.6	4.8	1.4	-7.6	-4.0	8.1
2006	6.4	12.9	7.2	8.0	7.8	-4.4	-5.8	3.3	4.2	5.3	16.6	23.4	38.9	12.8	9.1	11.4	14.6	15.8	8.7	9.0	7.7	2.4
2010	20.4	32.1	25.3	9.2	20.9	10.9	8.6	8.2	9.9	14.5	17.9	18.2	-17.3	18.2	10.7	8.6	7.4	8.2	3.0	-2.8	-2.6	3.8
2013	-18.2	-25.2	-7.8	4.8	-22.4	-30.6	-22.6	-23.7	-7.1	-7.3	-13.5	-24.1	-1.4	7.0	17.7	16.3	12.6	6.6	16.6	30.6	21.6	-5.7
2016	24.9	30.4	42.5	44.8	41.4	42.9	18.3	29.0	7.2	1.9	-0.8	5.0	4.1	-6.2	-6.3	-2.3	-6.8	-9.2	2.7	2.4	5.9	26.9
2017	32.0	28.0	7.5	5.5	2.7	10.2	15.5	0.0	-2.4	-7.7	-22.3	-40.0	-51.4	-11.4	-9.1	0.0	3.5	10.0	6.5	6.8	8.1	8.9
2018	-0.2	3.3	-14.5	-2.3	11.8	-0.1	-0.5	1.4	5.1	6.4	15.6	26.1	31.0	4.8	9.8	5.9	10.5	6.0	1.8	2.1	-0.5	0.2

Table 0.6: HWR measurements relative to 1994 position in metres

HWR	**150**	**175**	**200**	**225**	**250**	**275**	**300**	**325**	**350**	**375**	**400**	**425**	**450**	**475**	**500**	**525**	**550**	**575**	**600**	**625**	**650**	**675**
1994-2004	78.5	8.5	0.0	19.6	13.8	30.8	55.2	90.3	56.0	80.4	106.5	51.4	18.3	126.1	78.1	42.5	55.6	72.3	86.0	49.3	51.3	55.9
1994-2016	100.5	2.9	62.4	56.5	65.4	86.1	138.1	162.9	126.9	91.4	112.9	162.1	159.9	176.2	119.3	46.3	64.3	87.5	167.4	159.4	82.3	84.2
1994-2017	100.5	1.8	65.5	59.5	68.9	88.2	145.8	163.5	125.7	93.5	111.9	173.2	160.3	174.9	120.5	48.4	73.9	96.3	173.8	164.9	84.4	87.3
1994-2018	100.9	3.2	69.1	62.8	70.0	90.0	145.8	165.8	128.1	93.2	113.9	173.2	160.1	176.0	120.9	55.8	78.1	98.6	179.6	170.0	91.1	93.5

Table 0.7: Volume data calculated from transect slices. Values can be multiplied by 25 for the 25 m wide volume slice, and summed for total volume

Volume	**150**	**175**	**200**	**225**	**250**	**275**	**300**	**325**	**350**	**375**	**400**	**425**	**450**	**475**	**500**	**525**	**550**	**575**	**600**	**625**	**650**	**675**
2004	2641	2275	2166	2117	2434	2608	2659	2824	2594	2570	2898	3381	3383	3202	2612	2318	2177	2282	2652	2591	2199	1793
2016	1946	1764	1380	1164	1205	1264	1218	1274	1512	1822	2311	2308	2415	1731	1753	1766	1508	1479	1556	1626	1922	1553
2017	1825	1648	1288	1014	1065	1057	1139	1187	1411	1785	2131	2127	2141	1579	1645	1693	1467	1480	1538	1556	1852	1482
2018	1763	1625	1099	919	1020	990	976	1178	1426	1682	1988	2031	1985	1598	1502	1563	1423	1438	1498	1524	1726	1449

Table 0.8: Elevation and slope data for 2018

2018	150	175	200	225	250	275	300	325	350	375	400	425	450	475	500	525	550	575	600	625	650	675
Avg 150 m	10.4	9.8	4.8	4.1	4.5	4.0	3.6	5.3	6.7	8.7	9.3	8.3	6.5	6.1	6.6	8.5	7.5	7.3	7.3	6.8	8.3	7.0
Avg 100 m	10.1	8.8	2.8	2.9	3.6	3.1	2.6	4.9	5.5	6.4	7.3	5.1	2.9	3.8	4.1	6.9	5.9	5.2	4.8	4.6	7.7	6.8
Avg 70 m	9.5	7.2	1.8	2.1	2.9	2.1	1.7	4.4	4.6	5.3	4.7	3.2	2.3	3.2	3.4	3.8	3.7	3.8	3.5	3.8	7.8	6.7
Avg 50 m	7.8	5.5	1.1	2.0	2.1	1.8	1.3	3.7	3.6	3.8	2.9	2.9	1.8	3.1	3.1	3.2	3.2	3.6	3.3	3.5	7.2	6.3
Avg 30 m	4.5	4.2	0.7	1.6	2.0	1.5	0.8	2.1	1.9	2.2	2.0	2.4	1.3	2.8	2.9	2.8	2.6	3.1	3.2	2.9	5.6	4.9
Max 150 m	14.7	13.9	11.6	7.7	7.3	6.7	6.3	7.3	11.4	14.9	17.8	17.6	16.9	12.3	15.3	15.4	13.5	12.6	12.9	11.9	10.3	9.1
Max 100 m	14.7	13.9	9.1	6.1	5.7	5.7	5.4	6.5	8.2	9.4	16.9	16.8	5.2	5.4	6.3	15.4	13.3	12.6	12.8	11.2	10.3	9.1
Max 70 m	14.7	13.9	7.2	3.0	5.6	5.4	3.1	7.0	7.1	10.2	13.2	4.7	4.2	4.2	5.0	6.8	6.0	5.2	4.7	4.8	10.3	9.1
Max 50 m	14.7	8.7	2.7	3.0	2.7	2.6	2.9	7.0	7.1	9.9	6.3	3.9	3.7	4.2	4.4	4.4	4.5	4.7	4.1	4.8	10.3	9.1
Max 30 m	9.4	7.2	1.8	2.8	2.6	2.5	2.0	5.8	5.0	3.9	4.0	3.9	2.4	4.2	4.4	4.3	4.0	4.3	4.1	4.6	10.3	9.1
Slope 150 m	2.1	3.6	4.0	2.8	2.3	2.3	2.5	1.6	3.0	5.2	5.8	6.4	6.6	4.3	4.9	4.8	4.3	4.4	4.9	4.3	1.5	0.9
Slope 100 m	6.0	7.1	3.8	2.5	3.0	3.1	3.2	3.2	4.5	5.6	8.8	6.2	2.6	2.0	2.4	8.5	6.9	4.7	4.2	3.2	2.0	2.3
Slope 70 m	12.8	9.6	3.5	1.4	3.3	2.2	2.3	5.9	6.6	8.6	8.9	2.4	3.0	1.4	2.3	3.5	3.3	1.9	1.3	2.6	6.4	5.2
Slope 50 m	18.7	8.7	2.7	2.4	1.4	1.9	3.1	9.1	9.4	9.1	5.5	3.6	3.7	2.6	2.7	3.1	4.4	3.4	1.8	4.4	11.8	10.5
Slope 30 m	21.2	14.5	3.4	4.4	3.2	4.0	3.7	10.5	8.9	7.6	6.9	6.9	5.0	7.1	8.2	8.1	8.0	6.0	5.8	8.5	23.5	21.7

Table 0.9: Elevation and slope data for 2017

2017	150	175	200	225	250	275	300	325	350	375	400	425	450	475	500	525	550	575	600	625	650	675
Avg 150 m	10.4	8.9	6.7	4.8	4.1	4.4	4.8	5.5	6.9	9.4	10.4	7.7	5.2	5.1	6.3	9.0	7.4	6.6	6.6	7.0	9.0	7.4
Avg 100 m	10.0	7.4	6.1	3.9	3.3	3.7	4.4	5.3	5.9	7.2	8.7	3.4	2.9	2.7	3.5	7.4	5.4	3.8	3.6	4.8	8.7	7.5
Avg 70 m	9.1	5.3	5.0	3.1	2.3	2.9	4.0	4.9	5.0	6.2	6.9	2.9	2.4	2.4	3.3	4.2	3.4	3.0	2.9	3.9	8.2	7.5
Avg 50 m	7.2	4.3	3.9	2.1	1.6	2.0	3.7	4.2	4.2	4.8	3.0	2.7	2.2	2.0	3.0	3.4	2.8	2.6	2.6	3.5	7.7	7.4
Avg 30 m	4.9	2.9	2.8	1.5	1.3	1.5	2.6	2.7	2.6	3.1	2.5	2.8	1.9	1.1	2.2	3.0	2.2	2.0	2.1	3.0	6.2	6.7
Max 150 m	14.7	14.1	11.9	7.4	6.4	6.3	6.3	7.3	11.7	15.3	18.9	19.0	18.1	12.4	15.1	16.0	14.0	13.5	13.2	12.2	10.8	8.9
Max 100 m	14.7	14.1	11.9	6.1	5.9	5.9	6.3	7.3	10.7	10.9	18.9	15.5	5.1	4.1	5.8	16.0	14.0	8.9	9.1	11.6	10.6	8.9
Max 70 m	14.7	9.5	9.4	5.7	5.7	5.5	6.3	7.3	7.3	10.9	18.9	3.4	4.0	3.8	4.4	15.4	5.7	4.4	4.1	5.3	10.6	8.9
Max 50 m	14.5	7.6	7.1	5.3	2.5	5.0	6.3	7.2	7.3	10.7	5.8	3.4	2.7	3.8	4.4	4.3	4.5	3.7	4.0	4.9	10.6	8.9
Max 30 m	8.5	5.6	5.6	2.2	2.5	2.8	5.8	6.0	6.2	4.3	3.0	3.3	2.4	2.5	4.4	4.1	3.6	3.7	4.0	4.8	10.6	8.9
Slope 150 m	2.2	4.4	2.3	2.5	2.4	2.1	1.3	1.2	2.6	4.9	5.4	6.8	4.8	4.5	4.9	5.0	4.9	5.1	5.3	4.3	1.5	0.2
Slope 100 m	5.9	7.6	5.1	3.6	3.6	3.5	2.2	3.0	4.3	5.3	9.2	1.8	1.7	1.8	1.6	9.1	6.5	3.1	2.7	3.5	3.4	0.9
Slope 70 m	11.7	6.9	6.9	4.7	3.4	4.5	3.4	5.9	6.3	8.4	14.9	1.2	1.4	3.2	2.8	4.4	3.7	2.8	2.5	2.7	5.9	2.6
Slope 50 m	13.9	8.7	7.5	3.9	1.7	3.8	6.8	9.1	9.4	10.1	3.2	1.4	1.4	4.7	4.9	3.2	4.2	4.1	4.1	3.9	11.3	6.2
Slope 30 m	15.0	12.9	10.6	3.2	3.9	5.1	12.4	12.9	11.8	5.9	5.7	1.6	1.9	4.3	8.2	6.7	7.3	7.5	8.2	6.9	24.2	16.0

Table 0.10: Elevation and slope data for 2016

2016	150	175	200	225	250	275	300	325	350	375	400	425	450	475	500	525	550	575	600	625	650	675
Avg 150 m	8.9	8.0	7.0	5.6	4.9	5.2	4.7	6.1	7.4	10.0	9.0	11.5	11.9	7.6	8.3	9.5	7.5	6.4	6.8	7.1	9.2	7.5
Avg 100 m	7.3	5.7	6.4	5.0	4.3	4.9	4.1	5.9	6.6	8.3	6.9	10.4	10.4	5.4	5.9	8.1	5.5	3.4	3.9	5.0	8.9	7.5
Avg 70 m	4.6	4.0	5.4	4.5	3.7	4.5	3.6	5.5	5.7	7.6	6.0	7.3	7.5	3.5	3.8	5.2	2.9	2.9	2.9	3.5	8.5	7.6
Avg 50 m	3.1	3.1	4.4	4.1	3.1	4.3	2.8	4.8	5.0	7.1	4.7	4.4	4.1	3.4	3.5	3.2	2.7	2.7	2.8	3.2	8.1	7.4
Avg 30 m	1.6	1.9	3.7	3.5	2.0	3.8	1.2	3.6	3.6	5.0	2.7	4.1	3.1	3.0	3.2	2.7	2.1	2.2	2.5	2.9	6.7	6.5
Max 150 m	14.9	14.2	12.3	7.7	6.7	6.6	6.6	8.1	12.2	15.3	15.0	20.0	18.4	12.8	15.6	15.8	14.2	13.4	13.2	11.9	10.8	9.3
Max 100 m	14.9	14.2	12.3	6.6	6.0	6.1	6.6	8.1	12.2	13.1	10.4	20.0	18.4	11.5	12.1	15.8	14.2	13.4	12.4	11.7	10.6	9.3
Max 70 m	10.3	7.7	9.5	5.8	5.7	6.1	6.6	8.1	7.9	10.7	10.4	20.0	17.8	4.5	8.5	15.6	4.0	3.5	3.7	5.2	10.5	9.3
Max 50 m	6.6	5.5	7.0	5.4	5.4	6.1	6.1	7.4	7.6	10.7	10.1	5.3	12.3	4.1	4.6	4.0	3.7	3.5	3.7	5.2	10.5	9.3
Max 30 m	5.0	5.0	5.5	4.8	5.0	5.5	4.1	6.3	6.7	9.9	3.9	5.3	5.2	4.0	4.6	4.0	3.7	3.4	3.7	5.2	10.4	9.3
Slope 150 m	5.2	5.4	2.1	1.6	1.8	1.1	1.9	1.1	2.5	3.5	4.7	4.9	5.6	4.9	5.6	5.0	5.1	5.1	5.4	4.6	1.3	0.2
Slope 100 m	9.5	6.4	4.4	2.2	2.9	1.6	3.1	2.7	4.2	3.9	5.1	11.4	11.9	5.3	5.9	10.0	7.4	2.3	3.3	4.8	2.9	1.1
Slope 70 m	8.4	6.1	5.6	3.0	4.5	2.1	5.4	5.6	5.6	6.3	8.1	12.3	14.1	1.6	2.2	9.2	2.1	1.8	1.3	2.0	5.2	3.4
Slope 50 m	8.4	7.4	5.3	4.2	6.8	3.7	7.4	8.2	8.6	12.5	10.7	2.9	6.5	2.9	2.5	3.3	3.6	3.1	2.6	2.7	10.2	7.3
Slope 30 m	10.0	11.6	8.7	7.4	9.8	9.3	4.2	13.5	12.3	20.2	4.8	7.1	7.6	5.8	6.4	7.1	6.6	5.6	5.9	7.3	21.7	17.8

Table 0.11: Elevation and slope data for 2004

2004	150	175	200	225	250	275	300	325	350	375	400	425	450	475	500	525	550	575	600	625	650	675
Avg 150 m	9.6	6.0	4.6	4.3	5.7	8.7	10.4	12.9	12.3	12.7	13.6	15.1	14.9	12.7	9.0	9.7	9.3	9.6	10.9	9.5	7.7	7.3
Avg 100 m	6.7	4.4	3.5	3.0	3.8	6.4	7.6	10.7	9.8	11.0	12.0	13.7	13.5	11.0	6.5	7.2	7.2	7.7	9.7	8.0	6.7	7.2
Avg 70 m	4.4	3.3	3.0	2.4	2.5	4.6	5.5	7.6	7.7	8.5	9.3	11.2	11.1	8.5	4.8	5.5	5.6	5.7	7.9	6.7	5.5	6.9
Avg 50 m	6.1	2.9	2.5	1.9	1.7	3.2	4.0	6.0	6.2	6.0	4.8	9.0	7.9	5.8	3.5	4.3	4.4	4.4	5.9	5.2	4.0	6.2
Avg 30 m	2.0	2.0	1.6	1.0	0.9	1.7	1.9	4.3	4.9	3.7	2.1	3.0	3.0	2.2	1.2	3.0	3.1	3.3	3.9	2.3	1.5	4.8
Max 150 m	16.3	10.8	8.4	8.8	10.7	13.9	17.3	19.8	18.3	18.2	18.9	20.3	19.5	17.9	17.6	16.1	14.4	14.9	14.3	12.8	10.2	8.6
Max 100 m	16.3	9.4	5.6	4.7	7.8	12.2	15.3	19.8	16.7	17.4	18.9	20.3	19.5	17.9	11.4	14.5	12.2	14.3	14.2	11.9	9.8	8.6
Max 70 m	8.8	5.1	4.4	4.2	5.6	8.6	10.3	14.7	12.5	16.3	18.9	19.6	19.5	16.1	8.7	10.0	10.1	10.7	13.3	10.7	9.6	8.6
Max 50 m	6.4	4.5	4.0	3.4	3.9	6.4	8.5	9.6	9.5	12.2	9.3	19.6	19.5	14.1	7.6	7.2	7.5	7.7	11.9	10.0	8.6	8.6
Max 30 m	2.9	3.0	4.0	2.3	2.3	4.1	5.9	7.3	7.1	6.6	6.2	14.1	10.3	7.6	3.7	6.1	5.6	5.3	3.9	7.5	4.1	8.1
Slope 150 m	6.8	3.7	2.7	2.9	4.4	5.7	6.9	6.6	6.1	5.6	6.0	5.7	5.8	6.1	6.3	5.8	5.1	5.0	4.2	4.2	3.4	1.0
Slope 100 m	8.3	4.0	2.5	2.7	4.8	7.3	8.5	10.7	8.3	10.7	12.2	12.2	12.5	11.5	7.2	6.7	6.4	7.5	8.3	7.0	6.4	2.9
Slope 70 m	6.8	3.5	3.7	3.7	4.7	8.0	9.4	9.6	8.8	13.8	16.7	17.7	19.9	15.6	8.7	7.6	7.1	7.3	11.6	10.6	9.7	5.7
Slope 50 m	6.8	4.8	5.7	4.6	4.4	8.6	11.1	10.4	9.1	13.1	14.7	26.6	23.8	17.3	10.6	8.4	8.0	7.2	13.1	14.7	12.6	9.9
Slope 30 m	5.7	5.3	9.1	4.8	4.8	9.3	10.1	14.1	14.7	14.8	17.8	17.0	14.6	9.8	5.4	13.6	11.3	11.1	20.0	13.1	8.7	17.7

Table 0.12: SL2HW distance in metres

	150	175	200	225	250	275	300	325	350	375	400	425	450	475	500	525	550	575	600	625	650	675
1994	166.9	142.1	162.8	193.8	197.6	183.9	115.1	95.4	105.2	80.8	63.5	47.6	52.2	37.2	80.4	82.9	77.5	74.6	0.0	5.1	12.4	11.8
2004	167.7	150.4	157.0	198.2	180.8	149.7	122.5	121.1	98.9	101.9	124.2	60.2	37.3	134.2	123.5	92.8	97.4	101.7	39.8	16.0	16.4	11.4
2016	129.6	92.2	152.2	167.3	184.7	186.3	206.8	176.9	156.1	157.7	111.0	148.4	154.6	152.5	133.6	62.6	78.3	95.5	90.2	87.0	14.8	12.6
2018	95.7	64.0	165.9	171.5	174.7	180.1	199.5	178.4	154.1	159.6	118.5	173.4	175.2	158.8	134.7	66.2	78.0	90.6	94.1	88.7	16.0	12.8

Appendix 3

Figure 0.1 and Figure 0.2 display the surface air temperatures for the individual thaw season months. Figure 0.3 and Figure 0.4 display the meridional winds for the individual thaw season months. Table 0.13 presents data on the active HWR rates and headwall constituents for 2016, 2017 and 2018.

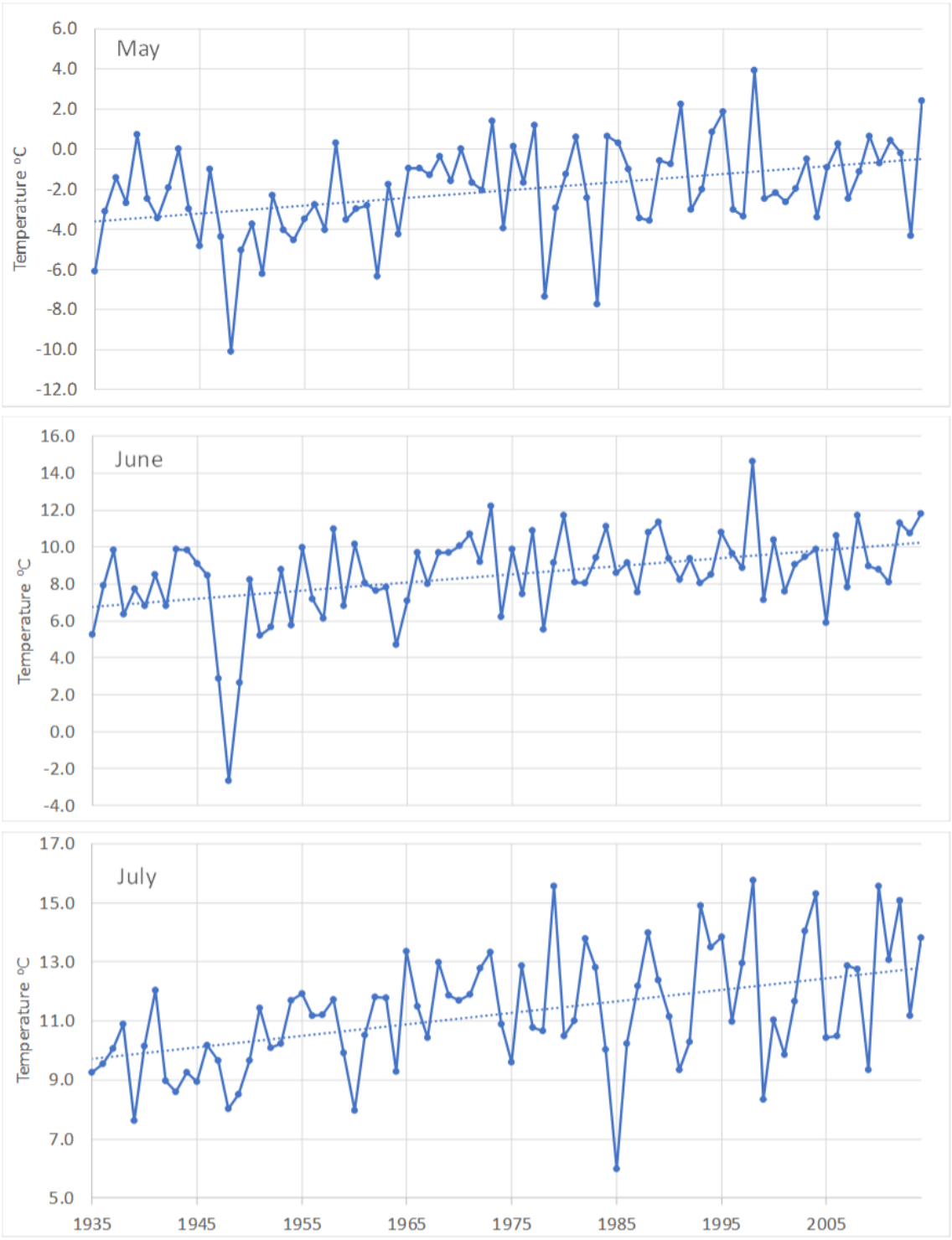

Figure 0.1: Surface air temperatures for May, June and July

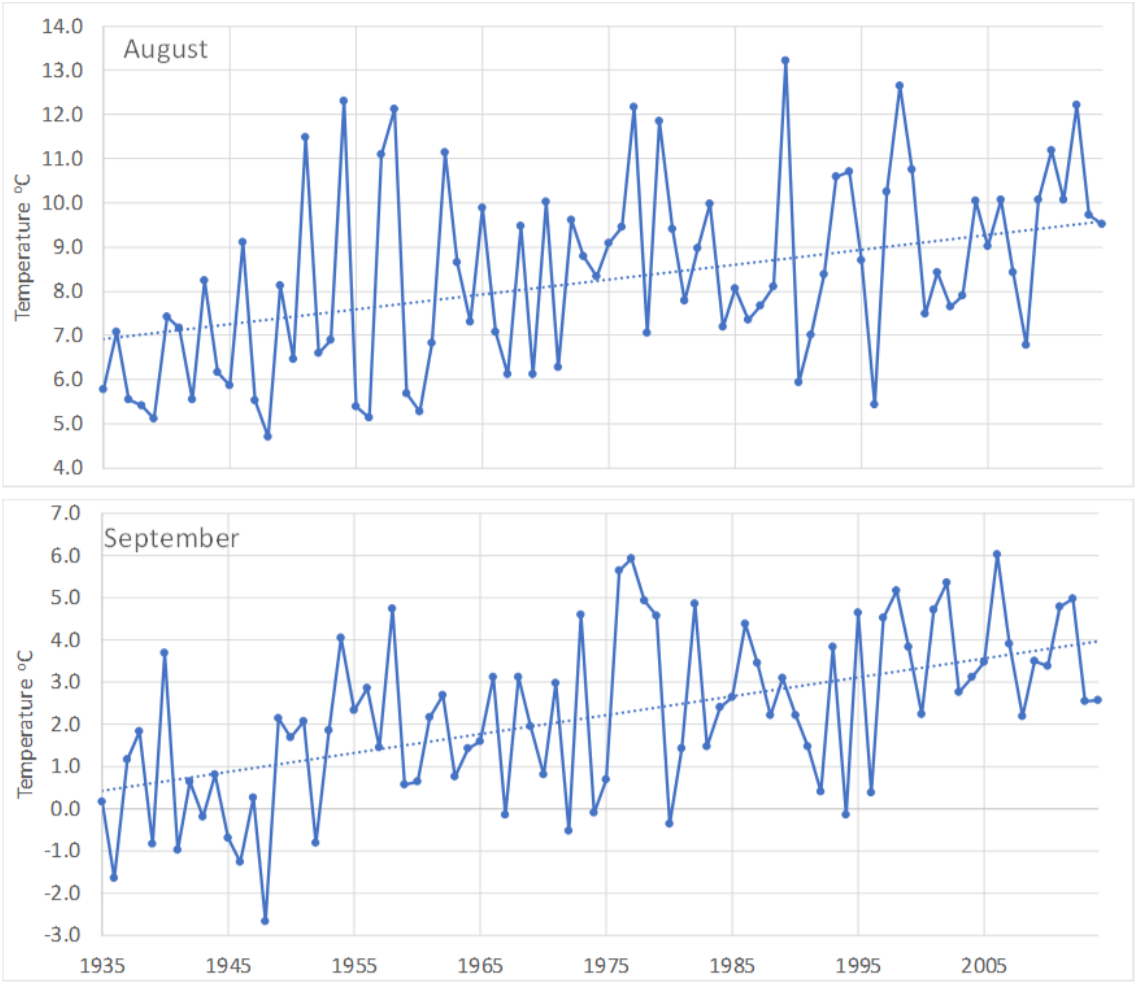

Figure 0.2: Surface air temperatures for August and September

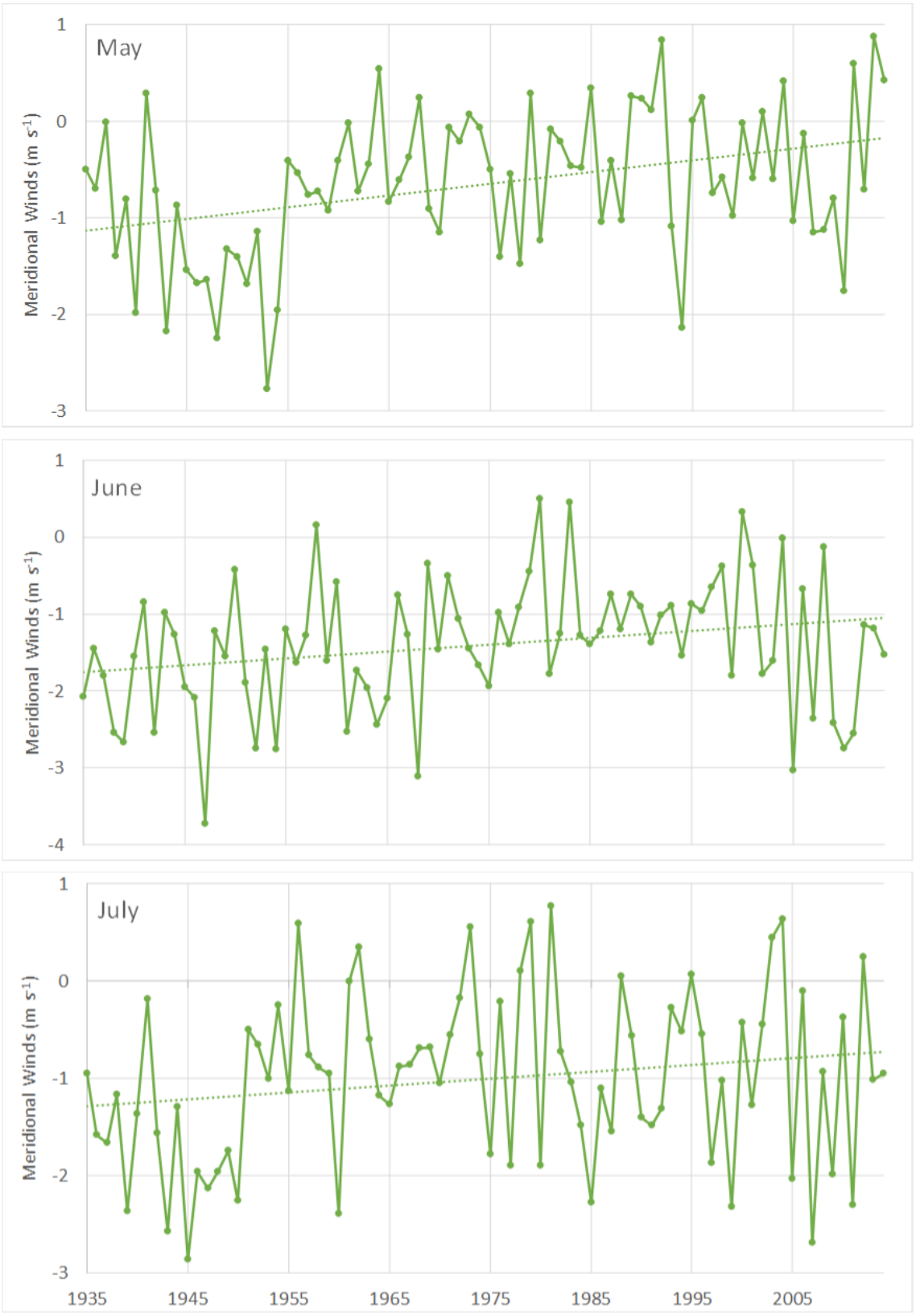

Figure 0.3: Meridional winds for May, June and July

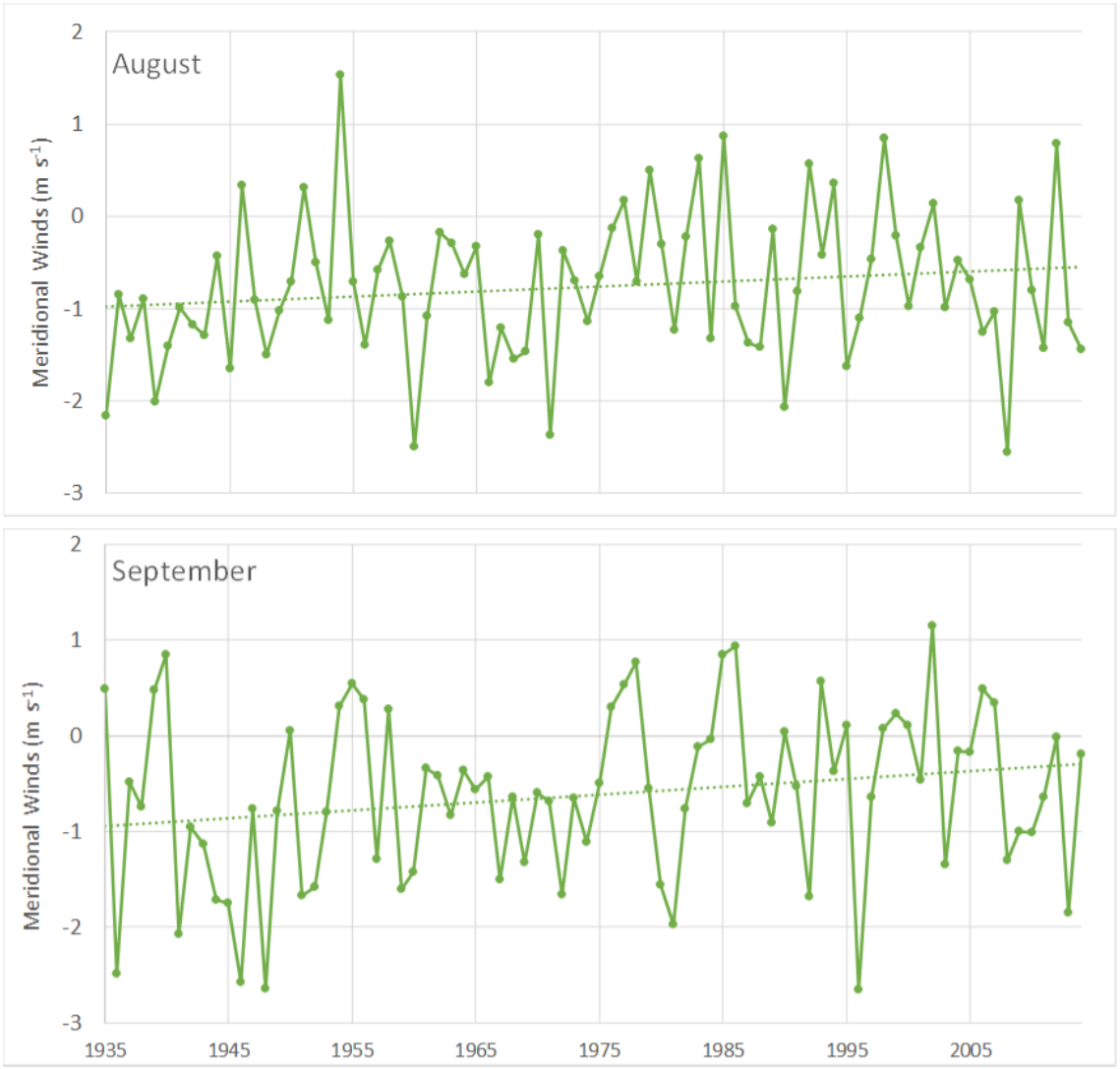

Figure 0.4:Mmeridional winds for August and September

Table 0.13: Active headwall constituents and retreat rates. PI is proportion of ice, IT is ice thickness and OB is overburden thickness.

Total HWR	HWR17	HWR18	PI16	PI17	PI18	IT16	IT17	IT18	OB16	OB17	OB18
3.6	3.6	0	0-15	0	0	0-2	0	0	4-6	4-6	4-6
3.6	2.2	1.4	0	0	0	0	0	0	6-8	6-8	6-8
5.8	4.2	1.6	0	0	0	0	0	0	6-8	4-6	4-6
6	3	3	15-30	0	0	0-2	0	0	4-6	4-6	4-6
6.6	3.8	2.8	45-60	0	0	2-4	0	0	2-4	4-6	4-6
6.6	3.8	2.8	0	0	0	0	0	0	4-6	4-6	4-6
8.2	4.8	3.4	30-45	0	0	2-4	0	0	4-6	4-6	4-6
8.4	5.6	2.8	0	0	0	0	0	0	2-4	0-2	0-2
8.4	5	3.4	75-90	0-15	0	6-8	0-2	0	0-2	2-4	2-4
9.4	3.8	5.6	75-90	0-15	0	6-8	0-2	0	0-2	4-6	4-6
9.4	7.2	2.2	15-30	0	0	0-2	0	0	8-10	8-10	6-8
9.8	5.8	4	60-75	0-15	0	4-6	0-2	0	2-4	4-6	2-4

10.4	7.6	2.8	15-30	0	0	0-2	0	0	4-6	6-8	6-8
10.6	10.6	0	30-45	0	0	2-4	0	0	6-8	>10	8-10
11	4.6	6.4	60-75	0	0	4-6	0	0	0-2	4-6	4-6
11.4	9	2.4	0-15	0	0	0-2	0	0	2-4	>10	8-10
12	8.6	3.4	15-30	0	0	0-2	0	0	2-4	>10	8-10
12.2	6.2	6	0	0	0	0	0	0	8-10	8-10	8-10
12.6	9.2	3.4	0-15	0	0	0-2	0	0	8-10	6-8	6-8
12.8	7.4	5.4	30-45	0	0	2-4	0	0	4-6	>10	8-10
13.4	4	9.4	0	0-15	0	0	0-2	0	>10	>10	>10
14.6	8.2	6.4	0-15	0	0	0-2	0	0	2-4	0-2	0-2
15	6	9	45-60	0	0	4-6	0	0	2-4	6-8	6-8
15	10.4	4.6	45-60	0	0	2-4	0	0	2-4	>10	8-10
15.4	9.4	6	75-90	60-75	75-90	6-8	2-4	2-4	0-2	0-2	0-2
15.6	8.4	7.2	30-45	0	0	2-4	0	0	4-6	6-8	6-8
16.6	7.6	9	0-15	0-15	0	0-2	0-2	0	>10	>10	>10
17.2	9.6	7.6	75-90	60-75	45-60	6-8	2-4	0-2	0-2	0-2	0-2
17.6	8	9.6	15-30	15-30	0	0-2	2-4	0	8-10	>10	>10
18.2	13.4	4.8	60-75	0-15	0	2-4	0-2	0	0-2	8-10	8-10
18.8	10.8	8	60-75	60-75	60-75	6-8	2-4	2-4	0-2	2-4	2-4
18.8	15.2	3.6	30-45	30-45	0	0-2	0-2	0	2-4	2-4	2-4
20.6	13.4	7.2	15-30	0-15	0	0-2	0-2	0	2-4	4-6	6-8
21.6	13.8	7.8	0-15	0-15	0	0-2	0-2	0	6-8	8-10	8-10
23.6	13.2	10.4	45-60	45-60	0	2-4	4-6	0	4-6	4-6	>10
23.8	11.6	12.2	30-45	30-45	0	0-2	2-4	0	6-8	6-8	>10
23.8	12.6	11.2	15-30	15-30	0	0-2	2-4	0	8-10	>10	>10
24	14	10	60-75	60-75	0	2-4	4-6	0	2-4	2-4	8-10
24.6	7.6	17	0	0-15	15-30	0	0-2	0-2	0-2	2-4	0-2
25	11	14	45-60	45-60	45-60	2-4	2-4	2-4	2-4	2-4	0-2
26.8	11.8	15	0-15	15-30	30-45	0-2	0-2	0-2	2-4	2-4	0-2
27.8	13	14.8	0	0	45-60	0	0-2	2-4	2-4	2-4	0-2
29	9.2	19.8	15-30	30-45	0	0-2	0-2	0-2	2-4	2-4	0-2
30	19.6	10.4	45-60	45-60	0	2-4	4-6	0	2-4	2-4	8-10
39.8	18	21.8	45-60	60-75	60-75	2-4	4-6	2-4	2-4	2-4	0-2
44	26	18	0	0	15-30	0	0	0-2	2-4	0-2	2-4
50.6	33.6	17	0-15	45-60	15-30	0-2	0-2	0-2	2-4	0-2	2-4
52.2	23.6	28.6	30-45	45-60	30-45	0-2	0-2	0-2	0-2	2-4	0-2
56	22.2	33.8	0-15	15-30	30-45	0-2	0-2	0-2	0-2	0-2	2-4
61.4	32.8	28.6	30-45	45-60	30-45	0-2	0-2	0-2	2-4	0-2	0-2
63.4	33.8	29.6	45-60	45-60	15-30	0-2	0-2	0-2	0-2	0-2	2-4
71.2	35.8	35.4	0	60-75	60-75	0	0-2	0-2	2-4	0-2	0-2
71.6	17.6	54	45-60	45-60	60-75	0-2	2-4	2-4	0-2	0-2	0-2
73	20	53	15-30	15-30	30-45	0-2	0	0-2	0-2	2-4	0-2

References

Abbott, B. W., Jones, J. B., Schuur, E. A., Chapin III, F. S., Bowden, W. B., Bret-Harte, M. S., ... & Mack, M. C. (2016). Biomass offsets little or none of permafrost carbon release from soils, streams, and wildfire: an expert assessment. *Environmental Research Letters*, *11*(3), 034014. https://doi.org/10.1088/1748-9326/11/3/034014

Agisoft PhotoScan Professional, Version 1.2.4 (Software). (2016*). Retrieved from http://www.agisoft.com/downloads/installer/

Alexanderson, H., Adrielsson, L., Hjort, C., Möller, P., Antonov, O., Eriksson, S., & Pavlov, M. (2002). Depositional history of the North Taymyr ice-marginal zone, Siberia—a landsystem approach. *Journal of Quaternary Science: Published for the Quaternary Research Association*, *17*(4), 361-382. https://doi.org/10.1002/jqs.677

AMAP. (2017). Snow, Water, Ice and Permafrost in the Arctic (SWIPA). *Arctic Monitoring and Assessment Programme (AMAP), Oslo, Norway. xiv* + 269 pp

Aré, F. E. (1988). Thermal abrasion of sea coasts (part I). *Polar Geography and Geology*, *12*(1), 1. https://doi.org/10.1080/10889378809377343

Arp, C. D., Jones, B. M., Schmutz, J. A., Urban, F. E., & Jorgenson, M. T. (2010). Two mechanisms of aquatic and terrestrial habitat change along an Alaskan Arctic coastline. *Polar Biology*, *33*(12), 1629-1640. https://doi.org/10.1007/s00300-010-0800-5

Balme, M. R., & Gallagher, C. (2009). An equatorial periglacial landscape on Mars. *Earth and Planetary Science Letters*, *285*(1-2), 1-15. https://doi.org/10.1016/j.epsl.2009.05.031

Balser, A. W., Jones, J. B., & Gens, R. (2014). Timing of retrogressive thaw slump initiation in the Noatak Basin, northwest Alaska, USA. *Journal of Geophysical Research: Earth Surface*, *119*(5), 1106-1120. https://doi.org/10.1002/2013JF002889

Barnhart, K. R., Anderson, R. S., Overeem, I., Wobus, C., Clow, G. D., & Urban, F. E. (2014a). Modeling erosion of ice-rich permafrost bluffs along the Alaskan Beaufort Sea coast. *Journal of Geophysical Research: Earth Surface*, *119*(5), 1155-1179. https://doi.org/10.1002/2013JF002845

Barnhart, K. R., Overeem, I., & Anderson, R. S. (2014b). The effect of changing sea ice on the physical vulnerability of Arctic coasts. *Cryosphere*, *8*(5). https://doi:10.5194/tc-8-1777-2014

Biskaborn, B. K., Smith, S. L., Noetzli, J., Matthes, H., Vieira, G., Streletskiy, D. A., ... & Allard, M. (2019). Permafrost is warming at a global scale. *Nature communications*, *10*(1), 264. https://doi.org/10.1038/s41467-018-08240-4

Brown, R.J.E. (1967). Comparison of permafrost conditions in Canada and the USSR. *Polar Record*, *13*(87), pp.741-751. https://doi.org/10.1017/S0032247400058411

Burn, C. R., & Friele, P. A. (1989). Geomorphology, vegetation succession, soil characteristics and permafrost in retrogressive thaw slumps near Mayo, Yukon Territory. *Arctic*, 31-40. https://doi.org/10.14430/arctic1637

Burn, C. R., & Lewkowicz, A. G. (1990). Canadian landform examples-17 retrogressive thaw slumps. *Canadian Geographer/Le Géographe canadien*, *34*(3), 273-276. https://doi.org/10.1111/j.1541-0064.1990.tb01092.x

Burn, C. R. (2000). The thermal regime of a retrogressive thaw slump near Mayo, Yukon Territory. *Canadian Journal of Earth Sciences*, *37*(7), 967-981. https://doi.org/10.1139/e00-017

Burn, C. R., & Kokelj, S. V. (2009). The Environment and Permafrost of the Mackenzie Delta Area. *Permafrost and Periglacial Processes*, *12*(January), 53–68. https://doi.org/10.1002/ppp

Carrivick, J. L., Smith, M. W., & Quincey, D. J. (2016). *Structure from Motion in the Geosciences*. John Wiley & Sons.

Chipman, M. L., Kling, G. W., Lundstrom, C. C., & Hu, F. S. (2016). Multiple thermo-erosional episodes during the past six millennia: Implications for the response of Arctic permafrost to climate change. *Geology*, *44*(6), 439-442. https://doi.org/10.1130/G37693.1

Clapuyt, F., Vanacker, V., & Van Oost, K. (2016). Reproducibility of UAV-based earth topography reconstructions based on Structure-from-Motion algorithms. *Geomorphology*, *260*, 4-15. https://doi.org/10.1016/j.geomorph.2015.05.011

Clement, J. P., J. L. Bengtson, and B. P. Kelly. (2013). Managing for the future in a rapidly changing Arctic. A report to the President. Interagency Working Group on Coordination of Domestic Energy Development and Permitting in Alaska (D. J. Hayes, Chair), Washington, D.C., 59 p.

CloudCompare v2.7.0 (2020). [GPL software]. Retrieved from http://www.cloudcompare.org/

Collins, M., Knutti, R., Arblaster, J., Dufresne, J. L., Fichefet, T., Friedlingstein, P., ... & Shongwe, M. (2013). Long-term climate change: projections, commitments and irreversibility. In *Climate Change 2013-The Physical Science Basis: Contribution of Working Group I to the Fifth Assessment Report of the Intergovernmental Panel on Climate Change* (pp. 1029-1136). Cambridge University Press.

Comiso, J.C., 2006. Arctic warming signals from satellite observations. *Weather*, *61*(3), pp.70-76. https://doi.org/10.1256/wea.222.05

Compo, G. P., Whitaker, J. S., Sardeshmukh, P. D., Matsui, N., Allan, R. J., Yin, X., ... & Brönnimann, S. (2011). The twentieth century reanalysis project. *Quarterly Journal of the Royal Meteorological Society*, *137*(654), 1-28. https://doi.org/10.1002/qj.776

Couture N. and Spiridonov, V. (2006). Coastal changes. WWF Arctic Bulletin. 1.06:15-16

Couture, N. J., & Pollard, W. H. (2017). A Model for Quantifying Ground-Ice Volume, Yukon Coast, Western Arctic Canada. Permafrost and Periglacial Processes, 28(3), 534-542. https://doi.org/10.1002/ppp.1952

Couture, N. J., Irrgang, A., Pollard, W., Lantuit, H., & Fritz, M. (2018). Coastal erosion of permafrost soils along the Yukon Coastal Plain and fluxes of organic carbon to the Canadian Beaufort Sea. Journal of Geophysical Research: Biogeosciences, 123, 406–422. https://doi.org/10.1002/2017JG004166

Crowther, T. W., Todd-Brown, K. E. O., Rowe, C. W., Wieder, W. R., Carey, J. C., Machmuller, M. B., … Bradford, M. A. (2016). Quantifying global soil carbon losses in response to warming. *Nature*, *540*(7631), 104–108. Retrieved from http://dx.doi.org/10.1038/nature20150

Cultrera, M., Antonelli, R., Teza, G., & Castellaro, S. (2012). A new hydrostratigraphic model of Venice area (Italy). *Environmental earth sciences*, *66*(4), 1021-1030. https://doi.org/10.1007/s12665-011-1307-2

Cunliffe, A. M., Tanski, G., Radosavljevic, B., Palmer, W. F., Sachs, T., Lantuit, H., ... & Myers-Smith, I. H. (2019). Rapid retreat of permafrost coastline observed with aerial drone photogrammetry. *The Cryosphere*, *13*(5), 1513-1528. https://doi.org/10.5194/tc-13-1513-2019

Farquharson, L. M., Mann, D. H., Swanson, D. K., Jones, B. M., Buzard, R. M., & Jordan, J. W. (2018). Temporal and spatial variability in coastline response to declining sea-ice in northwest Alaska. *Marine Geology*, *404*, 71-83. https://doi.org/10.1016/j.margeo.2018.07.007

Farquharson, L. M., Romanovsky, V. E., Cable, W. L., Walker, D. A., Kokelj, S., & Nicolsky, D. (2019). Climate change drives widespread and rapid thermokarst development in very cold permafrost in the Canadian High Arctic. *Geophysical Research Letters*. https://doi.org/10.1029/2019GL082187

Fischler, M. A., & Bolles, R. C. (1981). Random sample consensus: a paradigm for model fitting with applications to image analysis and automated cartography. *Communications of the ACM*, *24*(6), 381-395. https://doi.org/10.1145/358669.358692

Forbes, D. L. (2011). *State of the Arctic coast 2010: scientific review and outlook*. Land-Ocean Interactions in the Coastal Zone, Institute of Coastal Research.

Francis, J. A., & Vavrus, S. J. (2012). Evidence linking Arctic amplification to extreme weather in mid-latitudes. *Geophysical Research Letters*, *39*(6). https://doi.org/10.1029/2012GL051000

Francis, J. A., & Vavrus, S. J. (2015). Evidence for a wavier jet stream in response to rapid Arctic warming. *Environmental Research Letters*, *10*(1), 014005. https://doi.org/10.1088/1748-9326/10/1/014005

Frederick, J. M., Thomas, M. A., Bull, D. L., Jones, C. A., & Roberts, J. D. (2016). The Arctic coastal erosion problem. *Sandia Nat. Lab., Albuquerque, NM, USA, Tech. Rep. SAND2016-9762*. https://doi.org/10.2172/1431492

French, H. M. (1974). Active thermokarst processes, eastern Banks Island, western Canadian arctic. *Canadian Journal of Earth Sciences*, *11*(6), 785-794. https://doi.org/10.1139/e74-078

Fritz, M., Vonk, J.E. and Lantuit, H., 2017. Collapsing Arctic coastlines. *Nature Climate Change*, *7*(1), pp.6-7. https://doi.org/10.1038/nclimate3188

Gibbs, A. E., Harden, E. L., Richmond, B. M., & Erikson, L. H. (2011). Regional shoreline change and coastal erosion hazards in Arctic Alaska. In *Solutions to Coastal Disasters 2011* (pp. 258-272). https://doi.org/10.3133/ofr20171107

Gibbs, A.E., & Richmond, B.M., (2015) National assessment of shoreline change—Historical shoreline change along the north coast of Alaska, U.S.–Canadian border to Icy Cape: *U.S. Geological Survey Open-File Report 2015*–1048, 96 p., https://dx.doi.org/10.3133/ofr20151048.

Gibbs, A. E., & Richmond, B. M. (2017). National assessment of shoreline change—summary statistics for updated vector shorelines and associated shoreline change data for the north coast of Alaska. *US Geological Survey Open-File Report*, *1107*(2017), 21.

Gilbert, G. L., Kanevskiy, M., & Murton, J. B. (2016). Recent advances (2008–2015) in the study of ground ice and cryostratigraphy. *Permafrost and Periglacial Processes*, *27*(4), 377-389. https://doi.org/10.1002/ppp.1912

Gorelick, N., Hancher, M., Dixon, M., Ilyushchenko, S., Thau, D., & Moore, R. (2017). Google Earth Engine: Planetary-scale geospatial analysis for everyone. *Remote sensing of Environment*, *202*, 18-27. https://doi.org/10.1016/j.rse.2017.06.031

Gorokhovich, Y., & Leiserowiz, A. (2012). Historical and future coastal changes in Northwest Alaska. *Journal of Coastal Research*, *28*(1A), 174-186. https://doi.org/10.2112/JCOASTRES-D-11-00031.1

Grigoriev, M. N., Razumov, S. O., Kunitzkiy, V. V., & Spektor, V. B. (2006). Dynamics of the Russian East Arctic Sea coast: Major factors, regularities and tendencies. *Earth's Cryosphere, X*, *4*, 74-94.

Grigoriev, M. N., Kunitsky, V. V., Chzhan, R. V., & Shepelev, V. V. (2009). On the variation in geocryological, landscape and hydrological conditions in the Arctic zone of East Siberia in connection with climate warming. *Geography and Natural Resources*, *30*(2), 101-106. https://doi.org/10.1016/j.gnr.2009.06.002

Günther, F., Overduin, P. P., Sandakov, A. V., Grosse, G., & Grigoriev, M. N. (2013). Short-and long-term thermo-erosion of ice-rich permafrost coasts in the Laptev Sea region. *Biogeosciences*, *10*, 4297-4318. https://doi.org/10.5194/bg-10-4297-2013

Günther, F., Overduin, P. P., Yakshina, I. A., Opel, T., Baranskaya, A. V., & Grigoriev, M. N. (2015). Observing Muostakh disappear: permafrost thaw subsidence and erosion of a ground-ice-rich island in response to arctic summer warming and sea ice reduction. *The Cryosphere*, *9*(1), 151-178. https://doi.org/10.5194/tc-9-151-2015

Hakkinen, S., Proshutinsky, A., & Ashik, I. (2008). Sea ice drift in the Arctic since the 1950s. *Geophysical Research Letters*, *35*(19), 1–5. https://doi.org/10.1029/2008GL034791

Harris S.A., French H.M., Heginbottom J.A., Johnston G.H., Ladanyi B., Sego D.C., Van Everdingen R.O. (1988). Glossary of Permafrost and Related Ground-Ice Terms. *National Research Council of Canada, Ottawa, Technical Memorandum* No. 142,

Heginbottom, J. A. (1984). Continued headwall retreat of a retrogressive thaw flow slide, eastern Melville Island, Northwest Territories. *Geological Survey of Canada, Current Research part B, Paper*, 363-365. https://doi.org/10.4095/119594

Hequette, A., & Barnes, P. W. (1990). Coastal retreat and shoreface profile variations in the Canadian Beaufort Sea. *Marine Geology*, *91*(1-2), 113-132. https://doi.org/10.1016/0025-3227(90)90136-8

Hoque, M. A., & Pollard, W. H. (2009). Arctic coastal retreat through block failure. *Canadian Geotechnical Journal*, *46*(10), 1103–1115. https://doi.org/10.1139/T09-058

Hoque, M. A., & Pollard, W. H. (2016). Stability of permafrost dominated coastal cliffs in the Arctic. *Polar Science*, *10*(1), 79–88. https://doi.org/10.1016/j.polar.2015.10.004

Hugelius, G., Strauss, J., Zubrzycki, S., Harden, J.W., Schuur, E., Ping, C.L., Schirrmeister, L., Grosse, G., Michaelson, G.J., Koven, C.D. and O'Donnell, J.A., (2014). Estimated stocks of circumpolar permafrost carbon with quantified uncertainty ranges and identified data gaps. *Biogeosciences*, 11(23), pp.6573-6593. https://doi.org/10.5194/bg-11-6573-2014

Immerzeel, W. W., Kraaijenbrink, P. D. A., Shea, J. M., Shrestha, A. B., Pellicciotti, F., Bierkens, M. F. P., & De Jong, S. M. (2014). High-resolution monitoring of Himalayan glacier dynamics using unmanned aerial vehicles. *Remote Sensing of Environment*, *150*, 93-103. https://doi.org/10.1016/j.rse.2014.04.025

Irrgang, A. M., Lantuit, H., Manson, G. K., Günther, F., Grosse, G., & Overduin, P. P. (2018). Variability in rates of coastal change along the Yukon coast, 1951 to 2015. *Journal of Geophysical Research: Earth Surface*, *123*(4), 779-800. https://doi.org/10.1002/2017JF004326

James, T.S., Henton, J.A., Leonard, L.J., Darlington, A., Forbes, D.L., and Craymer, M., 2014). Relative Sea level Projections in Canada and the Adjacent Mainland United States; *Geological Survey of Canada*, Open File 7737, 72 p. https://doi.org/10.4095/295574

James, M. R., & Robson, S. (2012). Straightforward reconstruction of 3D surfaces and topography with a camera: Accuracy and geoscience application. *Journal of Geophysical Research: Earth Surface*, *117*(F3). https://doi.org/10.1029/2011JF002289

Johannessen, O. M., Kuzmina, S. I., Bobylev, L. P., & Miles, M. W. (2016). Surface air temperature variability and trends in the Arctic: new amplification assessment and regionalisation. *Tellus A: Dynamic Meteorology and Oceanography*, *68*(1), 28234. https://doi.org/10.3402/tellusa.v68.28234

Jones, B. M., Hinkel, K. M., Arp, C. D., & Eisner, W. R. (2008). Modern erosion rates and loss of coastal features and sites, Beaufort Sea coastline, Alaska. *Arctic*, *61*(4), 361–372. https://doi.org/10.14430/arctic44

Jones, B. M., Arp, C. D., Jorgenson, M. T., Hinkel, K. M., Schmutz, J. A., & Flint, P. L. (2009a). Increase in the rate and uniformity of coastline erosion in Arctic Alaska. *Geophysical Research Letters*, *36*(3). https://doi.org/10.1029/2008GL036205

Jones, B. M., Arp, C. D., Beck, R. A., Grosse, G., Webster, J. M., & Urban, F. E. (2009b). Erosional history of Cape Halkett and contemporary monitoring of bluff retreat, Beaufort Sea coast, Alaska. *Polar Geography*, *32*(3-4), 129-142. https://doi.org/10.1080/10889370903486449

Jones, B. M., Farquharson, L. M., Baughman, C. A., Buzard, R. M., Arp, C. D., Grosse, G., ... & Kasper, J. L. (2018). A decade of remotely sensed observations highlight complex processes linked to coastal permafrost bluff erosion in the Arctic. *Environmental Research Letters*, *13*(11), 115001. https://doi.org/10.1088/1748-9326/aae471

Jones, M. K. W., Pollard, W. H., & Jones, B. M. (2019). Rapid initialization of retrogressive thaw slumps in the Canadian high Arctic and their response to climate and terrain factors. *Environmental Research Letters*, *14*(5), 055006. https://doi.org/10.1088/1748-9326/ab12fd

Jorgenson, M. T., Shur, Y. L., & Pullman, E. R. (2006). Abrupt increase in permafrost degradation in Arctic Alaska. *Geophysical Research Letters*, *33*(2), 2–5. https://doi.org/10.1029/2005GL024960

Kobayashi, N. (1985). Formation of thermoerosional niches into frozen bluffs due to storm surges on the Beaufort Sea coast. *Journal of Geophysical Research: Oceans*, *90*(C6), 11983-11988. https://doi.org/10.1029/JC090iC06p11983

Kobayashi, N., & Aktan, D. (1986). Thermoerosion of frozen sediment under wave action. *Journal of waterway, port, coastal, and ocean engineering*, *112*(1), 140-158. https://doi.org/10.1061/(ASCE)0733-950X(1986)112:1(140)

Kokelj, S. V., & Lewkowicz, A. G. (1999). Salinization of permafrost terrain due to natural geomorphic disturbance, Fosheim Peninsula, Ellesmere Island. *Arctic*, 372-385. https://doi.org/10.14430/arctic942

Kokelj, S. V., Lantz, T. C., Kanigan, J., Smith, S. L., & Coutts, R. (2009). Origin and polycyclic behaviour of tundra thaw slumps, Mackenzie Delta region, Northwest Territories, Canada. *Permafrost and Periglacial Processes*, *20*(2), 173-184. https://doi.org/10.1002/ppp.642

Kokelj, S. V., & Jorgenson, M. T. (2013). Advances in thermokarst research. *Permafrost and Periglacial Processes*, *24*(2), 108-119. https://doi.org/10.1002/ppp.1779

Kokelj, S. V., Lacelle, D., Lantz, T. C., Tunnicliffe, J., Malone, L., Clark, I. D., & Chin, K. S. (2013). Thawing of massive ground ice in mega slumps drives increases in stream sediment and solute flux across a range of watershed scales. *Journal of Geophysical Research: Earth Surface*, *118*(2), 681-692. https://doi.org/10.1002/jgrf.20063

Kokelj, S. V., Tunnicliffe, J., Lacelle, D., Lantz, T. C., Chin, K. S., & Fraser, R. (2015). Increased precipitation drives mega slump development and destabilization of ice-rich permafrost terrain, northwestern Canada. *Global and Planetary Change*, *129*, 56-68. https://doi.org/10.1016/j.gloplacha.2015.02.008

Kokelj, S. V., Lantz, T. C., Tunnicliffe, J., Segal, R., & Lacelle, D. (2017). Climate-driven thaw of permafrost preserved glacial landscapes, northwestern Canada. *Geology*, *45*(4), 371-374. https://doi.org/10.1130/G38626.1

Lacelle, D., Bjornson, J., Lauriol, B., Clark, I. D., & Troutet, Y. (2004). Segregated-intrusive ice of subglacial meltwater origin in retrogressive thaw flow headwalls, Richardson Mountains, NWT, Canada. *Quaternary Science Reviews*, *23*(5-6), 681-696. https://doi.org/10.1016/j.quascirev.2003.09.005

Lacelle, D., Brooker, A., Fraser, R. H., & Kokelj, S. V. (2015). Distribution and growth of thaw slumps in the Richardson Mountains–Peel Plateau region, northwestern Canada. *Geomorphology*, *235*, 40-51. https://doi.org/10.1016/j.geomorph.2015.01.024

Lantuit, H., & Pollard, W. H. (2005). Temporal stereophotogrammetric analysis of retrogressive thaw slumps on Herschel Island, Yukon Territory. https://doi.org/10.5194/nhess-5-413-2005

Lantuit, H., & Pollard, W. H. (2008). Fifty years of coastal erosion and retrogressive thaw slump activity on Herschel Island, southern Beaufort Sea, Yukon Territory,

Canada. *Geomorphology*, *95*(1-2), 84-102. https://doi.org/10.1016/j.geomorph.2006.07.040

Lantuit, H., Atkinson, D., Paul Overduin, P., Grigoriev, M., Rachold, V., Grosse, G., & Hubberten, H. W. (2011). Coastal erosion dynamics on the permafrost-dominated Bykovsky Peninsula, north Siberia, 1951–2006. *Polar Research*, *30*(1), 7341. https://doi.org/10.3402/polar.v30i0.7341

Lantuit, H., Overduin, P. P., Couture, N., Wetterich, S., Aré, F., Atkinson, D., ... & Graves-Gaylord, A. (2012a). The Arctic coastal dynamics database: a new classification scheme and statistics on Arctic permafrost coastlines. *Estuaries and Coasts*, *35*(2), 383-400. https://doi.org/10.1007/s12237-010-9362-6

Lantuit, H., Pollard, W. H., Couture, N., Fritz, M., Schirrmeister, L., Meyer, H., & Hubberten, H. W. (2012b). Modern and late Holocene retrogressive thaw slump activity on the Yukon coastal plain and Herschel Island, Yukon Territory, Canada. *Permafrost and Periglacial Processes*, *23*(1), 39-51. https://doi.org/10.1002/ppp.1731

Lantuit, H., Overduin, P. P., & Wetterich, S. (2013). Recent progress regarding permafrost coasts. *Permafrost and Periglacial Processes*, *24*(2), 120–130. https://doi.org/10.1002/ppp.1777

Lantuit, H. (2016, March 29). What is permafrost? Retrieved January 17, 2020, from https://ipa.arcticportal.org/publications/occasional-publications/what-is-permafrost

Lantz, T. C., & Kokelj, S. V. (2008). Increasing rates of retrogressive thaw slump activity in the Mackenzie Delta region, NWT, Canada. Geophysical Research Letters, 35(6). https://doi.org/10.1029/2007GL032433

Letterly, A. (2018, December 20). The Recent State of Permafrost, 2017-2018. *Global Cryosphere Watch*. (Accessed 2019, December 1). Retrieved from: https://globalcryospherewatch.org/assessments/permafrost/

Lewkowicz, A. G. (1987A). Headwall retreat of ground-ice slumps, Banks Island, Northwest Territories. *Canadian Journal of Earth Sciences*, *24*(6), 1077-1085. https://doi.org/10.1139/e87-105

Lewkowicz, A. G. (1987B). Nature and importance of thermokarst processes, Sand Hills moraine, Banks Island, Canada. Geografiska Annaler: Series A, Physical Geography, 69(2), 321-327. https://doi.org/10.1080/04353676.1987.11880218

Lewkowicz, A. G., & Way, R. G. (2019). Extremes of summer climate trigger thousands of thermokarst landslides in a High Arctic environment. *Nature communications*, *10*(1), 1329. https://doi.org/10.1038/s41467-019-09314-7

Liljedahl, A. K., Boike, J., Daanen, R. P., Fedorov, A. N., Frost, G. V., Grosse, G., … Zona, D. (2016). Pan-Arctic ice-wedge degradation in warming permafrost and influence on tundra hydrology. *Nature Geoscience*, *9*(April), 312 – 318. https://doi.org/10.1038/ngeo2674

Lim, M., Dunning, S. A., Burke, M., King, H., & King, N. (2015). Quantification and implications of change in organic carbon bearing coastal dune cliffs: A multiscale analysis from the Northumberland coast, UK. *Remote Sensing of Environment*, *163*, 1-12. https://doi.org/10.1016/j.rse.2015.01.034

Lowe, D. G. (2004). Distinctive image features from scale-invariant keypoints. *International journal of computer vision*, *60*(2), 91-110. https://doi.org/10.1023/B:VISI.0000029664.99615.94

Lucieer, A., Jong, S. M. D., & Turner, D. (2014). Mapping landslide displacements using Structure from Motion (SfM) and image correlation of multi-temporal UAV photography. *Progress in Physical Geography*, *38*(1), 97-116. https://doi.org/10.1177%2F0309133313515293

Luo, J., Niu, F., Lin, Z., Liu, M., & Yin, G. (2019). Recent acceleration of thaw slumping in permafrost terrain of Qinghai-Tibet Plateau: An example from the Beiluhe Region. *Geomorphology*, *341*, 79-85. https://doi.org/10.1016/j.geomorph.2019.05.020

Mackay, J. R. (1963). *The Mackenzie Delta Area, N.W.T.* Queen's printer. Retrieved from https://books.google.co.uk/books?id=MWfIMgAACAAJ

Mackay, J. R. (1966). Segregated epigenetic ice and slumps in permafrost, Mackenzie Delta area, NWT. *Geographical Bulletin*, 8, 59-80.

Mackay, J. R. (1971). *Canadian Journal of Earth Sciences*, *8*(4), 397-422. The origin of massive icy beds in permafrost, western Arctic coast, Canada. https://doi.org/10.1139/e71-043

Mackay, J. R. (1986). Fifty years (1935-1985) of coastal retreat west of Tuktoyaktuk, District of Mackenzie. *Geological Survey of Canada*, 727-735. https://doi.org/10.4095/120445

Mackay, J. R., & Dallimore, S. R. (1992). Massive ice of the Tuktoyaktuk area, western Arctic coast, Canada. *Canadian Journal of Earth Sciences*, *29*(6), 1235–1249. https://doi.org/10.1139/e92-099

Mann, M. E., Rahmstorf, S., Kornhuber, K., Steinman, B. A., Miller, S. K., & Coumou, D. (2017). Influence of anthropogenic climate change on planetary wave resonance and extreme weather events. *Scientific Reports*, *7*, 45242. https://doi.org/10.1038/srep45242

Manson, G. K., Solomon, S. M., Forbes, D. L., Atkinson, D. E., & Craymer, M. (2005). Spatial variability of factors influencing coastal change in the western Canadian Arctic. *Geo-Marine Letters*, *25*(2-3), 138-145. https://doi.org/10.1007/s00367-004-0195-9

Manson, G. K., & Solomon, S. M. (2007). Past and future forcing of Beaufort Sea coastal change. *Atmosphere-Ocean*, *45*(2), 107-122. https://doi.org/10.3137/ao.450204

Marchenko, S., & Etzelmuller, B. (2013). Permafrost: Formation and Distribution, Thermal and Mechanical Properties. Treatise on Geomorphology, 8, 202–222. https://doi.org/10.1016/B978-0-12-374739-6.00207-4

Markus, T., Stroeve, J.C. and Miller, J. (2009). Recent changes in Arctic sea ice melt onset, freeze up, and melt season length. *Journal of Geophysical Research: Oceans*, *114*(C12). https://doi.org/10.1029/2009JC005436

McClearn, M. (2019). Tuktoyaktuk teetering: Hamlet's shoreline erosion a warning to rest of Canada's North. *The Globe and Mail, Canada.* (https://www.theglobeandmail.com/canada/article-tuktoyaktuk-teetering-hamlets-shoreline-erosion-a-warning-to-rest-of/) (Last accessed: 3 April 2020).

Mars, J. C., & Houseknecht, D. W. (2007). Quantitative remote sensing study indicates doubling of coastal erosion rate in past 50 yr along a segment of the Arctic coast of Alaska. *Geology*, *35*(7), 583-586. https://doi.org/10.1130/G23672A.1

McGuire, A. D., Macdonald, R. W., Schuur, E. A., Harden, J. W., Kuhry, P., Hayes, D. J., ... & Heimann, M. (2010). The carbon budget of the northern cryosphere region. *Current Opinion in Environmental Sustainability*, *2*(4), 231-236. https://doi.org/10.1016/j.cosust.2010.05.003

McRoberts, E. C., & Morgenstern, N. R. (1974). Stability of slopes in frozen soil, Mackenzie Valley, NWT. *Canadian Geotechnical Journal*, *11*(4), 554-573. https://doi.org/10.1139/t74-058

Moorman, B. J., Michel, F. A., & Wilson, A. T. (1998, June). The development of tabular massive ground ice at Peninsula Point, NWT, Canada. In *Proceedings of the Seventh International Conference on Permafrost, Lewkowicz AG, Allard M (eds). Collection Nordicanada* (No. 57, pp. 757-762).

Mudryk, L., Brown, R., Derksen, C., Luojus, K., Decharme, B., and Helfrich, S. (2009). Terrestrial Snow Cover. *Arctic Report Card 2019*, J. Richter-Menge, M. L. Druckenmiller, and M. Jeffries, Eds., http://www.arctic.noaa.gov/Report-Card

Muja, M., & Lowe, D. G. (2009). Fast approximate nearest neighbors with automatic algorithm configuration. *VISAPP (1)*, *2*(331-340), 2. https://doi.org/10.5220/0001787803310340

Murton, J. B., Whiteman, C. A., Waller, R. I., Pollard, W. H., Clark, I. D., & Dallimore, S. R. (2005). Basal ice facies and supraglacial melt-out till of the Laurentide Ice Sheet, Tuktoyaktuk Coastlands, western Arctic Canada. *Quaternary Science Reviews*, *24*(5–6), 681–708. https://doi.org/10.1016/j.quascirev.2004.06.008

Murton, J. B. (2009). Stratigraphy and palaeoenvironments of Richards Island and the eastern Beaufort Continental Shelf during the last glacial-interglacial cycle. *Permafrost and Periglacial Processes*, *20*(2), 107-125. https://doi.org/10.1002/ppp.647

Nakamura, Y. (1989). A method for dynamic characteristics estimation of subsurface using microtremor on the ground surface. *Railway Technical Research Institute, Quarterly Reports*, *30*(1). https://doi.org/10.1109/IGARSS.2015.7326874

Novikova, A., Belova, N., Baranskaya, A., Aleksyutina, D., Maslakov, A., Zelenin, E., ... & Ogorodov, S. (2018). Dynamics of permafrost coasts of Baydaratskaya Bay (Kara Sea) based on multi-temporal remote sensing data. *Remote Sensing*, *10*(9), 1481. https://doi.org/10.3390/rs10091481

Obanawa, H. (2015, July). Quantitative measurement of the topographic change at overhanging sea cliff with small UAV survey system. In *2015 IEEE International Geoscience and Remote Sensing Symposium (IGARSS)* (pp. 4684-4687). IEEE. https://doi.org/10.1109/IGARSS.2015.7326874

Obu, J., Lantuit, H., Fritz, M., Pollard, W. H., Sachs, T., & Günther, F. (2016). Relation between planimetric and volumetric measurements of permafrost coast erosion: a case study from Herschel Island, western Canadian Arctic. *Polar Research*, *35*(1), 30313. https://doi.org/10.3402/polar.v35.30313

Obu, J., Lantuit, H., Grosse, G., Günther, F., Sachs, T., Helm, V., & Fritz, M. (2017). Coastal erosion and mass wasting along the Canadian Beaufort Sea based on annual airborne LiDAR elevation data. *Geomorphology*, *293*, 331-346. https://doi.org/10.1016/j.geomorph.2016.02.014

Orgel, C., Hauber, E., van Gasselt, S., Reiss, D., Johnsson, A., Ramsdale, J. D., ... & Balme, M. R. (2019). Grid Mapping the Northern Plains of Mars: A New Overview of Recent Water-and Ice-Related Landforms in Acidalia Planitia. *Journal of Geophysical Research: Planets*, *124*(2), 454-482. https://doi.org/10.1029/2018JE005664

Overland, J., Dunlea, E., Box, J. E., Corell, R., Forsius, M., Kattsov, V., ... & Wang, M. (2019). The urgency of Arctic change. *Polar Science*, *21*, 6-13. https://doi.org/10.1016/j.polar.2018.11.008

Peltier, W. R. (1994). Ice age paleotopography. *Science*, *265*(5169), 195-201. https://doi.org/10.1126/science.265.5169.195

Ping, C. L., Michaelson, G. J., Guo, L., Jorgenson, M. T., Kanevskiy, M., Shur, Y., ... & Liang, J. (2011). Soil carbon and material fluxes across the eroding Alaska Beaufort Sea coastline. *Journal of Geophysical Research: Biogeosciences*, *116*(G2). https://doi.org/10.1029/2010JG001588

Pizhankova, E. I. (2016). Modern climate change at high latitudes and its influence on the coastal dynamics of the Dmitriy Laptev Strait area. *Earths Cryosphere*, *20*(1), 46-59.

Pollard, W. H. (1990). The nature and origin of ground ice in the Herschel Island area, Yukon Territory. In Proceedings, Fifth Canadian Permafrost Conference, Québec (pp. 23-30).

Pollard, W. H. (2000). Distribution and characterization of ground ice on Fosheim Peninsula, Ellesmere Island, Nunavut. *Environmental Response to Climate Change in the Canadian High Arctic*, *529*, 207-233. https://doi.org/10.4095/211959

Quick Terrain Modeller v8.0.5.2. (2019). Retrieved from http://appliedimagery.com/

Rachold, V., Grigoriev, M. N., Are, F. E., Solomon, S., Reimnitz, E., Kassens, H., & Antonow, M. (2000). Coastal erosion vs riverline sediment discharge in the Arctic shelfx seas. *International Journal of Earth Sciences*, *89*(3), 450–459. https://doi.org/10.1007/s005310000113

Radosavljevic, B., Lantuit, H., Pollard, W., Overduin, P., Couture, N., Sachs, T., ... & Fritz, M. (2016). Erosion and flooding—threats to coastal infrastructure in the Arctic: a case study from Herschel Island, Yukon Territory, Canada. *Estuaries and Coasts*, *39*(4), 900-915. https://doi.org/10.1007/s12237-015-0046-0

Ramage, J. L., Irrgang, A. M., Herzschuh, U., Morgenstern, A., Couture, N., & Lantuit, H. (2017). Terrain controls on the occurrence of coastal retrogressive thaw slumps along the Yukon Coast, Canada. *Journal of Geophysical Research: Earth Surface*, *122*(9), 1619-1634. https://doi.org/10.1002/2017JF004231

Ramage, J. L., Irrgang, A. M., Morgenstern, A., & Lantuit, H. (2018). Increasing coastal slump activity impacts the release of sediment and organic carbon into the Arctic Ocean. *Biogeosciences*, *15*(5), 1483-1495. https://doi.org/10.5194/bg-15-1483-2018

Rampton, V. N., & Mackay, J. R. (1971). Massive ice and icy sediments throughout the Tuktoyaktuk peninsula, Richards Island, and nearby areas, District of Mackenzie. *Geological Survey of Canada*. https://doi.org/10.4095/100645

Ravens, T. M., Jones, B. M., Zhang, J., Arp, C. D., & Schmutz, J. A. (2012). Process-Based Coastal Erosion Modeling for Drew Point, North Slope, Alaska. *American Society of Civil Engineers*. https://doi.org/10.1061/(ASCE)WW.1943-5460.0000106

Razumov, S.O. and Grigoriev, M.N., 2011. Coastal erosion as a destabilizing factor of carbonate balance in the East Siberian Arctic seas. EARTH, 15(4), pp.65-68.

Robinson, S.D., 2000: Thaw-slump-derived thermokarst near Hot Weather Creek, Ellesmere Island, Nunavut; in Environmental Response to Climate Change in the Canadian High Arctic, (ed.) M. Garneau and B.T. Alt; *Geological Survey of Canada, Bulletin* 529, p. 335–345

Rudy, A. C. A., Lamoureux, S. F., Kokelj, S. V., Smith, I. R., & England, J. H. (2017). Accelerating Thermokarst Transforms Ice-Cored Terrain Triggering a Downstream Cascade to the Ocean. *Geophysical Research Letters*, *44*(21), 11-080. https://doi.org/10.1002/2017GL074912

Segal, R. A., Lantz, T. C., & Kokelj, S. V. (2016). Acceleration of thaw slump activity in glaciated landscapes of the Western Canadian Arctic. *Environmental Research Letters*, *11*(3), 034025. https://doi.org/10.1088/1748-9326/11/3/034025

Schuur, E. A. G., McGuire, A. D., Grosse, G., Harden, J. W., Hayes, D. J., Hugelius, G., … Kuhry, P. (2015). Climate change and the permafrost carbon feedback. *Nature*, *520*(January 2016), 171–179. https://doi.org/10.1038/nature14338

Scheib, A. J. (2014). The application of passive seismic to estimate cover thickness in greenfields areas of western Australia—method, data interpretation and recommendations. *Geological Survey of Western Australia, Record*, *201*.

Schweiger, A., Lindsay, R., Zhang, J., Steele, M., Stern, H., & Kwok, R. (2011). Uncertainty in modeled Arctic sea ice volume. *Journal of Geophysical Research: Oceans*, *116*(C8). https://doi.org/10.1029/2011JC007084

Seitz, S. M., Curless, B., Diebel, J., Scharstein, D., & Szeliski, R. (2006, June). A comparison and evaluation of multi-view stereo reconstruction algorithms. In *2006 IEEE computer society conference on computer vision and pattern recognition (CVPR'06)* (Vol. 1, pp. 519-528). IEEE. https://doi.org/10.1109/CVPR.2006.19

Séjourné, A., Costard, F., Gargani, J., Soare, R. J., & Marmo, C. (2012). Evidence of an eolian ice-rich and stratified permafrost in Utopia Planitia, Mars. *Planetary and Space Science*, *60*(1), 248-254. https://doi.org/10.1016/j.pss.2011.09.004

Semiletov, I., Pipko, I., Gustafsson, Ö., Anderson, L. G., Sergienko, V., Pugach, S., ... & Andersson, A. (2016). Acidification of East Siberian Arctic Shelf waters through addition of freshwater and terrestrial carbon. *Nature Geoscience*, *9*(5), 361. https://doi.org/10.1038/ngeo2695

Serreze, M. C., & Francis, J. A. (2006). The arctic amplification debate. *Climatic Change*, *76*(3-4), 241–264. https://doi.org/10.1007/s10584-005-9017-y

Sinitsyn, A., Guegan, E., Shabanova, N., Kokin, O., & Ogorodov, S. (2019). Fifty four years of coastal erosion and hydrometeorological parameters in the Varandey region, Barents Sea. *Coastal Engineering*, 103610. https://doi.org/10.1016/j.coastaleng.2019.103610

Smith, M. W., Carrivick, J. L., & Quincey, D. J. (2016). Structure from motion photogrammetry in physical geography. *Progress in Physical Geography*, *40*(2), 247-275. https://doi.org/10.1177%2F0309133315615805

Snavely, N., Seitz, S. M., & Szeliski, R. (2008). Modeling the world from internet photo collections. *International journal of computer vision*, *80*(2), 189-210. https://doi.org/10.1007/s11263-007-0107-3

Soare, R. J., Séjourné, A., Pearce, G., Costard, F., & Osinski, G. R. (2011). The Tuktoyaktuk Coastlands of northern Canada: A possible “wet” periglacial analog of Utopia Planitia, Mars. *Geol. Soc. Am. Spec. Pap*, *483*, 203-218. https://doi.org/10.1130/2011.2483(13)

Solomon, S. M. (2005). Spatial and temporal variability of shoreline change in the Beaufort-Mackenzie region, Northwest Territories, Canada. *Geo-Marine Letters*, *25*(2-3), 127-137. https://doi:10.1007/s00367-004-0194

Steele, M., Ermold, W., & Zhang, J. (2008). Arctic Ocean surface warming trends over the past 100 years. *Geophysical Research Letters*, *35*(2), 1–6. https://doi.org/10.1029/2007GL031651

Stroeve, J.C., Markus, T., Boisvert, L., Miller, J. and Barrett, A. (2014). Changes in Arctic melt season and implications for sea ice loss. *Geophysical Research Letters*, *41*(4), pp.1216-1225. https://doi.org/10.1002/2013GL058951

Tallett-Williams, S., Gosh, B., Wilkinson, S., Fenton, C., Burton, P., Whitworth, M., ... & Novellis, V. (2016). Site amplification in the Kathmandu Valley during the 2015 M7. 6 Gorkha, Nepal earthquake. *Bulletin of Earthquake Engineering*, *14*(12), 3301-3315. https://doi.org/10.1007/s10518-016-0003-8

Ulrich, M., Morgenstern, A., Günther, F., Reiss, D., Bauch, K. E., Hauber, E., ... & Schirrmeister, L. (2010). Thermokarst in Siberian ice-rich permafrost: Comparison to asymmetric scalloped depressions on Mars. *Journal of Geophysical Research: Planets*, *115*(E10). https://doi.org/10.1029/2010JE003640

van der Bilt, W. G., D'Andrea, W. J., Werner, J. P., & Bakke, J. (2019). Early Holocene temperature oscillations exceed amplitude of observed and projected warming in Svalbard lakes. *Geophysical Research Letters*. https://doi.org/10.1029/2019GL084384

Vasiliev, A. A. (2003, July). Permafrost controls of coastal dynamics at the Marre-Sale key site, Western Yamal. In *Proceedings of the 8th International Conference on Permafrost* (Vol. 2, pp. 1173-1178). https://doi.org/10.1007/s00367-004-0192-z

Vasiliev, A., Kanevskiy, M., Cherkashov, G., & Vanshtein, B. (2005). Coastal dynamics at the Barents and Kara Sea key sites. *Geo-Marine Letters*, *25*(2-3), 110-120. https://doi.org/10.1007/s00367-004-0192-z

Vonk, J. E., Sánchez-García, L., Van Dongen, B. E., Alling, V., Kosmach, D., Charkin, A., ... & Eglinton, T. I. (2012). Activation of old carbon by erosion of coastal and subsea permafrost in Arctic Siberia. *Nature*, *489*(7414), 137-140. https://doi.org/10.1038/nature11392

Whalen, D., Fraser, R., and MacLeod, R. (2017). The acceleration of change – how UAV technology is being used to better understand coastal permafrost landscapes in the Mackenzie-Beaufort Region, NT, ArcticNet, available at:

http://www.arcticnet.ulaval.ca/ pdf/media/IRIS-1-newsletter-Dec-2017.pdf (last access: 22 January 2020).

Wang, B., Paudel, B., & Li, H. (2009). Retrogression characteristics of landslides in fine-grained permafrost soils, Mackenzie Valley, Canada. *Landslides*, *6*(2), 121-127. https://doi.org/10.1007/s10346-009-0150-y

Warner, N., Gupta, S., Kim, J. R., Lin, S. Y., & Muller, J. P. (2010). Hesperian equatorial thermokarst lakes in Ares Vallis as evidence for transient warm conditions on Mars. *Geology*, *38*(1), 71-74. https://doi.org/10.1130/G30579.1

Wegner, C., Bennett, K. E., de Vernal, A., Forwick, M., Fritz, M., Heikkilä, M., ... & O'Regan, M. (2015). Variability in transport of terrigenous material on the shelves and the deep Arctic Ocean during the Holocene. *Polar Research*, *34*(1), 24964. https://doi.org/10.3402/polar.v34.24964

Westoby, M. J., Brasington, J., Glasser, N. F., Hambrey, M. J., & Reynolds, J. M. (2012). 'Structure-from-Motion'photogrammetry: A low-cost, effective tool for geoscience applications. *Geomorphology*, *179*, 300-314. https://doi.org/10.1016/j.geomorph.2012.08.021

Westoby, M. J., Lim, M., Hogg, M., Pound, M. J., Dunlop, L., & Woodward, J. (2018). Cost-effective erosion monitoring of coastal cliffs. *Coastal Engineering*, *138*, 152-164. https://doi.org/10.1016/j.coastaleng.2018.04.008

Wobus, C., Anderson, R., Overeem, I., Matell, N., Clow, G., & Urban, F. (2011). Thermal erosion of a permafrost coastline: Improving process-based models using time-lapse photography. *Arctic, Antarctic, and Alpine Research*, *43*(3), 474-484. https://doi.org/10.1657/1938-4246-43.3.474

Yin, J., Griffies, S.M. and Stouffer, R.J. (2010). Spatial variability of sea level rise in twenty-first century projections. *Journal of Climate*, *23*(17), pp.4585-4607. http://dx.doi.org/10.1175/2010JCLI3533.1

Zhang, X., Walsh, J. E., Zhang, J., Bhatt, U. S., & Ikeda, M. (2004). Climatology and interannual variability of Arctic cyclone activity: 1948-2002. *Journal of Climate*, *17*(12), 2300–2317. https://doi.org/10.1175/1520-0442(2004)017<2300:CAIVOA>2.0.CO;2

Zwieback, S., Kokelj, S. V., Günther, F., Boike, J., Grosse, G., & Hajnsek, I. (2018). Sub-seasonal thaw slump mass wasting is not consistently energy limited at the landscape scale. *The Cryosphere*, *12*(2), 549-564. https://doi.org/10.3929/ethz-b-000244496